ONE AND TWO-DIMENSIONAL NMR CHARACTERIZATION OF ORGANOFUNCTIONALIZED SILICA GELS

by

PATRICIA PAULINA AROCA

B.Sc. (Honours) Windsor University, 1989

A THESIS SUBMITTED IN PARTIAL FULFILLMENT OF

THE REQUIREMENTS FOR THE DEGREE OF

DOCTOR OF PHILOSOPHY

in

THE FACULTY OF GRADUATE STUDIES

DEPARTMENT OF CHEMISTRY

We accept this thesis as conforming

to the required standard

THE UNIVERSITY OF BRITISH COLUMBIA

April 1995

(authorization)

In presenting this thesis in partial fulfilment of the requirements for an advanced degree at the University of British Columbia, I agree that the Library shall make it freely available for reference and study. I further agree that permission for extensive copying of this thesis for scholarly purposes may be granted by the head of my department or by his or her representatives. It is understood that copying or publication of this thesis for financial gain shall not be allowed without my written permission.

(Signature)

Department of CHEMISTRY

The University of British Columbia
Vancouver, Canada

Date April 20 / 1995

DE-6 (2/88)

ABSTRACT

An alternative preparation is proposed in this thesis for the synthesis of organofunctionalized silica gels based on the copolymerization of tetraethoxysilane (TEOS) and an organofunctionalized triethoxysilane. The principal analytical techniques used to determine the integrity and distribution of the functionality in the copolymer matrix were solution and solid state NMR.

The model copolymer chosen for these studies is methyltriethoxysilane (MTES)/TEOS. One-dimensional ^{29}Si solid state NMR was used to establish the integrity of the system and relative proportions of the different silicon environments present. Two-dimensional ^{1}H-^{29}Si heteronuclear correlation NMR experiments unambiguously demonstrated that the monomers in the copolymer were "mixed" and not phase-separated.

To quantify the extent of mixing of the two monomers in the copolymer, kinetic studies were undertaken with the objective of determining reactivity ratios for each monomer. The acid catalyzed hydrolysis and dimer formation reactions of the TEOS and MTES monomers were characterized at a number of catalyst concentrations in order to determine the pH independent kinetic rate constants. With both homopolymers well characterized, the hydrolysis and dimer formation kinetic rate constants were determined for the copolymer. From these kinetic data reactivity ratios were calculated which suggest that the MTES/TEOS system tends to form a random copolymer.

One interesting possible application of organofunctionalized silica gels is in the manufacturing of low temperature functionalized glasses. The synthesis of large pieces of glasses from the copolymerization of TEOS and MTES requires the usage of a drying chemical control agent (DCCA) to prevent cracking. The most commonly used DCCA is formamide. Solution NMR was used to determine the integrity and interaction of formamide

in the polymerization process. Another step taken to characterize the suitability of these compounds for the manufacturing of low temperature functionalized glasses was to characterize the thermal stability of numerous organic functionalities by thermal analysis techniques and NMR. Of all the functionalities studied the methyl group had the highest thermal stability, up to 700°C when thermally treated under nitrogen, showing promise for the synthesis of methyl functionalized glasses.

The cross polarization (CP) dynamics of a number of MTES/TEOS copolymers were then studied, to determine the distance range between the methyl group and the fully condensed unfunctionalized silane ($Si(OSi)_4$). These results further support the conclusion that the functionality in the MTES/TEOS copolymer is quite evenly distributed throughout the copolymer matrix.

TABLE OF CONTENTS

LIST OF FIGURES

LIST OF TABLES

LIST OF SYMBOLS

γ	gyromagnetic ratio
σ	chemical shift
υ_o	Larmor frequency
$<\Delta\upsilon^2>$	second moment
ω_o	angular velocity
$\underline{B}_o$	external magnetic field
$\underline{I}$	nuclear spin vector
T_1	spin lattice relaxation time
$\hbar$	Planck's constant / 2π
r_{IS}	distance vector between I and S spins
C_S	Curie constant for the S nucleus
C_{IS}	geometrical constant in equation (1.18)
k_{T1}-k_{T5}	kinetic constants referring to TEOS monomer polymerization reactions
k_{M1}-k_{M4}	kinetic constants referring to the MTES monomer polymerization reactions
k_{C10}	kinetic constant referring to MTES-TEOS codimer formation reaction
t_1	encoding period in a 2D experiment
t_2	detection period in a 2D experiment
T_L	temperature of the lattice
T_S	temperature in the spin locking field
T_{cp}	cross polarization time constant
$T_{1\rho}$	relaxation time constant

Frequently used Abbreviations

CP	cross polarization
DCCA	drying chemical control agent
DSC	differential scanning calorimetry
ETES	ethyltriethoxysilane
FID	free induction decay
MAS	magic angle spinning
MTES	methyltriethoxysilane
PTES	phenyltriethoxysilane
PETES	phenethyltriethoxysilane
TFPTMS	3,3,3-trifluoropropyltrimethoxysilane
TEOS	tetraethoxysilane
TMOS	tetramethoxysilane
TGA	thermogravimetric analysis
TG/MS	thermogravimetric analysis with mass spectroscopy
T-T	TEOS-TEOS homodimer
T-M, M-T	TEOS-MTES codimer
M-M	MTES-MTES homodimer

ACKNOWLEDGEMENT

I would like to thank Dr. Colin Fyfe for his insight and guidance, and for giving me the opportunity to learn more about NMR.

There are a number of other people, whose support, expertise and friendship has been invaluable to me throughout this thesis. Dr. Hiltrud Grondey who has not only helped me improve my writing skills but who has had the time and patience to provide hope and encouragement when things looked a little bleak. Tom Markus whose patience and priceless knowledge concerning Bruker spectrometers has made parts of this thesis possible. I would also like to thank Dr. Ken MacKenzie who did the TG/MS work and Bruker Canada who lent me the 10 mm broad-band probe which was used in the kinetic studies.

I wish to thank my husband Patric, who supported all my decisions and whose unconditional love and confidence are my pillar of strength. I would like to thank my parents, whose encouragement, moral support, model and love give me the strength to strive for my dreams. Gracias por todo! To my brother, Ricardo (Pumpkin), and my sister, Marcella, who are always there for me, thank you for your love, support and example. Finally, I want to thank my sons, Miguel André and Stéphane Tomás who put life into perspective and who have endured the pains of having a mom in a doctorate program.

CHAPTER 1

INTRODUCTION

1.1 IMMOBILIZED REAGENTS

Reagents immobilized onto inert surfaces are of great technical and industrial importance. One of the most common substrates onto which reagents are immobilized is silica gel because it is inexpensive, non-swelling and possesses a very high surface area. Organofunctionalized silanes (R'-Si$(OR)_3$), where R' is the organic functionality determined by the intended application, can be anchored onto silica gel to create immobilized reagents which are usually represented as illustrated in Figure 1.1.

In industry, these immobilized reagents are used to obtain a higher degree of control over product formation. The immobilization of chemical species facilitates the handling of toxic compounds, such as (≡Si-β-pyrrole), as well as the conservation of expensive catalysts, for example (≡Si-O-Si$(CH_2)_2PPh_2$Rh(acac)CO) which is used for hydroformylation reactions.[1.16] Industrial applications involve quantities between 100 to 1000 tons worldwide per year of organofunctionalized silanes in: glass-fiber reinforced thermosetting and thermoplastic resins, mineral-filled rubbers (elastomers), sealants and foundry sand molds.[1.1]

Chromatography columns are often silica gel supports with immobilized functionalities which control the characteristics of the column.[1.6]

Organofunctionalized silanes can act as adhesion promoters between two incompatible surfaces because of the coexistence of both inorganic and organic moieties in the same molecule. For example, dental varnishes and filling materials involve organic polymers adhering to an inorganic surface.

In the textile fiber industry, treatment with organofunctionalized silanes, such as

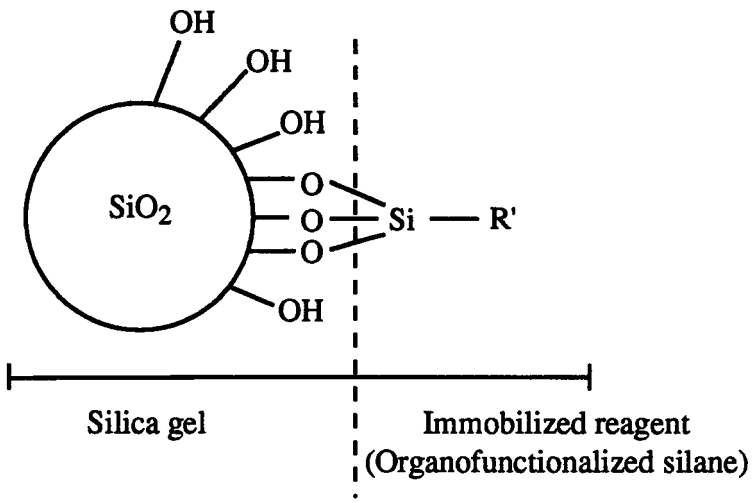

Figure 1.1 - An organofunctionalized silane anchored onto silica gel. On the immobilized reagent, R' is an organofunctionality dictated by the application.

3-(trimethoxysilyl)-propyldimethyloctadecyl ammonium chloride, produces materials which exhibit bactericidal and algicidal activity essential for surgical drapes and other such materials.

Tailoring electrode characteristics, via immobilization of an organofunctionalized silane, presents opportunities to create specific electrocatalytic properties on the surface and provides a fundamentally new approach to the study of electrochemical reactions.[1.17]

The immobilization of highly selective biological species such as enzymes on the surface of a polymer matrix is used commercially to isomerize glucose to fructose and to produce optically pure amino acids.[1.8]

In summary, organofunctionalized silanes play an important role in the manufacturing of many products, in the extraction of chemicals, in the analysis of mixtures and in controlling reactions via immobilized catalysts. The overall objective of the present work is to contribute to the understanding of the formation and structure of these immobilized reagents synthesized by an alternative preparative route.

1.2 CHARACTERIZATION

Silica gel and organofunctionalized siloxane polymers consist of long chains that are coiled up, intertwined and cross-linked with each other. Techniques commonly used in structural studies of ordered crystalline materials, for instance X-ray diffraction, cannot be used to characterize these disordered systems.[1.3] Consequently, their solid state structures in general are poorly characterized.

A number of techniques have been used to gather general structural information about these systems. For example, infrared (IR) and Raman vibrational spectroscopies have been used to study silica gel and organofunctionalized silica gels, both in solution and in the solid state, to obtain information about the relative numbers and types of bonds present. The application of IR and Raman vibrational spectroscopies to these systems is limited by the fact that they cannot differentiate between silicons in two very similar structural units, for example $Si(OSi)_3(OH)$ and $Si(OSi)_4$. Size exclusion chromatography/Fourier transform infrared (SEC/FTIR) spectroscopy has also been used to obtain molecular weight and functional group information about species in solution. However, SEC does not resolve the different silanol species formed during the synthesis of functionalized or unfunctionalized silica gels.[1.42]

The formation of silica gel has been studied invasively using gas chromatography [1.43] and chemical analysis [1.41]. General macroscopic information about the gelation process of silica gel has been obtained using viscosity measurements.[1.43]

However, none of the above mentioned techniques provides a comprehensive structural characterization of amorphous silica gel or related materials.

The pioneering work of Maciel and co-workers in 1980 [1.20] showed that silica gel and functionalized silica gels could be characterized and studied non-invasively in the solid state by nuclear magnetic resonance (NMR) spectroscopy. High resolution NMR

spectroscopy, unlike the above mentioned techniques, clearly differentiates between the different structural units present in silica gel and organofunctionalized silica gel. High resolution solid state NMR spectra providing structural information for amorphous materials not otherwise obtainable have only been possible with recent major advances in solid state NMR spectroscopy. During gel synthesis, ^{29}Si solution NMR is invaluable for studying the kinetic processes since it can resolve all the hydrolysis species and some of the smaller oligomers. Thus, information about both the formation and structure of the final solid product of both native and derivatized silica gels can be obtained using NMR spectroscopy. NMR is the major experimental technique that will be used in this work, and therefore a discussion of solution and solid state NMR spectroscopy is presented in the following section.

1.3 NUCLEAR MAGNETIC RESONANCE

Nuclear magnetic resonance (NMR) spectroscopy deals with the interaction between nuclear magnetic moments and magnetic fields. Nuclei with a spin greater than zero have a nuclear magnetic moment (μ). In an external magnetic field (B_o) a torque is exerted on the nuclear magnetic moment causing it to precess about B_o. The frequency of precession is known as the Larmor frequency (υ_o) and is proportional to the gyromagnetic ratio (γ, a characteristic of each nucleus) and to the external magnetic field as shown in equation (1.1),

$$\omega_o = 2\pi\nu_o = \gamma B_o \tag{1.1}$$

where ω_o is the corresponding angular velocity.

All the nuclei of interest in this research, such as ^1H and ^{29}Si, have a spin quantum number (I) of ½, and since the multiplicity of eigenstates is given by 2I+1, they both have two energy levels. The placement of a sample containing such nuclei in an external magnetic field removes the degeneracy of the eigenstates (energy levels) resulting in a small majority of the magnetic moments being in the more energetically favorable state, i.e. aligned parallel or antiparallel with the external magnetic field depending on whether γ is positive or negative, respectively. The transition between the two energy levels is stimulated by an applied radiofrequency (rf) field (B_1) whose direction is perpendicular to the external magnetic field and whose frequency matches the resonance frequency of the nucleus of interest. The resonance frequency for a nucleus at a specific field strength is dependent on its gyromagnetic ratio. These transitions disturb the equilibrium distribution (M_z) of the spin orientations. The re-establishment of the equilibrium distribution depends on the spin-lattice interactions.

The signal recorded after application of an on-resonance rf pulse as a function of time S(t), is called the free induction decay (FID) and is Fourier transformed to obtain the

frequency spectrum $S(\upsilon)$.

The nucleus most commonly observed is ^{1}H because of its high natural abundance, nearly 100%, and its relatively short spin-lattice relaxation time (T_1). These two attributes make it possible to acquire a spectrum with a good signal-to-noise ratio in a relatively short time period. For nuclei other than protons, for example ^{29}Si, it is often more challenging to acquire an NMR spectrum due to the lower sensitivity, which can be a consequence of a lower natural abundance, lower γ, longer T_1 or in the worst case a combination of all three. The special techniques developed to overcome these experimental difficulties will be discussed in section 1.5. The next section discusses the interactions present for spin ½ nuclei in both solution and solid state NMR.

1.4 BASIC INTERACTION TERMS

At high magnetic fields, the dominant interaction that a nucleus experiences is that with the external magnetic field (Zeeman interaction). In addition to this, the nuclear magnetic moment experiences several other interactions that perturb the energy levels. For a spin ½ nucleus, these include:

1) the through space interaction with other nuclear magnetic dipoles (direct dipole-dipole interactions),
2) the interaction with the electrons of the atom (chemical shielding),
3) the interaction with other nuclear magnetic dipoles through bonds (indirect spin-spin interactions or J couplings).

1.4.1 Zeeman Interaction

The interaction with the external magnetic field (B_o) is called the Zeeman interaction. It represents, at high magnetic fields, the largest term in the Hamiltonian, and it removes the degeneracy of the energy levels.

$$H_z = -\gamma \hbar \bar{I} \cdot \bar{B}_o \quad . \tag{1.2}$$

In equation (1.2), H_z is the Zeeman term of the Hamiltonian, γ is the gyromagnetic ratio, and $\bar{I}$ is the nuclear spin vector.[1.18]

In many cases, the remaining interactions can be considered perturbations to the Zeeman interaction. The relative importance of the different perturbation terms mentioned above varies for different experimental situations; for example at low magnetic fields the Zeeman interaction may no longer be dominant.

1.4.2 Dipole-Dipole Interactions

The direct dipole-dipole interaction is a through space interaction between two nuclei. The dipolar Hamiltonian term (H_D) between two spins, S and I, is [1.18, 1.22]

$$H_D = \frac{\mu_o \gamma_I \gamma_S \hbar^2}{4\pi} \left[\frac{\bar{I}_I \cdot \bar{I}_S}{r_{IS}^3} - \frac{3(\bar{I}_I \cdot \bar{r}_{IS})(\bar{I}_S \cdot \bar{r}_{IS})}{r_{IS}^5} \right] \tag{1.3}$$

where $\bar{r}_{IS}$ refers to the distance vector between the I and S spins; the subscripts I and S of the gyromagnetic ratio (γ) and spin vector ($\bar{I}$) indicates which spin it refers to. Equation (1.3) shows that the dipolar-dipolar interaction is independent of the external magnetic field and is proportional to the gyromagnetic ratio of both nuclei.[1.22]

The interaction that will be of concern in this research is the heteronuclear dipolar interaction, i.e. in equation (1.3) the S spin refers to the sensitive or abundant nuclei and the I spin refers to the insensitive or dilute nuclei.

Equation (1.3) can be expanded by re-expressing the spin operators in terms of raising and lowering operators and in terms of spherical coordinates.[1.22] The final expression is shown below.[1.18]

$$H_D = \frac{\mu_o \gamma_I \gamma_S \hbar^2}{4\pi} [A + B + C + D + E + F]$$

$$A = -\bar{I}_{Sz} \bar{I}_{Iz} (3\cos^2\theta - 1)$$

$$B = \frac{1}{4} [\bar{I}_{S+} \bar{I}_{I-} + \bar{I}_{S-} \bar{I}_{I+}](3\cos^2\theta - 1)$$

$$C = \frac{3}{2} [\bar{I}_{Sz} \bar{I}_{I+} - \bar{I}_{S+} \bar{I}_{Iz}] \sin\theta \cos\theta \, e^{(-i\phi)}$$

$$D = -\frac{3}{2} [\bar{I}_{Sz} \bar{I}_{I-} + \bar{I}_{S-} \bar{I}_{Iz}] \sin\theta \cos\theta \, e^{(i\phi)}$$

$$E = -\frac{3}{4}\bar{I}_{S+}\bar{I}_{I+}\sin^2\theta\, e^{(-2i\phi)}$$

$$F = -\frac{3}{4}\bar{I}_{S-}\bar{I}_{I-}\sin^2\theta\, e^{(2i\phi)}$$

For most practical purposes the resulting expression of the dipolar Hamiltonian can be simplified by omitting the last four terms which describe the weak absorptions at zero and $2\omega_o$ and since the case of interest is the heteronuclear dipolar interaction, where the I and S spins have different Larmor frequencies, the second term can also be omitted.[1.22, 1.30] The simplified form of the heteronuclear Hamiltonian, equation (1.4) illustrates that the dipolar-dipolar interaction has a strong dependence on the distance ($1/r^3_{IS}$) between the two nuclei and depends on the angle (θ_{IS}) between the internuclear vector ($\bar{r}_{IS}$) and the external magnetic field.[1.18, 1.19C, 1.30] The significance of these dependencies will be expanded on in the discussions of magic angle spinning (MAS) and cross polarization in section 1.5.

$$H_{D_{(IS)}} = \frac{\gamma_I\gamma_S\hbar^2\mu_o}{4\pi r_{IS}^3}\,(1-3\cos^2\theta_{IS})\,(\bar{I}_{Iz}\cdot\bar{I}_{Sz}) \qquad (1.4)$$

Of great practical importance is the case of two systems of spins; the heteronuclear dipolar Hamiltonian is now the summation over all the pair-wise interactions, equation (1.5), [1.22]

$$H_D = \frac{\gamma_I\gamma_S\hbar^2\mu_o}{4\pi}\sum_i^{N_i}\sum_m^{N_m}\frac{(1-3\cos^2\theta_{im})}{r_{im}^3}\,(I_{iz}\,I_{mz}) \qquad (1.5)$$

where N_i refers to the number of S (sensitive) spins and N_m refers to the number of I (insensitive) spins.

In solution the fast molecular motion averages the dipole-dipole interactions to zero and therefore they are not directly observed. This is not the case in solid state NMR. For

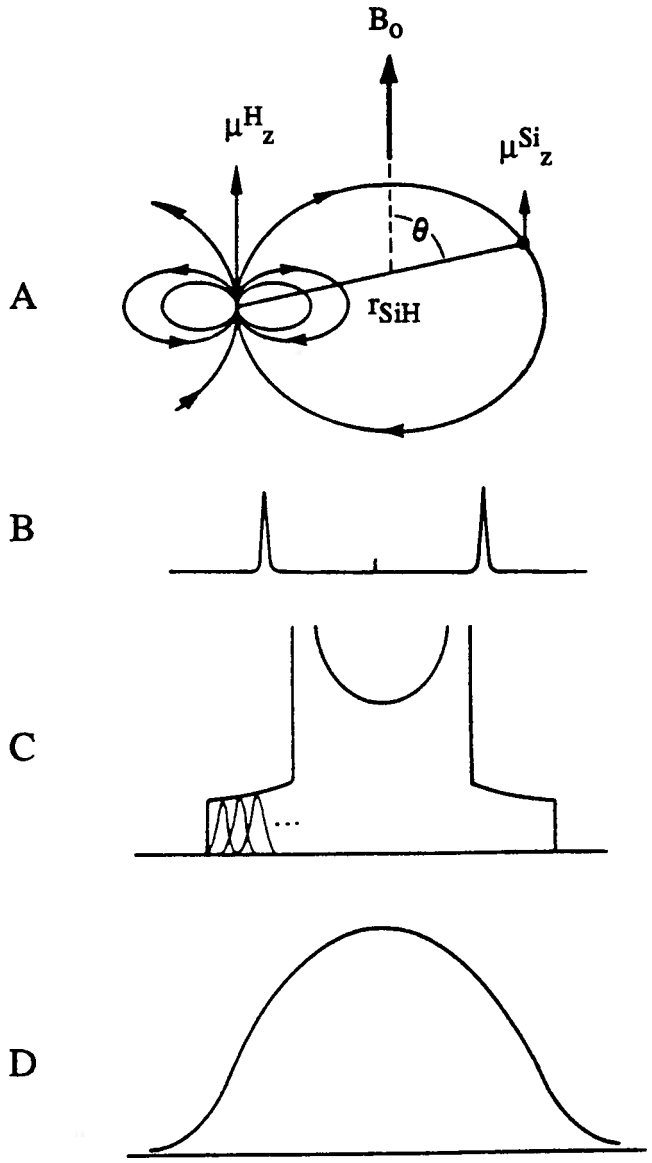

Figure 1.2 - Schematic representation of the effect of the heteronuclear dipolar interaction on a solid state ^{29}Si NMR spectrum.
A) The dipolar interaction between a spin pair of ^{29}Si and ^{1}H nuclei. μ^x_z are the z components of the nuclear magnetic moments.
B) The dipolar interaction of an isolated Si-H pair at one angle to the external magnetic field.
C) The Pake pattern expected for isolated Si-H spin pairs with a distribution of angles to the external magnetic field in a powder sample.
D) An approximate Gaussian lineshape observed for non-isolated Si-H spin pairs considering all the dipolar interactions.[1.23]

example, a ^{29}Si solid state NMR spectrum of an isolated ^{1}H-^{29}Si pair at a fixed angle to the external magnetic field (Figure 1.2A), will consist of two signals, from the effect of the two possible proton spin states. This is illustrated in Figure 1.2B. Isolated ^{1}H-^{29}Si pairs with a distribution of angles (θ) will produce a Pake pattern which is shown in Figure 1.2C. This is the case in a powder sample where all orientations are possible. When the ^{1}H-^{29}Si pairs are not isolated and more than a single pair of dipolar interactions occur, a broad featureless line will be observed (Figure 1.2D). In order to obtain high resolution NMR spectra of solids, magic angle spinning and high power decoupling are used to narrow the broadening produced by dipole-dipole interactions.[1.11]

1.4.3 Chemical Shift Interaction

The induced movement of the electrons surrounding a nucleus by an external magnetic field produces a current which results in a secondary magnetic field. This additional magnetic field adds to the external magnetic field and changes the local field experienced by the nucleus. Different resonance frequencies ("chemical shifts") are observed for nuclei in different local magnetic fields. Therefore the chemical shifts reflect the chemical surrounding of a nucleus, giving a very sensitive probe of the immediate chemical environment of the nucleus.

The chemical shift Hamiltonian (H_{cs}) term is shown in equation (1.6).

$$H_{CS} = \gamma_I \hbar \bar{I} \cdot \delta \cdot \bar{B}_o \tag{1.6}$$

where the chemical shift tensor (δ) describes the orientation and magnitude of this three-dimensional shielding. It is evident from equation (1.6) that the size of the chemical shifts is directly proportional to the external magnetic field ($\bar{B}_o$). In order to facilitate comparison of data from different B_o values, chemical shifts are usually given in ppm (parts per million) of the applied field, and measured with respect to a convenient reference standard.

In terms of the chemical shielding, a single signal will be observed for a nucleus in a single crystal (in the absence of other interactions). The position of this signal will depend on the orientation of the crystal with respect to B_o, as shown in Figure 1.3A. For a powder sample, a characteristic chemical shift anisotropy pattern will be observed depending on the symmetry of the chemical shift tensor and the amount of molecular motion present. Figure 1.3 shows two schematic chemical shift anisotropy patterns for axially symmetric (Figure 1.3B) and nonsymmetric (Figure 1.3C) shieldings. Any molecular motion will cause at least a partial narrowing of the chemical shift tensor powder pattern and possibly a change in its

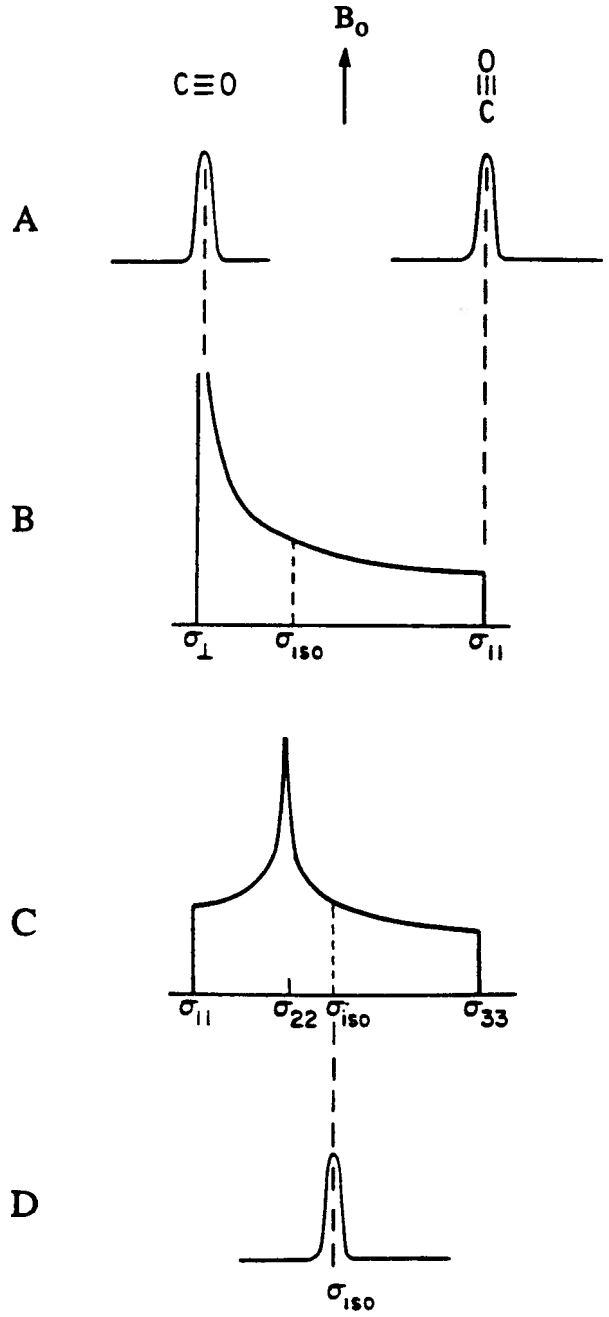

Figure 1.3 - Schematic representation of the effects of the chemical shift anisotropy on solid state NMR spectra(A-C).

A) The chemical shifts observed for two orientations of a carbon monoxide single crystal relative to the external magnetic field.

B) This axially symmetrical chemical shift anisotropy powder pattern is observed for axially symmetrical molecules such as polycrystalline carbon monoxide.

C) A general anisotropic chemical shift anisotropy powder pattern for nonsymmetrical molecules.

D) The isotropic chemical shift observed in solution NMR. [1.25]

symmetry.

The chemical shift anisotropy, like the dipolar interaction has a spatial dependency that can be seen in equation (1.7).[1.45]

$$\sigma_{csa} = \tfrac{1}{2}(\sigma_{zz} - \sigma_{iso})(3\cos^2\theta - 1) + \tfrac{1}{2}(\sigma_{zz} - \sigma_{iso})\sin^2\theta\, cos2phi\, \eta_{iso}$$
$$\eta_{iso} = \frac{\sigma_{xx} - \sigma_{yy}}{\sigma_{zz} - \sigma_{iso}} \qquad (1.7)$$

where σ_{xx}, σ_{yy} and σ_{zz} are the diagonal elements of the chemical shift tensor and θ and ϕ are polar coordinates.[1.45]

In solution NMR, the chemical shift tensor is averaged to its trace, since the molecules tumble freely and isotropically. This "isotropic chemical shift" (Figure 1.3D) can be calculated from the principal elements of the diagonalized chemical shift tensor:

$$\sigma_{iso} = \frac{1}{3}(\sigma_{xx} + \sigma_{yy} + \sigma_{zz}) \quad . \qquad (1.8)$$

Silicon-29 has a chemical shift range of about 500 ppm, with iodine-containing silicon halogenides at one end (for example SiI_4 at -351.71 ppm) and some organic silicon chlorides (for example $Cl_2Si[Fe(CO)_2(C_5H_5)]_2$ at 146.65 ppm) at the other.[1.3] The chemical shifts for ^{29}Si NMR spectra are usually given with respect to that of tetramethylsilane (TMS) which is assigned a value of 0.0 ppm.

1.4.4 Indirect Spin-Spin or J-Coupling Interaction

The Hamiltonian (H_J) shown in equation (1.9) describes the indirect interaction of two spins (I and S) via their intervening bonding electrons.[1.10]

$$H_J = h\, \bar{I}_I \cdot \hat{J} \cdot \bar{I}_S \qquad (1.9)$$

where $\hat{J}$ is the indirect coupling tensor.[1.18] This spin-spin interaction is independent of the magnetic field strength. The orientational dependency of the $\hat{J}$ tensor is usually not very strong and this coupling is often referred to as a scalar coupling.

If two inequivalent spins I and S (with a spin ½) are coupled to each other, the I resonance will be split into N+1 lines (where N is the number of equivalent attached S nuclei). The S resonance will also be split, in this case into M+1 lines (where M is the number of equivalent attached I nuclei). The separation of the lines is referred to as the scalar coupling constant and since its value does not depend on the external magnetic field it is usually given directly in Hertz.

In solution NMR, the scalar coupling is often an important feature of the NMR spectrum. For example, in the ^{29}Si solution NMR spectrum shown in Figure 1.4 the nine ^{1}H nuclei (S) in the three equivalent methyl groups couple to the ^{29}Si nucleus (I) and split the resonance line into 10 lines separated by 7.3 Hertz.

In most cases, the coupling constant is similar in magnitude in both solution and solid-state NMR, however, the broad lines in solid state NMR spectroscopy of static samples due to the direct dipole-dipole interactions and the chemical shift anisotropy usually conceal the scalar couplings. The next section discusses three techniques that improve the resolution and signal to noise ratio in solid state NMR spectroscopy, namely high-power dipolar decoupling, magic angle spinning and cross-polarization.

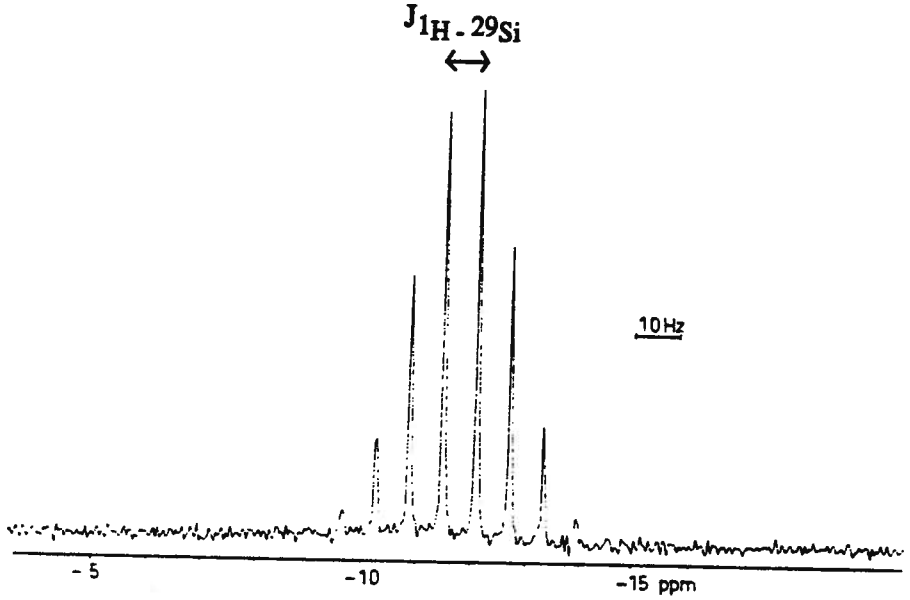

Figure 1.4 - High resolution ^{29}Si solution NMR spectrum for $(CH_3)_3SiCN$, $J_{Si-H} = 7.3Hz$.[1.13]

1.5 HIGH RESOLUTION SOLID STATE NMR SPECTROSCOPY

1.5.1 High-Power Dipolar Decoupling

For nuclei of low natural abundance, such as ^{29}Si, the dominant dipolar interaction is heteronuclear, usually involving ^{1}H and thus it can be removed by the application of a powerful decoupling field applied at the S nucleus (^{1}H) frequency while observing the I nucleus.

High power proton decoupling is achieved by applying an additional radio frequency (rf) field at the proton Larmor frequency (400 MHz in a 9.4 Tesla field). The irradiation of the protons induces rapid transitions, or spin flips, between the two allowed energy levels. This results in the abundant nuclei generating a heteronuclear dipolar field that is in the time average zero and thus "decouples" the abundant spins (^{1}H) from those of interest (^{29}Si).[1.28]

The difference between solid state and solution NMR proton decoupling is the magnitude of the rf field necessary for decoupling. In solid state NMR spectroscopy the dipolar coupling is tens of kilohertz which requires a decoupling power up to approximately one kilowatt. In solution NMR spectroscopy, the J-coupling interaction is usually of the order of hundreds of Hertz requiring relatively a low power level (around 5 watts).[1.29]

1.5.2 Magic Angle Spinning

All interactions with an angular dependence of $(3\cos^2\theta-1)$, such as the dipolar interaction and the chemical shift anisotropy, can be averaged using a technique proposed and implemented independently by Lowe [1.12B] and Andrew et al [1.12A] in 1958-1959. This technique, called magic angle spinning (MAS), involves imposing an external motion on a solid sample. This external motion is a fast rotation around an axis forming an angle β with the magnetic field (Figure 1.5). For the rotation, equation (1.10) can be written:

$$<3\cos^2\theta - 1> = \frac{1}{2}(3\cos^2\alpha - 1)(3\cos^2\beta - 1) \qquad (1.10)$$

where α, β and θ are as defined in Figure 1.5. When $\beta = 54.74°$, which is known as the "Magic Angle", the whole angular dependence term becomes zero. In the time average the dipolar interactions are reduced to zero and the chemical shift (and J-coupling interactions) to their isotropic values. In other words, magic angle spinning (MAS) has a similar effect to rapid random motion in solution NMR.[1.18, 1.22]

In order for MAS experiments to succeed in narrowing the chemical shift anisotropy properly, the spinning rate has to be greater than the frequency spread caused by the spin interactions. If the spinning frequency is not larger than the chemical shift anisotropy, spinning side bands are observed on either side of the isotropic peak, separated by the spinning frequency. The sideband intensities approximately reflect the profile of the chemical shift anisotropy powder pattern.

Linebroadening resulting from dipolar interactions is narrowed by magic angle spinning. The spinning speed determines the extent of this reduction in the linewidth. The combination of magic angle spinning (MAS) and high-power decoupling, makes the elimination of the heteronuclear dipolar interactions technically feasible.

In summary, the combination of magic angle spinning with high-power decoupling makes it possible for high resolution NMR spectra of solids to be obtained that are comparable to those in solution.[1.10, 1.27]

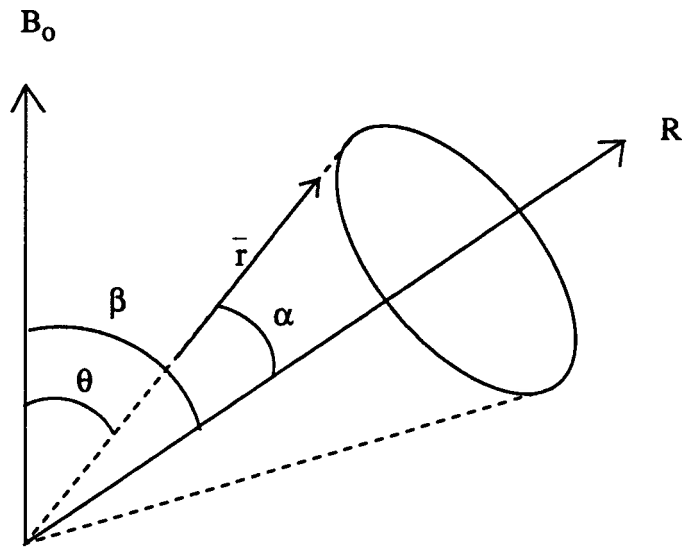

Figure 1.5 - A schematic representation of the relevant angles involved in the rotation of a macroscopic sample at an angle (β) to the applied magnetic field B_0. R is the rotation axis about which the sample is spun. A typical internuclear vector r is inclined at the angle α with respect to R.[1.18, 1.22]

1.5.3 Cross Polarization

In solid state NMR, a direct one-pulse ^{29}Si NMR experiment will often be very inefficient due to the low sensitivity of ^{29}Si and its long longitudinal relaxation time (T_1).

The technique of cross polarization (CP) was introduced by Pines, Gibby and Waugh to overcome the sensitivity problem in the observation of dilute nuclei.[1.19] It involves enhancing the signal of the dilute nucleus such as ^{29}Si by taking advantage of the heteronuclear dipolar coupling between the dilute (I for insensitive) and abundant (S for sensitive) spins.

The equilibrium magnetization (M_{S0}) in a static magnetic field (B_o) is given by Curie's law, equation (1.11) (shown for the S spins).[1.19C]

$$M_{S0} = \frac{C_S B_o}{T_L} \tag{1.11}$$

where T_L is the temperature of the lattice and C_S is the Curie constant of the S nucleus.

The transfer of magnetization in a cross polarization experiment (Figure 1.6) is carried out in three steps. First, a 90° radiofrequency pulse is applied to the S spins (for example, ^1H) along the x' axis in the rotating frame, rotating the magnetization onto the y' axis. The second step involves spin locking the S spins (^1H or ^{19}F) in the xy plane with a B_{1S} field along y' which is static in the rotating frame. The B_{1S} field forces the proton spins to precess about y' with a frequency ω_{1S} which depends on the magnitude of the B_{1S} field. For any non-equilibrium state of the magnetization it is possible to define a "spin temperature" T_s such that Curie's law is still fulfilled, provided that the magnetization does not change too quickly.

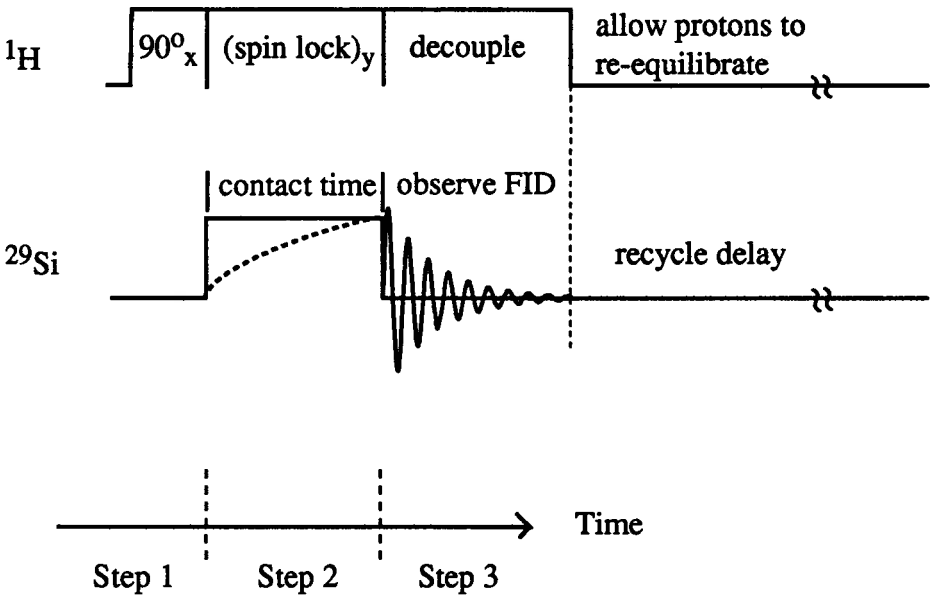

Figure 1.6 - The cross polarization (CP) pulse sequence illustrated for ^{1}H-^{29}Si CP NMR experiments.

The magnetization of the S spins in the spin locking field (B_{1S}) is given by equation (1.12).[1.19C]

$$M_S = \frac{C_S B_{1S}}{T_S} \tag{1.12}$$

where T_S is the spin temperature in the spin locking field, in the rotating frame. The amplitude of M has not changed; therefore the magnetization M_S is equal to M_{S0} (the equilibrium magnetization) . The applied magnetic field (B_{1S}) is significantly smaller than the external static magnetic field (B_o); therefore the relationship (1.13) is true.

$$T_S <<< T_L \tag{1.13}$$

This implies that spin locking the S (^{1}H or ^{19}F) magnetization along the B_{1S} field corresponds to a "cooling" of the spins.

Simultaneous with the spin locking of the S spins, another long rf pulse with an amplitude B_{1I} is applied to the I spins (^{29}Si) causing the I spins to precess with a frequency ω_{1I} around B_{1I}. If the two spin reservoirs are coupled via the Hartmann-Hahn condition by choosing appropriate values for B_{1I} and B_{1S}, [1.19C]

$$\begin{aligned} \omega_{1S} &= \omega_{1I} \\ \gamma_S B_{1S} &= \gamma_I B_{1I} \end{aligned} \tag{1.14}$$

their momentary precession frequencies ω_{1I} and ω_{1S} become equal and energy exchange between them is possible. The I spins (^{29}Si) have a lower spin temperature in the spin locking field than the S spins (^{1}H or ^{19}F).[1.26] Therefore energy flows from the S spins to the I spins until both the S and I spins have the same final spin temperature, equation (1.15).[1.5, 1.26]

$$T_s^f = T_I^f = T_L(\frac{B_{1S}}{B_o}) \approx 10^{-3}T_L \qquad (1.15)$$

This energy flow to the I spins is manifested as a growth of the I magnetization along the spin locking field B_{II}.

Step three involves observing the free induction decay of the ^{29}Si signal. The B_{1S} field may be kept on during the acquisition period if decoupling is needed. This pulse sequence is repeated and the FID's added until a sufficiently good signal to noise ratio is attained.

A cross polarization experiment has two advantages with respect to the signal to noise ratio (S/N) over a simple 90° pulse experiment. Firstly, there is the direct enhancement factor, γ_S/γ_I, of the I magnetization [1.5, 1.19C], which in the case of ^{29}Si can be up to a factor of 5, even though in practice this maximum enhancement is rarely achieved. Secondly, the pulse sequence can be repeated after a delay determined by the T_1 of the S nuclei (^{1}H) which is normally much shorter than that of the I nuclei (^{29}Si). The shorter recycle period and the enhanced signal to noise of each scan result in a higher signal to noise ratio in a CP versus a simple 90° pulse experiment in a fixed period of time.

Cross polarization is transmitted via the heteronuclear dipolar interactions between the dilute and abundant nuclei. Therefore this technique, like the dipolar interaction itself, has a very strong inverse dependence on the distance between the two nuclei [1.18, 1.22] providing a possible tool to measure internuclear distances.

1.5.4 Distance determination from CP curves

Spin locked magnetization decays exponentially with a relaxation time constant $T_{1\rho}$ (spin-lattice relaxation in the rotating frame), equation (1.16).[1.31]

$$M_y(t) = M_y(0)\, e^{-\frac{t}{T_{1\rho}}} \tag{1.16}$$

The $T_{1\rho}$ values of the S and I magnetizations limit the time for polarization transfer (step two in the pulse program, Figure 1.6). In this thesis, the $T_{1\rho}$ (^{29}Si) was large enough for its effect to be neglected in this regard. The $T_{1\rho}$ (^{1}H), however, represents an important characteristic of the polarization transfer and has to be taken into account in all quantitative experiments. In this case, the change in the magnetization of the I spins being observed is given by equation (1.17).[1.5, 1.19C]

$$M_I(t) = M_{I0}\,\frac{\gamma_S}{\gamma_I}\left(\frac{\frac{1}{T_{cp}}}{\frac{1}{T_{cp}} - \frac{1}{T_{1\rho_S}}}\right)\left(e^{-\frac{t}{T_{1\rho_S}}} - e^{-\frac{t}{T_{cp}}}\right). \tag{1.17}$$

The rate of cross-polarization T_{cp}^{-1} can thus be determined by fitting the change in intensity of the ^{29}Si signals as a function of contact time using equation (1.17).[1.5]

The relationship between the cross polarization rate (T_{cp}^{-1}) and the internuclear distance between the S spins and the I spins is given approximately in equation (1.18).[1.19C]

$$\frac{1}{T_{cp}} = C_{IS} * \frac{\langle \Delta\nu^2 \rangle_{IS}}{\sqrt{\langle \Delta\nu^2 \rangle_{SS}}} \tag{1.18}$$

C_{IS} is here a geometrical factor given by expression (1.19):[1.19C]

$$C_{IS} = 3\pi \sqrt{\frac{\sum_{i \neq j} a_{ij}^2 \sum_i b_{im}^2}{N_S \sum_{i \neq j} a_{ij}^2 \left[(2b_{im} + b_{jm})^2 + (b_{im} + 2b_{jm})^2 \right]}} \tag{1.19}$$

where

$$a_{ij} = -\frac{\gamma_S^2 \hbar^2 (3\cos^2\theta_{ij}-1)}{2 r_{ij}^3} \qquad (1.19A)$$

$$b_{im} = \frac{\gamma_I \gamma_S \hbar^2 (3\cos^2\theta_{im} - 1)}{r_{im}^3} \qquad (1.19B)$$

and i through j refer to the S nuclei and m to the I nuclei. As well, r_{ij} and r_{im} are the internuclear vectors and θ_{ij} and θ_{im} are the angles that the internuclear vectors r_{ij} and r_{im} make with the external magnetic field, (Figure 1.7).[1.18]

The expressions for the second moment, equation (1.20) and (1.21), were first published by J.H. Van Vleck.[1.34] He developed the method of moments to compute the properties of a resonance line without knowing explicitly the energy eigenstates and eigenvalues.[1.34] $\langle\Delta\nu^2\rangle_{SS}$ is the homonuclear second moment for abundant nuclei (^{1}H or ^{19}F) in a rigid lattice: [1.18, 1.22]

$$\langle\Delta\nu^2\rangle_{SS} = \frac{3}{4}\left(\frac{\gamma_S^2 \hbar \mu_o}{4\pi}\right)^2 S(S+1) \sum_i \frac{(3\cos^2\theta_{ij}-1)^2}{r_{ij}^6} \qquad (1.20)$$

where μ_o is the permeability constant and S is the spin quantum number.[1.18] If two different types of spins are involved, the heteronuclear second moment $\langle\Delta\nu^2\rangle_{IS}$ is given by equation (1.21).[1.18, 1.22] This equation is only valid in the absence of motion.

$$\langle\Delta\nu^2\rangle_{IS} = \frac{1}{3}\left(\frac{\gamma_I\gamma_S\hbar\mu_o}{4\pi}\right)^2 I(I+1) \sum_i \frac{(3\cos^2\theta_{im}-1)^2}{r_{im}^6} \qquad (1.21)$$

I is the spin quantum number.[1.18] In both cases, equations (1.20) and (1.21), the sum is over all the relevant nuclei i, in relation to the considered nucleus j or m, respectively.[1.18, 1.22] The effect of motion on these second moment calculations is discussed in Chapter 7.

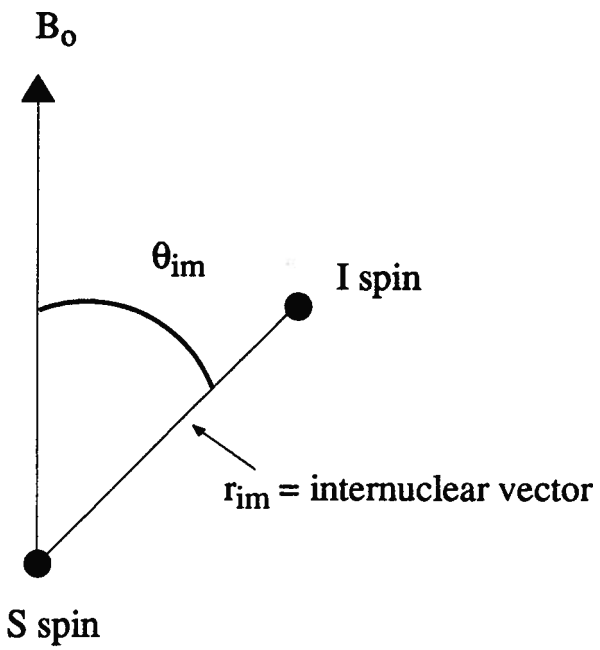

Figure 1.7 - The geometric relationship of two spins I and S in an external magnetic field.[1.18, 1.22]

1.6 TWO-DIMENSIONAL NMR SPECTROSCOPY

The concept of two-dimensional NMR experiments was first suggested by Jeener [1.36] in 1971. There was a rapid growth in the application and development of high resolution two-dimensional (2D) NMR after Ernst and co-workers demonstrated that a large variety of 2D NMR experiments were possible.[1.37-1.39]

All multidimensional NMR pulse sequences consist of three parts: preparation, evolution and detection periods. The preparation period can include one or more pulses. The spin system then evolves under the influence of different interactions depending on the experiment during the evolution period (t_1). Then the signal (FID) is acquired during the detection period (t_2).

In a 2D NMR experiment the second time domain is introduced by acquiring a series of 1D experiments where the evolution time, t_1 is incremented. The incrementation of t_1 *creates a second frequency domain reflecting the interactions within the spin system during this time.*

The data are arranged in a two-dimensional matrix, $S(t_1,t_2)$ with n rows (number of FIDs gathered, i.e. number of increments of t_1) and k columns (number of data points collected in t_2). After Fourier transformation of these data in one dimension, $S(t_1,t_2) \rightarrow S(t_1,F_2)$, a series of spectra is obtained that are phase modulated. A second Fourier transformation of corresponding columns in the data set yields a 2D data matrix, $S(F_1,F_2)$.

A 2D NMR experiment is always possible if a systematic change in the evolution period results in a periodic change of the phase and/or amplitude of the spectra. The second Fourier transform determines the frequency of these modulations and provides the second dimension for the spectrum. This dimension reflects the effect of the interactions under which the spin system evolves during t_1.

A 2D experiment can be carried out to obtain heteronuclear correlations in the solid state. Ernst and coworkers were the first to describe a 2D heteronuclear correlation experiment in solution.[1.38] The pulse sequence for an analogous 2D heteronuclear correlation solid state NMR experiment is shown in Figure 1.8. This experiment takes advantage of the cross polarization between a dilute and abundant nuclei. In a ^{1}H-^{29}Si heteronuclear correlation experiment for example, the proton frequency is encoded during a period (t_1), following the 90° proton pulse. The remaining component of the proton magnetization is spin-locked and cross polarized to silicon. The silicon magnetization is then observed during the period t_2. Thus, the proton chemical shift will be on one axis and the silicon chemical shift on the other. Examples of the application of this technique will be presented in Chapter 2.

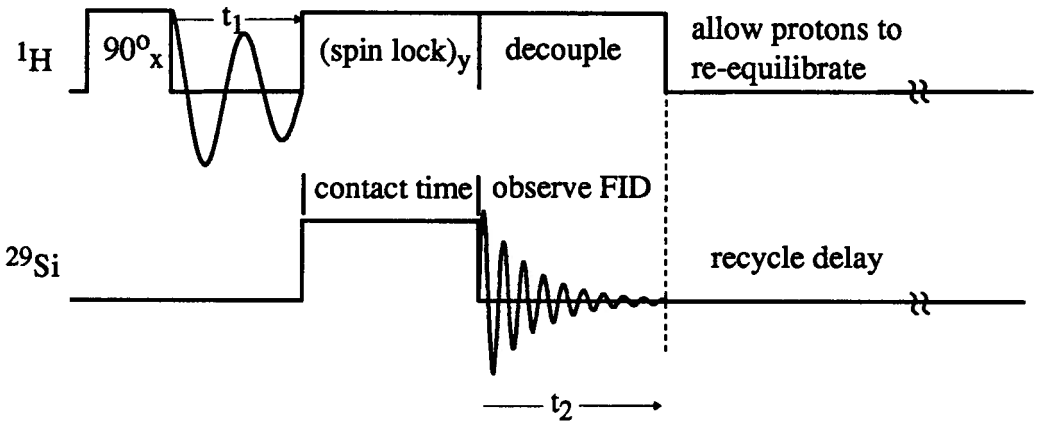

Figure 1.8 - The pulse sequence used for a 2D ^{1}H - ^{29}Si heteronuclear correlation NMR experiment with ^{1}H decoupling. The corresponding 1D cross polarization pulse sequence is illustrated for ^{1}H-^{29}Si in Figure 1.6.

1.7 OBJECTIVES OF THE THESIS

Traditionally, the preparation of organofunctionalized silica gels has involved the condensation of a functionalized polychloro- or polyalkoxy- silane onto the surface of solid silica gel. The general reaction is usually represented as

$$SiO_2 + (RO)_3Si\text{-}R' \rightarrow SiO_2 \begin{matrix} O \\ -O- \\ O \end{matrix} Si\text{-}R' \qquad (1.22)$$

where RO = alkoxy ligand
R' = organic functionality

The establishment of the anhydrous conditions required to obtain a monolayer coverage of the functionalized silane on silica gel is hindered by the hydrophilic nature of silica gel. The presence of water favours both surface and self-condensation of the functionalized silane resulting in the formation of siloxane oligomers and polymers. These polymers may or may not bind to the surface and if they do there is no guarantee that their functionalities will be accessible for further reactions. Consequently, irreproducible products result. Generally, operational success determines the concentrations used industrially.

Silica gel can be synthesized by hydrolyzing $SiCl_4$ or tetraethoxysilane (TEOS) to form $Si(OH)_4$ which undergoes repeated condensation reactions. In this thesis an alternative preparation is proposed for the synthesis of these organofunctionalized silica gels via the copolymerization of the silica gel monomer (TEOS) with the organofunctionalized trialkoxysilane as shown in reaction (1.23).

$$Si(OH)_4 + R'\text{-}Si(OH)_3 \rightarrow \begin{matrix} | & | \\ R'\text{-}Si\text{-}O\text{-}Si\text{-} \\ | & | \end{matrix} + 3H_2O \qquad (1.23)$$

It is hypothesized that the final organofunctionalized product is produced directly during the formation of the gel.

The objectives of this thesis are to determine the integrity and distribution of the functionalities in organofunctionalized silica gel samples prepared using the alternative synthesis described above. Solution and solid state NMR are the principal analytical tools used in these investigations.

The chosen model for a functionality was a methyl group. Functionalized silica gel was prepared by the copolymerization of methyltriethoxysilane (MTES) and tetraethoxysilane (TEOS). Chapter 2 describes the sample preparation and the experiments carried out to characterize the functionalized silica gel in its solid form. The first step was to determine whether the functionality remained intact in the final copolymer product. The next task was to determine whether the two siloxane components produced a phase separated or a mixed copolymer.

The copolymerization kinetics were studied in order to estimate the reactivity ratios which determine the extent of mixing in the copolymer formation. In order to study the more complex kinetics of the copolymerization, the homopolymerization processes of both monomers have to be well known. Therefore, the hydrolysis and dimer formations of the tetraethoxysilane (TEOS) and methyltriethoxysilane (MTES) monomers were characterized in detail as described in Chapters 3 and 4. In Chapter 3 the kinetic constants for the TEOS hydrolysis intermediate reactions and dimer formation were experimentally determined. To obtain the kinetic constants independent of the acid concentration, the polymerization of TEOS was studied and analyzed over a range of pH values. Chapter 4 discusses the kinetic constants obtained for the MTES hydrolysis reactions and dimer formation. This is followed by a kinetic analysis of the copolymerization reaction. In addition, in Chapter 4 the ratios of the different dimers formed in a variety of MTES/TEOS copolymerizations are determined by ^{29}Si solution NMR.

One of the potential applications of functionalized silica gels is in the manufacturing of low temperature organofunctionalized glasses where the functionality is distributed throughout the glass matrix. Chapter 5 deals with the effect of formamide, a commonly used drying agent, on the hydrolysis and dimer formation kinetics of TEOS and MTES homopolymers and the MTES/TEOS copolymer. The integrity of the drying agent over a period of a few months was probed by ^{29}Si, ^{1}H, ^{15}N and ^{13}C solution NMR. The focus of Chapter 6 is to determine the suitability of different functionalized silica gels to make low temperature glasses by establishing the thermal stability of these compounds using differential scanning calorimetry (DSC), thermogravimetric analysis (TGA), thermogravimetric analysis accompanied by mass spectroscopy (TG/MS), as well as ^{29}Si, ^{13}C and ^{1}H solid state NMR.

Chapter 7 presents the results of an additional study using solid state NMR that attempts to further characterize the distribution of the functionalities in functionalized silica gel samples. The distance range between the functionality and the fully condensed unfunctionalized silicons is deduced and the percentage of condensed unfunctionalized silicons within this distance range determined.

A summary of all the conclusions and suggestions for future research are presented in Chapter 8.

CHAPTER 2

CHARACTERIZATION OF SILICA GEL AND FUNCTIONALIZED SILICA GEL BY 1D & 2D SOLID STATE NMR EXPERIMENTS

2.1 INTRODUCTION

Industrially, immobilized reagents are synthesized by reacting a trichloro- or trialkoxy-substituted silane with hydroxyl groups on an activated silica gel surface, as illustrated in Figure 2.1.[1.10] Trichloro- and trialkoxy- organofunctionalized silanes are used because they can be synthesized directly and cheaply by the reaction of trichlorosilane with an appropriate alkene as in equation (2.1).

$$Cl_3Si-H + CH_2=CH-R' \rightarrow Cl_3Si-CH_2CH_2-R' \qquad (2.1)$$

These trialkoxy- and trichloro- substituted silanes are potential monomers; therefore, besides reacting with the silica gel surface, they can undergo self-polymerization. Consequently, the preparation of immobilized reagents by reacting a trichloro- or trialkoxy-substituted silane with silica gel results in organofunctionalized silanes whose probable structure is much more complicated than that shown in Figure 2.1. In order to prevent the oligomers of the functionalized silane from attaching to the silica gel surface, monomers such as X-Si$(CH_3)_2$R' (where X is either an alkoxide or a halide and R' is the functionality) can be used instead of the trichloro- or trialkoxy- substituted silane. However, this is more expensive and therefore seldom used.

Maciel and co-workers were the first group to use solid state NMR to study silica gel. Using ^{29}Si CP/MAS NMR they identified the different silicon environments found in silica gel, i.e. $(Si(OH)_2(OSi)_2$, $Si(OH)_3(OSi)$ and $Si(OSi)_4)$ shown in Figure 2.2.[1.20] They went on

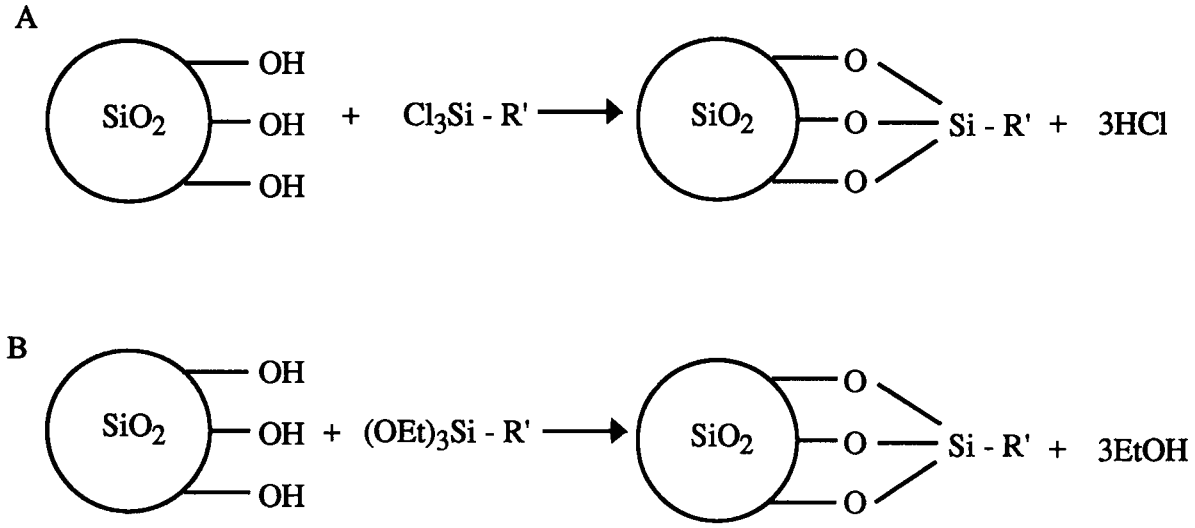

Figure 2.1 - Industrial synthesis of functionalized silica gels.

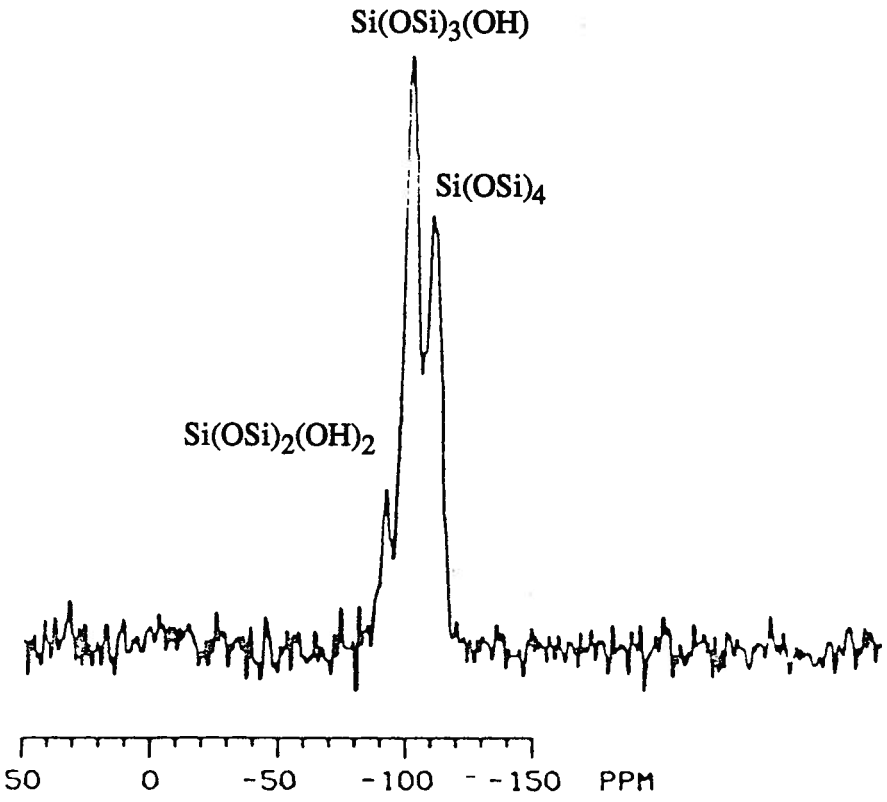

Figure 2.2 - ^{29}Si CP/MAS NMR spectrum of silica gel with the three different silicon environments labelled according to Maciel and co-workers.[1.20]

to determine the $T_{1\rho}(^1H)$ and the cross polarization time constants ($T_{H\text{-}Si}$) for all three silicon resonances.[1.20]

In this chapter an alternative approach for the preparation of functionalized silica gels of the general type shown in Figure 2.1 is proposed. The resulting products are characterized by one and two-dimensional solid state NMR spectroscopy to determine the integrity, quantity and distribution of the functionalities in the functionalized silica gel. The complete characterization involves establishing the chemical integrity of the organic functionality in the gel, then the relative proportions of the different silicon environments in the sample and finally, the distribution of the functionality, with respect to the question of a phase separated or mixed copolymer.

2.2 INTRODUCTION TO THE ALTERNATIVE SYNTHESIS

The alternative preparation for functionalized silica gel is based on considering silica gel as a crosslinked polymer made via a condensation polymerization of SiX_4 where X can be either an alkoxy group or a halide. A functionalized silica gel with the functionality spread throughout the silica gel surface could therefore be considered a crosslinked copolymer synthesized in a one-step reaction by copolymerizing the functionalized silane monomer concurrently with tetraethoxysilane (used to synthesize silica gel), (2.2).

$$n\ Si(OH)_4 + n\ R'\text{-}Si(OH)_3 \rightarrow \left[R'\text{-}\underset{\underset{O}{|}}{\overset{\overset{O}{|}}{Si}}\text{-}O\text{-}\underset{\underset{O}{|}}{\overset{\overset{O}{|}}{Si}}\text{-}O\right]_n + n\ H_2O \qquad (2.2)$$

A random distribution of the functionality throughout the silica gel matrix would be ideal, since this gives minimal interactions between the functionalities.

A functionalized silica gel which consists of tetraethoxysilane (TEOS) and methyltriethoxysilane (MTES) with the methyl group representing the immobilized functionality was chosen for the present work.

2.3 EXPERIMENTAL

2.3.1 Silica Gel

2.3.1.1 Silica Gel - Fast Gel Preparation

Silica gel was synthesized by the acid hydrolysis of tetraethoxysilane (TEOS) using the method described by Peri and Hensley.[2.1] Ten ml of concentrated HCl were added dropwise while stirring to 0.2242 mole of TEOS in 75 ml of ethanol (40% by volume). The solution gelled in a few hours. The gel was broken into small pieces after standing overnight and placed in 200 ml ethanol/distilled water (50% by volume). After standing for 12 hours, the gel was washed with distilled water several times until the eluate had a pH of 7. The sample was dried at 100°C for at least one day and ground to a fine powder.

2.3.1.2 Silica Gel - Preparation Used in the Kinetic Studies

0.08967 mole of TEOS was mixed with 0.5171 mole of ethanol and then 0.9928 mole of acidified water (pH=2.76) was added dropwise to the solution. The sample was left to gel at room temperature and normal pressure, a process which took several days. These are the conditions used in the kinetic studies discussed in later chapters. The gel was not washed with water since in this preparation; the eluate was found to be neutral. The sample was crushed and dried in the oven at 100°C for 24 hours and then ground to a fine powder.

2.3.2 Methyltriethoxysilane Homopolymer

Methyltriethoxysilane homopolymer samples were prepared by the same procedures as those used for the silica gels (preparation 2.3.1.1 and 2.3.1.2) above, except that the starting material was methyltriethoxysilane (MTES) instead of TEOS.

2.3.3 Methyl Substituted Silica Gel

2.3.3.1 Reaction with Preformed Silica Gel

The methyl substituted silane was anchored onto preformed silica gel using the

following procedure. Silica gel (Fisher s-157; approximately 5 g) was pre-dried in vacuo at ~150°C overnight, and was then refluxed with an excess of MTES in dry toluene for 12 hours. After filtration, the solid was soxhlet-extracted with dry toluene for 12 hours and then dried in vacuo at ~150°C for 12 hours.

2.3.3.2 Copolymerization - Fast Gel Preparation

MTES and TEOS were mixed in various mole ratios in ethanol. The preparation then proceeded as in 2.3.1.1 for silica gel.

2.3.3.3 Copolymerization - Under Kinetic Conditions

MTES and TEOS were mixed in various mole ratios in ethanol. The preparation then proceeded as in 2.3.1.2 for silica gel.

2.3.4 Solid State NMR Spectra

Quantitative ^{29}Si solid state MAS NMR spectra were acquired on a Bruker AM 400 spectrometer at 79.495 MHz with a home-built narrow bore MAS probe with a 9 mm spinner system. For the experiments a 45° ^{29}Si pulse and 180 seconds ($3*T_1$) recycle delay were used.

The cross polarization experiments, both 1D and 2D, were performed on a Bruker MSL 400 spectrometer at a spectral frequency of 79.495 MHz. All the 2D spectra consist of 64 experiments, and unless otherwise stated, they were acquired with a 22 milliseconds contact time, 3 seconds recycle delay and a 4-4.3 kHz spinning speed. The spinning rate for all the experiments on the MTES/TEOS mixed and copolymer samples was carefully chosen to prevent overlap of spinning sidebands and the ^{29}Si resonances. Specific experimental conditions are given in the figure captions.

The Bruker program "Glinfit" program was used for the deconvolution of the spectra. It was found that the spectra were best fitted using a Gaussian lineshape.

2.4 RESULTS AND DISCUSSION

2.4.1 Characterization of the Functionalized Silica Gel by 1D NMR Experiments

One-dimensional high resolution ^{13}C and ^{29}Si solid state CP/MAS NMR spectroscopy was used to determine if the functionality was intact in the MTES/TEOS copolymer. The ^{13}C and ^{29}Si CP/MAS NMR spectra of silica gel incorporating approximately 25% methyltriethoxysilane (preparation 2.3.3.3) are shown in Figure 2.3. The assignments are made in accordance to those previously reported in the literature. [1.10, 1.20] The ^{13}C and ^{29}Si spectra clearly show that the functionality is intact and attached to silicon.

The relative concentrations of the different types of silanes were determined via deconvolution of the overlapping peaks in the quantitative ^{29}Si MAS NMR spectra. The principle difference between the preparations (2.3.1.1 and 2.3.1.2) and (2.3.3.1 and 2.3.3.3) is that one set is synthesized with no additional water and concentrated HCl, while the other uses excess water and a much smaller concentration of HCl. The quantitative ^{29}Si MAS NMR spectra of the samples synthesized under either preparations (2.3.1.1 and 2.3.1.2) or (2.3.3.2 and 2.3.3.3) show that they have essentially the same composition. In Table 2.1, when the code name starts with A it refers to samples prepared with either preparation 2.3.1.1 or 2.3.3.2 and when it starts with B it refers to preparations 2.3.1.2 or 2.3.3.3. The next 3 or 4 numbers in the code refer to the percentage of the monomers in the copolymer.

Figure 2.4 shows the ^{29}Si CP/MAS NMR spectra of two functionalized silica gel samples (preparation 2.3.3.1 and 2.3.3.2) and a physical mixture of the MTES and TEOS homopolymers. The amorphous nature of these samples creates a distribution of isotropic shifts resulting in broad lines in the spectra. All the spectra have the same number of peaks at approximately the same chemical shifts. The differences in intensities come from composition differences and different cross polarization characteristics of the samples.

Table 2.1 - A summary of the deconvoluted peak areas (i.e. concentration) from the quantitative 1D ^{29}Si MAS NMR spectra.

CODE*	Concentration (%)**				
	$CH_3Si(OSi)_{3-n}(OH)_n$		$Si(OSi)_{4-n}(OH)_n$		
	n=1	n=0	n=2	n=1	n=0
A100	-	-	4	39	57
B100			4	36	60
A2575	6	17	5	29	44
B2575	5	19	4	30	41
A5050	8	38	4	20	29
B5050	8	40	2	17	33
A7525	9	59	4	10	19
B7525	15	61	-	11	13

* Code names starting with A are samples prepared with either preparation 2.3.1.1 or 2.3.3.2. Code names starting with B are samples prepared with either preparation 2.3.1.2 or 2.3.3.3. The next 3 to 4 numbers refer to the percentage of the monomers in the copolymer. For example A2575 was a copolymer synthesized using preparation 2.3.3.2 using 25% MTES and 75% TEOS.

** Estimated error 10%.

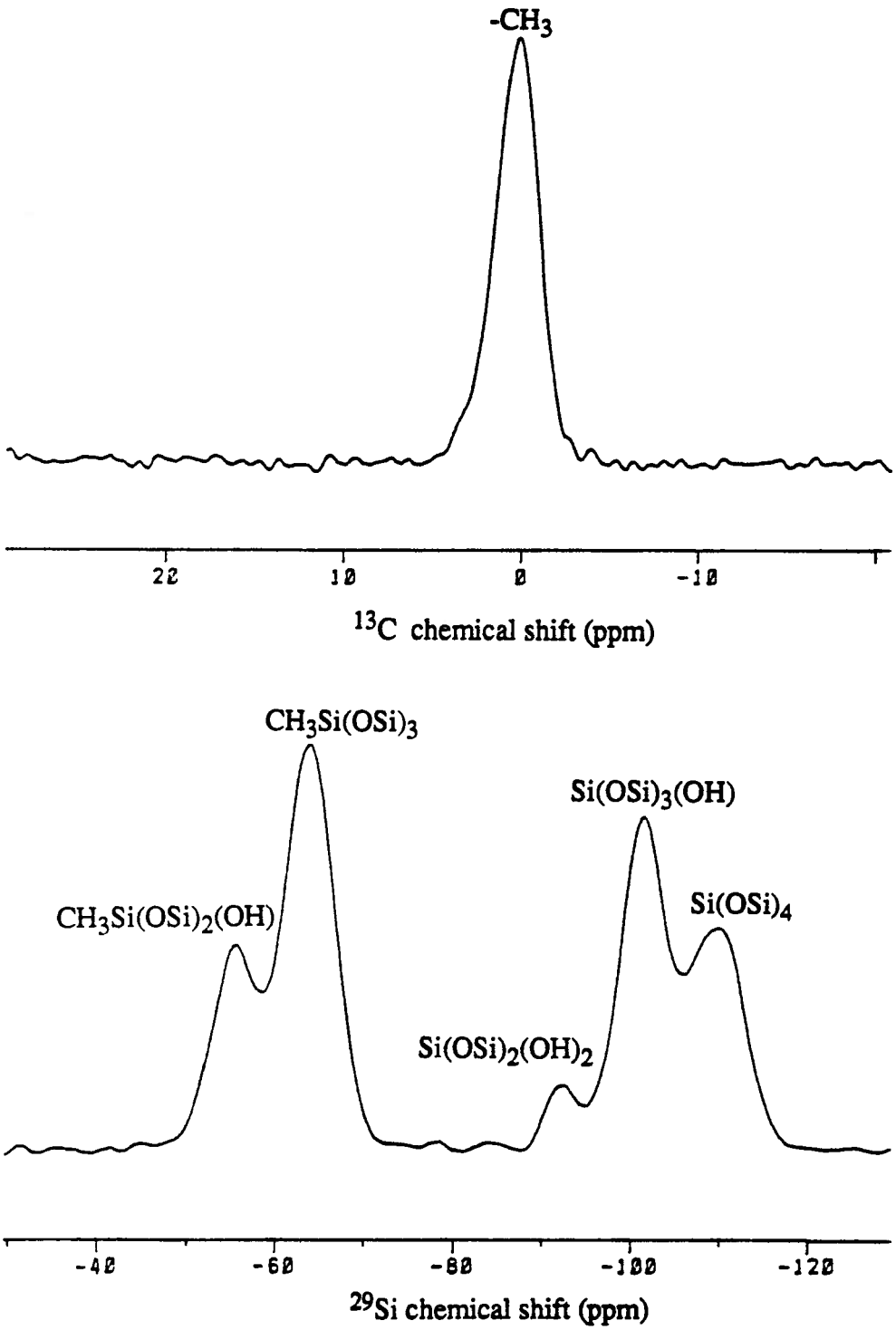

Figure 2.3 - The ^{13}C and ^{29}Si CP/MAS solid state NMR spectra of an MTES/TEOS copolymer sample obtained at 100.3 and 79.5MHz, respectively.

A - ^{13}C CP/MAS NMR spectrum; 296 scans were acquired using a 5msec contact time and 4s recycle delay.

B - ^{29}Si CP/MAS NMR spectrum; 100 scans were acquired using a 10msec contact time and 10s recycle delay.

Therefore the intensity differences cannot be used conveniently to distinguish between the three different preparations. No information describing the nature of the incorporation of the functionalized silane onto the silica gel can be obtained from the 1D CP/MAS NMR spectra in Figure 2.4.

Since there is no significant difference in the chemical shift to differentiate between a phase separated and a mixed copolymer, another way to distinguish between a-a and a-b pairs (shown in Figure 2.5) must be found.

The possible sources for cross polarization in a ^{1}H-^{29}Si CP/MAS experiment are the methyl and hydroxyl protons. In a phase separated sample (in the extreme case, MTES and TEOS homopolymers are only physically mixed), the ^{29}Si magnetization originating from the MTES homopolymer should cross polarize mainly from the methyl protons while the ^{29}Si magnetization within the TEOS homopolymer should only cross polarize from hydroxyl protons. In a random copolymer however, the TEOS silicons should also cross polarize from the methyl protons.

The presence of hydroxyl groups poses a problem. They can cross polarize to all the ^{29}Si since they are present throughout the copolymer. In order to prove that the methyl protons of the MTES monomer cross polarize to the silicons in the TEOS monomer and therefore the existence of a mixed copolymer, any cross polarization from hydroxyls has to be ruled out. To completely eliminate the hydroxyl protons is extremely difficult due to the hydrophilic nature of silica gel. A more viable and less ambiguous option is to identify the source of cross-polarization for each ^{29}Si signal using a 2D NMR experiment.

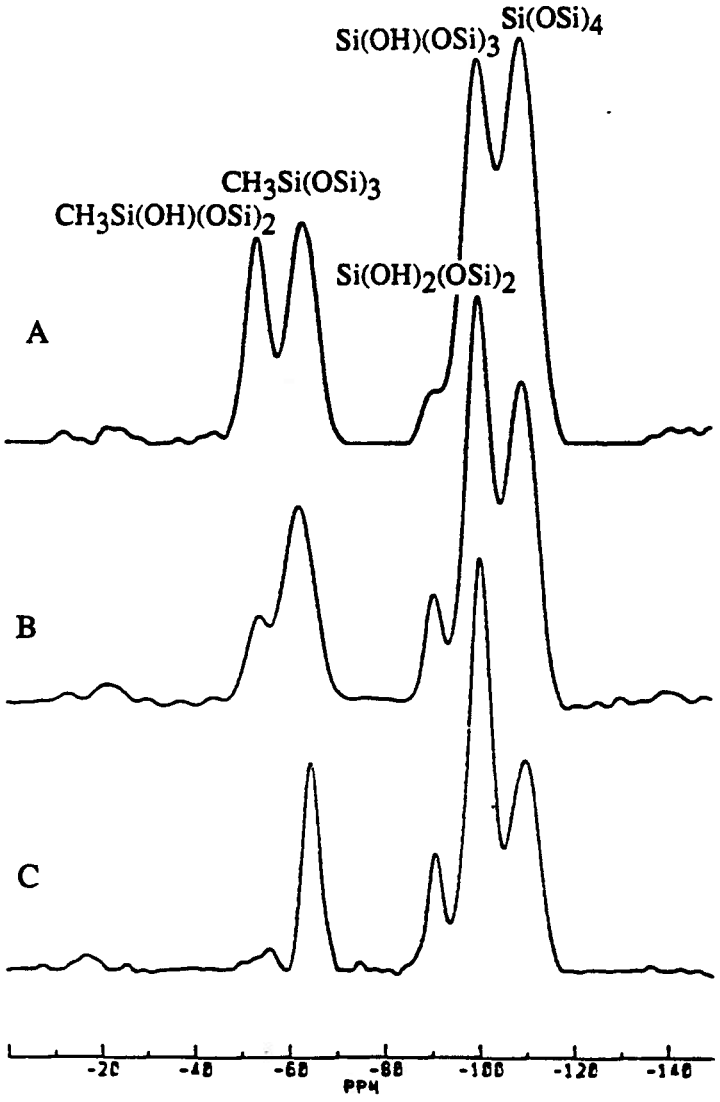

Figure 2.4 - ^{29}Si CP/MAS NMR spectra of different types of functionalized silica gels and mixtures. The spectra were obtained at 79.5MHz, 320 scans were accumulated using a 22 ms contact time and 5s repetition time. The samples were spun at 3.2kHz.

A - Methylsubstituted silica gel prepared by method 2.3.3.1

B - Methylsubstituted silica gel prepared by method 2.3.3.3

C - A mechanical mixture of silica gel and polymethylsiloxane.

MTES homopolymer

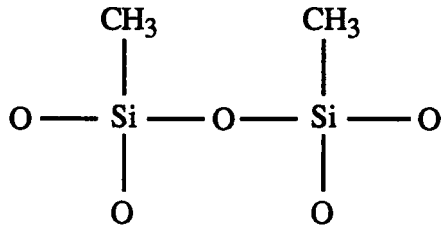

a a

MTES/TEOS copolymer

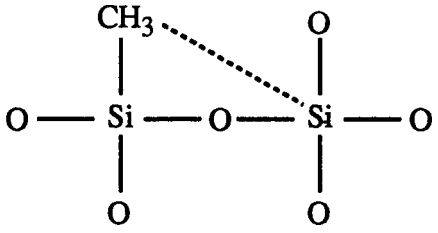

a b

Figure 2.5 - Schematic diagram illustrating the possible local silicon environments in an MTES homopolymer and an MTES/TEOS copolymer.

2.4.2 Two-Dimensional Heteronuclear Correlation NMR Experiments

One approach to determine the extent of mixing of the two monomers is to integrate cross polarization into a 2D experiment to identify the proton polarization sources.

A 2D heteronuclear correlation ^{1}H-^{29}Si NMR experiment (pulse sequence Figure 1.8) identifies the source of polarization. In this 2D experiment, one dimension is the ^{29}Si chemical shift and the other is the ^{1}H chemical shift. Cross peaks appear between each ^{29}Si peak and those proton signals that are sources of magnetization transfer. In the proton MAS spectrum of a mixture or copolymer of the TEOS and MTES monomers the -OH and -CH_3 signals are resolved. However, the lines are fairly broad and if the -OH peak is too dominant it overlaps with the -CH_3 signal. To obtain a clear correlation of the cross polarization sources and the different silicons, the contribution of the hydroxyl groups must be minimized. Sometimes the experimental parameters can be chosen to discriminate against some components of the spectrum. One possibility to differentiate the two proton sources would be via T_1 or T_2 weighing. The T_1 values for hydroxyl and methyl protons in a MTES/TEOS copolymer sample were measured to be 358 msec and 364 msec, respectively. The T_2 values of the hydroxyl and methyl protons are 1.2 msec and 1.4 msec, respectively. These measurements show that both types of protons have equal relaxation times (within the experimental error) which suggests that a common spin-temperature exists. Thus T_1 and T_2 discrimination cannot be used to differentiate between the hydroxyl and methyl proton peaks.

Another option is to physically replace the hydroxyl groups by -OD groups by washing with D_2O. This proved to be a more viable approach. All the samples were filtered, dried and washed repeatedly with D_2O. After the last washing the samples were quickly dried and packed under nitrogen, into the spinner.

The observation of a cross peak in the 2D spectrum correlating the methyl protons and

the TEOS silicon peaks would signify that cross polarization occurs between the MTES methyl group and the silicon nuclei of the TEOS monomer. This would prove that the MTES monomers are spatially close to the TEOS monomers, providing evidence that a "mixed" copolymer has been formed.

The reliability of the 2D ^{1}H-^{29}Si heteronuclear correlation experiment was established by investigating two systems of known structure; a TEOS homopolymer and a physical mixture of the MTES and TEOS homopolymers. The two 2D heteronuclear correlation spectra for the TEOS homopolymer before and after washing with D_2O are shown in Figures 2.6A and 2.6B, respectively. The 1D spectra shown along the F1 and F2 dimensions are the projections of the 2D experiment.

The 2D spectra in Figure 2.6 clearly demonstrate that the hydroxyls are a good source of cross polarization to all three types of silicons in the unfunctionalized silica gel. As already mentioned, this is a problem and therefore the challenge is to minimize the concentration of hydroxyls in the samples. As is shown in the bottom 2D spectrum, washing the sample with D_2O twice, drying it at 100°C and avoiding subsequent exposure to air (packed in a dry N_2 atmosphere) substantially decreases the intensity of the hydroxyl cross peaks but does not eliminate them.

Two-dimensional spectra from the other test case, the physically mixed MTES and TEOS homopolymers, before and after washing with D_2O, are shown in Figure 2.7. In the case of the physical mixture no cross peaks should exist between the methyl protons and the TEOS silicon nuclei, since this is clearly a phase separated structure. In the mixture that was not washed with D_2O, there is significant cross polarization from the hydroxyl protons to all the different silicon environments. In addition, cross polarization from the methyl protons to the MTES silicons is observed, showing a characteristic extensive sideband pattern.

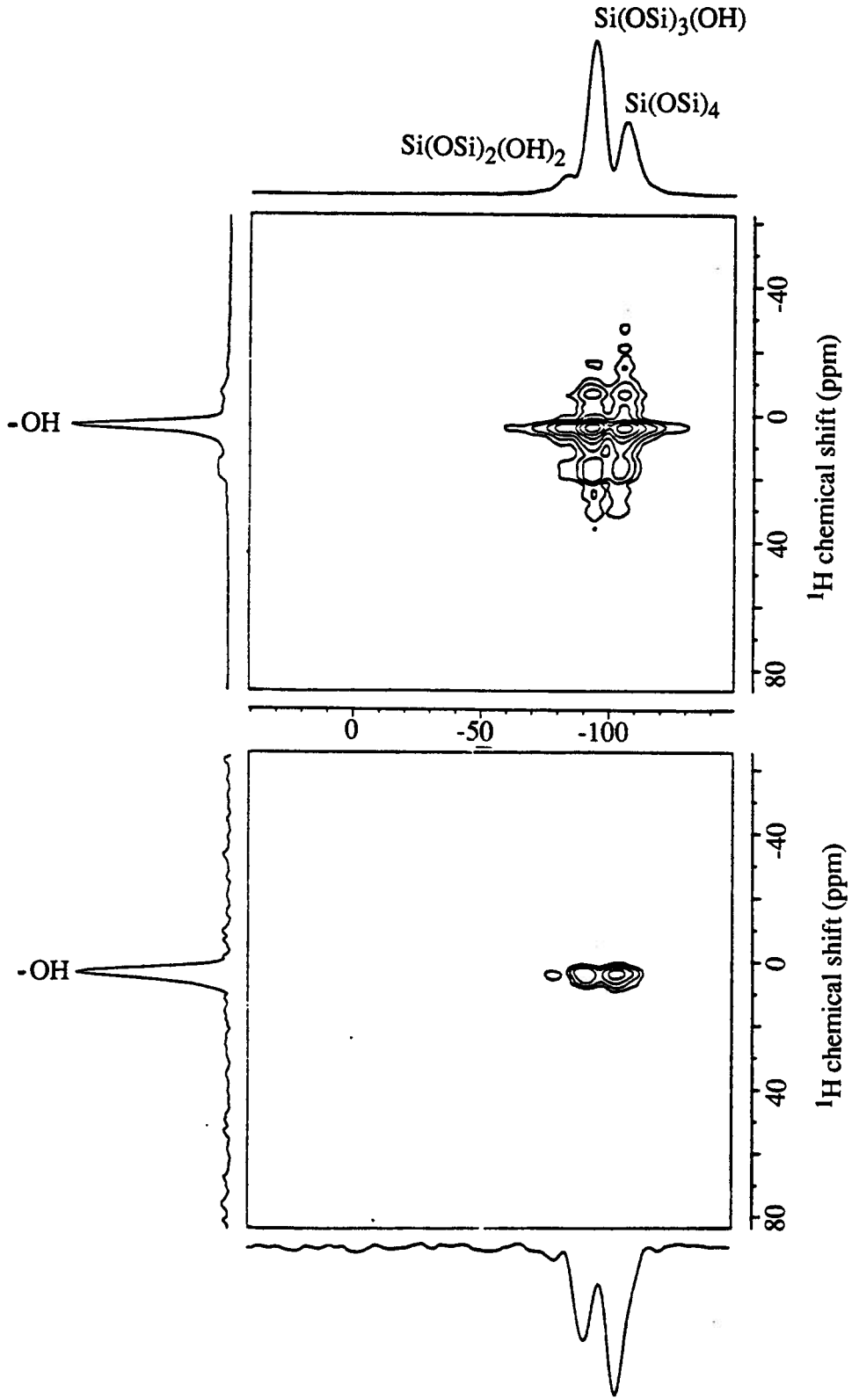

Figure 2.6 - 2D ^{1}H - ^{29}Si heteronuclear correlation NMR experiments for silica gel (preparation 2.3.1.1). The top spectrum is of the unwashed sample with 80 scans per experiment. The bottom spectrum is of the same sample washed with D_2O several times with 200 scans per experiment.

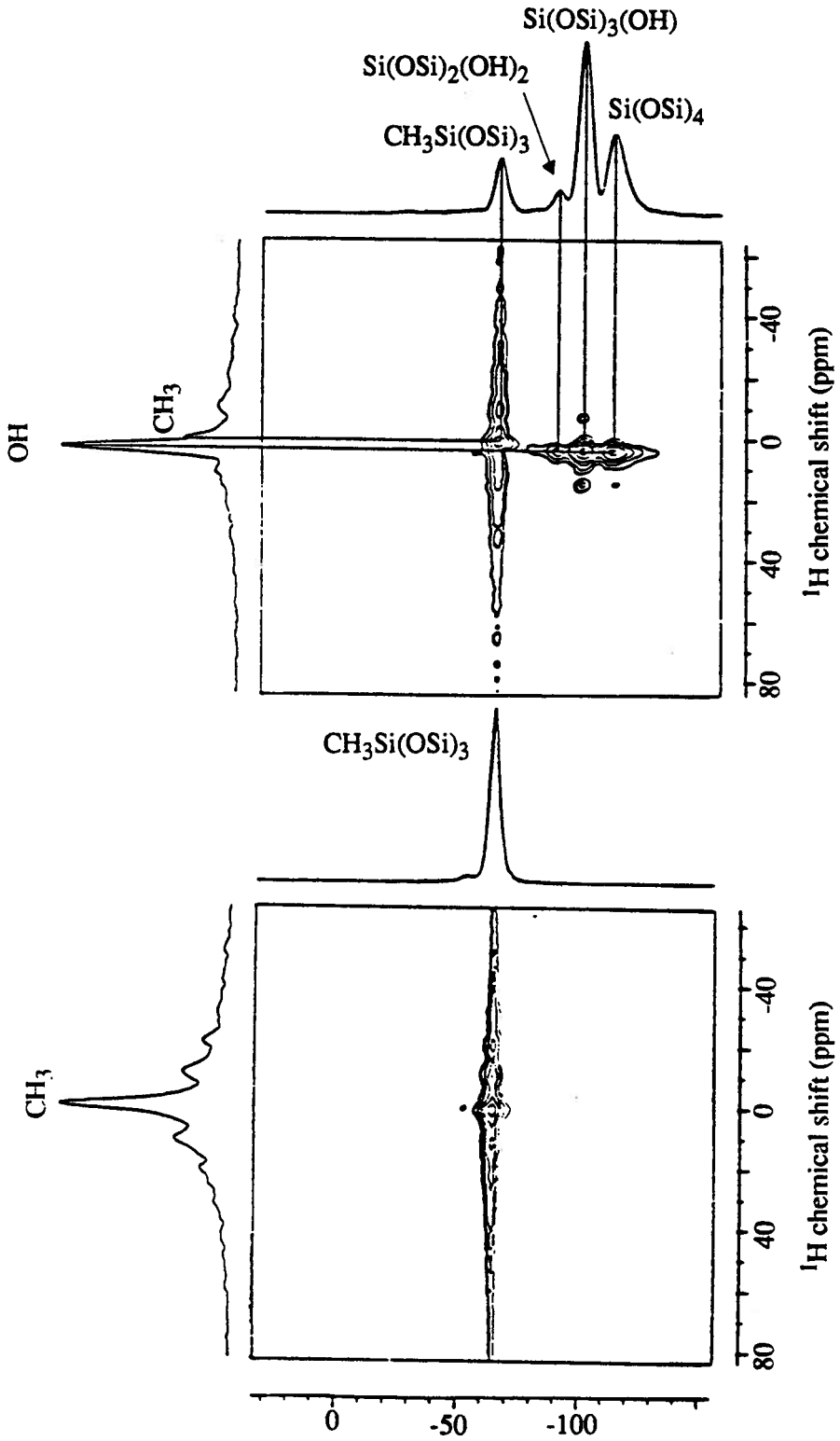

Figure 2.7 - 2D ^{1}H - ^{29}Si heteronuclear correlation NMR experiments for a mixture of silica gel and polymethylsiloxane. The top spectrum is of the unwashed sample with 80 scans per experiment. The bottom spectrum is of the same sample washed with D_2O several times with 200 scans per experiment.

In Figure 2.7 the bottom 2D spectrum is of the same physical mixture of MTES and TEOS homopolymers after several washings with D_2O. As in the TEOS homopolymer, the hydroxyl cross peak is reduced remarkably, to the extent that the methyl cross peak is by far the dominant interaction observed. These spectra of the MTES/TEOS physical mixture allow for the unambiguous identification of the cross polarization sources: the methyl and hydroxyl groups for the MTES silicons and hydroxyl groups for the TEOS silicons. It should be noted that the efficiency with which the hydroxyl groups were removed in this sample was not attainable for all the preparations, presumably due to differences in their microstructures.

These results show that the 2D heteronuclear correlation experiments are reliable enough to be used on samples where the extent of mixing is not known, such as the MTES/TEOS copolymer (preparation 2.3.3.2 and 2.3.3.3). These gels were washed with D_2O and dried to enhance the contribution from the methyl group relative to those from the hydroxyls. The 2D spectra for the MTES/TEOS copolymers are shown in Figures 2.8 and 2.9 (preparation 2.3.3.2 in Figure 2.8 and preparation 2.3.3.3 in Figure 2.9). In both cases, the TEOS silicons show small connectivities to the residual hydroxyl protons, as well as very clear connectivities to the methyl protons. The observed sidebands in the connectivities are consistent with the origin of the polarization being the methyl groups. In both cases, there is clear evidence for the incorporation of the methyl-substituted silicons throughout the matrix, i.e. the absence of phase separation, and the presence of substantial numbers of local structures of the type a-b (Figure 2.5).

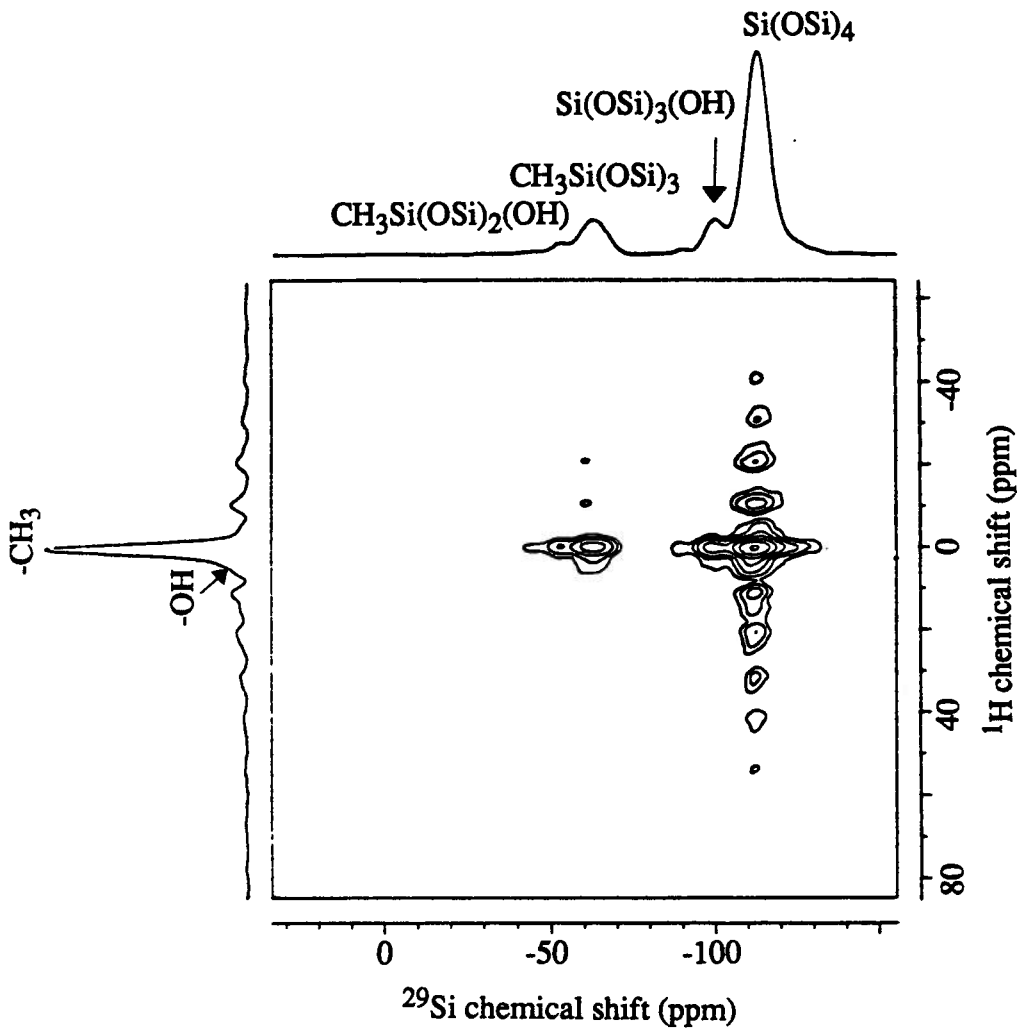

Figure 2.8 - 2D ^{1}H - ^{29}Si heteronuclear correlation NMR experiment, for a D_2O washed 25/75 MTES/TEOS copolymer (preparation 2.3.3.2). with 280 scans per experiment using a contact time of 22 msec.

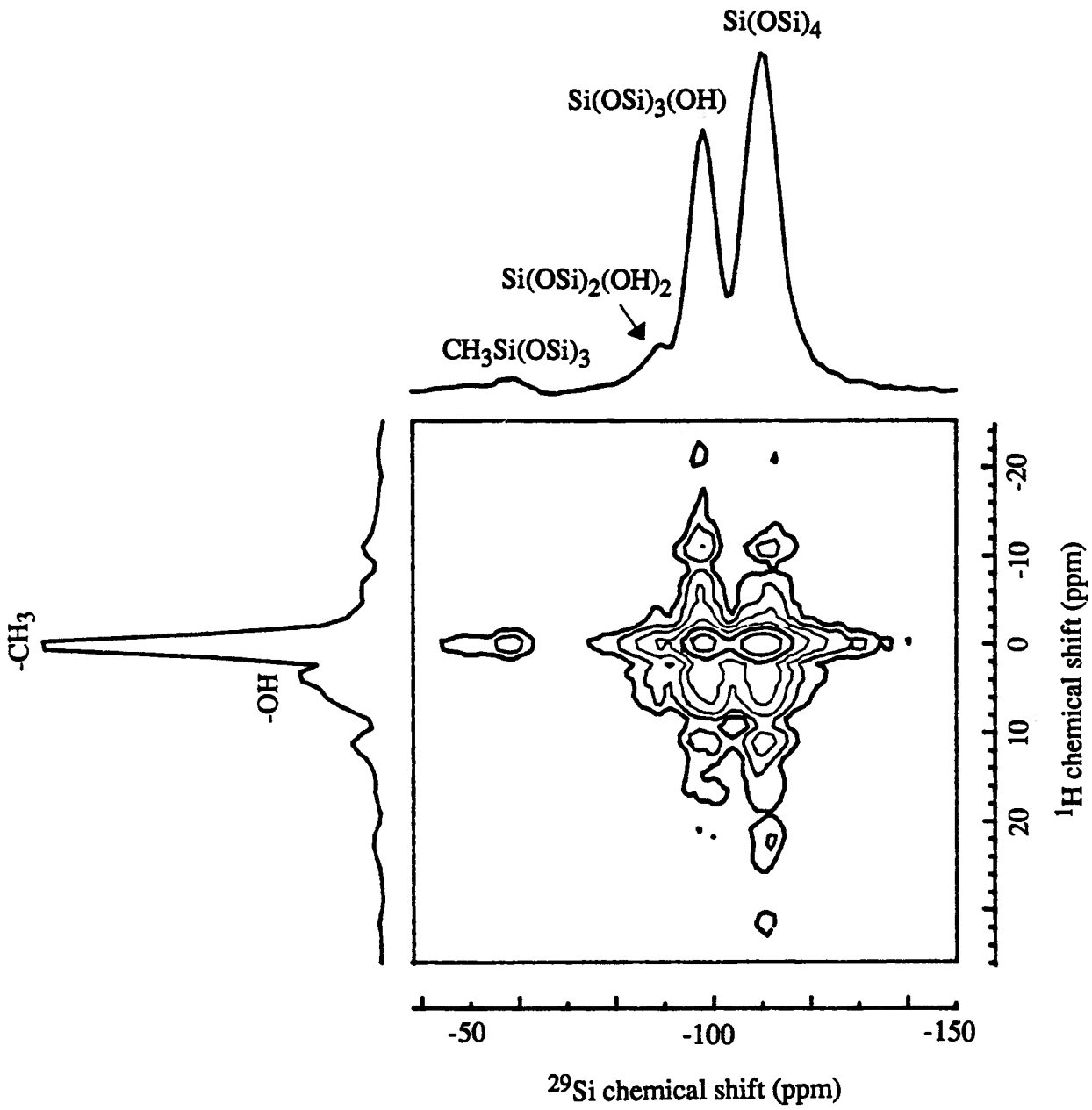

Figure 2.9 - 2D ^{1}H - ^{29}Si heteronuclear correlation NMR experiment, for a D_2O washed 10/90 MTES/TEOS copolymer (preparation 2.3.3.3). with 320 scans per experiment using a contact time of 10 msec.

2.5 CONCLUSIONS

Using ^{13}C and ^{29}Si solid state CP/MAS NMR, it has been shown that the functionalities in the MTES/TEOS copolymer prepared by the alternative copolymerization preparations are intact. One-dimensional NMR experiments were not able to provide unambiguous information on the extent of mixing of the two monomers due to the linewidths of the ^{29}Si resonances and the presence of hydroxyl groups. Therefore, two-dimensional ^{1}H-^{29}Si heteronuclear correlation experiments were used to identify the sources of cross polarization to the different silicon peaks. These experiments demonstrated that the MTES and TEOS monomers in the MTES/TEOS copolymer are "mixed" and not "phase separated". However, these 2D NMR experiments do not provide quantitative information on the degree of mixing. It was anticipated that this information could be obtained from kinetic investigations of the hydrolysis and the initial stages of condensation in solution. These studies for the TEOS and MTES homopolymers, and MTES/TEOS copolymer are described in Chapters 3 and 4.

CHAPTER 3

HIGH RESOLUTION ^{29}Si SOLUTION NMR INVESTIGATION OF THE HYDROLYSIS AND DIMER FORMATION REACTIONS OF TETRAETHOXYSILANE (TEOS)

3.1 INTRODUCTION

The results presented in the previous chapter demonstrate that the methyltriethoxysilane (MTES) and tetraethoxysilane (TEOS) monomers are "mixed" in the solid MTES/TEOS copolymer gel. To determine the extent of mixing a kinetic study of the formation of the copolymer dimer was undertaken, but first the hydrolysis and dimer formation kinetics of both monomers had to be well understood.

Despite the versatility and wide usage of silica gel, the details of the individual sequential reactions during the hydrolysis and condensation of TEOS are not well described in the literature. In early literature on the hydrolysis and condensation of TEOS, different types of chromatography (GC-[3.12], GLPC-[3.11], GPC-[3.10]), and IR and Raman spectroscopy [3.9] were used to obtain global kinetic rate constants of the hydrolysis and condensation stages, i.e. the hydrolysis and condensation are described by two reactions. The general assumption in these works was that only the ligand involved in the reaction had an effect on the hydrolysis and condensation rate constants. Some NMR investigations (principally ^{1}H NMR) were done during this time period but at best global kinetic constants were experimentally determined.[3.13, 3.10, 3.14] In general, the majority of investigations carried out to date have dealt with simplified kinetic models which only permit the evaluation of global hydrolysis and condensation rate constants. [3.10, 3.15-3.23] The increase in global

reaction rates with acid concentration was observed indirectly from hydrolysis time versus condensation time curves. [3.10, 3.17, 3.24, 3.25]

More recently, Assink and Kay have used ^{1}H and ^{29}Si NMR spectroscopy to study the hydrolysis and polymerization of a related system, tetramethoxysilane (TMOS), under substoichiometric water conditions. In their work, they developed a statistical reaction model assuming that both hydrolysis and condensation reactions depended solely on the functional group reactivity, not on the local silicon environments or structures.[3.13, 3.22, 3.23] From their global kinetic hydrolysis constants they deduced kinetic constants for each sequential hydrolysis reaction assuming that the rate coefficient of a given species is simply the product of a statistical factor and the appropriate functional group rate coefficient.[3.28] From their statistical model they concluded that the relative magnitudes of the sequential hydrolysis kinetic rate constants $k_1:k_2:k_3:k_4$ were 4:3:2:1.

Turner et al. studied the hydrolysis of TEOS with varying concentrations of water.[3.26] By qualitative arguments based on the information obtained from their ^{1}H NMR data they found that the concentration of water did not affect the kinetics over the range studied and concluded that k_1 is predominant.[3.26]

Contradicting the above results, Pouxviel's group proposed that for TEOS polymerization at water/silane ratios of 4 and 10 the relative magnitudes of the kinetic constants increased with each sequential hydrolysis, i.e. $k_1<k_2<k_3<k_4$.[3.27] Pouxviel's group numerically simulated the concentration versus time graphs, obtained from ^{29}Si NMR data, for a number of species over a four hour period. In their simulation they considered reactions between sites, not molecules, and the water concentration was kept constant. Unfortunately, further details about their analysis were not presented in their paper. They concluded however, that the hydrolysis rate constants increased as the number of hydroxyls

increased.[3.27]

Hui's group found the same trend as Pouxviel et al. for the kinetic constants. They estimated their individual kinetic constants using the data obtained from ^{1}H NMR spectroscopy and gel permeation chromatography (GPC), and a Linear Free Energy Relationship (the ratios used were not stated) to give a systematic change in the k_i values.[3.10]

Chojnowski et al. studied TEOS at substoichiometric concentrations of water in a neutral solvent (dioxane).[3.24A] They quenched the reaction at different times, trimethylsilated the intermediates and determined their relative concentrations by gas chromatography/mass spectrometry (GC/MS). The individual kinetic constants were deduced by numerically solving the kinetic equations using the Runge-Kutta-Fehlberg method [3.24B], and optimized by the Rosenbrock procedure [3.24C].

At the present time Chojnowski et al. and Pouxviel et al. are the only two groups that have published experimentally determined kinetic constants for the sequential hydrolysis reactions of TEOS, although in both cases their results contain a pH dependence. These will be discussed in more detail subsequently in terms of the results from the present work.

Unfortunately, several literature results contradict each other, possibly due to the fact that some studies have been done at substoichiometric concentrations of water [3.13, 3.24A, 3.26] where a good separation of the hydrolysis and condensation processes was not established; some have used peak heights not areas from the NMR spectra for quantitative analysis of the components [3.10, 3.15, 3.26], and in some cases there was no control of the temperature at which the kinetics were studied [3.10, 3.15]. Of the few studies that do present kinetic rate constants for the individual hydrolysis reactions, most use either relationships between the kinetic constants that may not be valid [3.10] or assume unproven

generalizations about the reactivity of groups [3.13, 3.22, 3.23]. Consequently, a detailed characterization of the hydrolysis and dimer formation reactions of TEOS was undertaken. This study will serve as a reference for investigations of the effects of functionality, formamide and copolymerization in later chapters.

The polymerization of TEOS involves three general reactions; [3.19]

1) hydrolysis:

$$Si(OEt)_4 + H_2O \rightarrow Si(OEt)_3(OH) + EtOH \tag{3.1}$$

$$Si(OEt)_3(OH) + H_2O \rightarrow Si(OEt)_2(OH)_2 + EtOH$$

etc. until the TEOS monomer is completely hydrolyzed

2) condensation with the elimination of water:

$$2\,Si(OH)_4 \rightarrow \equiv SiOSi\equiv + H_2O \tag{3.2}$$

and 3) condensation with the elimination of an alcohol:

$$Si(OH)_4 + Si(OH)_3(OEt) \rightarrow \equiv SiOSi\equiv + EtOH \quad . \tag{3.3}$$

This chapter presents the kinetic model used to determine individual kinetic constants. The pH dependent kinetic constants were determined experimentally for the sequential TEOS hydrolysis reactions and for the first time the pH independent kinetic constants for the hydrolysis and dimer formation reactions were calculated.

3.2 EXPERIMENTAL

3.2.1 Chemicals and Reaction Mixtures

The experimental reaction conditions of TEOS were chosen to simplify the kinetics study. Acid catalysis and high water/silane ratios were used so that a good separation of the hydrolysis and condensation reactions was achieved.[3.1, 3.11]

Tetraethoxysilane (TEOS) was studied instead of tetramethoxysilane (TMOS) because it is less hazardous and there is a greater chemical shift difference between the resonances of the intermediates.[3.2] The composition of the TEOS reaction mixture was: 4 ml (0.0179 mole) TEOS, 6.07 ml (0.1034 mole) ethanol, 3.58 ml (0.1981 mole) water acidified with concentrated HCl (various acid concentrations) and 0.075 g (0.000215 mole) of chromium acetylacetonate ($Cr(acac)_3$). Chromium acetylacetonate is a paramagnetic compound added to increase the nuclear relaxation rates, i.e. decrease T_1.[3.8]

Deuterium oxide needed for the NMR lock signal was added to the water. At least two independent experiments were done at each pH value (3.35, 3.04, 2.88, 2.76, 2.55, 2.45 and 2.33). pH values between 2.33 and 3.35 were used since outside these limits the reaction proceeded either too quickly or too slowly to accurately characterize the hydrolysis and dimer formation rates by ^{29}Si solution NMR spectroscopy. Time zero in the experiments corresponds to the time when the acidified water was added to the reaction mixture.

3.2.2 NMR Measurements

^{29}Si solution NMR spectroscopy was used to quantitatively characterize each step of the hydrolysis and dimer formation of the acid catalyzed homopolymerization of TEOS in water/ethanol. The resonances of the intermediate species in the TEOS hydrolysis can be clearly resolved in a 1D ^{29}Si solution NMR spectrum.

A Bruker AMX 500 MHz spectrometer with a 10 mm broad-band probe was used and a temperature control unit maintained a constant sample temperature of 300.0 ± 0.1 K. A relaxation agent, chromium acetylacetonate ($Cr(acac)_3$) was added to reduce the ^{29}Si spin-lattice relaxation time (T_1) allowing for a faster repetition time between scans. The ^{29}Si spin-lattice relaxation times (T_1) of TEOS, in water and in water/ethanol, were determined for different concentrations of $Cr(acac)_3$ (0.01575 to 0.002711 M). The water/silane, ethanol/silane and water/ethanol ratios were kept the same as those used in the kinetic studies. The $Cr(acac)_3$ concentration of 0.016 M was chosen since this concentration approaches the limit of solubility in the solvent system. No significant line broadening due to the $Cr(acac)_3$ was observed in the ^{29}Si spectrum. Previous studies have shown that the presence of a relaxation agent has no effect on the polymerization process. [3.2, 3.3]

In the presence of 0.016 M $Cr(acac)_3$, the ^{29}Si resonance of TEOS has a T_1 value of 1.7 sec. Two kinetic runs with different recycle delays ($1*T_1$ and $2*T_1$) gave identical concentration profiles (within the ± 2% experimental scatter), implying that the ^{29}Si T_1 values for TEOS and all the hydrolyzed intermediate species are virtually the same. Consequently, no bias exists in the measured concentrations. The Ernst angle equation [3.4] was therefore used to optimize the signal/noise ratio. In both of these kinetic experiments and in all further ones, the total ^{29}Si signal intensity observed was constant within ± 2%.

As a compromise between signal/noise ratio and a disproportionate averaging of the fast reacting species eight scans were accumulated per spectrum with a repetition time of one second and a 60° pulse angle on the ^{29}Si channel. Proton gated decoupling was used to ensure there were no negative NOE effects [3.4], even though previous data indicate that the negative NOE effect is negligible.[3.22, 3.23] A complete kinetic experiment consisted of acquiring 64 spectra at two minute intervals with a spectral accumulation time of 10 seconds.

3.3 RESULTS AND DISCUSSION

3.3.1 Experimental Results

A typical ^{29}Si spectrum obtained during the hydrolysis of tetraethoxysilane (TEOS) is shown in Figure 3.1. The assignment of the different ^{29}Si environments is in agreement with the literature.[3.6] At 500 MHz, under these reaction conditions, the resonances of all the monomeric species are clearly separated while those of the condensation products are less well-resolved, limiting the study of the formation of oligomers more complex than the dimer. A typical example of the time dependence of the spectra during the reaction is presented in Figure 3.2.

The concentration versus time curves for the hydrolysis intermediates were determined by integration over fixed individual frequency ranges in the spectra. These integrated areas were used to calculate the percentages of the total concentration. The total integrated area for the initial ^{29}Si spectrum was taken to be 100%. The relative concentration versus time graphs for all the intermediate species from one typical experiment (pH=2.55) are shown in Figure 3.3.

3.3.2 Kinetic Analysis

The data obtained from the kinetic experiments was analyzed by modifying existing software to deal with the specific set of equations which were dictated by the kinetic model. From the analysis of the data, kinetic constants for each of the hydrolysis steps and for the first condensation step have been determined. The TEOS hydrolysis rate constants that were independent of the catalyst concentration (HCl) were calculated from the pH dependence of the kinetic constants.

The simplest model describing the hydrolysis of TEOS involves a series of sequential reactions that proceed from TEOS to the formation of the fully hydrolyzed dimer. These five

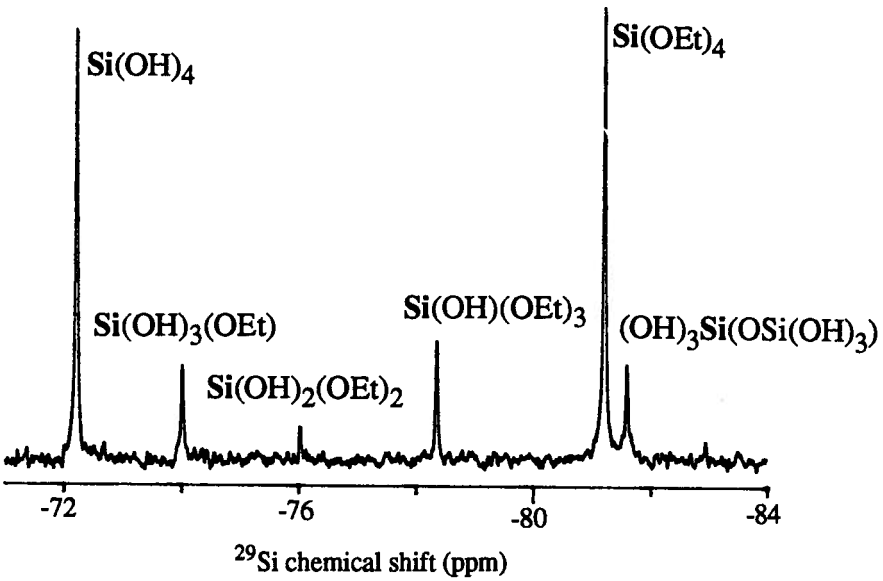

Figure 3.1 - A typical ^{29}Si spectrum obtained during the hydrolysis of TEOS with the peaks assigned as indicated.

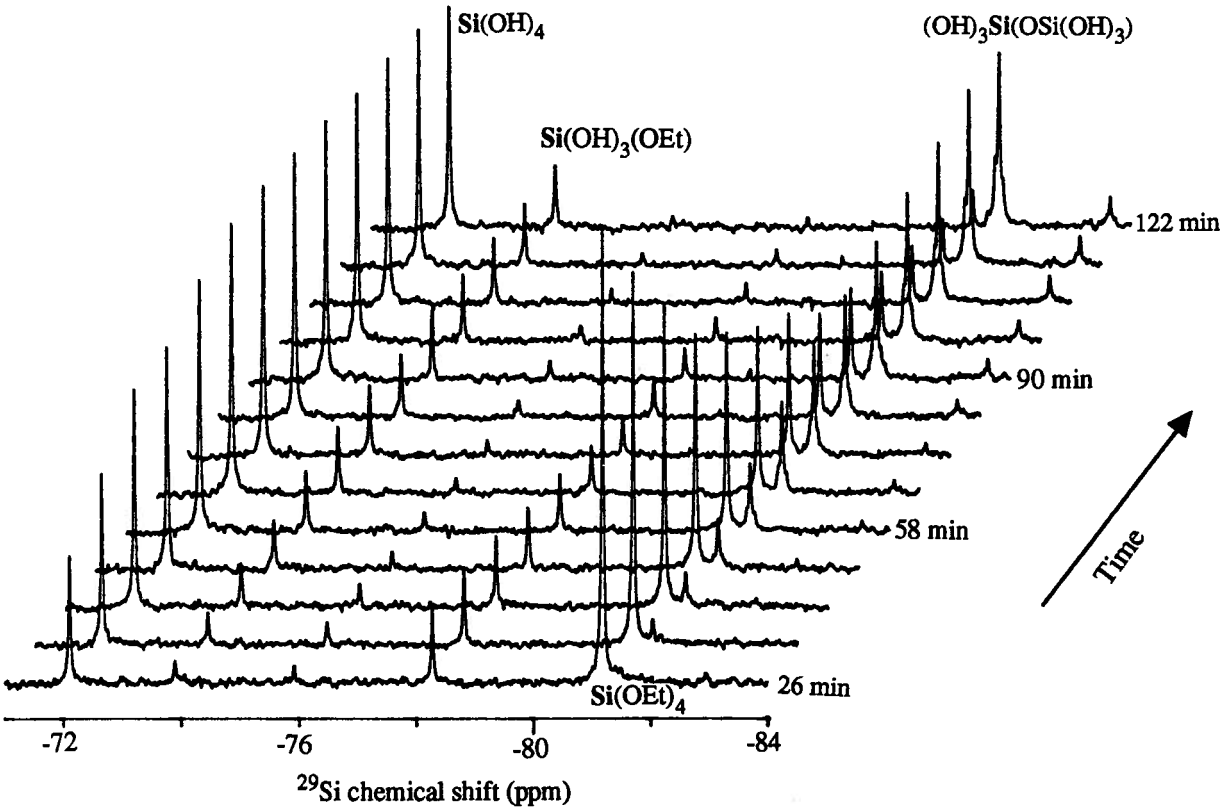

Figure 3.2 - Stacked plot of the one-dimensional ^{29}Si NMR spectra obtained during the polymerization of tetraethoxysilane at the times indicated: the water was acidified to pH=2.55, and 8 scans/spectrum were acquired using a 1 second recycle delay and a 60^{o} pulse.

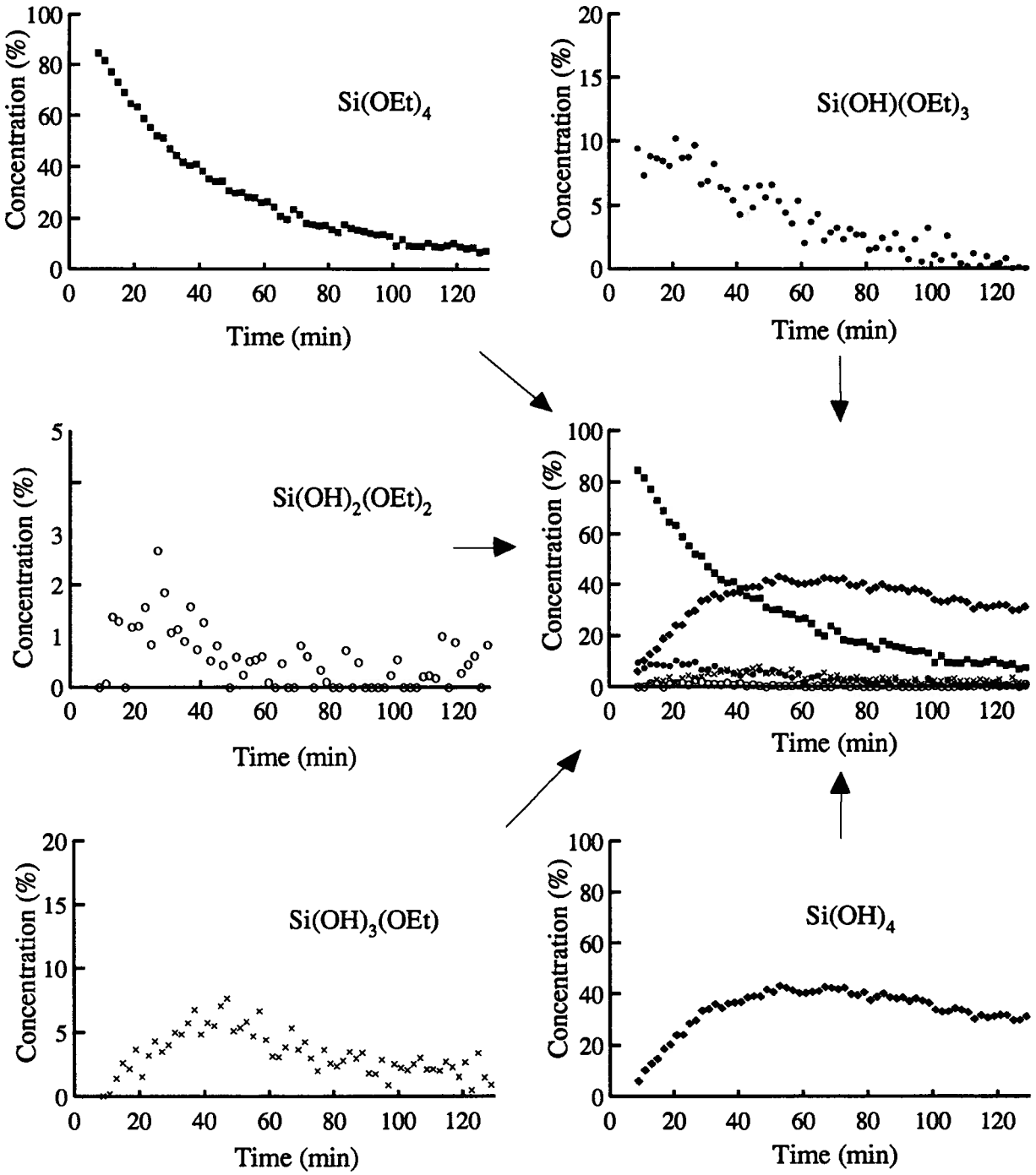

Figure 3.3 - The time dependence of the relative concentrations of all of the intermediate species involved in the hydrolysis of TEOS. TEOS hydrolysis data at pH=2.55. The experimental error is ±2%.

reactions are:

$$Si(OEt)_4 + H_2O \xrightarrow{k_{T1}} Si(OH)(OEt)_3 + EtOH \tag{3.4}$$

$$Si(OH)(OEt)_3 + H_2O \xrightarrow{k_{T2}} Si(OH)_2(OEt)_2 + EtOH \tag{3.5}$$

$$Si(OH)_2(OEt)_2 + H_2O \xrightarrow{k_{T3}} Si(OH)_3(OEt) + EtOH \tag{3.6}$$

$$Si(OH)_3(OEt) + H_2O \xrightarrow{k_{T4}} Si(OH)_4 + EtOH \tag{3.7}$$

$$2Si(OH)_4 \xrightarrow{k_{T5}} Si(OH)_3OSi(OH)_3 + H_2O \tag{3.8}$$

where OEt represents the ethoxy ligand.

In the literature, the determination of a global hydrolysis rate constant (k_H) involves the assumption that reactions (3.4)-(3.7) can be described by a single reaction:

$$\equiv Si(OEt) + H_2O \xrightarrow{k_H} \equiv Si(OH) + EtOH$$

Under the conditions chosen there is a good separation of the hydrolysis reactions and the condensation product formation, which justifies that the kinetic analysis include reactions up to the fully hydrolyzed dimer formation. For example, at pH=2.55, the first indications of condensed species in the spectra occur after 25 minutes, and after 40 minutes, only 9% conversion to dimer species has occurred. The separation is even clearer at higher pH values.

The kinetic curves, such as those shown in Figure 3.3, were fitted sequentially over a four stage process which is outlined in the following paragraphs. Successive stages of the fitting process involved the controlled introduction of additional variables.

The initial step in the fitting procedure involved a non-linear least squares fit considering only the first four kinetic reactions (3.4)-(3.7) as forward (irreversible) reactions.

The corresponding kinetic equations for the reactions (3.4)-(3.7) are (3.9)-(3.12).

$$\frac{d[TEOS]}{dt} = -k_{T1}[TEOS]_t\,[H_2O]_o \tag{3.9}$$

$$\frac{d[Si(OH)(OEt)_3]}{dt} = (k_{T1}[TEOS]_t - k_{T2}[Si(OH)(OEt)_3]_t)\,[H_2O]_o \tag{3.10}$$

$$\frac{d[Si(OH)_2(OEt)_2]}{dt} = (k_{T2}[Si(OH)(OEt)_3]_t - k_{T3}[Si(OH)_2(OEt)_2]_t)\,[H_2O]_o \tag{3.11}$$

$$\frac{d[Si(OH)_3(OEt)]}{dt} = (k_{T3}[Si(OH)_2(OEt)_2]_t - k_{T4}[Si(OH)_3(OEt)]_t)\,[H_2O]_o \tag{3.12}$$

Explicit expressions (3.13)-(3.16) for each monomeric species can be obtained upon integration of the derivatives (3.9)-(3.12).

$$\frac{[TEOS]_t}{[TEOS]_o} = e^{-k_{T1}[H_2O]_o t} \tag{3.13}$$

$$\frac{[Si(OH)(OEt)_3]_t}{[TEOS]_o} = \frac{k_{T1}}{(k_{T2} - k_{T1})}\left(e^{-k_{T1}[H_2O]_o t} - e^{-k_{T2}[H_2O]_o t}\right) \tag{3.14}$$

$$\frac{[Si(OH)_2(OEt)_2]_t}{[TEOS]_o} = \frac{k_{T1}k_{T2}}{(k_{T2} - k_{T1})}\left[\frac{e^{-k_{T1}[H_2O]_o t}}{(k_{T3} - k_{T1})} - \frac{e^{-k_{T2}[H_2O]_o t}}{(k_{T3} - k_{T2})} + \left(\frac{1}{(k_{T3} - k_{T2})} - \frac{1}{(k_{T3} - k_{T1})}\right) e^{-k_{T3}[H_2O]_o t}\right] \quad (3.15)$$

$$\frac{[Si(OH)_3(OEt)]_t}{[TEOS]_o} = \frac{k_{T3}k_{T2}k_{T1}}{(k_{T2} - k_{T1})}\left[\frac{e^{-k_{T1}[H_2O]_o t}}{(k_{T3} - k_{T1})(k_{T4} - k_{T1})} - \frac{e^{-k_{T2}[H_2O]_o t}}{(k_{T3} - k_{T2})(k_{T4} - k_{T2})} + \left(\frac{1}{(k_{T3} - k_{T2})(k_{T4} - k_{T3})} - \frac{1}{(k_{T3} - k_{T1})(k_{T4} - k_{T3})}\right) e^{-k_{T3}[H_2O]_o t}\right.$$

$$\left. + \left(\frac{\left(\frac{1}{(k_{T4} - k_{T3})} - \frac{1}{(k_{T4} - k_{T1})}\right)}{(k_{T3} - k_{T1})} + \frac{\left(\frac{1}{(k_{T4} - k_{T2})} - \frac{1}{(k_{T4} - k_{T3})}\right)}{(k_{T3}k_{T2})}\right) e^{-k_{T4}[H_2O]_o t}\right] \quad (3.16)$$

The expressions (3.13)-(3.16) were entered into a non-linear least squares fitting program to provide the first approximations to the kinetic constants. In this first approximate analysis, all condensation and possible equilibrium reactions are ignored and the water concentration was assumed to be constant ($[H_2O]_o$= initial concentration of water). Inspection of the experimental results in Figure 3.3 reveals that the intermediate species $Si(OH)_2(OEt)_2$ and $Si(OH)_3(OEt)$ never reach concentrations greater than 9±1%. In fact, the $Si(OH)_2(OEt)_2$ concentration is never greater than 2 ± 1%. This limits the accuracy with which k_{T3} and subsequent rate constants can be determined. Figure 3.4 presents the experimental and calculated curves from this process for pH=2.55.

To minimize the errors in the assumptions made in this approach, large water/silane and ethanol/silane ratios (11.05 and 5.8 respectively) were chosen for the reaction mixture. These high ratios reduce the variation in both the water concentration and the solvent composition as the reaction progresses. In addition, a high water/silane ratio favours the hydrolysis process, producing a better separation between the hydrolysis and condensation

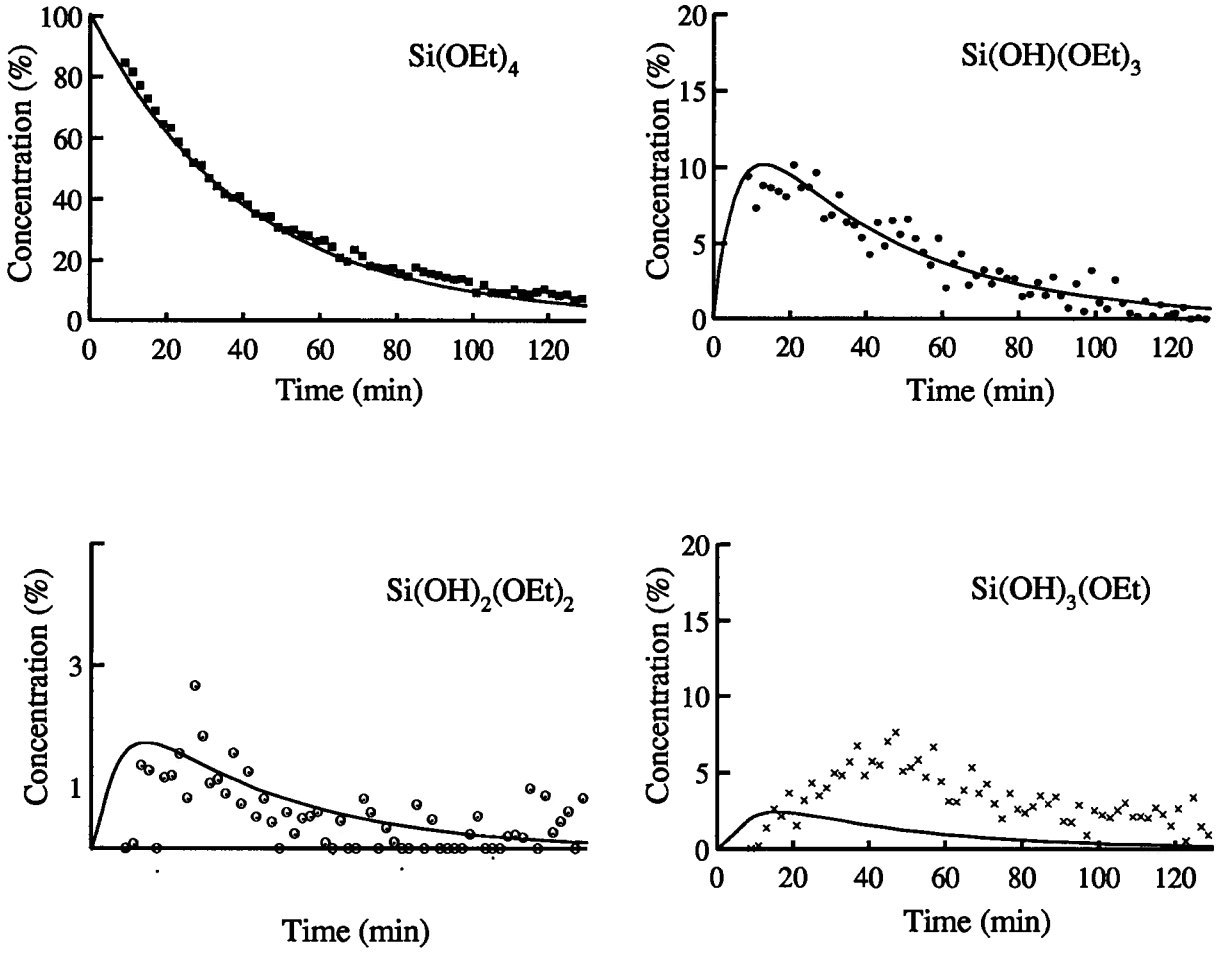

Figure 3.4 - Calculated curves from the least squares fitting of equations (3.13-3.16) for the time dependence of the relative concentrations of the intermediate species formed during the TEOS hydrolysis assuming a constant water concentration. The experimental error is ±2%.

reactions, and minimizes condensation between partially hydrolyzed species.[1.43] This approach is limited mainly by the sensitivity of the NMR experiments. A relatively high ethanol/silane ratio was needed to prevent phase separation.

The calculated curves shown for the hydrolysis intermediate species in Figure 3.4 describe to a good approximation what is happening in the reaction vessel. Only the fit for $[Si(OH)_3(OEt)]$ does not match well with the experimental data. The next step in the fitting process was aimed at improving the fit of this curve by taking into account the change in water concentration. Consequently, $[H_2O]_o$ is now replaced by η_t (3.17) in equations (3.9)-(3.12):

$$\eta_t = [H_2O]_o - [Si(OEt)_3(OH)]_t - 2*[Si(OEt)_2(OH)_2]_t - 3*[Si(OEt)(OH)_3]_t - 4*[Si(OH)_4]_t \quad (3.17)$$

The resulting interdependent differential equations are now not explicitly solvable and the solutions must be obtained numerically.

A new set of subroutines was written in order to call a program called LSODE which numerically solves interdependent differential equations.[3.7] It uses a backward differential formula approach which is a multi-step method first implemented by C.W. Gear.[3.7] The results from the first fit (Appendix 1) were refined in this step and these numerical solutions were the starting points for the next step in the fitting procedure.

In general, including the water concentration variation had a very small effect on the curves, as seen in Figure 3.5. Thus it is not considered to be a critical factor in the fitting of the kinetic curves for these reactions, at least not under the conditions used. Nevertheless, it was included in all the final calculated curves for completeness.

The next addition to the fitting procedure was to include the first condensation

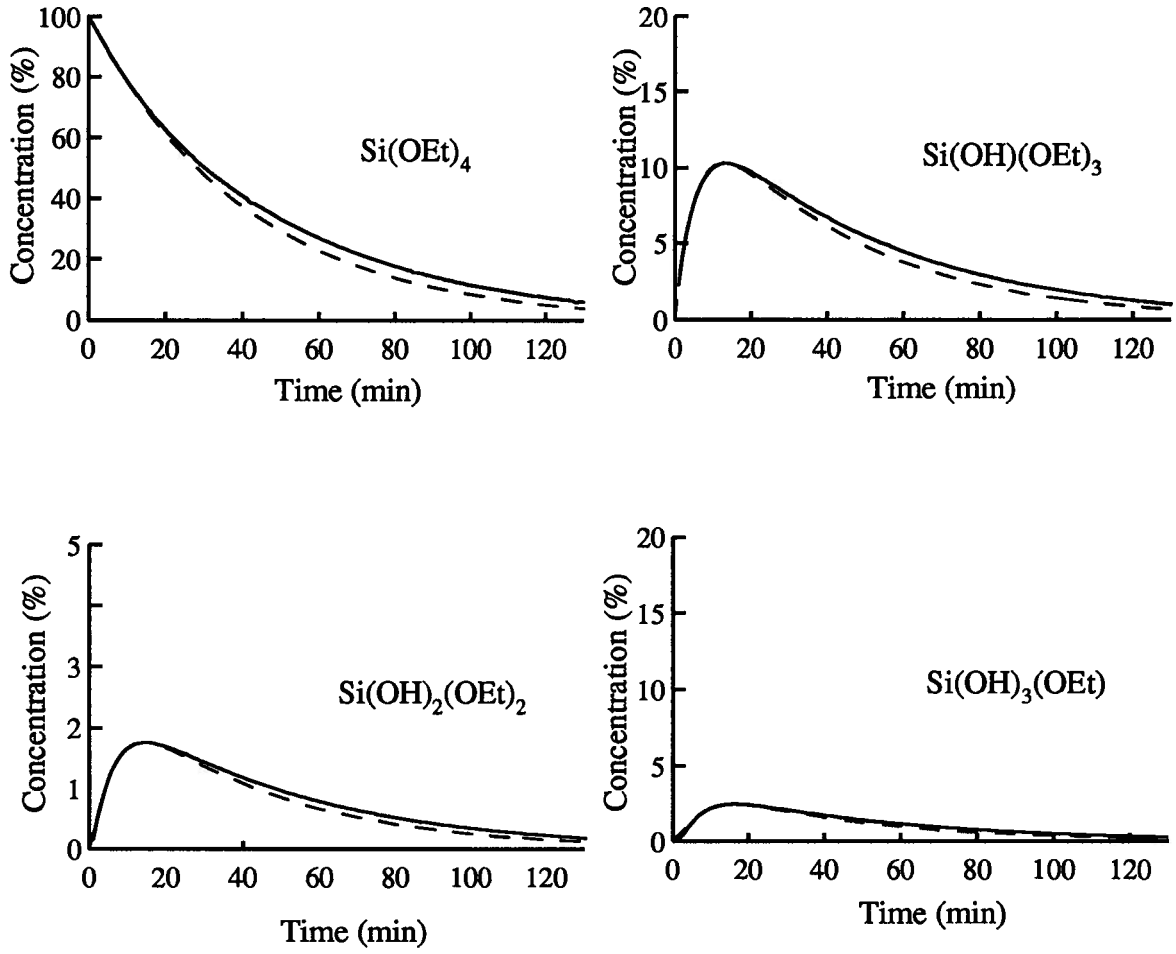

Figure 3.5 - Comparison of different calculated curves for the TEOS system (pH=2.55). The fits obtained when the water concentration is held constant (dashed lines) and when the change in water concentration is taken into account as the reactions progresses (solid lines) are shown. The experimental error ±2%.

reaction to the kinetic scheme by adding equation (3.18) to the series of kinetic equations.

$$\frac{d[Si(OH)_4]}{dt} = (k_{T4}[Si(OH)_3(OEt)]_t\ \eta_t - k_{T5}[Si(OH)_4]_t^2) \qquad (3.18)$$

By including the effect of the first condensation reaction, the $Si(OH)_4$ species concentration as a function of time could be fitted.

The net effect was to reproduce reasonably well the time dependence of the $Si(OH)_4$ product but no significant change was detected for the calculated curve of the low concentration $Si(OH)_3(OEt)$ intermediate (Figure 3.6A). Thus the fit for the $Si(OH)_3(OEt)$ species was still inadequate.

In order to satisfactorily fit the concentration profile of the $Si(OH)_3(OEt)$ intermediate species, an additional process had to be included in the model. The model used up to this point predicts a curve for the $Si(OH)_3(OEt)$ concentration that reaches a maximum and then decays to zero, which obviously does not agree with the experimental data. The experimental data are characterized by a plateau after the maximum which suffers minimal decay as the reaction proceeds, suggesting that an equilibrium is established between $Si(OH)(OEt)_3$ and $Si(OH)_4$. Therefore, in order to reproduce the curve shapes for the decay of $Si(OH)_3(OEt)$ and the formation of $Si(OH)_4$, an equilibrium between these two species was considered. This means that equations (3.12) and (3.18) must be modified leading to a new set of differential equations. Equations (3.20)-(3.22) correspond to equation (3.9)-(3.11), taking the change in the water concentration into account. Equations (3.23) and (3.24) incorporate the back reaction just discussed resulting in the inclusion of the change in ethanol concentration during the reaction.

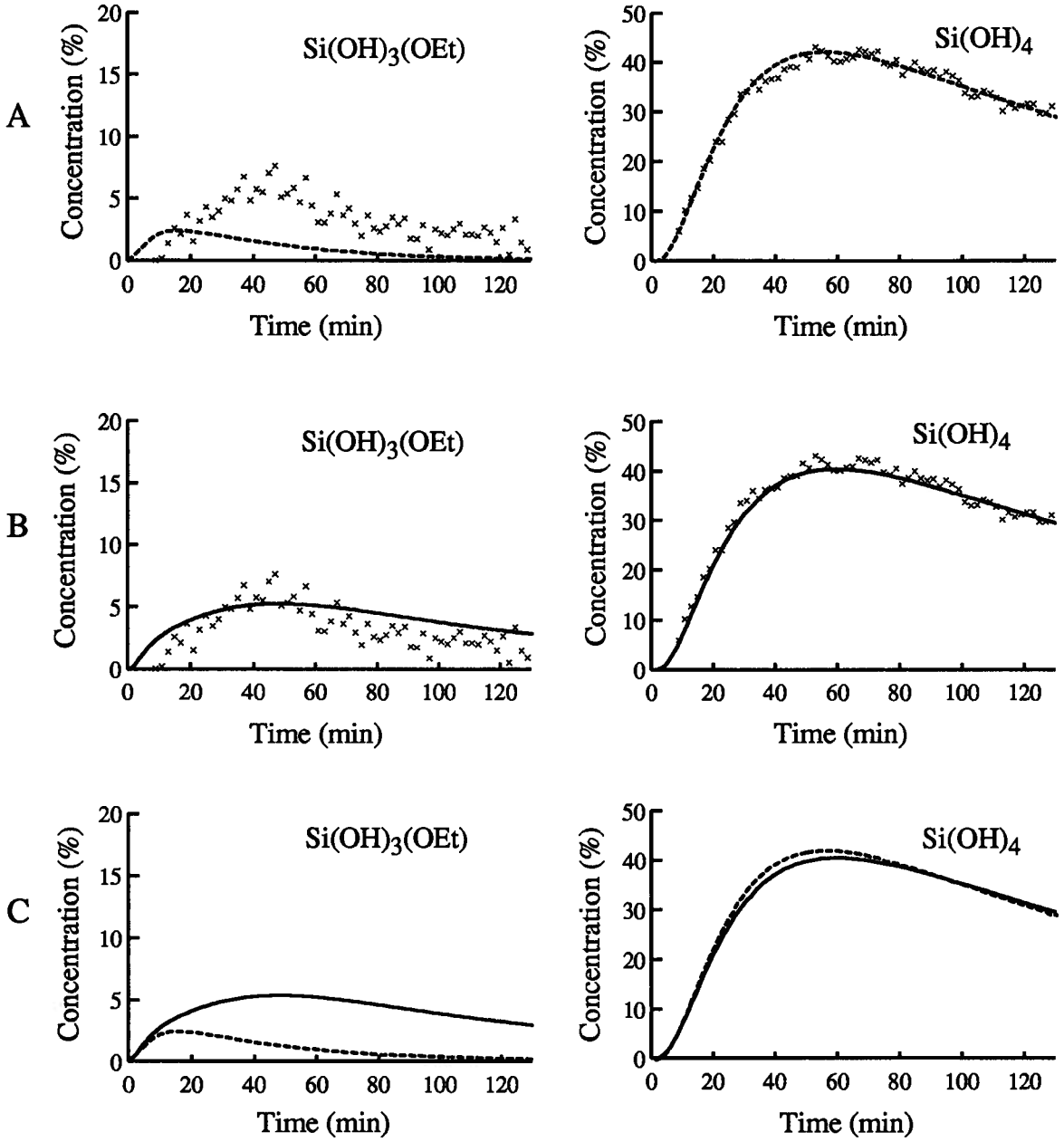

Figure 3.6 - Calculated curves of the relative concentrations of $Si(OH)_3(OEt)$ and $Si(OH)_4$ intermediates (acidified water was at pH=2.55).
The experimental error is ±2%.
A - is the shape of the curve when not considering the equilibrium back reaction.
B - is the shape of the curve when considering the equilibrium back reaction. The experimental data is also shown in both A and B.
C - is a comparison of these two curves without the experimental data.

$$\frac{d[TEOS]}{dt} = -k_{T1}[TEOS]_t \eta_t \tag{3.19}$$

$$\frac{d[Si(OH)(OEt)_3]}{dt} = (k_{T1}[TEOS]_t - k_{T2}[Si(OH)(OEt)_3]_t) \eta_t \tag{3.20}$$

$$\frac{d[Si(OH)_2(OEt)_2]}{dt} = (k_{T2}[Si(OH)(OEt)_3]_t - k_{T3}[Si(OH)_2(OEt)_2]_t) \eta_t \tag{3.21}$$

$$\frac{d[Si(OH)_3(OEt)]}{dt} = (k_{T3}[Si(OH)_2(OEt)_2]_t - k_{T4_f}[Si(OH)_3(OEt)]_t)\eta_t + k_{T4_b}[Si(OH)_4]_t \varepsilon_t \tag{3.22}$$

$$\frac{d[Si(OH)_4]}{dt} = k_{T4_f}[Si(OH)_3(OEt)]_t \eta_t - k_{T4_b}[Si(OH)_4]_t \varepsilon_t - k_{T5}[Si(OH)_4]_t^2 \tag{3.23}$$

where

$$\varepsilon_t = [EtOH]_o + [Si(OH)(OEt)_3]_t + 2[Si(OH)_2(OEt)_2]_t + 3[Si(OH)_3(OEt)]_t + 4[Si(OH)_4]_t \tag{3.24}$$

The inclusion of the back reaction, condensation reaction and the change in water and ethanol concentrations again precludes the possibility of explicitly integrating this final set of differential equations. Consequently, these interdependent differential equations were numerically solved using LSODE with the previous $k_{T1\text{-}T5}$ values as starting values. The effect of this modification on the $Si(OH)_3(OEt)$ and $Si(OH)_4$ curves is illustrated in Figure 3.6B and C. The results from this fourth fitting procedure are presented in Figure 3.7 for

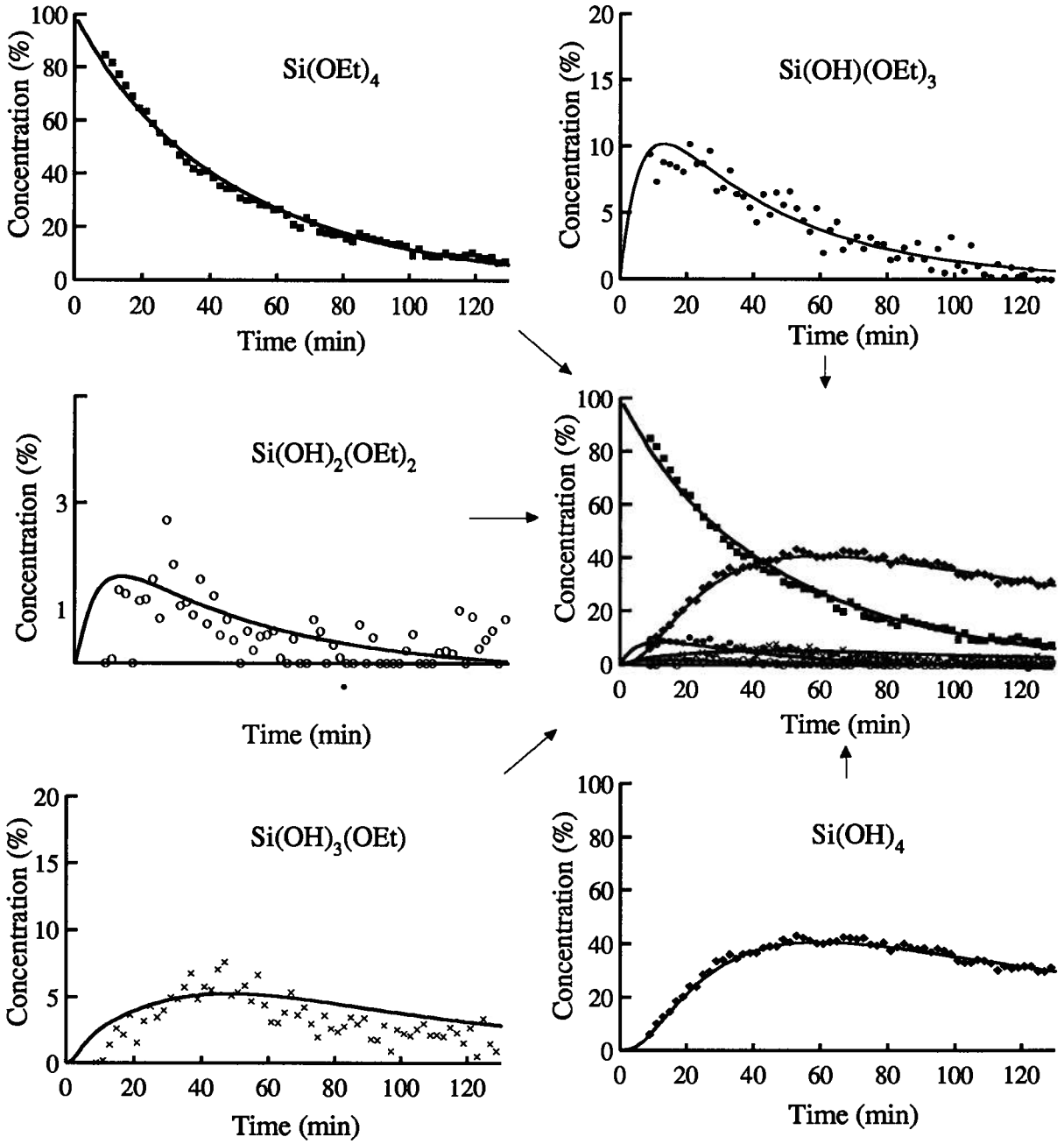

Figure 3.7 - The time dependence of the relative concentrations of all the intermediate species involved in the hydrolysis of TEOS together with the calculated curves. The data are from the kinetic run of TEOS at pH=2.55.
The experimental error is ±2%.

all of the intermediate hydrolysis species of TEOS at pH=2.55.

The final analysis procedure was done in terms of five sequential chemical reactions (3.4)-(3.8) and their kinetic equations (3.19)-(3.23). This set of equations considers reaction (3.7) as an equilibrium process and includes the condensation reaction between two fully hydrolyzed monomers, reaction (3.8). In addition, it assumes that the dimer formation reaction is the only reaction depleting the monomer concentration.

3.3.3 Justification for Not Including Other Reactions

In the time frame used to study the kinetic reactions, dimers but no significant amounts of higher oligomers were detected. There are three possible types of condensation reactions that could form a dimer, (3.25)-(3.27): [3.24]

$$2\,Si(OH)_4 \rightarrow \equiv SiOSi\equiv + H_2O \tag{3.25}$$

$$Si(OH)_4 + Si(OEt)(OH)_3 \rightarrow \equiv SiOSi\equiv + H_2O \tag{3.26}$$

$$Si(OH)_4 + Si(OEt)(OH)_3 \rightarrow \equiv SiOSi\equiv + EtOH \tag{3.27}$$

Condensation between partially hydrolyzed species can be ignored because their concentrations are not significant compared to $Si(OH)_4$ (see Figure 3.3), making reaction (3.25) the predominant dimer formation reaction under these experimental conditions.

The polymerization of TEOS could involve other reactions, such as re-esterification. One such reaction was included in equation (3.23) for the $Si(OH)_4$ fully hydrolyzed species. In order to rule out other re-esterification reactions for TEOS and the other intermediate hydrolysis species, an experiment was designed using ^{13}C labelled ethanol ($CH_3{}^{13}CH_2OH$), to determine directly the total extent of trans- and re-esterification. Figure 3.8 shows a natural abundance ^{13}C solution NMR spectrum obtained during the hydrolysis of TEOS. Figure 3.9 shows the $\equiv SiOCH_2$- region of the spectra obtained from two kinetic runs, one with ^{13}C natural abundance ethanol (Figure 3.9A) and the other with 99.99% ^{13}C enriched ethanol ($CH_3{}^{13}CH_2OH$) (Figure 3.9B).

The total area of the $-CH_3$ chemical shift region is proportional to the ethoxy ligand concentration, including those in the form of ethanol and those attached to silicon. Therefore, the integral of the $\equiv SiOCH_2$- region divided by the total $-CH_3$ area gives the percent of ethoxy

ligand attached to silicon. After 100 minutes of the natural abundance kinetic run, the concentration of $\equiv SiOCH_2CH_3$ is 54% of its initial concentration. This decrease is due to the hydrolysis, compensated by any trans- and re-esterification reactions which may occur. The enriched ^{13}C ethanol kinetic run shows a growth to 163% of the initial $\equiv SiOCH_2CH_3$ concentration. The natural abundance of ^{13}C is 1.11% and 99.99% enriched ethanol was used, therefore the trans- and re-esterification reactions appear magnified by a factor of 99. With this information, it was calculated that only about 1% of the $\equiv SiOH$ and of the $\equiv SiOCH_2CH_3$ ligands are involved in trans- or re-esterification reactions. This result shows that the extent of trans- and re-esterification reactions under the chosen experimental conditions is small and therefore justifies the assumption in the kinetic model that the only re-esterification reaction occurring to any extent involves $Si(OH)_4$.

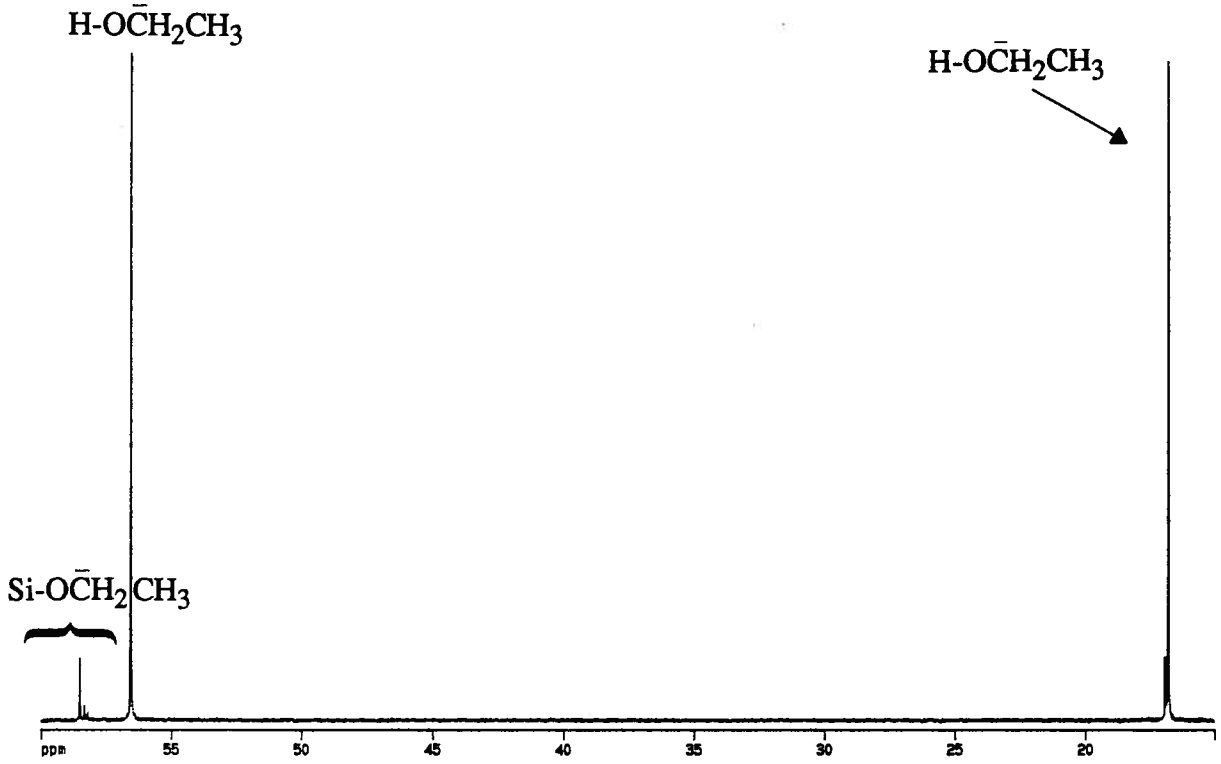

Figure 3.8 - ^{13}C solution NMR spectrum for the TEOS polymerization reaction with natural abundance ^{13}C ethanol. The spectrum was obtained after 131 minutes with 32 scans, using a recycle delay of 3.5s and a 60^{o} pulse.

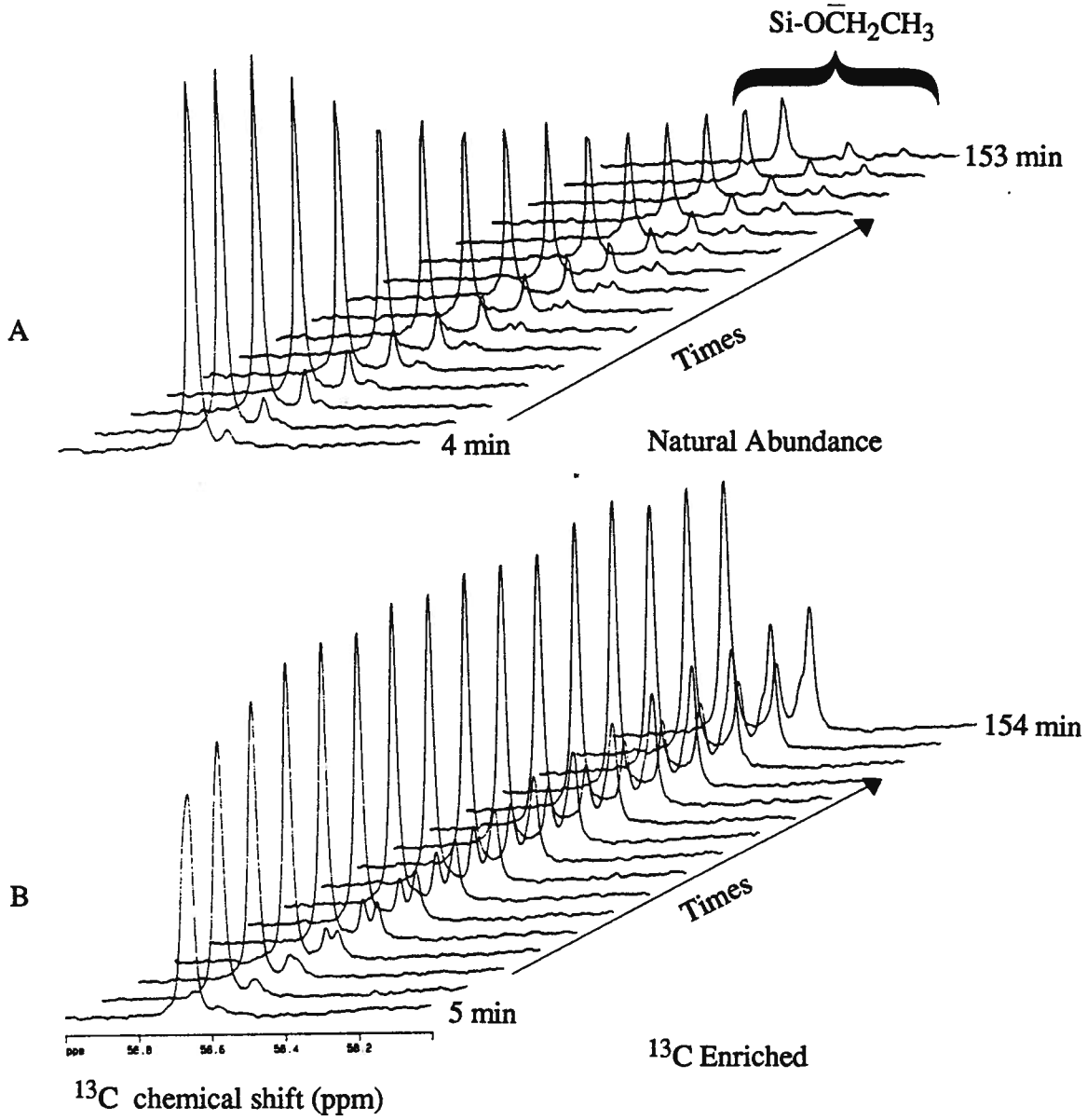

Figure 3.9 - Series of ^{13}C solution NMR spectra for the TEOS polymerization reaction (A) with natural abundance and (B) with ^{13}C enriched ethanol. The spectra were obtained with 32 scans, a recycle delay of 3.5s and a 60^{o} pulse. A spectrum was acquired every 2.5 minutes, but only every fourth spectrum is shown.

3.4 GENERAL DISCUSSION

The average kinetic rate constants for all the pH values studied are presented in Table 3.1. These kinetic constants contain the acid catalyst concentrations. For the first time pH independent rate constants can now be obtained for the individual reactions. Four kinetic constants showed a linear dependency on the acid concentration while those derived from intermediate species with very small maximum concentrations are less well defined due to the much larger errors, Figure 3.10. The linear relationships confirm that the acid is only a catalyst, in agreement with previous findings.[3.10, 3.17, 3.24, 3.25, 3.29] The pH independent rate constants are presented in Table 3.2.

The general trend observed is that rate constants (k_{T1}-k_{T3}) increase as the number of hydroxyls increase, i.e. hydrolysis becomes easier as n increases in $Si(OEt)_{4-n}(OH)_n$. This is in agreement with some previous observations.[3.10, 3.24, 3.27] The notable exception is the last hydrolysis which occurs at about the same rate as the previous reaction.

It is clear from the data in Table 3.2 that the kinetic constants for the different reactions are neither equal nor related in some simple incremental manner as has been assumed in previous investigations.[3.10, 3.22] The present research shows that the approach taken by Hui et al. is not a valid one and that it is impossible to deduce individual rate constants from the experimentally determined global hydrolysis rate constant.[3.10]

Assink and Kay considered 15 distinguishable local silicon chemical environments but their kinetic constants were proportionally related to the number of directly attached hydroxyls.[3.22] The present results suggest that this nearest neighbour statistical model is not valid for the TEOS hydrolysis and dimer formation since no evident relationship exists between the kinetic constants.

Previously, two groups [3.24, 3.27] have determined experimentally the individual

Table 3.1 - Average pH dependent kinetic rate constants ($M^{-1}min^{-1}$) determined for the TEOS hydrolysis and dimer formation reactions, equations (3.4)-(3.8).

pH	k_{T1}	k_{T2}	k_{T3}	k_{T4f}	k_{T4b}	k_{T5}
3.35	0.00054	0.0036	0.015	0.07	0.01	0.012
3.04	0.00041	0.0035	0.033	0.083	0.011	0.023
2.88	0.0008	0.0043	0.017	0.06	0.014	0.016
2.76	0.0009	0.0065	0.034	0.08	0.016	0.02
2.55	0.0018	0.011	0.06	0.05	0.009	0.033
2.45	0.0027	0.014	0.06	0.05	0.013	0.042
2.33	0.0037	0.024	0.134	0.11	0.01	0.06
2.13	0.0072	0.038	0.36	0.085	0.016	0.1

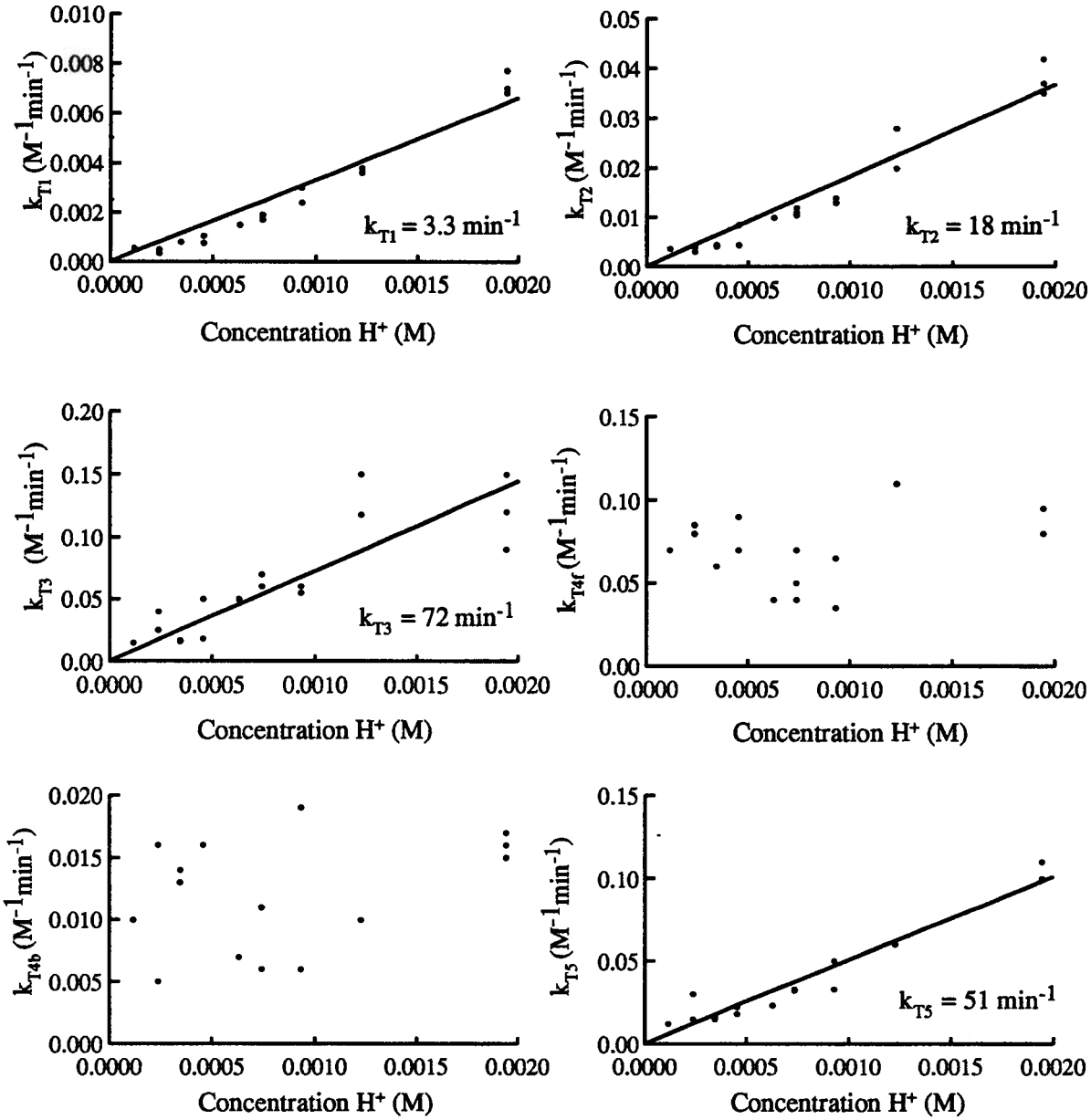

Figure 3.10 - Plots of the pH dependent kinetic constants versus acid concentration for the hydrolysis and dimer formation reactions of the TEOS homopolymerization. The fits were constrained such that the intercepts were at zero.

Table 3.2 - pH independent hydrolysis and dimer formation kinetic rate constants for TEOS (min^{-1}) with the standard error. The fits were constrained with the intercept at 0. The data for the forward and backward reactions for reaction (3.7) were not considered accurate enough to include in this table.

Kinetic rate constant	Value (min^{-1})	Reaction no.
k_{T1}	3.3 ± 0.1	3.4
k_{T2}	18 ± 1	3.5
k_{T3}	72 ± 5	3.6
k_{T5}	51 ± 2	3.8

kinetic rate constants for the sequential hydrolysis and condensation reactions of two systems similar to that used in the present study. Chojnowski et al [3.24] studied the hydrolysis of TEOS at a substoichiometric water/silane ratio of 2, in dioxane. The relative concentrations of the individual species were determined by GC/MS after quenching the reaction and trimethylsilating the intermediates at different times. They numerically solved the kinetic data to obtain the individual kinetic rate constants. Their results differ from those obtained in the present study when pH dependent values are compared. This is not unexpected given the large differences in the reaction conditions, i.e. they used substoichiometric concentrations of water and dioxane as the solvent. However, a general trend common to both experiments is an increase in the magnitude of the kinetic rate constants with increasing numbers of attached hydroxyl groups. Chojnowski suggested that the large differences in k_1 through to k_4, in their case 1000, is due to the strong hydrogen bonding of the silane hydroxyl groups to the dioxane. This was postulated to give additional polarization of the silane, increasing its reactivity.

Pouxviel et al. [3.27] is the only other group to have obtained experimental individual kinetic rate constants for a specific pH. The system studied was similar to that investigated in the present work with respect to the reactant and solvent concentrations. They determined one set of pH dependent kinetic constants from simulations of their data and their results are in part similar to those presented in this work. In particular, the ratios of the pH dependent kinetic constants k_{T1}/k_{T2} , k_{T2}/k_{T3} and k_{T4}/k_{T5} are all very similar to those presented here. A major difference is in k_{T3}/k_{T4}, where Pouxviel et al. determined a value twice as large as that found in this study.

The kinetic constants summarized in Tables 3.1 suggest that the dimer formation is slower than the formation of the fully hydrolyzed species. This is confirmed by the build-up

of the fully hydrolyzed species and the constant presence of a small quantity of $Si(OH)_3(OEt)$ in the reaction mixture. It is this build-up of the fully hydrolyzed species that necessitates the inclusion of the equilibrium reaction for the last hydrolysis.

3.5 CONCLUSIONS

It was possible to fit the quantitative kinetic data for the TEOS hydrolysis and dimer formation well in terms of a very simple kinetic model, which considered only the last hydrolysis as an equilibrium reaction. The TEOS kinetic constants for all the sequential hydrolysis steps and the dimer formation were experimentally determined for a series of pH values (Table 3.1). From these data, pH independent kinetic constants for the hydrolysis steps and dimer formation were derived for the first time (Table 3.2).

It is clear from the data obtained that the hydrolysis kinetic constants ($k_{T1\text{-}T3}$) are not the same or related in a simple incremental fashion although their magnitudes increase with the number of hydroxyls. It was also found that the main re-esterification reaction is from $Si(OH)_4$ to $Si(OH)_3(OEt)$ which are the only two monomeric species left when condensation starts under the reaction conditions chosen. In addition, the dimer formation for the TEOS system is slower than the hydrolysis, resulting in a build-up, to some extent, of the fully hydrolyzed species.

The pH dependent and independent kinetic constants for the hydrolysis and dimer formation of TEOS have been determined. These values will be the reference data when studying the effect of organic functionality (Chapter 4), organic drying agents (Chapter 5) and the formation of a functionalized copolymer (Chapter 4).

CHAPTER 4

HIGH RESOLUTION ^{29}Si SOLUTION NMR INVESTIGATION OF THE HYDROLYSIS AND DIMER FORMATION OF METHYLTRIETHOXYSILANE (MTES) HOMOPOLYMERIZATION AND MTES/TEOS COPOLYMERIZATION REACTIONS

4.1 INTRODUCTION

The previous chapter presented a detailed kinetic analysis of the tetraethoxysilane (TEOS) monomer. In order to do a kinetic analysis of the methyltriethoxysilane (MTES)/TEOS copolymer a detailed kinetic analysis for the MTES monomer is still needed.

Van Bommel and co-workers using a two step process (acid and then base catalysis) studied qualitatively the effect of substituents (methyl-, dimethyl- and phenyltriethoxysilanes) on the hydrolysis and condensation. They found that the alkyl-substituted triethoxysilanes have higher hydrolysis and condensation rates than TEOS.[4.5] This supports the general statement in the literature, that in an acid catalyzed reaction the presence of a non-hydrolyzable electron donating ligand on the silane results in higher hydrolysis rates.[3.29] Yet no literature data pertaining to the analysis of the hydrolysis and dimerization of functionalized triethoxysilanes could be found. Thus this chapter presents the first characterization (via kinetic rate constants) of the methyltriethoxysilane (MTES) hydrolysis and dimer formation.

The investigation of the MTES/TEOS copolymer focusses on the kinetics of the intermediate hydrolysis species and on the nature and concentration of the dimers formed, to provide insight into the extent and nature of the copolymerization process. The MTES/TEOS copolymer kinetic rate constants were determined using the TEOS and MTES homopolymer

pH dependent kinetic rate constants for the hydrolysis and dimer formation as a starting point. Reactivity ratios were calculated from the copolymer dimer formation rate constants. This information provides another indication of the extent of mixing of the MTES and TEOS monomer in the copolymer. No literature data are available on the extent of co-condensation between two different silane species.

4.2 EXPERIMENTAL

4.2.1 MTES Homopolymerization Reaction Conditions

The MTES homopolymerization reaction conditions in general follow those already outlined for the TEOS homopolymerization in the previous chapter. The samples used consist of: 3.57 ml (0.0179 mole) MTES, 6.07 ml (0.1034 mole) ethanol, 3.58 ml (0.1981 mole) water acidified with HCl and 0.075 g (0.000215 mole) chromium acetylacetonate ($Cr(acac)_3$). As previously, chromium acetylacetonate was added to reduce the spin-lattice relaxation times. The ^{29}Si T_1 value for MTES in ethanol/water with 0.016 M of $Cr(acac)_3$ was found to be 1.6 seconds.

All the spectra were acquired on a Bruker AMX 500 spectrometer using a 10 mm broadband probe maintaining the sample temperature at 300.0±0.1 K. For each spectrum, eight scans were acquired with a 0.8 s recycle delay and using a 60° pulse angle. To follow the concentrations of the different species as functions of time a new spectrum was obtained every 1.5-2 minutes. Two kinetic experiments were done at each pH value (2.45, 2.55, 2.76, 2.88, 3.04 and 3.35).

4.2.2 MTES/TEOS Copolymer Reaction Conditions

The MTES/TEOS copolymerization reaction was carried out at a pH of 2.55. The concentrations of the reagents in the control system were: 2 ml (0.0090 mole) TEOS, 1.79 ml (0.0090 mole) MTES, 6.07 ml (0.1034 mole) ethanol, 3.58 ml (0.1981 mole) water acidified with HCl and 0.075 g (0.000215 mole) chromium acetylacetonate ($Cr(acac)_3$). Each spectrum was acquired with eight scans using a 60° pulse angle and a 1 second recycle delay.

Copolymers were synthesized under a number of different conditions, Table 4.1, in order to determine the effect of different parameters on the relative dimer ratios. All reactions were carried out in duplicate.

Table 4.1 - Compositions of different samples used in the copolymer study.

TEOS (moles)	MTES (moles)	Ethanol (moles)	H_2O (moles) pH = 2.55	Ref. Name
0.0090	0.0090	0.1034	0.1981	CO111
0.0134	0.0045	0.1034	0.1981	CO271
0.0045	0.0134	0.1034	0.1981	CO721
0.0090	0.0090	0.1034	0.3962	CO112
0.0179	0.0179	0.1034	0.1981	CO221
0.0179	0.0179	0.1034	0.3962	CO222

Homo and co-dimers resonances are not very well resolved in the spectra and therefore the analysis of the dimer region required that the signals be deconvoluted to determine the extent of homo versus co-dimers present in the reaction mixture. The deconvolution used gaussian lineshapes and was performed using a program available with the Bruker UXNMR software on the Bruker AMX 500 spectrometer.

4.3.1 Kinetic Analysis of the MTES Hydrolysis and Dimer Formation Reactions

A typical MTES spectrum with the intermediate hydrolysis and dimer products labelled, is shown in Figure 4.1A. The dimer resonance is well separated and shifted significantly upfield from all the resonances of the hydrolysis products.

An experimental data set for the hydrolysis and dimer formation of MTES is shown in Figure 4.1B, which illustrates the good separation between the hydrolysis reactions (4.1)-(4.3), and condensation reaction (4.4). The peaks corresponding to the different intermediate species were integrated and their relative concentrations plotted as functions of time (as described in Chapter 3 for the TEOS polymerization). An example of the experimental data obtained from this is shown in Figure 4.2. After 20 minutes for the MTES polymerization at pH=2.55, there is still a clear differentiation between the hydrolysis and condensation reactions. At this time approximately 95% of the silicons are present in either $CH_3Si(OH)_2(OEt)$ or $CH_3Si(OH)_3$ which means that there are only approximately 5% of the silicons in the dimer form. Thus the important time period for the hydrolysis intermediates is up to 20 minutes, and these parts of the graphs were considered first in the analysis.

The model for the kinetic analysis is analogous to that outlined in the previous chapter, but one less hydrolysis reaction has to be considered. Four reactions (4.1)-(4.4) were used to fit the intermediate hydrolysis concentration curves for the MTES polymerization.

$$CH_3Si(OEt)_3 + H_2O \xrightarrow{k_{M1}} CH_3Si(OH)(OEt)_2 + EtOH \qquad (4.1)$$

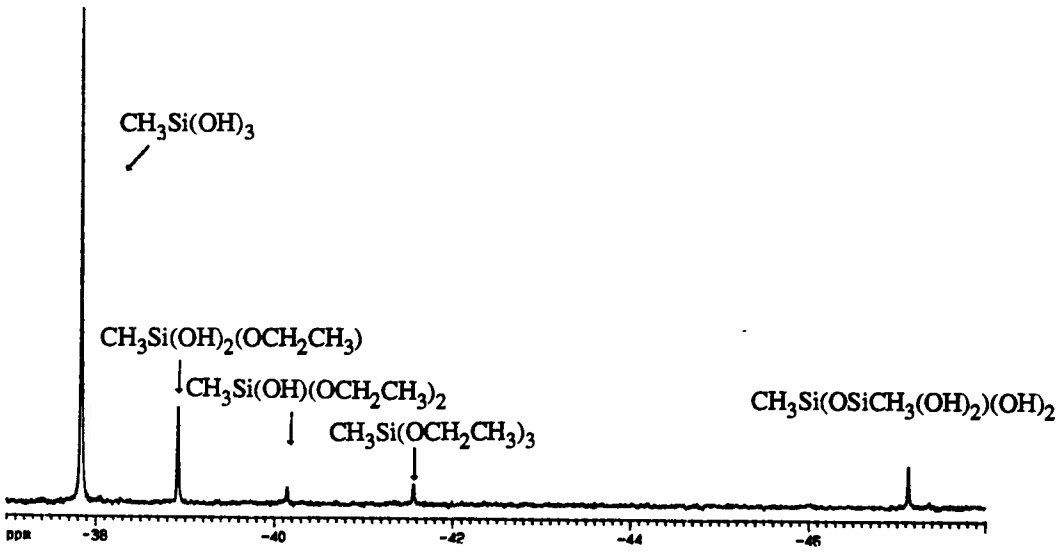

Figure 4.1A - A typical ^{29}Si spectrum obtained during the hydrolysis of MTES with the peaks assigned as indicated.

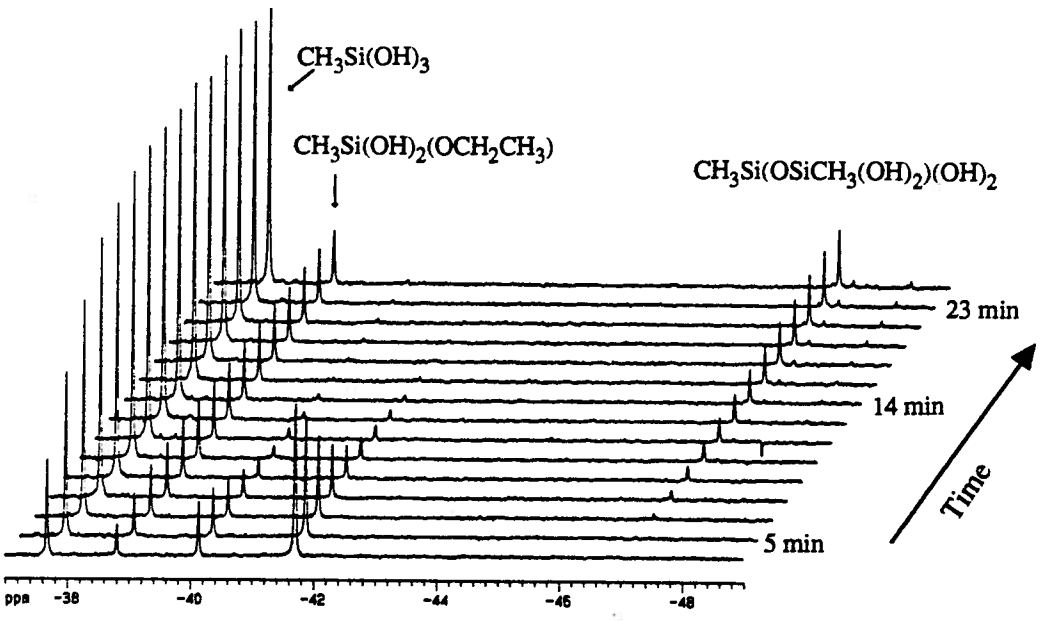

Figure 4.1B - Stacked plot of the one-dimensional ^{29}Si NMR spectra obtained during the polymerization of methyltriethoxysilane (water was acidified to pH=2.55). The acquisition parameters used were: 8 scans/spectrum with a recycle delay of 0.8 sec and a 60^{o} pulse angle.

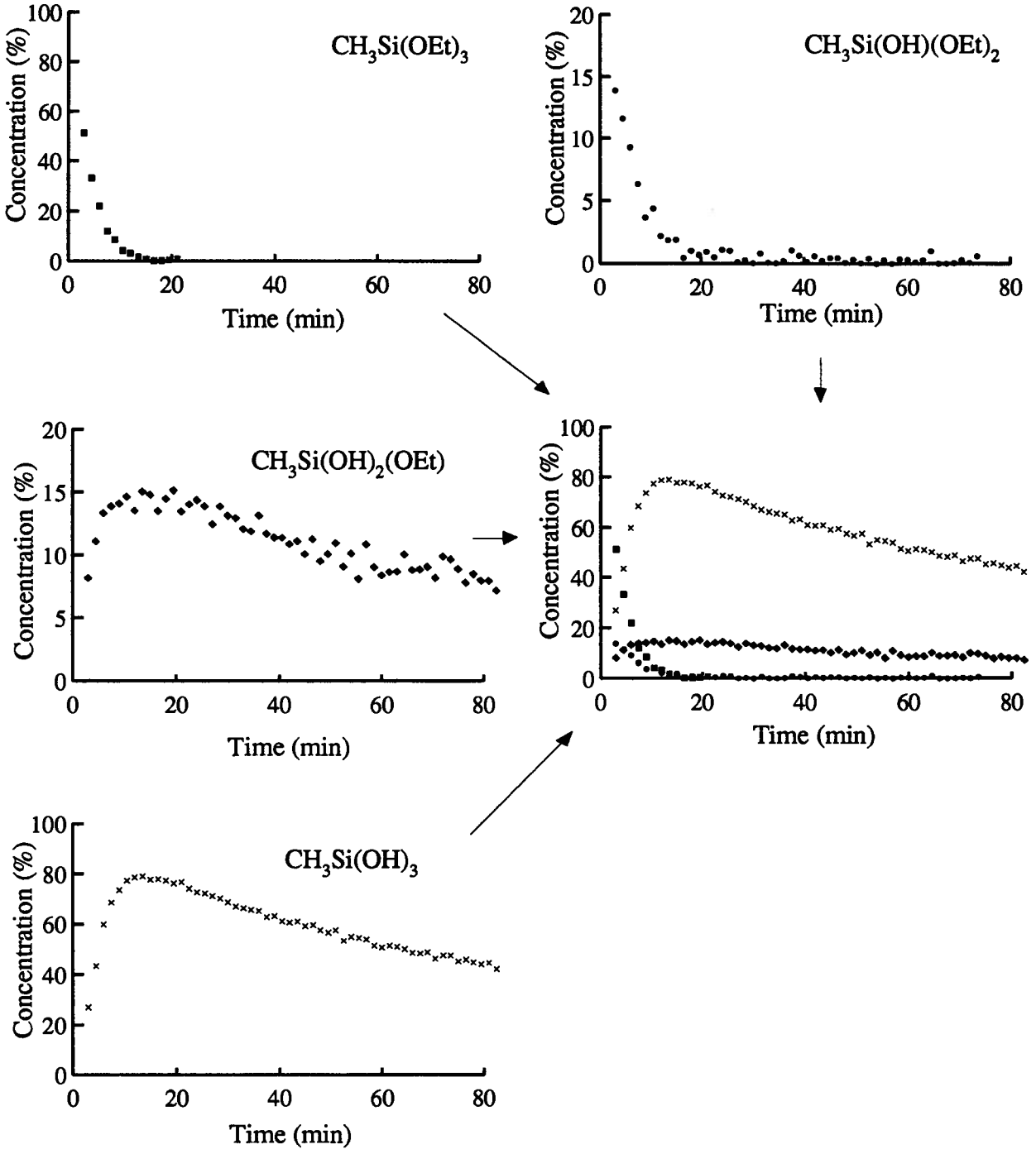

Figure 4.2 - The time dependence of the relative concentrations of all intermediate species involved in the hydrolysis of MTES. MTES hydrolysis data at pH=2.55. The experimental error is ± 2%.

$$CH_3Si(OH)(OEt)_2 + H_2O \xrightarrow{k_{M2}} CH_3Si(OH)_2(OEt) + EtOH \tag{4.2}$$

$$CH_3Si(OH)_2(OEt) + H_2O \xrightarrow{k_{M3}} CH_3Si(OH)_3 + EtOH \tag{4.3}$$

$$2CH_3Si(OH)_3 \xrightarrow{k_{M4}} CH_3Si(OH)_2(OSiCH_3(OH)_2) + H_2O \tag{4.4}$$

The kinetic constants for reactions (4.1)-(4.4) can be obtained by expressing the concentration changes of the hydrolysis species as functions of time, equations (4.5)-(4.8).

$$\frac{d[MTES]}{dt} = -k_{M1}[MTES]_t [H_2O]_t \tag{4.5}$$

$$\frac{d[CH_3Si(OH)(OEt)_2]}{dt} = (k_{M1}[MTES]_t - k_{M2}[CH_3Si(OH)(OEt)_2]_t)[H_2O]_t \tag{4.6}$$

$$\frac{d[CH_3Si(OH)_2(OEt)]}{dt} = (k_{M2}[CH_3Si(OH)(OEt)_2]_t - k_{M3}[CH_3Si(OH)_2(OEt)]_t)\,[H_2O]_t \tag{4.7}$$

$$\frac{d[CH_3Si(OH)_3]}{dt} = k_{M3}\,[CH_3Si(OH)_2(OEt)]_t\,[H_2O]_t - k_{M4}\,[CH_3Si(OH)_3]_t^2 \tag{4.8}$$

Equations (4.5)-(4.7) can be solved explicitly, giving equations (4.9)-(4.11) assuming the water concentration to be constant.

$$\frac{[MTES]_t}{[MTES]_o} = e^{-k_{M1}[H_2O]_o t} \tag{4.9}$$

$$\frac{[CH_3Si(OH)(OEt)_2]_t}{[MTES]_o} = \frac{k_{M1}}{(k_{M2}-k_{M1})}(e^{-k_{M1}[H_2O]_o t} - e^{-k_{M2}[H_2O]_o t}) \tag{4.10}$$

$$\frac{[CH_3Si(OH)_2(OEt)]_t}{[MTES]_o} = \frac{k_{M2}k_{M1}}{(k_{M2} - k_{M1})}\left[\frac{e^{-k_{M1}[H_2O]_o t}}{(k_{M3} - k_{M1})} - \frac{e^{-k_{M2}[H_2O]_o t}}{(k_{M3} - k_{M2})} + \left(\frac{1}{(k_{M3} - k_{M2})} - \frac{1}{(k_{M3} - k_{M1})}\right) e^{-k_{M3}[H_2O]_o t}\right] \tag{4.11}$$

The calculated curves using equations (4.9)-(4.11) are shown in Figure 4.3 and the kinetic rate constants determined by the non-linear least squares fit are summarized in Appendix 2. As can be seen, the curves except the one for $CH_3Si(OH)_2(OEt)$ fit the experimental data points well.

The next step to improve the fit of $CH_3Si(OH)_2(OEt)$ was to include the change in water concentration and the dimer formation in the differential equations. The concentration of water at any time t can be expressed by equation (4.12).

$$\eta_t^m = [H_2O]_o - [CH_3Si(OH)(OEt)_2]_t - 2[CH_3Si(OH)_2(OEt)]_t - 3[CH_3Si(OH)_3]_t \tag{4.12}$$

As in the TEOS case, the inclusion of the change in water concentration did not have a significant effect on the shape of the curves. To fit the decay of the fully hydrolyzed species, a dimer formation reaction was included. The differential equations (4.5)-(4.8) are now re-expressed, equations (4.13)-(4.16), taking into account the change in water concentration and the dimer formation.

$$\frac{d[MTES]}{dt} = -k_{M1}[MTES]_t \eta_t^m \tag{4.13}$$

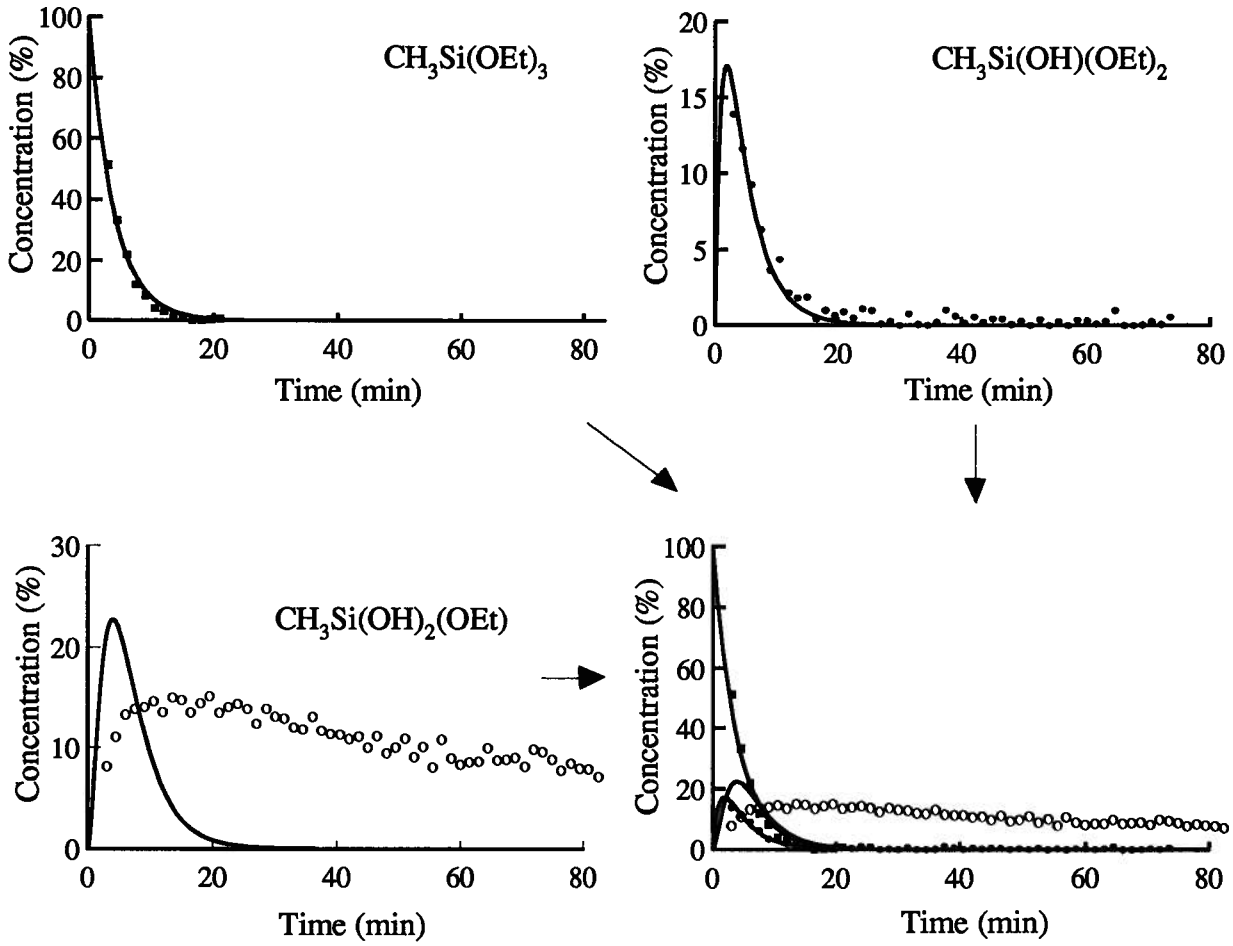

Figure 4.3 - Calculated curves for the time dependence of the MTES hydrolysis intermediate concentrations, equations (4.9)-(4.11), assuming a constant water concentration.
The experimental error is ± 2%.

$$\frac{d[CH_3Si(OH)(OEt)_2]}{dt} = (k_{M1}[MTES]_t - k_{M2}[CH_3Si(OH)(OEt)_2]_t)\ \eta_t^m \tag{4.14}$$

$$\frac{d[CH_3Si(OH)_2(OEt)]}{dt} = (\ k_{M2}[CH_3Si(OH)(OEt)_2]_t - k_{M3}[CH_3Si(OH)_2(OEt)]_t^2\ )\eta_t^m \tag{4.15}$$

$$\frac{d[CH_3Si(OH)_3]}{dt} = k_{M3}[CH_3Si(OH)_2(OEt)]_t\ \eta_t^m - k_{M4}[CH_3Si(OH)_3]_t^2 \tag{4.16}$$

These interdependent equations (4.13)-(4.16) were solved numerically, as previously, using the LSODE program. For the same reasons discussed previously for the TEOS case (section 3.3.2), it was found necessary to include a re-esterification reaction for the last hydrolysis species in order to respect the curve shape for $CH_3Si(OH)_2(OEt)$ (Figures 4.4A compared to Figure 4.4B). With this additional modification, equations (4.15) and (4.16) become equations (4.17) and (4.18) where ε_t^m is the concentration of ethanol at any time t given by equation (4.19).

$$\frac{d[CH_3Si(OH)_2(OEt)]}{dt} = (\ k_{M2}[CH_3Si(OH)(OEt)_2]_t - k_{M3f}[CH_3Si(OH)_2(OEt)]_t\ )\eta_t^m + k_{M3b}[CH_3Si(OH)_3]_t\varepsilon_t^m \tag{4.17}$$

$$\frac{d[CH_3Si(OH)_3]}{dt} = k_{M3f}[CH_3Si(OH)_2(OEt)]_t\eta_t^m - k_{M3b}[CH_3Si(OH)_3]_t\varepsilon_t^m - k_{M4}[CH_3Si(OH)_3]_t^2 \tag{4.18}$$

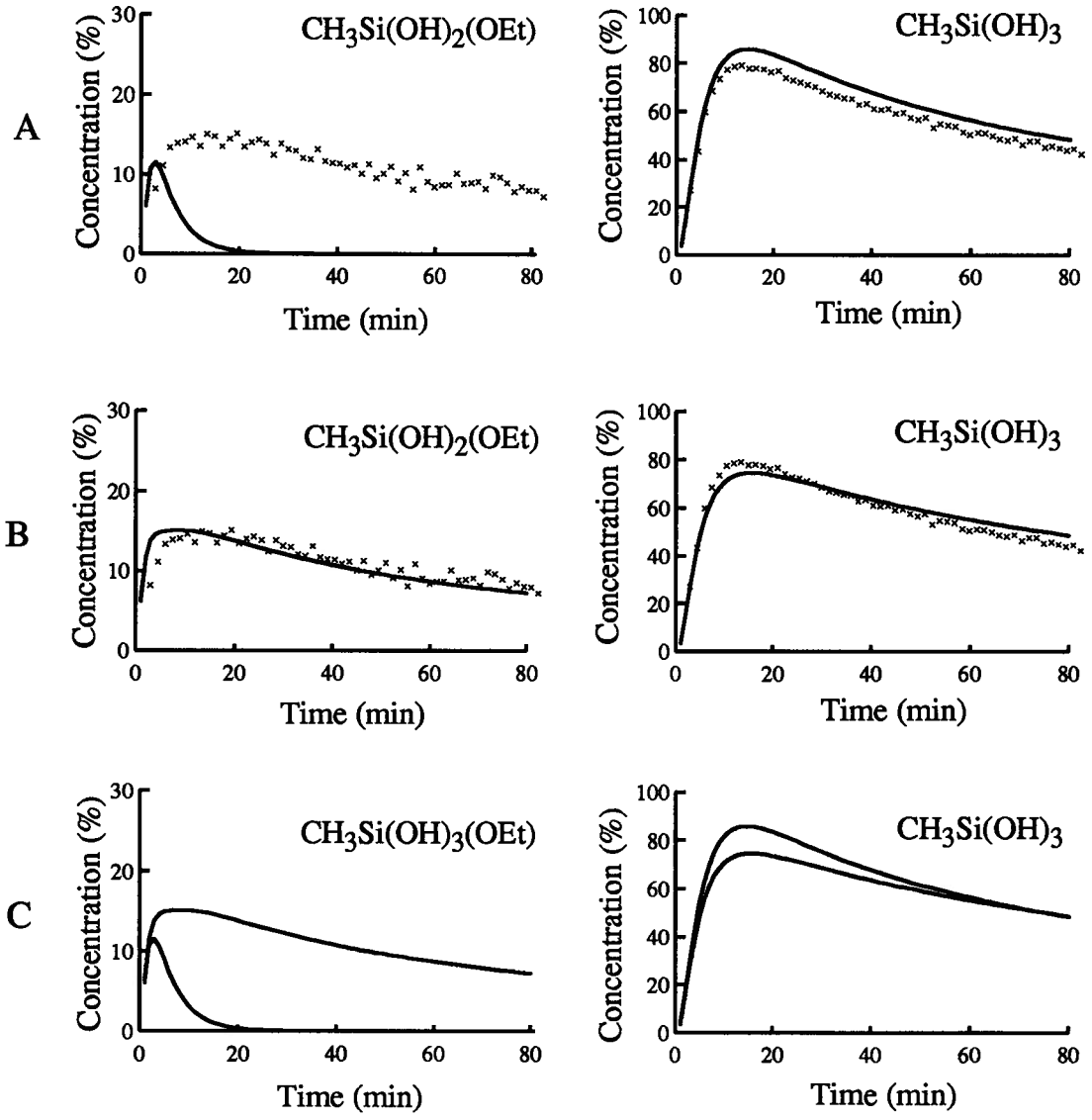

Figure 4.4 - Calculated curves of the relative concentrations of $CH_3Si(OH)_2(OEt)$ and $CH_3Si(OH)_3$ intermediates (A) excluding and (B) including the equilibrium back reaction, together with the experimental data. (C) is a comparison of these two curves without the experimental data. The experimental error is ± 2%.

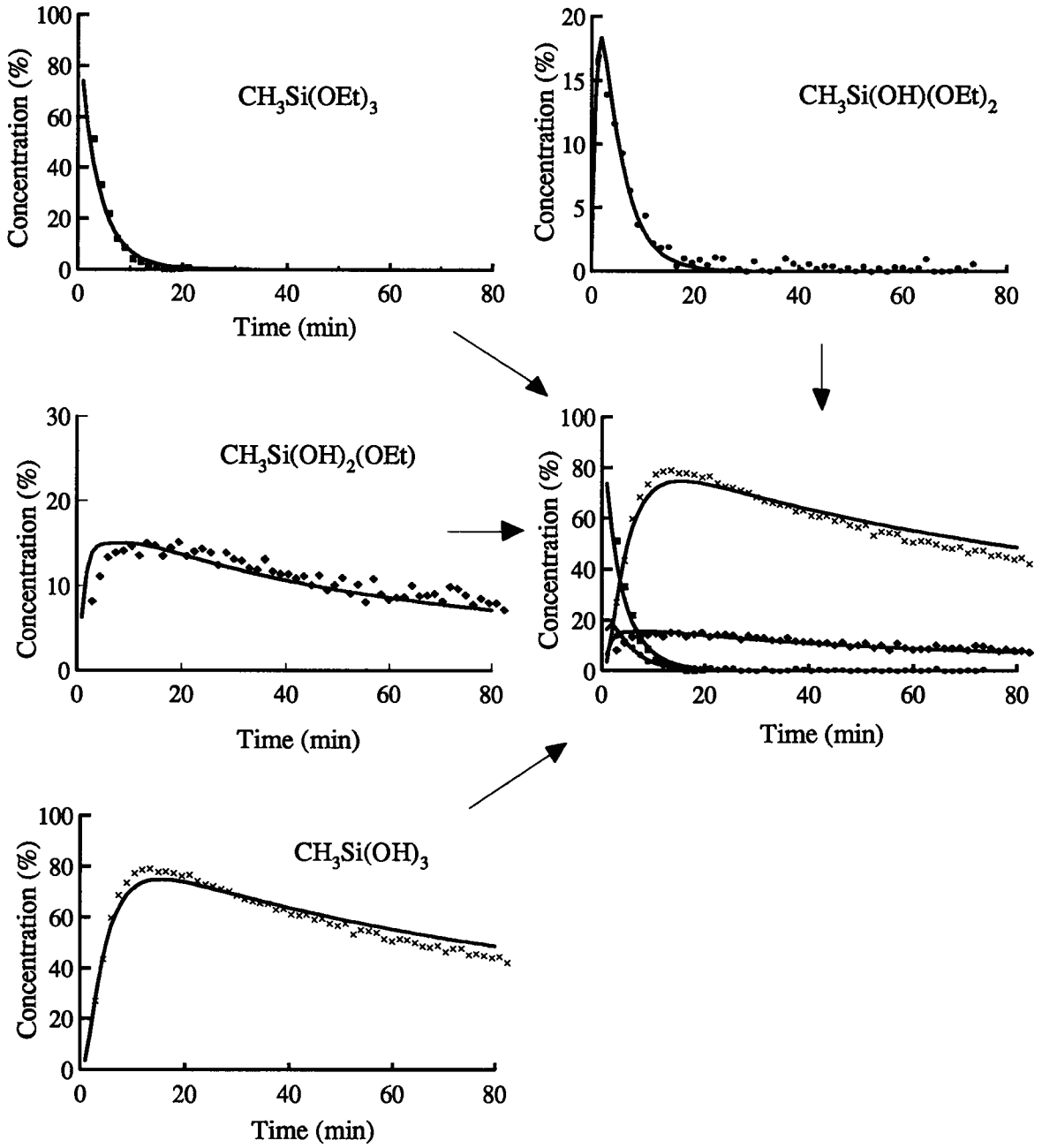

Figure 4.5 - The time dependence of the relative concentrations of all intermediate species involved in the hydrolysis of MTES together with the final calculated curves. The data are from the kinetic run of MTES at pH=2.55. The experimental error is ± 2%.

where

$$\varepsilon_t^m = [EtOH]_o + [CH_3Si(OH)(OEt)_2]_t + 2[CH_3Si(OH)_2(OEt)]_t + 3[CH_3Si(OH)_3]_t \quad (4.19)$$

The fitting of the experimental data was done using equations (4.13), (4.14), (4.17) and (4.18). An example of the results is shown in Figure 4.5. Experimentally, small signals indicative of trimer formation start to appear in the spectrum at longer reaction times (greater than 60 minutes). It is therefore expected that the calculated curve overestimates the dimer concentration at longer reaction times since it does not consider any depletion reactions for the dimer.

4.3.2 MTES Hydrolysis and Dimer Formation Kinetic Rate Constants

The average pH dependent kinetic constants obtained from this study are listed in Table 4.2. The pH independent rate constants were calculated from the slope of the pH dependent kinetic rate constants versus the acid concentrations as shown in Figure 4.6. These results are listed in Table 4.3 together with those previously obtained for the TEOS system. The kinetic rate constants describing the hydrolysis of MTES are greater than the corresponding ones for TEOS. This result is in agreement with the qualitative conclusion in the literature regarding the complete hydrolysis process, that alkyl-substituted alkoxysilanes hydrolyze faster than the corresponding tetraalkoxysilane. [4.1, 4.2]

The data in Table 4.3 show that the rate of hydrolysis increases with the number of hydroxy ligands. This contradicts what one would expect from an inductive effect: a positively charged transition state would be further stabilized by an increasing number of alkoxy ligands since alkoxy groups are more electron donating than hydroxy groups [3.19, 3.29] implying that $k_1 > k_2 > k_3$.

Table 4.2 - The average pH dependent kinetic rate constants ($M^{-1}min^{-1}$) determined for the MTES homopolymerization hydrolysis and dimer formation reactions.

pH	k_{M1}	k_{M2}	k_{M3f}	k_{M3b}	k_{M4}
3.35	0.0015	0.0059	0.0085	0.0005	0.001
3.04	0.0052	0.019	0.023	0.001	0.005
2.88	0.006	0.024	0.035	0.0035	0.006
2.76	0.013	0.045	0.05	0.004	0.007
2.55	0.0205	0.0655	0.07	0.008	0.017
2.45	0.025	0.075	0.085	0.01	0.0215

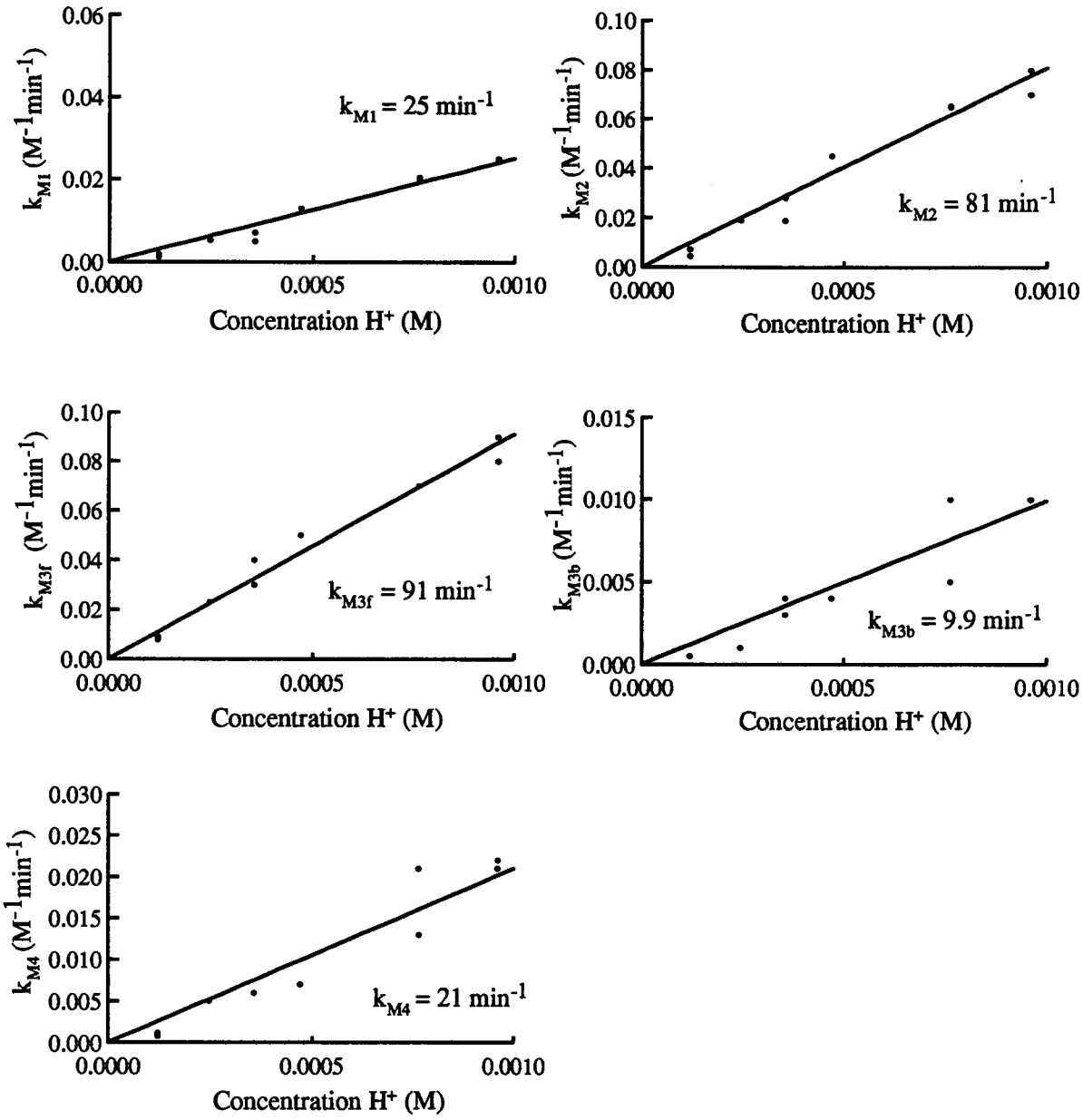

Figure 4.6 - Plots of the pH dependent kinetic constants versus acid concentration for the hydrolysis and dimer formation reactions of the MTES homopolymerization. The fits were constrained such that the intercepts were at zero.

Table 4.3 - pH independent hydrolysis and dimer formation kinetic rate constants (min^{-1}) for the MTES and TEOS homopolymers together with the estimated error (taken as the standard error of all the pH dependent values).

Kinetic Constants	MTES homopolymer (min^{-1})	TEOS homopolymer (min^{-1})
k_{M1}, k_{T1}	25 ± 1	3.3 ± 0.1
k_{M2}, k_{T2}	81 ± 3	18 ± 1
k_{M3f}, k_{T3}	91 ± 2	72 ± 5
k_{M3b}	9.9 ± 0.7	
k_{T4f}		59 ± 10
k_{T4b}		11 ± 2
k_{M4}, k_{T5}	21 ± 1	51 ± 2

Interestingly, the dimer formation kinetic constant is greater for TEOS than MTES. There are two possible reasons for this. It is possible that in the dimer formation involving the reaction of two $CH_3Si(OH)_3$, the methyl groups' inductive effect retards the reaction. In addition there maybe more steric hinderance involved in the MTES dimerization, since both monomers contain a methyl group, in comparison to the TEOS homodimerization. The result is that TEOS dimerizes faster than MTES.

Even though the relative rates of the reactions differ significantly, there are a number of similarities between the MTES and TEOS reactions. Both systems display the same trend for the first three sequential hydrolysis rate constants, $k_1 < k_2 < k_3$. Both require the inclusion of a re-esterification reaction for the last hydrolysis in order to respect the general shape of the second to last hydrolysis product curve. This re-esterification reaction is in both cases smaller than the forward hydrolysis reaction by at least a factor of five, i.e. TEOS: $k_{T4f} >> k_{T4b}$ and MTES: $k_{M3f} >> k_{M3b}$. In both cases, the dimer formation is slower than the last hydrolysis, $k_{T4f} > k_{T5}$ (TEOS) and $k_{M3f} > k_{M4}$ (MTES), so that at all pH values studied, there is an accumulation of the fully hydrolyzed monomers.

4.3.3 MTES/TEOS Copolymer Kinetic Analysis

The hydrolysis and dimer formation of a 50/50 MTES/TEOS copolymer was analyzed in detail to determine how the kinetic constants compared to those from the MTES and TEOS homopolymerizations. Reactivity ratios for the MTES and TEOS monomers were determined using the kinetic constants for dimerization. The different dimer concentrations were then estimated from the reactivity ratios.

A typical collection of spectra obtained during the copolymerization reaction is shown in Figure 4.7. As expected, the intermediates created by the hydrolysis during the MTES/TEOS copolymerization are the same as those observed in the homopolymer cases (Figures 3.1 and 4.1). The concentration curves for the intermediate hydrolysis species as functions of time in the MTES/TEOS copolymerization are shown in Figures 4.8 and 4.9.

Seven hydrolysis reactions are considered in modelling the MTES/TEOS copolymerization:

$$Si(OEt)_4 + H_2O \xrightarrow{k_{T1}} Si(OH)(OEt)_3 + EtOH \tag{4.20}$$

$$Si(OH)(OEt)_3 + H_2O \xrightarrow{k_{T2}} Si(OH)_2(OEt)_2 + EtOH \tag{4.21}$$

$$Si(OH)_2(OEt)_2 + H_2O \xrightarrow{k_{T3}} Si(OH)_3(OEt) + EtOH \tag{4.22}$$

$$Si(OH)_3(OEt) + H_2O \xrightarrow{k_{T4}} Si(OH)_4 + EtOH \tag{4.23}$$

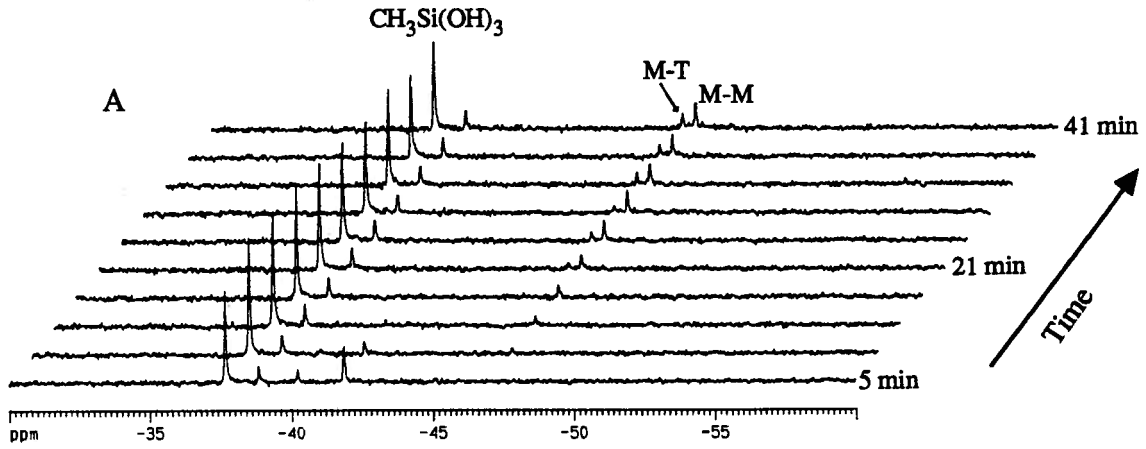

^{29}Si chemical shift (ppm)

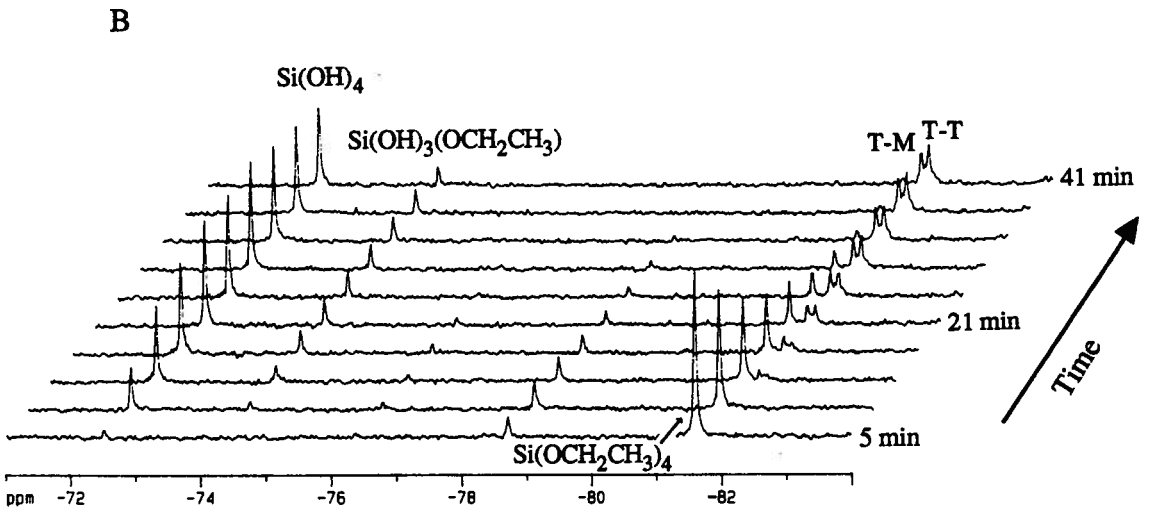

^{29}Si chemical shift (ppm)

Figure 4.7 - Series of 1D ^{29}Si solution NMR spectra, as functions of time, acquired during the MTES/TEOS copolymerization (water was acidified to pH=2.55). The acquisition parameters used were: 8 scans per spectrum, a 1 second recycle delay and a 60^{o} pulse. A) MTES region and B) TEOS region
T-T = TEOS-TEOS homodimer,
T-M and M-T = TEOS-MTES codimer and
M-M = MTES-MTES homodimer.

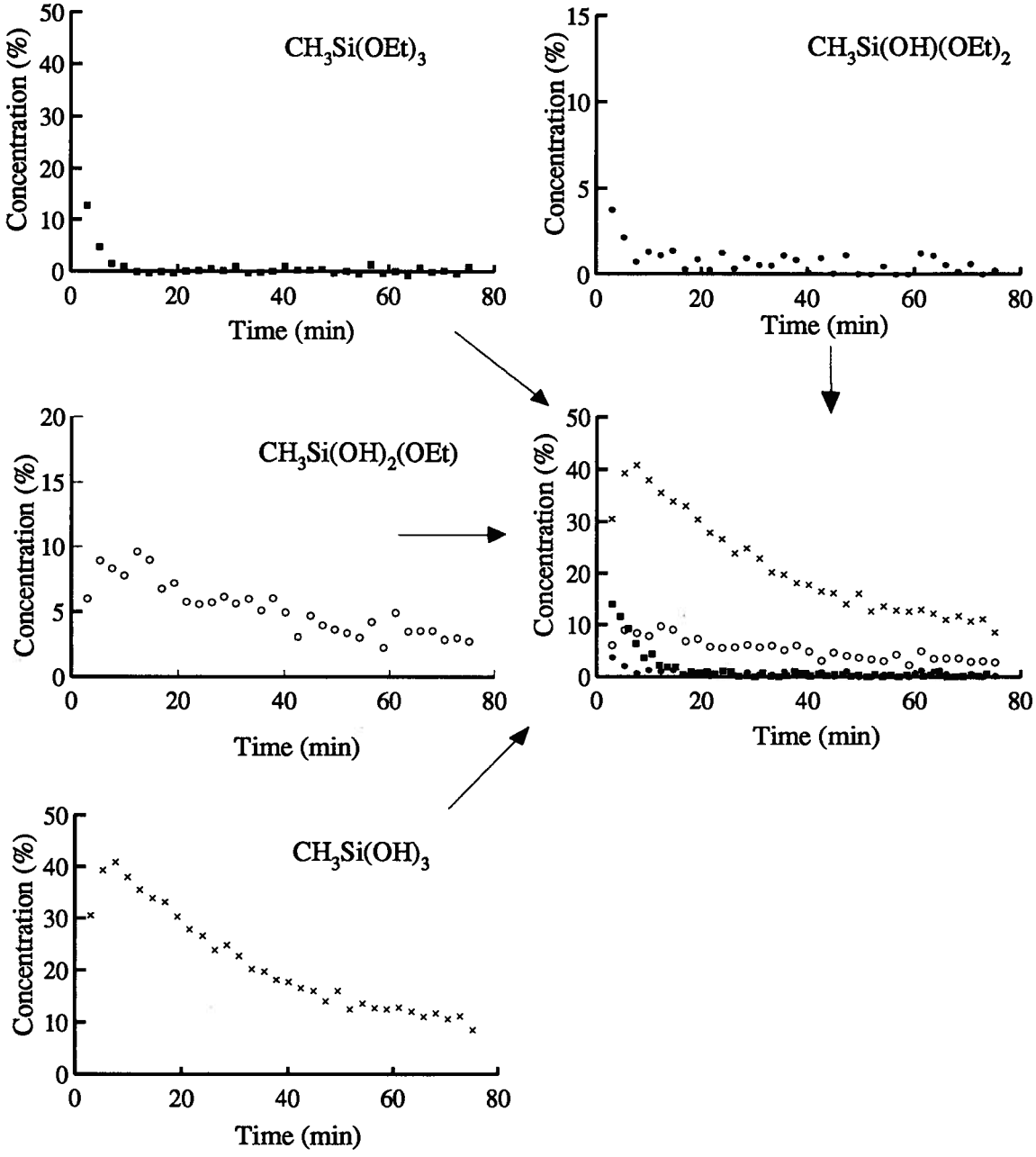

Figure 4.8 - Experimental relative concentration versus time curves for the MTES hydrolysis intermediates in the MTES/TEOS copolymerization. The experimental error is ± 2%.

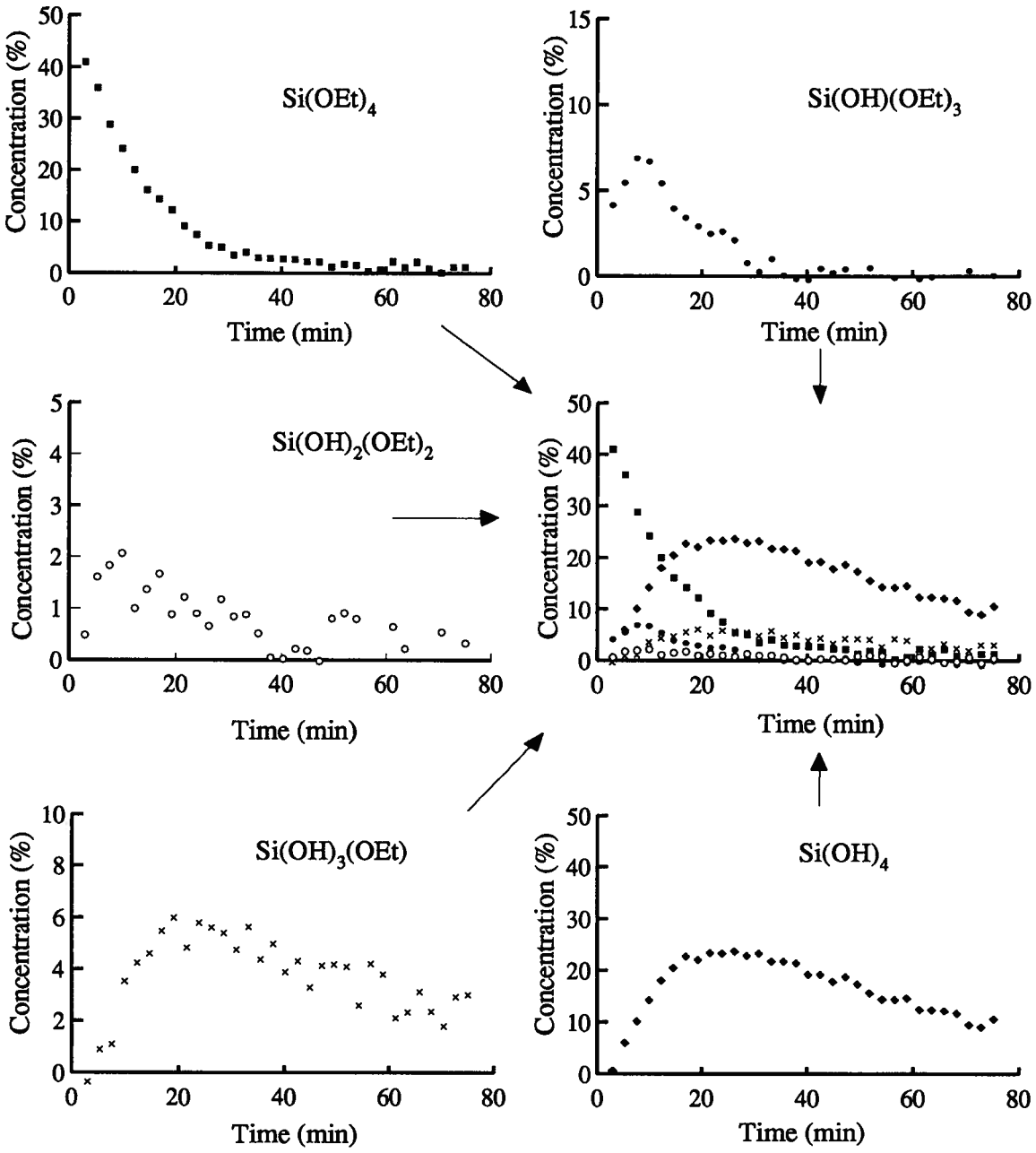

Figure 4.9 - Experimental relative concentration/time curves for the TEOS hydrolysis intermediates in the MTES/TEOS copolymerization. The experimental error is ± 2%.

$$CH_3Si(OEt)_3 + H_2O \xrightarrow{k_{M1}} CH_3Si(OH)(OEt)_2 + EtOH \tag{4.24}$$

$$CH_3Si(OH)(OEt)_2 + H_2O \xrightarrow{k_{M2}} CH_3Si(OH)_2(OEt) + EtOH \tag{4.25}$$

$$CH_3Si(OH)_2(OEt) + H_2O \xrightarrow{k_{M3}} CH_3Si(OH)_3 + EtOH \quad . \tag{4.26}$$

In addition three dimer formation reactions have to be considered:

$$2CH_3Si(OH)_3 \xrightarrow{k_{M4}} CH_3Si(OH)_2(\ O\,Si(CH_3)(OH)_2) + H_2O \tag{4.27}$$

$$2Si(OH)_4 \xrightarrow{k_{T5}} Si(OH)_3(OSi(OH)_3) + H_2O \tag{4.28}$$

$$Si(OH)_4 + CH_3Si(OH)_3 \xrightarrow{k_{C10}} CH_3Si(OH)_2(OSi(OH)_3) + H_2O \quad . \tag{4.29}$$

The only reaction that has not been encountered in dealing with the homopolymers is the one described by equation (4.29). Attempting to solve this set of differential equations numerically showed that the re-esterification reactions needed to fit the TEOS and MTES homopolymerizations had to be included. The final differential equations used to describe the hydrolysis kinetics of the copolymer are (4.30)-(4.40).

$$\frac{d\,[TEOS]}{dt} = -k_{T1}[TEOS]_t\,\eta_t^c \tag{4.30}$$

$$\frac{d[Si(OH)(OEt)_3]}{dt} = (k_{T1}[TEOS]_t - k_{T2}[Si(OH)(OEt)_3]_t)\,\eta_t^c \tag{4.31}$$

$$\frac{d[Si(OH)_2(OEt)_2]}{dt} = (k_{T2}[Si(OH)(OEt)_3]_t - k_{T3}[Si(OH)_2(OEt)_2]_t)\,\eta_t^c \tag{4.32}$$

$$\frac{d[Si(OH)_3(OEt)]}{dt} = (k_{T3}[Si(OH)_2(OEt)_2]_t - k_{T4f}[Si(OH)_3(OEt)]_t)\eta_t^c + k_{T4b}[Si(OH)_4]_t\varepsilon_t^c \tag{4.33}$$

$$\frac{d[Si(OH)_4]}{dt} = k_{T4f}[Si(OH)_3(OEt)]_t\eta_t^c - k_{T4b}[Si(OH)_4]_t\varepsilon_t^c - k_{T5}[Si(OH)_4]_t^2 - k_{C10}[CH_3Si(OH)_3]_t[Si(OH)_4]_t \tag{4.34}$$

$$\frac{d[MTES]}{dt} = -k_{M1}[MTES]_t\,\eta_t^c \tag{4.35}$$

$$\frac{d[CH_3Si(OH)(OEt)_2]}{dt} = (k_{M1}[MTES]_t - k_{M2}[CH_3Si(OH)(OEt)_2]_t)\,\eta_t^c \tag{4.36}$$

$$\frac{d[CH_3Si(OH)_2(OEt)]}{dt} = (k_{M2}[CH_3Si(OH)(OEt)_2]_t - k_{M3f}[CH_3Si(OH)_2(OEt)]_t)\,\eta_t^c + k_{M3b}[CH_3Si(OH)_3]_t\varepsilon_t^c \tag{4.37}$$

$$\frac{d[CH_3Si(OH)_3]}{dt} = k_{M3f}[CH_3Si(OH)_2(OEt)]_t\eta_t^c - k_{M3b}[CH_3Si(OH)_3]_t\varepsilon_t^c - k_{M4}[CH_3Si(OH)_3]_t^2 - k_{C10}[CH_3Si(OH)_3]_t[Si(OH)_4]_t \tag{4.38}$$

where

$$\eta_t^c = [H_2O]_o - [CH_3Si(OH)(OEt)_2]_t - 2[CH_3Si(OH)_2(OEt)]_t - 3[CH_3Si(OH)_3]_t - [Si(OH)(OEt)_3]_t - 2[Si(OH)_2(OEt)_2]_t - 3[Si(OH)_3(OEt)]_t - 4[Si(OH)_4]_t \quad (4.39)$$

$$\varepsilon_t^c = [EtOH]_o + [CH_3Si(OH)(OEt)_2]_t + 2[CH_3Si(OH)_2(OEt)]_t + 3[CH_3Si(OH)_3]_t + [Si(OH)(OEt)_3]_t + 2[Si(OH)_2(OEt)_2]_t + 3[Si(OH)_3(OEt)]_t + 4[Si(OH)_4]_t \quad (4.40)$$

The composition of the copolymerization reaction mixture was chosen such that it was most comparable to the homopolymer reaction mixtures previously studied. The water/silane and acid/silane ratios affect the kinetic process. The total silane concentration of both monomers and total acid concentration was chosen to be equal to the total silane and acid concentration in the homopolymer reactions, which means that the water/TEOS and water/MTES ratios in the copolymer reaction are double those used in the corresponding homopolymer reactions.

Thirteen hydrolysis and dimer species can be resolved in the spectra and their concentrations can be monitored simultaneously as functions of time. The kinetic curves for the copolymer system were fitted by making use of the kinetic constants determined for the homopolymers. This means that for eleven out of twelve kinetic constants reasonable starting values are available although it is anticipated that these may change as the concentration ratios of the reaction mixtures are different. The only kinetic rate constant in the system not previously determined is that of the co-dimerization reaction, equation (4.29). A brief discussion of the logic used in the variation of the rate constants from their starting values, is given in the following paragraphs.

A

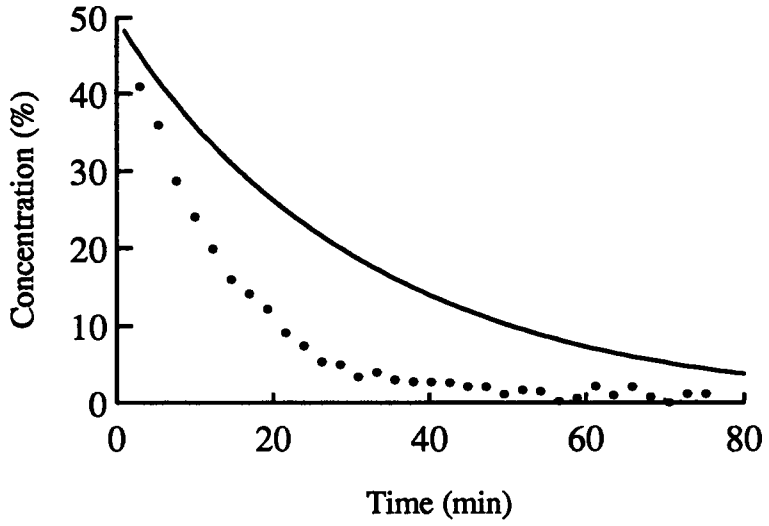

B

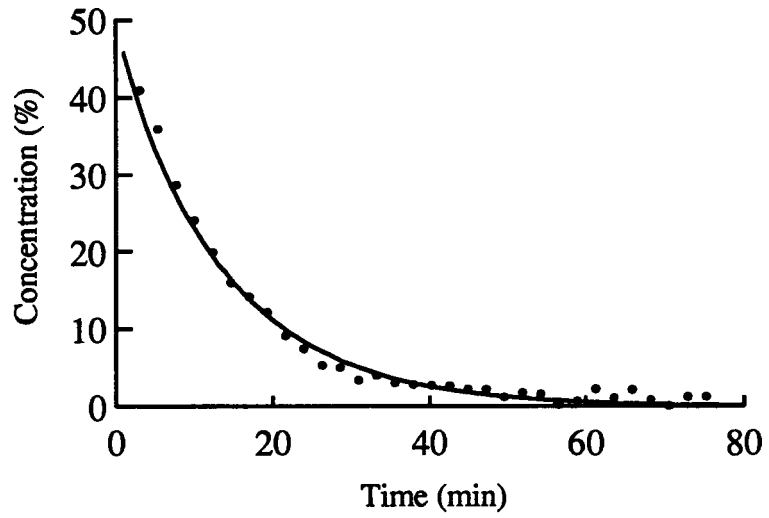

Figure 4.10 - Experimental data for the $Si(OEt)_4$ relative concentration as a function of time, during the MTES/TEOS copolymerization, together with the calculated curves assuming:
A - $k_{T1} = 0.0025$ B - $k_{T1} = 0.006$.
The experimental error is ± 2%.

In Figure 4.10A, the calculated curve obtained using the homopolymerization k_{T1} value is superimposed on the experimental TEOS concentration data for the MTES/TEOS copolymerization. As is illustrated in Figure 4.10 the initial hydrolysis rate of TEOS in the homopolymer is slower than in the copolymer by about a factor of two.

The data for the second hydrolysis reaction of the TEOS monomer in the copolymerization are shown in Figure 4.11. The calculated curve shown in Figure 4.11A was obtained with the k_{T2} from the homopolymerization of TEOS. It is clear that this rate constant underestimates the decay of the $Si(OH)(OEt)_3$ by about a factor of two. The curve in Figure 4.11B was obtained by optimizing k_{T2} for this experimental data set.

The experimental data and the calculated curves for the next two hydrolysis intermediates of the TEOS monomer are shown in Figure 4.12. Both of these intermediate species are present at very low concentrations and larger errors are associated with both the measurement and the fitting of these curves. The kinetic constant k_{T3} used to calculate the curves shown in Figure 4.12A is the same as in the homopolymerization. In this case, the curve fits the experimental data within the error limits and therefore, further variation was not necessary. In Figure 4.12B, the k_{T4f} value from the homopolymerization of TEOS was used to calculate the curve for $Si(OH)_3(OEt)$ which obviously underestimates the decay of this species. The calculated curve with an optimized value for k_{T4f} is shown in Figure 4.12C.

For the MTES hydrolysis products in the copolymerization, the concentration versus time curves for $CH_3Si(OEt)_3$ and $CH_3Si(OH)(OEt)_2$ are shown in Figure 4.13. Again, the calculated curves using the hydrolysis rate constants obtained from the homopolymerization are compared to those optimized for these experimental data.

Up to this stage, the codimerization reaction (4.29) has not been included in the analysis. The next step is to focus on the fully hydrolyzed species for both the TEOS and

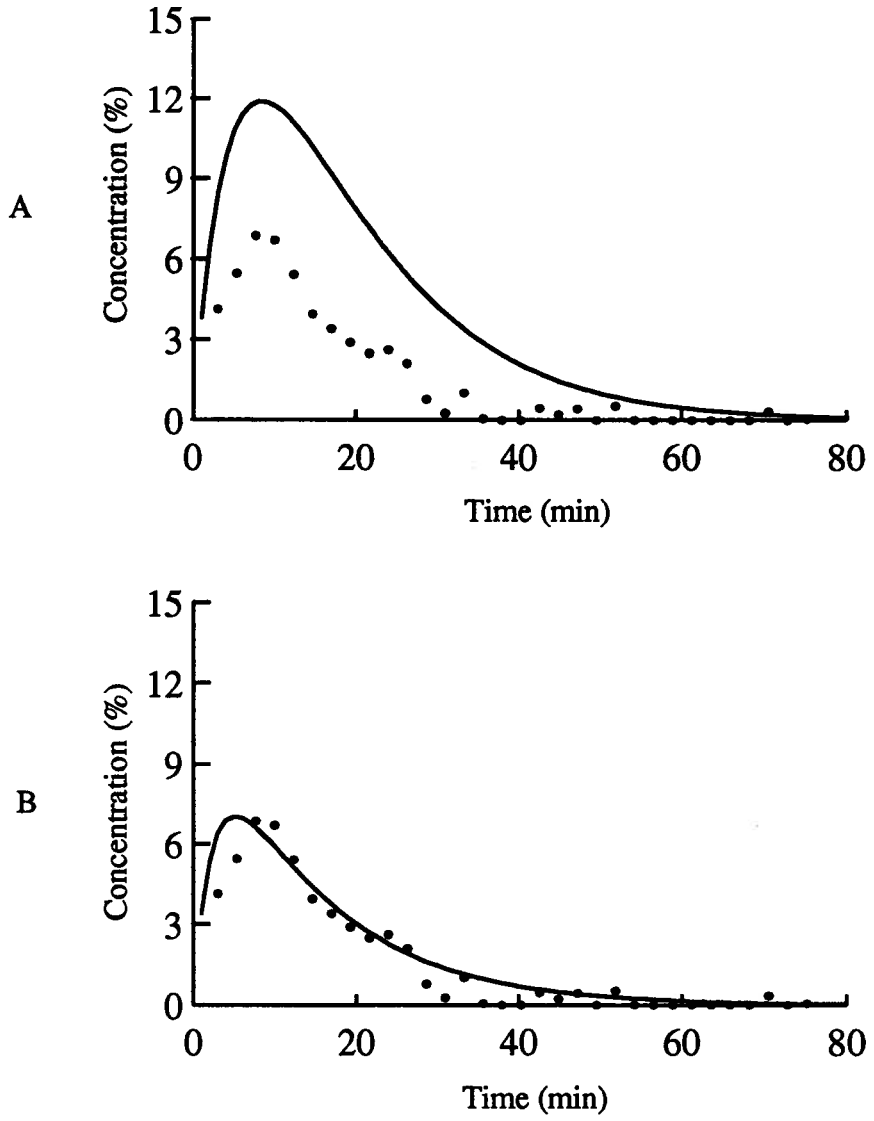

Figure 4.11 - Experimental data for the TEOS hydrolysis intermediate $Si(OH)(OEt)_3$ relative concentration as a function of time, during the MTES/TEOS copolymerization, together with the calculated curves assuming:
$k_{T1} = 0.006$ and A - $k_{T2} = 0.013$ B - $k_{T2} = 0.028$.
The experimental error is ± 2%.

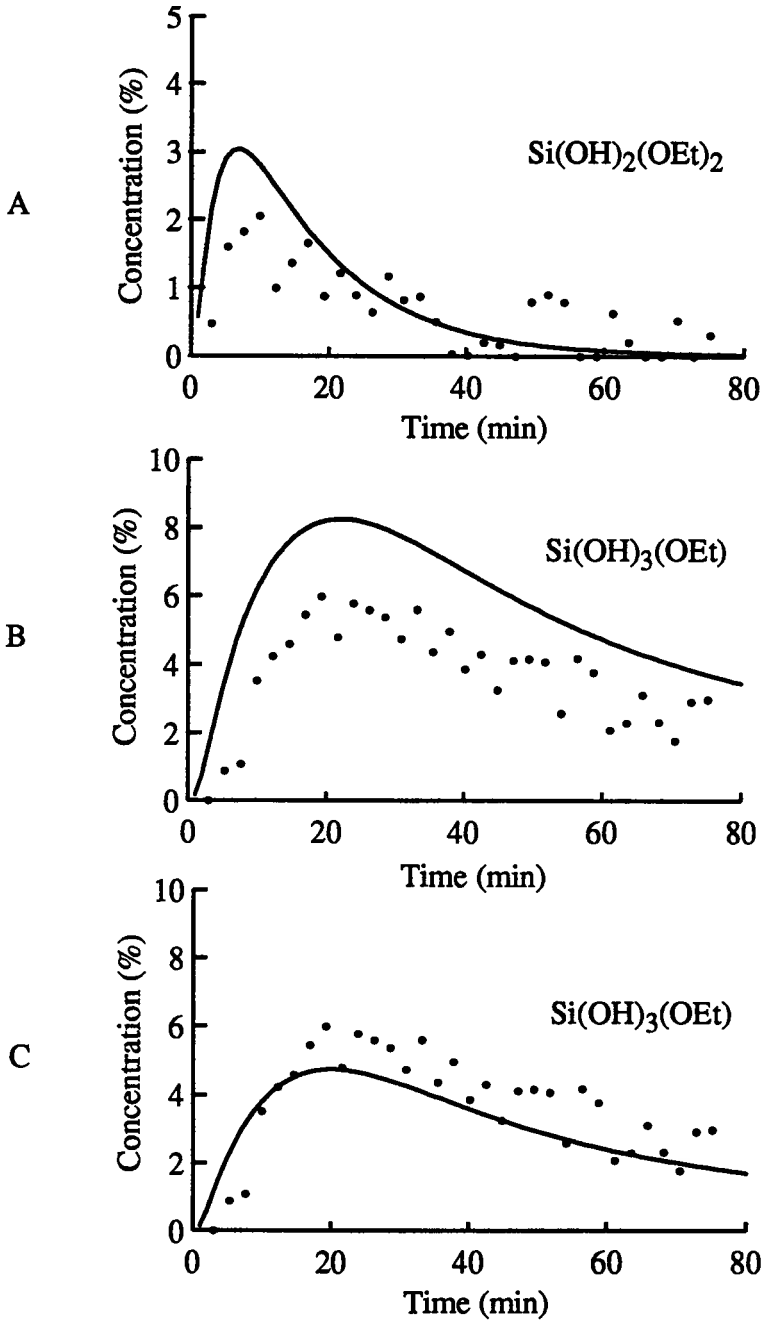

Figure 4.12 - Experimental data for the TEOS hydrolysis intermediates $Si(OH)_2(OEt)_2$ and $Si(OH)_3(OEt)$ relative concentrations as functions of time, during the MTES/TEOS copolymerization, together with the calculated curves assuming for A, B and C: $k_{T1} = 0.006$ $k_{T2} = 0.028$ $k_{T3} = 0.063$, and for B) $k_{T4f} = 0.053$; $k_{T4b} = 0.02$ and for C) $k_{T4f} = 0.1$; $k_{T4b} = 0.02$. The experimental error is ±2%.

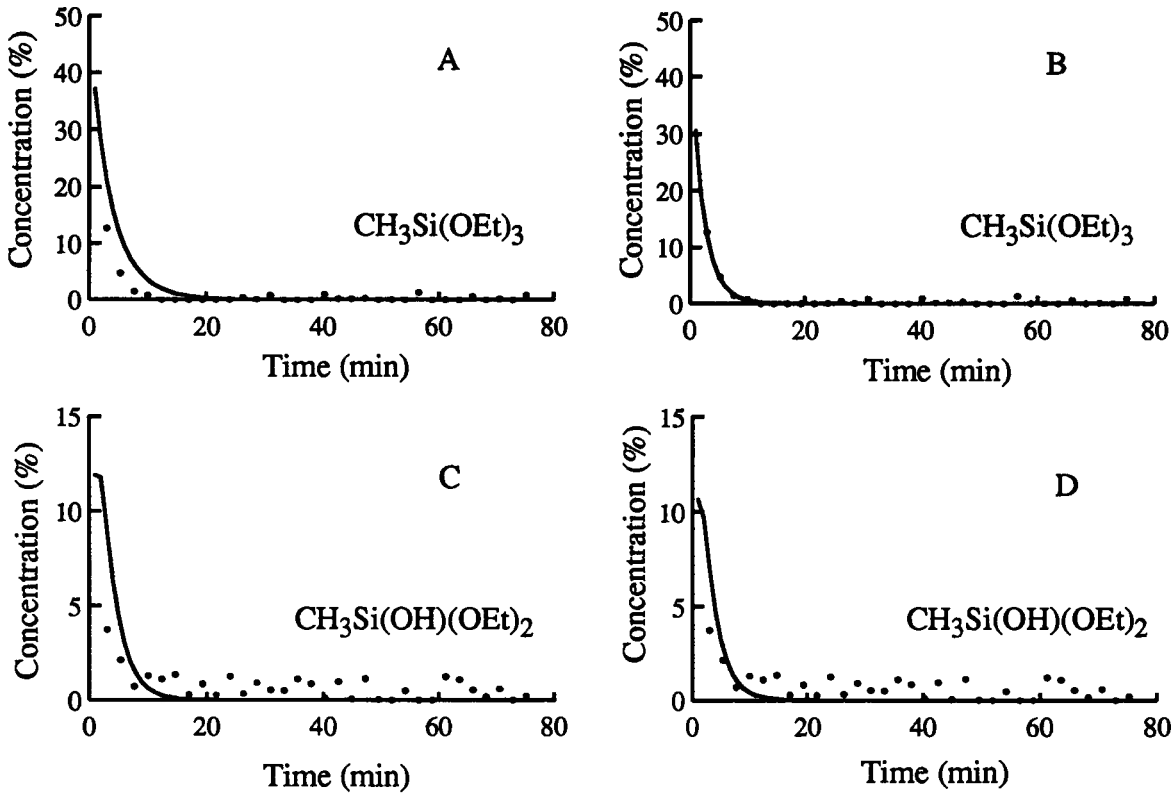

Figure 4.13 - Experimental data for $CH_3Si(OEt)_3$ and the MTES hydrolysis intermediate $CH_3Si(OH)(OEt)_2$ relative concentrations as functions of time, in the MTES/TEOS copolymerization, together with the curves calculated assuming :

A - $k_{M1} = 0.0203$ (homopolymerization value)

B - $k_{M1} = 0.034$

C - $k_{M1} = 0.034$ $k_{M2} = 0.068$ (homopolymerization values)

D - $k_{M1} = 0.034$ $k_{M2} = 0.085$.

The experimental error is ±2%.

MTES monomer in order to determine the dimer formation constants.

The approach taken to determine the kinetic constant for the codimer (k_{C10}) was to start with the homodimer kinetic constants (k_{T5} and k_{M4}) and a very small value for the codimer kinetic constant (k_{C10}). The variation of k_{C10} clearly showed that this parameter has a strong effect on the maxima of the calculated curves for the fully hydrolyzed species. The maximum value of k_{C10} was determined to be 0.05-0.06 $M^{-1}min^{-1}$. For larger values, the maximum of the $Si(OH)_4$ curve is too low to fit the experimental data; consequently, k_{C10} was set to 0.05 $M^{-1}min^{-1}$ and k_{T5} and k_{M4} were adjusted in order to best fit the experimental curves. The initial conditions and the final set of calculated curves for $Si(OH)_4$ and $CH_3Si(OH)_3$ are shown in Figure 4.14 together with experimental data.

The two back reactions in the copolymerization reaction scheme were addressed next. As is shown in Figures 4.15 and 4.16 the calculated curves for $Si(OH)_4$ and $CH_3Si(OH)_3$ are not very sensitive to k_{T4b} and k_{M3b} respectively; however the $Si(OH)_3(OEt)$ and $CH_3Si(OH)_2(OEt)$ curves prove to be very sensitive. These parameters were therefore optimized by evaluating their effect on the concentration curves of $Si(OH)_3(OEt)$ and $CH_3Si(OH)_2(OEt)$, respectively. Figure 4.15 compares the calculated curves obtained when the homopolymerization rate constants are used with those using the optimized value for k_{T4b}.

The experimental data for the remaining two hydrolysis species of the MTES monomer are shown in Figure 4.16. Again, two calculated curves are shown for each species, one calculated with k_{M3b} from the homopolymerization reaction and the other with the optimized value.

All the kinetic rate constants determined for the copolymerization and the homopolymerization cases are summarized in Table 4.4, and they show that the hydrolysis rate constants for the TEOS monomer have been significantly altered. A preliminary study on

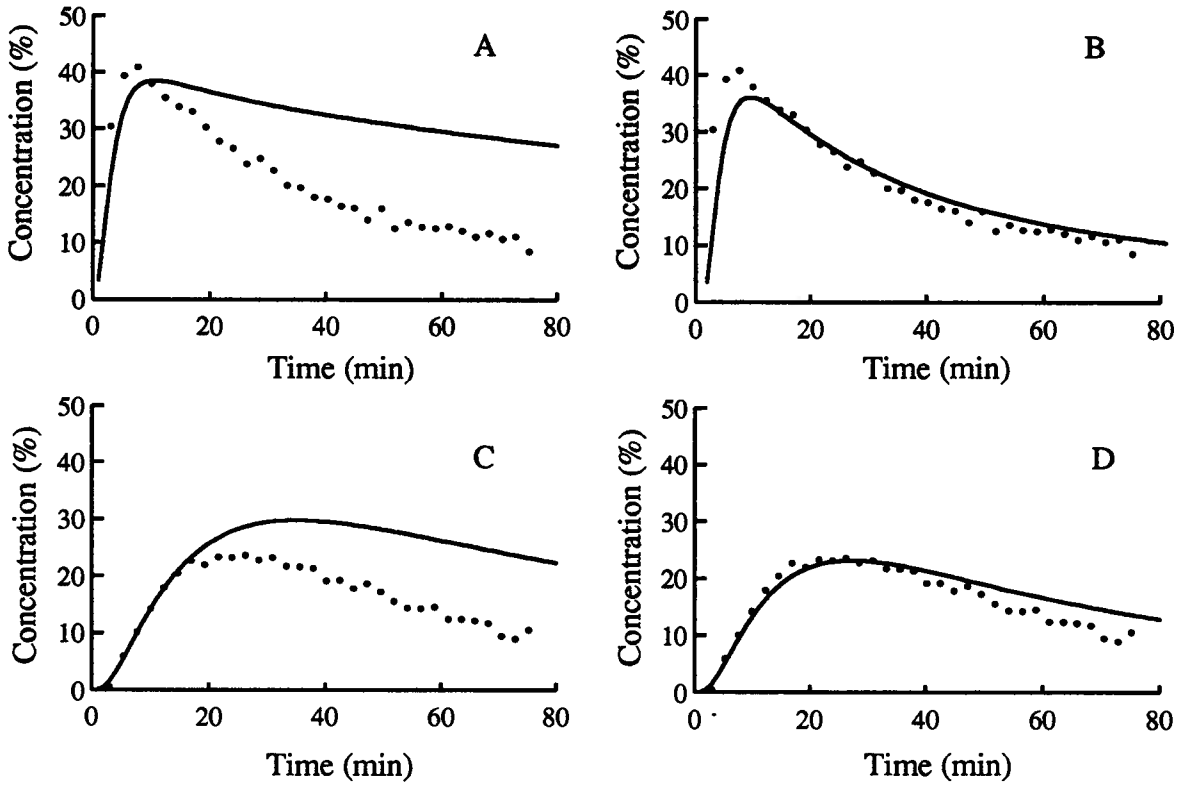

Figure 4.14 - Experimental data for the fully hydrolyzed monomers $CH_3Si(OH)_3$ (A, B) and $Si(OH)_4$ (C, D) relative concentrations as functions of time, during the MTES/TEOS copolymerization, together with the curves calculated assuming :
$k_{T5} = 0.035$ $k_{M4} = 0.015$ $k_{C10} = 0.001$ for A and C
$k_{T5} = 0.05$ $k_{M4} = 0.04$ $k_{C10} = 0.05$ for B and D .
The experimental error is ±2%.

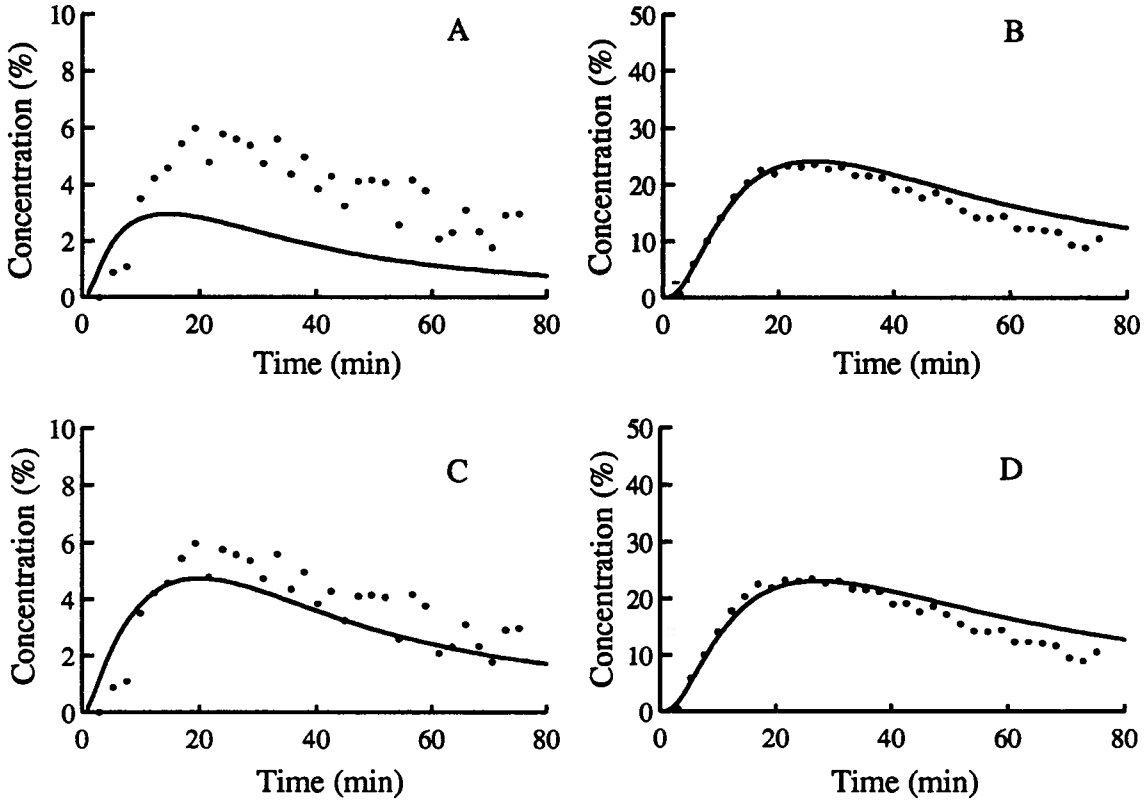

Figure 4.15 - Experimental data for the TEOS hydrolysis intermediates, $Si(OH)_3(OEt)$ and $Si(OH)_4$, relative concentrations as functions of time, during the MTES/TEOS copolymerization, together with the calculated curves assuming :
$k_{T1} = 0.006$, $k_{T2} = 0.028$, $k_{T3} = 0.063$, $k_{T4f} = 0.1$, $k_{C10} = 0.05$
A) $Si(OH)_3(OEt)$ and B) $Si(OH)_4$ with $k_{T4b} = 0.0093$, $k_{T5} = 0.05$
C) $Si(OH)_3(OEt)$ and D) $Si(OH)_4$ with $k_{T4b} = 0.02$, $k_{T5} = 0.05$.
The experimental error is ±2%

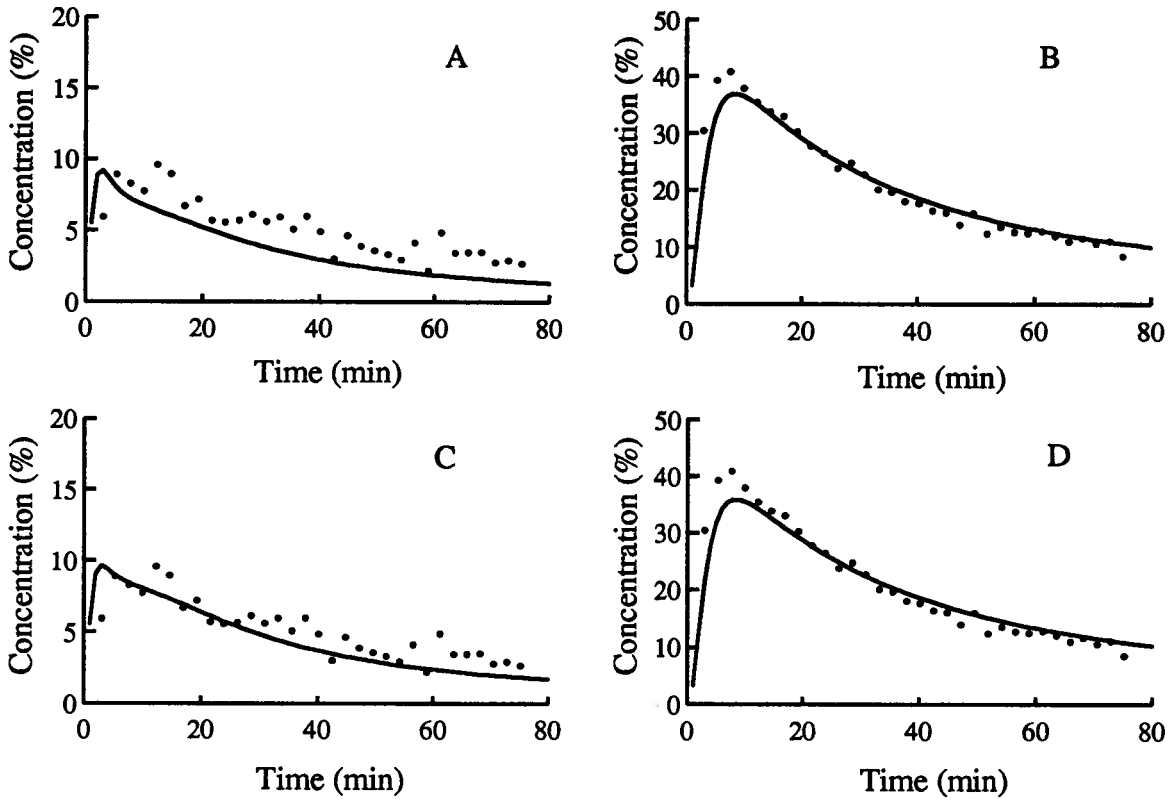

Figure 4.16 - Experimental data for the MTES hydrolysis intermediates, $CH_3Si(OH)_2(OEt)$ and $CH_3Si(OH)_3$, relative concentrations as functions of time, during the MTES/TEOS copolymerization, together with the calculated curves assuming :
$k_{M1} = 0.034$ $k_{M2} = 0.085$ $k_{M3f} = 0.1$ $k_{M4} = 0.04$ $k_{C10} = 0.05$
A) $CH_3Si(OH)_2(OEt)$ and B) $CH_3Si(OH)_3$ with $k_{M3b} = 0.02$
C) $CH_3Si(OH)_2(OEt)$ and D) $CH_3Si(OH)_3$ with $k_{M3b} = 0.025$.
The experimental error is ±2%.

Table 4.4 - Comparison of the pH dependent kinetic rate constants determined for the TEOS and MTES homopolymers and the MTES/TEOS copolymer at a pH=2.55.

	Homopolymer results	Copolymer results
TEOS		
k_{T1}	0.0018	0.006
k_{T2}	0.011	0.028
k_{T3}	0.06*	0.06*
k_{T4f}	0.05	0.1
k_{T4b}	0.009	0.02
k_{T5}	0.033	0.05
MTES		
k_{M1}	0.021	0.034
k_{M2}	0.066	0.085
k_{M3f}	0.07	0.10
k_{M3b}	0.01	0.025
k_{M4}	0.021	0.04
CODIMER		
k_{C10}		0.05

* no change in this case

the effect of the water/silane ratio on the hydrolysis of TEOS suggests that as the water/TEOS ratio increases the rate of the first hydrolysis decreases. This implies that the higher water/TEOS ratio compared to the TEOS homopolymerization cannot cause the increase in k_{T1}. However, the difference between the homopolymer and copolymer hydrolysis rate constants for the TEOS monomer may be explained by the presence of the MTES monomer. The presence of the MTES monomer in the copolymer reaction alters the solution properties, such as viscosity, polarity, etc, inevitably affecting the TEOS-water interactions. The MTES hydrolysis is also affected by the presence of TEOS, but to a lesser extent.

The kinetic constants obtained for the dimer formations are not unique solutions to the fitting of the experimental data. Other solutions were possible, but eliminated because they did not reflect the proper ratios of the different dimers present in the reaction medium at any moment in time.

Concentrations as functions of time can be now calculated for both homo- and codimers with the three dimer formation rate constants determined above. These calculated curves overestimate the dimer concentrations in all cases since no dimer depletion reactions, i.e. further condensation reactions, were included. The spectra indicate that such species are formed. The copolymerization spectrum acquired at 76 minutes is shown in Figure 4.17. After this reaction time, there are a number of small peaks in the regions of -84 ppm and of -91.5 ppm. The peaks at ~-84 ppm have been assigned to dimers or trimer end groups where there is an ethoxy ligand directly attached to the silicon, such as: $Si(OH)_2(OEt)(OSi)$.[3.1, 3.15] After 76 minutes, only 5% of silicons contribute to the signals in the -84 ppm region which supports the statement that few non-fully hydrolyzed monomers take part in condensation reactions up to this point in the reaction.

The signals at -91.5 ppm have been assigned to the center silicon in trimers,

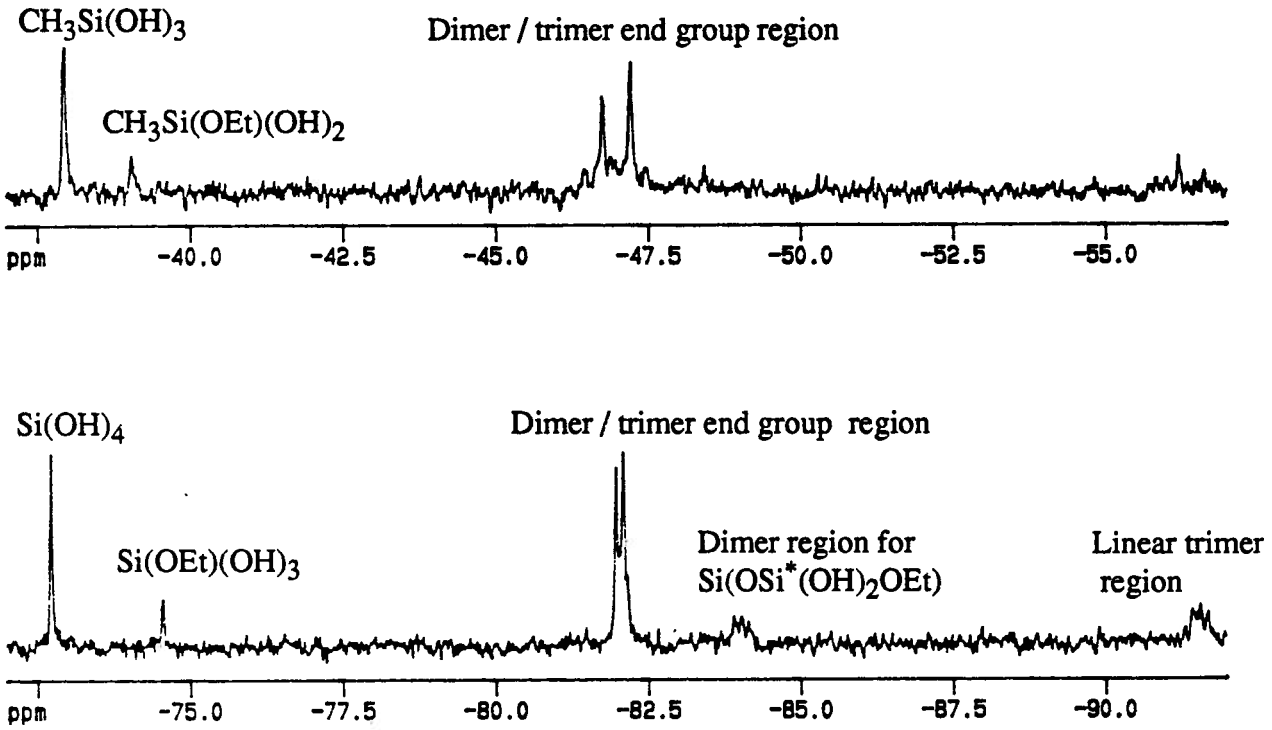

Figure 4.17 - ^{29}Si solution NMR spectrum, 76 minutes into the MTES/TEOS copolymerization (water acidified to pH=2.55). The spectrum was acquired with 8 scans and a 1 second recycle delay.
Top: MTES region.
Bottom: TEOS region.

$Si(OSi)_2(OH)_2$.[3.1, 3.15] The NMR spectrum shows no evidence for the existence of cyclic trimers whose signals appear at -90.6 ppm, -92.9 ppm and -95.2 ppm.[3.15] At 76 minutes, the total concentration of central silicons in trimers is 9% (the signals from silicons at the ends of the chain will appear in the dimer region). Thus, the total percentage of trimers is ~9%. The total concentration of silicons in dimers (excluding the trimer end group silicon signals that appear in this region) is approximately 50% which implies that the total concentration of dimers is 25%. Therefore, from the NMR intensities, the total dimer percentage including those that were consumed to form trimers is 34%. Using the kinetic constants for dimer formation, the total dimer concentration is predicted to be 37%. Considering the complexity of the problem when taking the dimer and trimer condensation products into account, the data in general support the kinetic rate constants obtained in the analyses for the formation of the dimer species.

Having determined the kinetic rate constants for the dimer formation, reactivity ratios can now be calculated for both MTES and TEOS monomers. A reactivity ratio [4.3] for the MTES and TEOS monomers is defined in equation (4.41).

$$R_{MTES} = \frac{k_{MTES\text{-}MTES}}{k_{MTES\text{-}TEOS}} = \frac{k_{M4}}{k_{C10}} \quad ; \quad R_{TEOS} = \frac{k_{TEOS\text{-}TEOS}}{k_{MTES\text{-}TEOS}} = \frac{k_{T5}}{k_{C10}} \tag{4.41}$$

The reactivity ratio for $CH_3Si(OH)_3$ or $Si(OH)_4$ is the homodimer kinetic constant over the codimer kinetic rate constant (k_{C10}). Using the data from Table 4.4, the reactivity ratios for MTES and TEOS are 0.8 and 1, respectively. This suggests that the copolymerization of MTES and TEOS monomers will tend to produce a random copolymer if subsequent condensation reactions follow the same trend. In fact, they are close enough to the ideal case that the copolymer composition should also approximate the reaction mixture composition at any given time.

In agreement with the reactivity ratios discussed above, the dimer intensities in the NMR spectrum, Figure 4.17, suggest that the TEOS homodimer concentration is approximately half that of the codimer concentration. This implies that the TEOS monomer has little preference whether it reacts with another TEOS monomer or with a MTES monomer. The same is true for the MTES monomer. Therefore, it is to be expected that in a MTES/TEOS copolymer the functionalized monomer will be randomly distributed in the silica gel matrix.

4.3.4 MTES/TEOS Copolymer Dimer Formation

To prove that the results obtained above are valid for other MTES/TEOS copolymer compositions, their dimer ratios were compared at specific reaction times. These different copolymers involved varying either the relative monomer ratio or the water/silane ratio. The relative dimer concentrations in a copolymer (homodimers versus codimers) provide a marker of the polymer composition, because silicon-oxygen bonds are not broken to any appreciable extent.[1.41, 4.4]

A variety of MTES/TEOS copolymer compositions (summarized in Table 4.1) were followed by high resolution ^{29}Si solution NMR. Within each data set two spectra were deconvoluted, those obtained after 101 and 131 minutes. The experimentally determined dimer concentrations are summarized in Table 4.5 and 4.6.

The MTES/TEOS copolymerization samples CO111, CO271 and CO721 have the same water/(total silane) ratio as in the homopolymerization studies but the relative ratios of the monomers were 50/50, 25/75 and 75/25, respectively. Assuming a random dimerization process, the theoretically expected ratios are also listed in Table 4.5 and 4.6. The measured concentrations of the dimers approximate those predicted for a random copolymer.

Table 4.5 - Dimer concentrations for the different copolymer samples after 101 minutes. The relative concentrations presented are in percent with respect to the total dimer concentration in each spectrum. The theoretical values are calculated for a completely random process. Sample composition codes are summarized in Table 4.1 and T-T = TEOS-TEOS homodimer, M-M = MTES-MTES homodimer and T-M = TEOS-MTES codimer.

DIMER	CO271 (25% MTES)	CO721 (75% MTES)	CO111 (50% MTES)
T-T	50 ± 2	18 ± 2	36 ± 2
THEORY	56	6	25
T-M	41 ± 2	26 ± 3	43 ± 3
THEORY	38	38	50
M-M	8 ± 2	56 ± 3	21 ± 1
THEORY	6	56	25

DIMER	CO112 (50% MTES)	CO221 (50% MTES)	CO222 (50% MTES)
T-T	31 ± 4	22 ± 1	26 ± 2
THEORY	25	25	25
T-M	46 ± 7	53 ± 2	47 ± 4
THEORY	50	50	50
M-M	23 ± 3	25 ± 1	28 ± 2
THEORY	25	25	25

Table 4.6 - Dimer concentrations for the different copolymer samples after 131 minutes. The relative concentrations are in percent with respect to the total dimer concentration in each spectrum. The theoretical values are calculated for a completely random process. Sample composition codes are summarized in Table 4.1 and T-T = TEOS-TEOS homodimer, M-M = MTES-MTES homodimer and T-M = TEOS-MTES codimer.

DIMER	CO271 (25% MTES)	CO721 (75% MTES)	CO111 (50% MTES)
T-T	53 ± 1	13 ± 1	27 ± 1
THEORY	56	6	25
T-M	37 ± 2	34 ± 4	51 ± 2
THEORY	38	38	50
M-M	11 ± 2	54 ± 3	23 ± 1
THEORY	6	56	25

DIMER	CO112 (50% MTES)	CO221 (50% MTES)	CO222 (50% MTES)
T-T	31 ± 3	23 ± 2	27 ± 3
THEORY	25	25	25
T-M	47 ± 5	51	49 ± 5
THEORY	50	50	50
M-M	23 ± 2	26 ± 2	25 ± 2
THEORY	25	25	25

In order to investigate the possible effect of the water/silane ratio the water concentration was doubled. The total number of moles of silane (CO112) was kept equal to the total number of moles of silane in the homopolymer case. There was no significant effect on the ratio of dimers formed. These results are summarized in Table 4.5-4.6 and support the fact that the MTES/TEOS copolymer tends to be a random copolymer under the conditions used in the kinetic study (CO111).

The other approach to varying the water/(total silane) ratio would be to keep the water concentration the same as in the homopolymerization and manipulate the total silane concentration. If the water/(total silane) ratio is half that in the homopolymerization (CO221 versus CO111) no significant effect is detected on the relative ratios of the codimer to homodimer ratios (Table 4.5-4.6). The difference in the NMR spectra for CO221 compared to CO111, is that in the CO221 case after a significant amount of dimer formation has occurred (131 minutes) there is still some unreacted $Si(OEt)_4$ present in the reaction vessel, a situation not encountered before. Interestingly, no unreacted $CH_3Si(OH)_3$ monomer is present.

Now, if the water/(total silane) ratio is the same as in the homopolymer case but the amount of water and total silane is doubled with respect to the homopolymer, CO222, the ratio of codimer versus homodimers formed is unaffected but again some unhydrolyzed TEOS monomer is detected.

4.4 CONCLUSIONS

For the first time, the pH dependent kinetic rate constants were determined for the hydrolysis and dimerization reactions of the MTES homopolymerization. pH independent kinetic rate constants were calculated from plots of the pH dependent kinetic constants as functions of acid concentration. These kinetic rate constants provide the first quantitative evidence that the MTES monomer hydrolyzes faster than the TEOS monomer at each sequential hydrolysis reaction. This implies that the methyl group stabilizes the transition state involved in the hydrolysis reactions.

The dimerization rate constant for the MTES homopolymerization is slower than that for the TEOS monomer, suggesting that the methyl ligand destabilizes the transition state involved in the MTES-MTES homodimerization reaction. As in the TEOS polymerization, an equilibrium reaction was required in the reaction model in order to respect the general curve shape of the second to last hydrolysis intermediate, $CH_3Si(OH)_2(OEt)$.

The determination of the MTES and TEOS homopolymerization hydrolysis and condensation rate constants provided a starting point for the determination of the MTES/TEOS copolymer hydrolysis and dimer formation rate constants. The hydrolysis kinetic rate constants obtained for the copolymerization suggest that in comparison with the homopolymerizations, the reaction kinetics of the TEOS monomer are significantly more affected than that of the MTES monomer. Reactivity ratios of 0.8 and 1 for the MTES and TEOS monomers, respectively, were calculated from the dimer formation kinetic rate constants determined for the MTES/TEOS copolymer. These reactivity ratios suggest that the MTES/TEOS copolymer tends to approximate a random copolymer. The effect of altering the relative monomer proportions, and the water/(total silane) ratio, further confirms that the MTES/TEOS copolymer has a strong tendency to form a random copolymer.

CHAPTER 5

THE EFFECT OF FORMAMIDE, A DRYING CHEMICAL CONTROL AGENT (DCCA) ON THE KINETICS OF THE TEOS, MTES AND MTES/TEOS POLYMERIZATIONS

5.1 INTRODUCTION

The copolymerization of TEOS and a functionalized silane provides a unique opportunity to make novel glasses, ceramics and composites with otherwise unattainable properties. To take full advantage of this new synthetic approach to form macroscopic pieces, the problem of cracking which generally occurs from the non-uniform shrinkage of the gel during the drying process, must be solved.[5.8] In order to prevent cracking, the drying stress must be minimized by either controlling the pore size distribution or rate of evaporation. To address this problem, Wallace and Hench suggested that drying chemical control agents (DCCA^s), such as formamide ($HCONH_2$), be introduced into the solvent mixture.[5.7] Formamide decreases the vapor pressure of the solvent; consequently the rate of evaporation decreases, resulting in a reduction in the drying stress and therefore the cracking.[5.7] In a series of subsequent publications, ^{29}Si NMR, SAXS, Raman, FTIR and different forms of chemical analysis [5.8-5.12] were used to further investigate what chemical processes might occur when formamide is present in the conversion of tetramethoxysilane (TMOS) to silica gel.

Wallace and Hench found that as the formamide concentration increased, the hardness and density of the sample decreased, the pore size distribution narrowed, and the average pore size increased.[5.8] Horiuchi studied the effect of DCCAs on the polymerization of silicic acid prepared from TEOS in an acid environment (HNO_3).[5.13] His data, in contrast to

those of Hench et al, suggest that the pore size distribution increases, as well as the average pore size, with increasing formamide concentration.

Hench et al. concluded, from an FTIR study, that formamide forms a protective layer on the gel surface facilitating the removal of water and pore liquor.[5.10] Orcel et al hypothesized, because of the differences observed between base and acid catalyzed gels, that formamide hydrogen bonds to the surface via the amide functionality to form a protective coating.[5.10] A study on amides with bulky substituents suggested that the amides form hydrogen bonds to silanol groups via the carbonyl group.[5.14]

The only study on the effect of formamide on the kinetics of TMOS was carried out by Orcel and Hench using ^{29}Si solution NMR.[5.9] The polymerization of TMOS was studied at high water/silane ratios (10:1), with no added acid and very high formamide concentrations (25-50 volume % of the TMOS volume used). From the NMR data, global hydrolysis rate constants were determined assuming that the reaction rates were independent of the substitution/polymerization of the silicons. These results suggested that as the formamide concentration increased, the global hydrolysis rate decreased.[5.9, 5.11]

Artaki et al [1.42] studied the effect of formamide on the polymerization of TMOS at high water/silane ratios with no added acid. Unfortunately the formamide concentrations used were not stated. Their ^{29}Si solution NMR spectra indicated that fewer hydrolyzed monomers were present in the sample containing formamide than in the sample without formamide, supporting the findings of Hench et al. that formamide inhibits hydrolysis. In addition, the ^{29}Si solution NMR chemical shifts and the Raman absorptions were unaffected by the presence of formamide which they interpreted as evidence that formamide is not chemically bonded to the silicon polymer.[1.42]

The studies of Boonstra et al. [5.15] and Horiuchi [5.15], are the only published

investigations to date, on the effect of formamide on the polymerization of TEOS. Boonstra et al. used ^{29}Si solution NMR to investigate the effect of formamide on a two step (first acid then base catalyzed) polymerization of TEOS.[5.15] They studied the reaction under different stoichiometric and substoichiometric water/silane ratios.[5.15] Boonstra et al.'s study concluded that when the reaction was acid catalyzed, the hydrolysis and dimerization rates were reduced as a function of the formamide concentration. In addition, they found that in the presence of formamide, as the water concentration increased, the total concentration of hydrolyzed species increased. They also concluded that the DCCA favors condensation of incompletely hydrolyzed species resulting in a larger percentage of ethoxy groups in the final gel.[5.15]

Supporting the findings of Hench et al. and Horiuchi [5.8,5.13], Boonstra et al. found that as the formamide concentration increased, the mean pore size increased.[5.15] In agreement with Artaki's study, they found no evidence in the ^{1}H and ^{29}Si solution NMR data for chemical bond formation between formamide and water or any ^{29}Si functionalities.[5.15]

In this chapter, the effect of formamide on the hydrolysis kinetics of tetraethoxysilane (TEOS), methyltriethoxysilane (MTES) and the MTES/TEOS copolymer was investigated using high resolution ^{29}Si solution NMR spectroscopy. The kinetic analysis for all three polymerizations presented in Chapters 3 and 4 provide the reference data for the effect of formamide on the hydrolysis reactions. For the first time, it is possible to isolate the effect of formamide on the individual hydrolysis reactions and dimer formation of the MTES, TEOS homopolymerizations and the MTES/TEOS copolymerization.

High resolution ^{1}H, ^{13}C, ^{15}N and ^{29}Si solution NMR spectroscopy were used to investigate the possibility of formamide bonding to the silica gel surface during the TEOS polymerization.

5.2 EXPERIMENTAL

5.2.1 Kinetics

The reaction mixture had the same composition as described in Chapter 3 (4 ml (0.018 mole) TEOS, 6.07 ml (0.1034 mole) ethanol, 3.58 ml (0.1981 mole) water acidified to pH=2.55, 0.075 g (0.000215 mole) $Cr(acac)_3$) with the difference that formamide was added to the reaction mixture. For the kinetic studies by ^{29}Si solution NMR the concentrations of the other reagents were kept constant and only the concentration of formamide was varied between 0 and 30 mole %. In the case of the MTES/TEOS copolymer 0.009 mole of TEOS and 0.009 mole of MTES were used.

The TEOS and MTES homopolymerizations, and MTES/TEOS copolymerization were acid catalyzed (pH=2.55) with a formamide/acid ratio of 400:1. The pH of the system is affected by the addition of formamide but concentrations were chosen such that the medium remained acidic (Table 5.1). Maintaining the acidic conditions is the principal difference between the present study and those of Orcel and Hench [5.9] and Artaki et al [1.42].

The reaction mixture used in the ^{1}H, ^{13}C and ^{15}N solution NMR study, contained 0.16 ml (0.004 mole) of ^{13}C or ^{15}N enriched formamide (20 mole %) and the water was acidified to pH=1.15. All the other concentrations were unchanged.

5.2.2 NMR

High resolution ^{1}H solution NMR spectra were obtained at a frequency of 500.13 MHz on a Bruker AMX 500 spectrometer and ^{13}C solution NMR spectra were obtained using the same spectrometer at a frequency of 125.76 MHz. A Varian 300 MHz spectrometer was used to acquire ^{15}N NMR spectra at a frequency of 30.406 MHz. In order to observe the $^{15}N/^{1}H$ couplings the data were collected using gated decoupling. The temperature was 298 K for all experiments. Specific experimental details are given in the figure captions.

Table 5.1 - The pH values and water/formamide ratios of the samples used in the kinetic investigations.

pH	Formamide (mole %)
2.55	0
2.83	5
3.13	10
3.63	20
3.94	30

5.3 RESULTS AND DISCUSSION

5.3.1 The Effect of Formamide on the Kinetics of the Hydrolysis and Dimer Formation Reactions

High resolution ^{29}Si solution NMR spectra were acquired as functions of reaction time during the TEOS and MTES homopolymerizations and MTES/TEOS copolymerization containing formamide. The spectra show that the presence of formamide does not affect the ^{29}Si chemical shifts of any of the hydrolyzed species.

A formamide concentration of 10 mole % or less has a small to negligible effect on the hydrolyses and dimer formation rates of the TEOS and MTES homopolymerizations, In Figures 5.1 and 5.2, the concentration curves are compared to those from the formamide free reaction.

Observable effects on the hydrolysis rates are detected when the concentration of formamide exceeds 10 mole %. The relative concentration versus time curves of the TEOS and MTES hydrolysis products, for reactions containing various amounts of formamide are shown in Figures 5.3 and 5.4, respectively. The concentration of the intermediate $Si(OH)_2(OEt)_2$ in the TEOS homopolymerization is so small that the effect of the formamide on the rate of decay is lost within the scatter of the data. It is obvious that formamide concentrations exceeding 10 mole % result in a dramatic retardation of the hydrolysis reactions. The kinetic constants are summarized in Tables 5.2 and 5.3.

The qualitative ^{29}Si NMR study of Boonstra et al. deals with TEOS and formamide concentrations of 0 to 42 mole %; the difference between their system and the reaction considered here is that they used a two step acid/base synthesis with substoichiometric to stoichiometric water concentrations.[5.15] At a water/silane ratio of 1, it is obvious from their figures that during the acid step just 8 mole % formamide affects the hydrolysis rates.

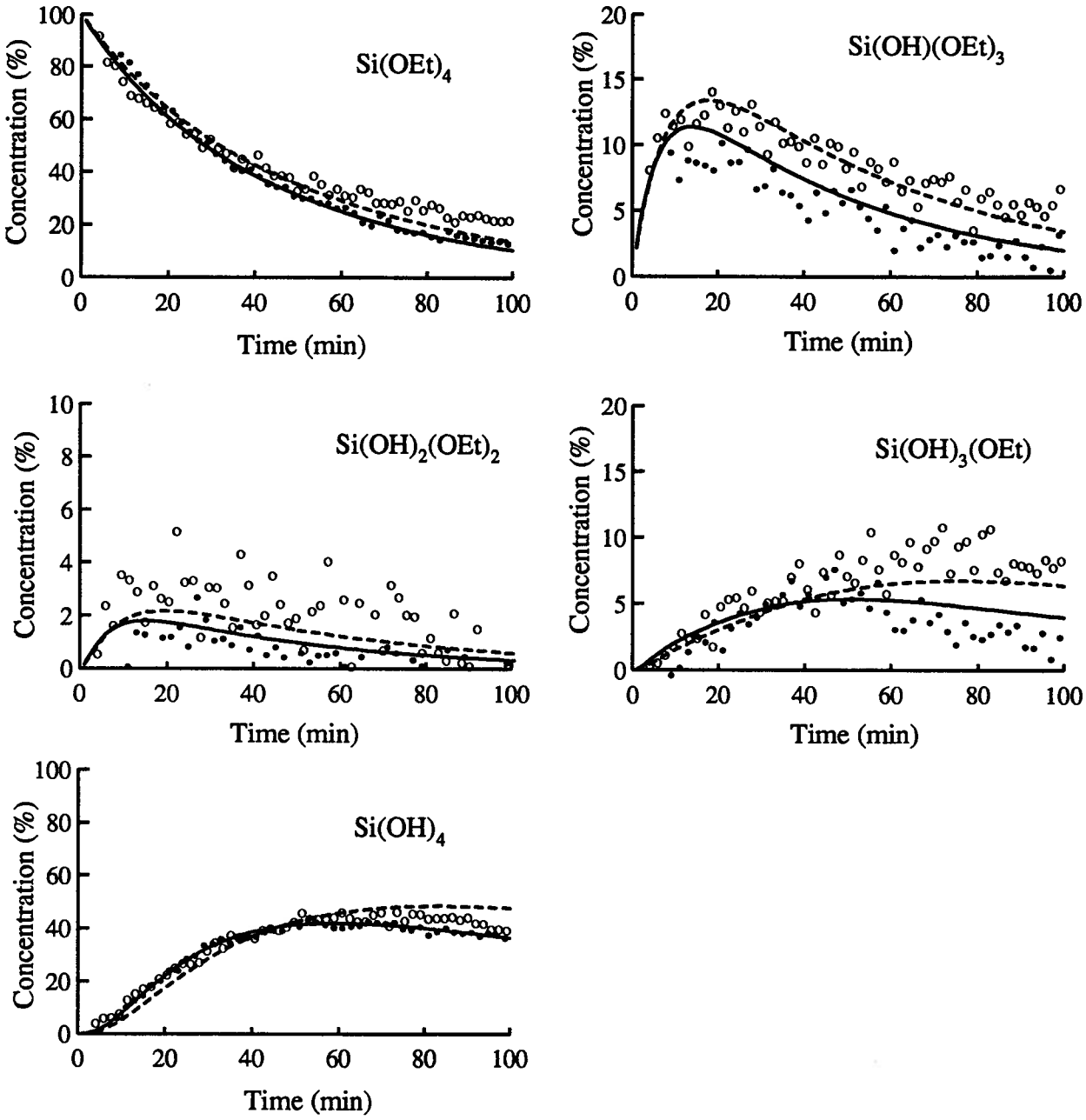

Figure 5.1 - Experimental data and calculated relative concentration curves for the hydrolysis intermediates as functions of reaction time for two TEOS homopolymerizations, involving 0 mole % formamide (circles and solid lines) and 10 mole % formamide (open circles and dashed lines). The experimental error is ±2%.

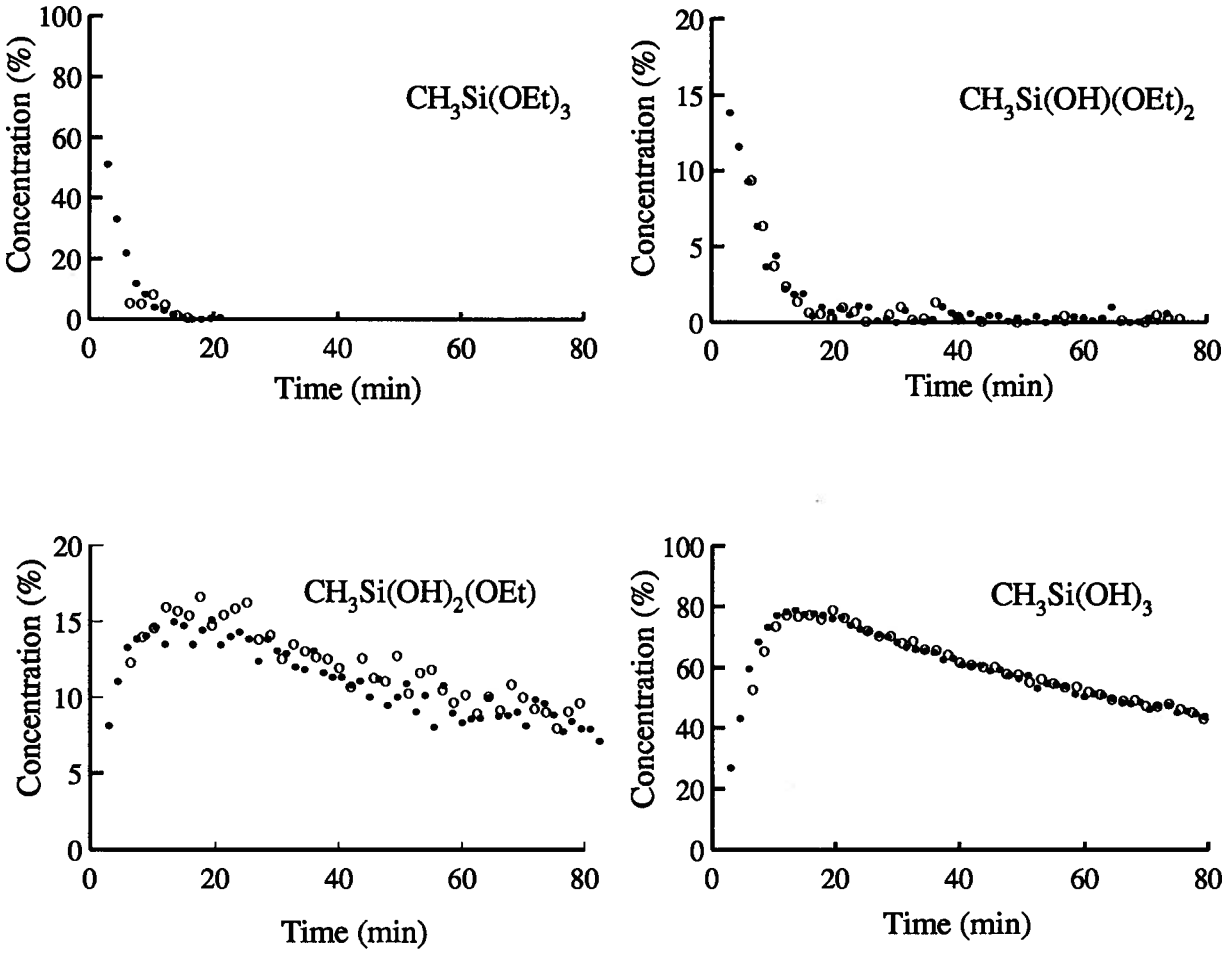

Figure 5.2 - Relative concentration curves of the hydrolysis intermediates as functions of reaction time, for two MTES homopolymerizations involving 0 mole % formamide (circles) and 10 mole % formamide (open circles).
The experimental error is ±2%.

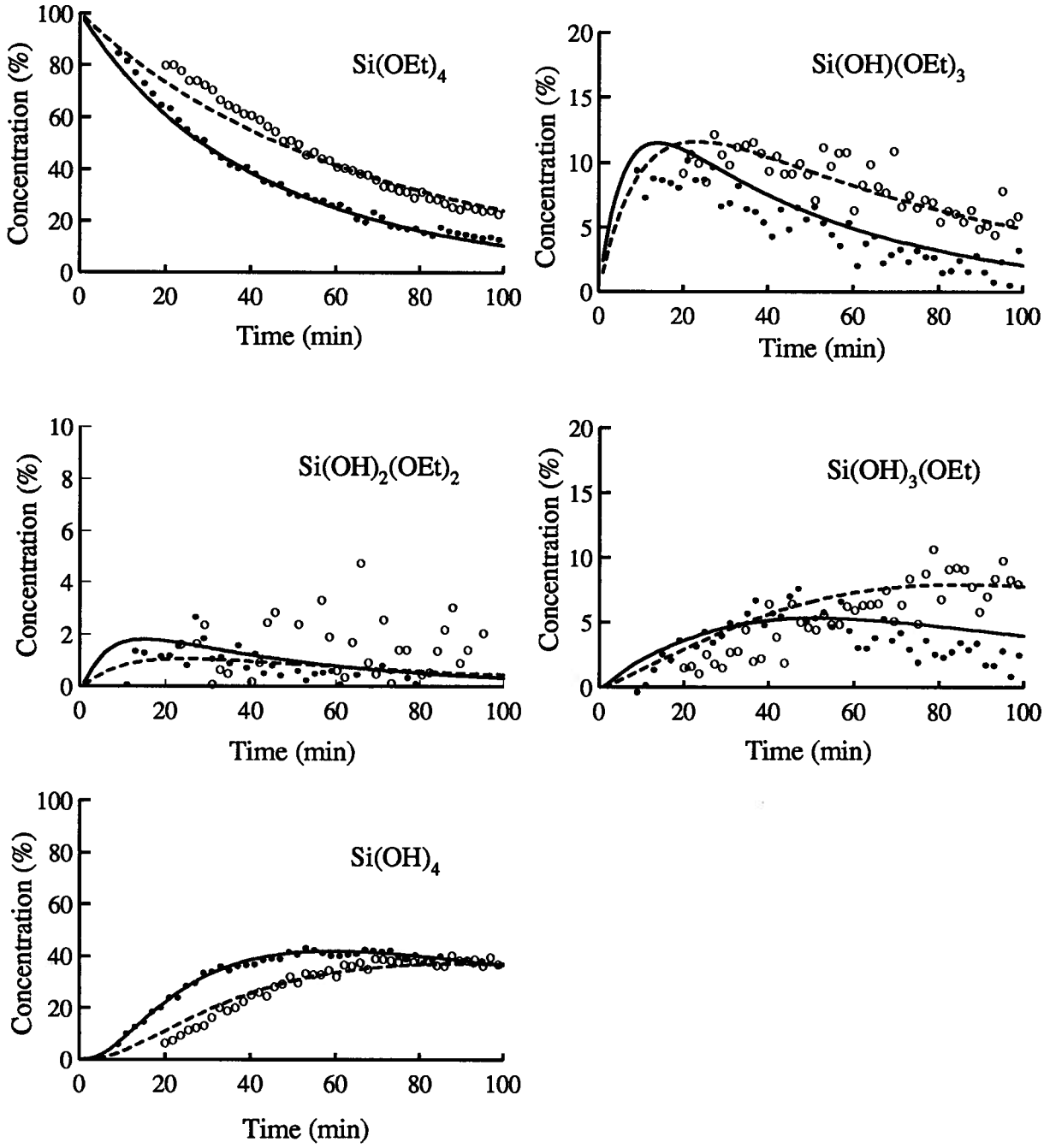

Figure 5.3 - Experimental data and calculated relative concentration curves for the hydrolysis intermediates as functions of time for two TEOS homopolymerizations, involving 0 mole % formamide (circles and solid lines) and 20 mole % formamide (open circles and dashed lines). The experimental error is ±2%.

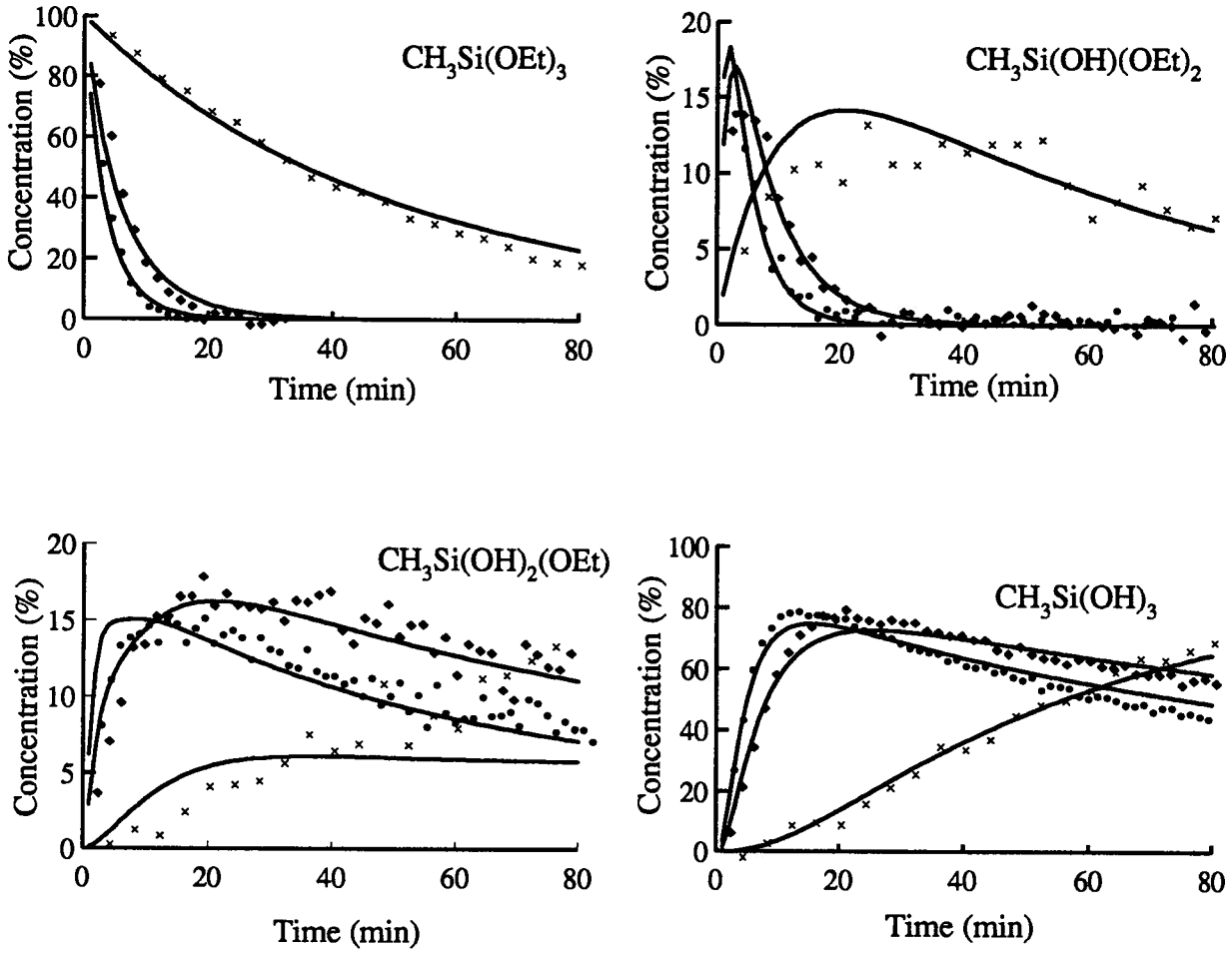

Figure 5.4 - Experimental data and calculated relative concentration curves for the hydrolysis intermediates as functions of time for three MTES homopolymerizations, involving 0 mole % formamide (circles), 20 mole % formamide (diamonds) and 30 mole % formamide (crosses). The experimental error is ±2%.

Table 5.2 - TEOS hydrolysis and dimerization kinetic rate constants, as defined in equations (3.4)-(3.8) (page 65), determined for different formamide concentrations. The formamide mole % is with respect to the total silane concentration. The water used in the reaction was acidified with HCl to pH=2.55. The effect of formamide on the pH is summarized in Table 5.1.

	Kinetic Constants $(M*min)^{-1}$			
Formamide (mole %)	0%	10%	20%	30%
k_{T1}	0.0018	0.0016	0.0011	0.000034
k_{T2}	0.011	0.008	0.0065	0.00021
k_{T3}	0.07	0.05	0.072	
k_{T4f}	0.07	0.07	0.05	
k_{T4b}	0.009	0.01	0.012	
k_{T5}	0.03	0.015	0.025	

Table 5.3 - MTES hydrolysis and dimerization kinetic rate constants, as defined in equations (4.1)-(4.4) (pages 91-92), determined for different formamide concentrations. The formamide mole % is with respect to the total silane concentration. The water used in the reaction was acidified with HCl to pH=2.55. The effect of formamide on the pH is summarized in Table 5.1.

	Kinetic Constants $(M*min)^{-1}$			
Formamide (mole %)	0%	10%	20%	30%
k_{M1}	0.0205	0.0205	0.012	0.0014
k_{M2}	0.066	0.066	0.043	0.0065
k_{M3f}	0.096	0.096	0.086	0.017
k_{M3b}	0.018	0.020	0.019	0.001
k_{M4}	0.011	0.011	0.007	0.0001

In addition, their results suggest that the higher the water concentration the greater the concentration of hydrolyzed species, even when formamide was present. All the polymerizations studied have a very high water concentration and the minimum formamide concentration influencing the hydrolysis rate was found to be higher. A comparison between Boonstra et al.'s work and the present results suggests that the water/formamide ratio is important in determining at what concentration the formamide influences the hydrolysis rate.

All the studies by Hench, Orcel et al. [5.8-5.10] focused on TMOS systems with high water ratios but involved very high formamide concentrations (76 to 385 mole % relative to TMOS). Their results are in accordance with our study which shows that the effect of formamide on the hydrolysis is significant at concentrations exceeding 10 mole %.

At much higher formamide concentrations (40 mole %) the concentration of hydrolysis products is reduced to the extent that after 27 hours only the TEOS and the first hydrolysis product peaks are detected in the ^{29}Si NMR spectra even though the system started to gel 24 hours later. A possible explanation for why the other intermediate species are not observed is that there is no build-up of any species except $Si(OH)(OEt)_3$ in the reaction sequence, consequently the concentration of any one intermediate species was not large enough to give a detectable NMR signal. Another possibility which has been suggested by Boonstra [5.15] is that condensation between partially hydrolyzed species is favoured. The ^{13}C CP/MAS NMR spectra of two TEOS polymer samples made with 0 % and 20 mole % formamide show that the ethoxy concentration is 1.6 ± 0.3 times greater in the sample synthesized with formamide. These findings support Boonstra's hypothesis.

The gelation time was taken as the time when the TEOS polymer has cross-linked to the extent that it no longer flows like a solution when the vial is tipped. The gelation times for the TEOS and MTES homopolymerizations as functions of formamide concentration are

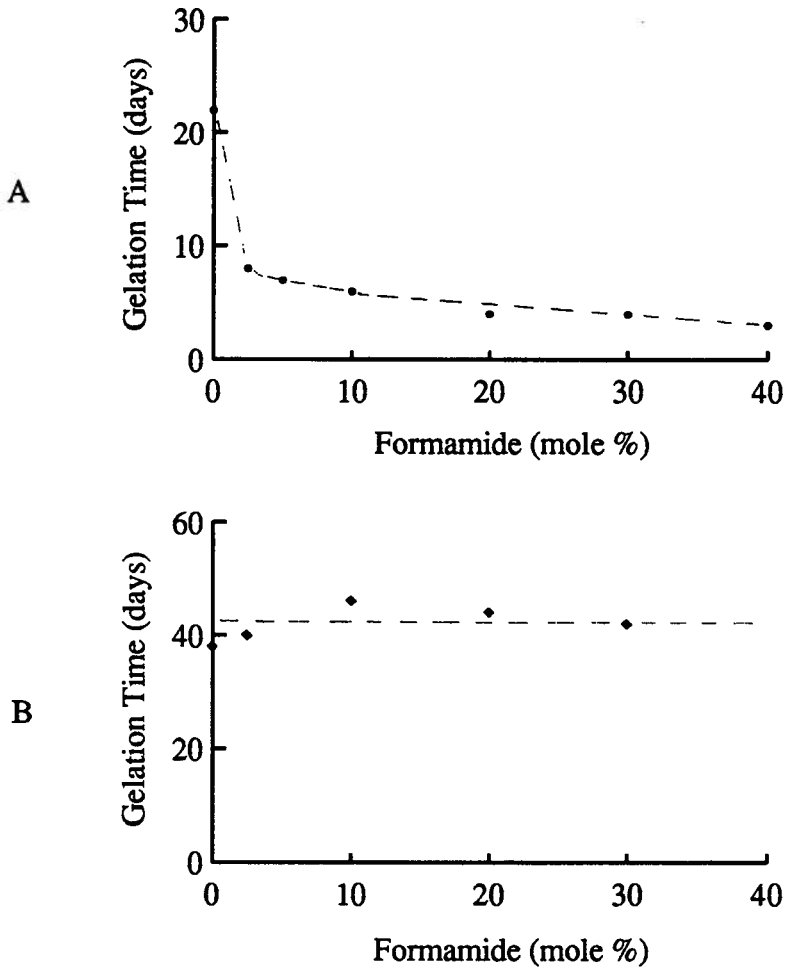

Figure 5.5 - The (A) TEOS and (B) MTES gelation times (days) versus formamide concentrations (mole %).

shown graphically in Figure 5.5. The largest observed change in the TEOS gelation time (from 22 to 6 days) occurs at low formamide concentrations (below 10 mole %) at pH=2.55. Formamide concentrations higher than 10 mole % affect the concentration distribution of the intermediate hydrolysis species but do not have a dramatic effect on the gelation time which only changes from 6 to 4 days. This suggests that the reduction of gelation time is not a consequence of a change in the hydrolysis mechanism of TEOS (Table 5.2). The present observations suggest that the formamide plays only an indirect role in the reactions between higher TEOS oligomers. At low concentrations, formamide may alter solution properties such as polarity and pH, favouring the cross-linking of higher oligomers which would result in a significant decrease of the gelation time. Horiuchi's small angle X-ray scattering (SAXS) data also suggest that the decrease in the gelation time results from an acceleration of the network formation.[5.13]

The electron donating capacity of the methyl group in the MTES monomer hinders the MTES-MTES dimer formation rate (relative to TEOS-TEOS dimer formation (Chapter 4)). In this case, the presence of formamide on the MTES homopolymerization reaction has little effect on the network formation process as reflected in the gelation times (Figure 5.5).

The ^{29}Si NMR spectra of the MTES/TEOS copolymer system are shown in Figures 5.6 and 5.7 for reactions in the presence of 0, 10 and 20 mole % formamide. These results clearly show that the concentrations of hydrolyzed monomers and dimers are not significantly affected at formamide concentrations of less than 10 mole %. However, as with the homopolymer systems the MTES/TEOS copolymerization is affected when formamide concentrations around 20 mole % are used (under these experimental conditions).

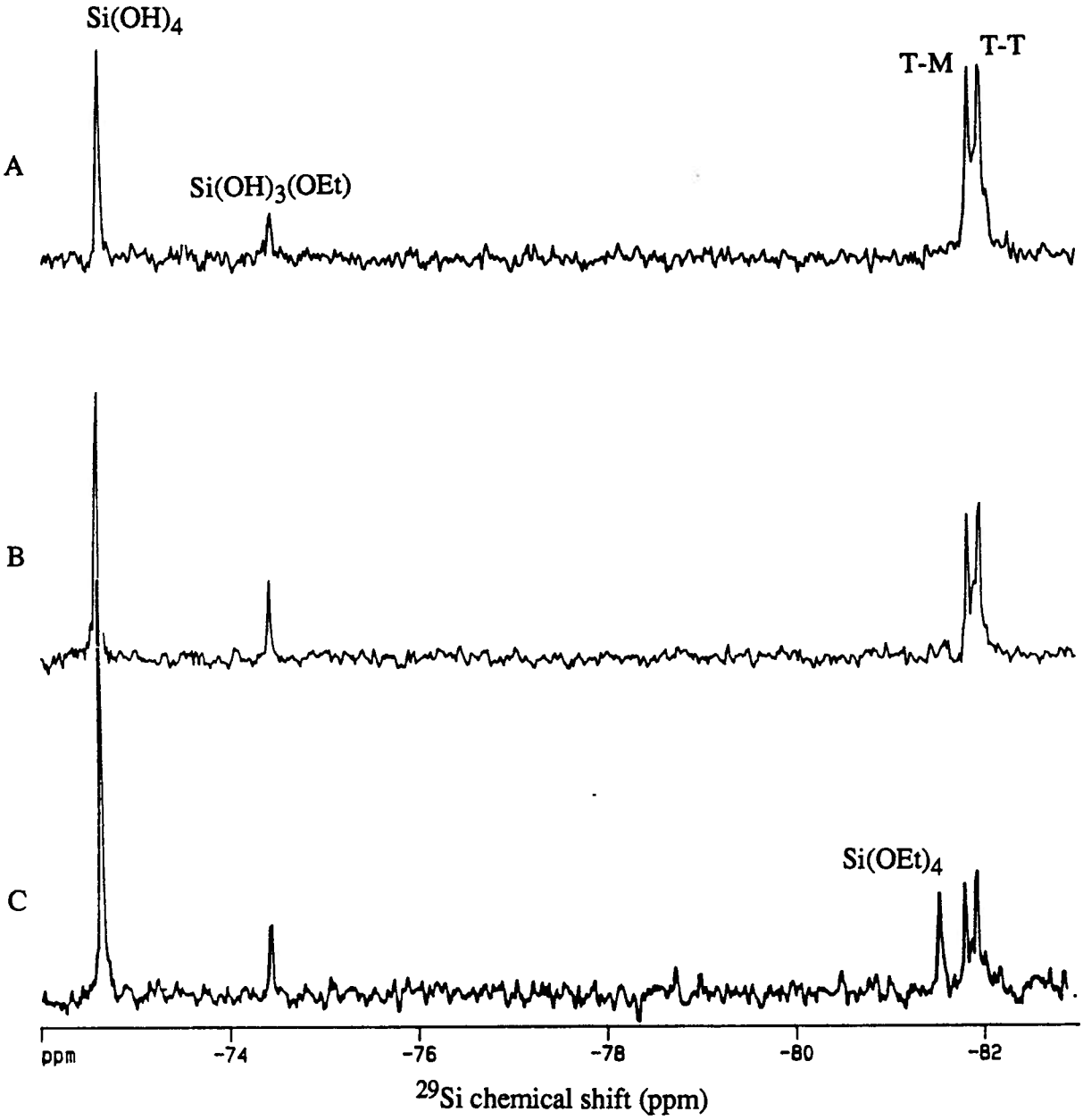

Figure 5.6 - The TEOS regions of the ^{29}Si NMR spectra of 50/50 MTES/TEOS copolymerizations at 130 minutes for reactions, involving
A - 0 mole % formamide
B - 10 mole % formamide
C - 20 mole % formamide.

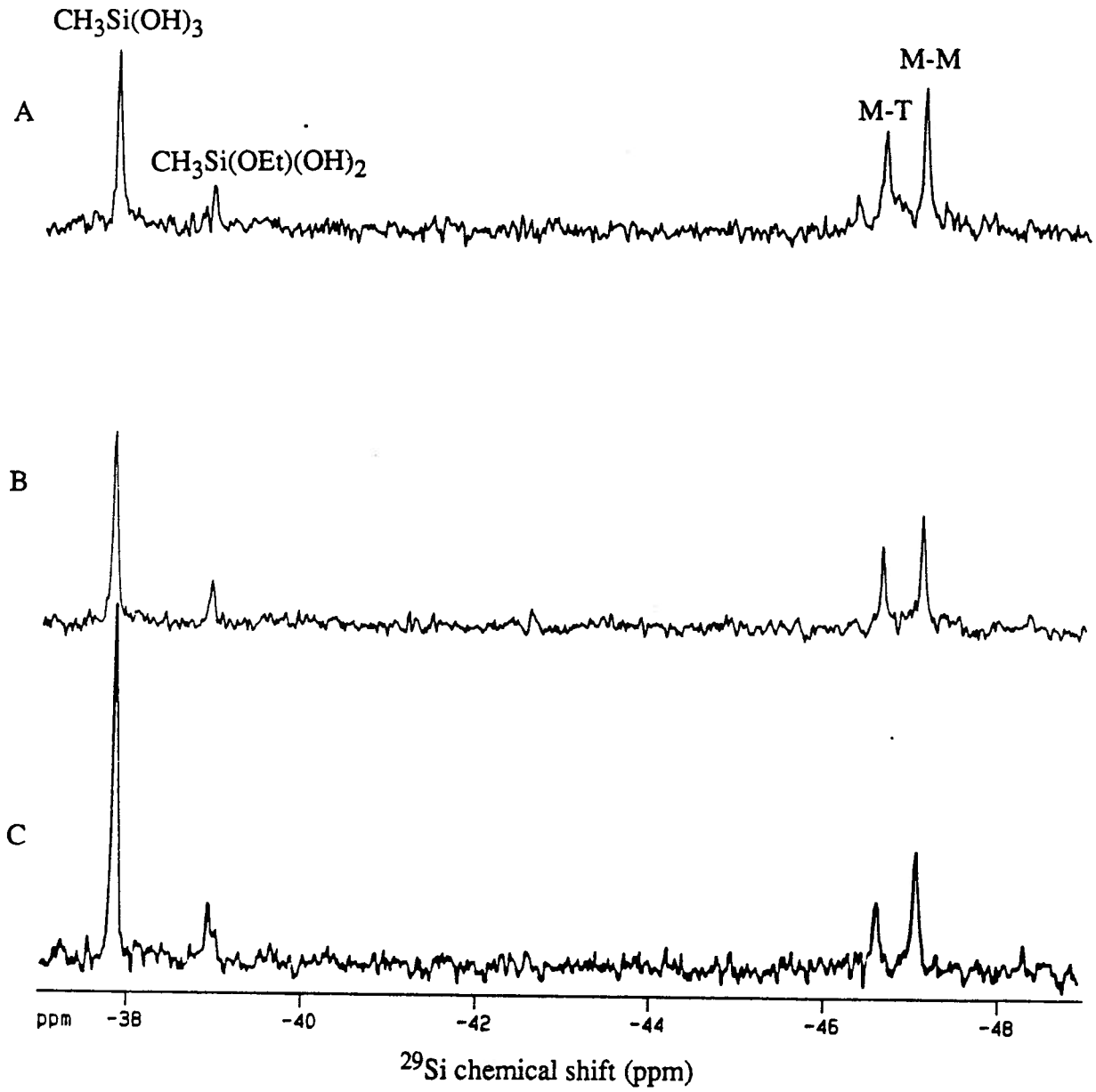

Figure 5.7 - The MTES regions of the ^{29}Si NMR spectra of 50/50 MTES/TEOS copolymerizations at 130 minutes for reactions, involving
A - 0 mole % formamide
B - 10 mole % formamide
C - 20 mole % formamide.

5.3.2 High Resolution ^{1}H Solution NMR Investigation

A typical ^{1}H NMR spectrum taken during the reaction of TEOS in the presence of 20 mole % formamide is shown in Figure 5.8B, where the upfield peaks are due to the ethanol and water protons as indicated. The downfield peaks have been magnified (by a factor of 100) in order to clearly observe the formamide proton resonances. An identical spectrum was acquired of a similar sample which did not contain TEOS since the TEOS proton peaks overlap with the ethanol signals. In particular, all of the formamide signals were identical in the two spectra.

The ^{1}H NMR spectra did not change over a period of 90 days suggesting that no covalent chemical bonding had occurred between the formamide protons and other functional groups present in the system. However, these results do not eliminate the possibility that a small percentage of the formamide protons might hydrogen bond to the silica gel in a fast exchange process. If this is the case, the concentration of such species must be very small since no chemical shift difference was observed.

5.3.3 High Resolution ^{15}N Solution NMR Investigation

High resolution ^{15}N solution NMR was used to follow ^{15}N enriched formamide during a TEOS hydrolysis to determine if the formamide molecule covalently bonds to or interacts strongly with the silanol groups via the amide functionality. ^{15}N has a very large chemical shift range [5.5] (hundreds of ppm compared to 10 ppm for ^{1}H) and therefore it was anticipated that even small interactions would be more easily detected than with the corresponding ^{1}H solution NMR data.

The high resolution ^{15}N solution NMR of neat formamide in deuterated acetone is shown in Figure 5.9B and consists of four doublets. The doublet $J_{a\text{-}c}$ of 90 Hz (for labelling

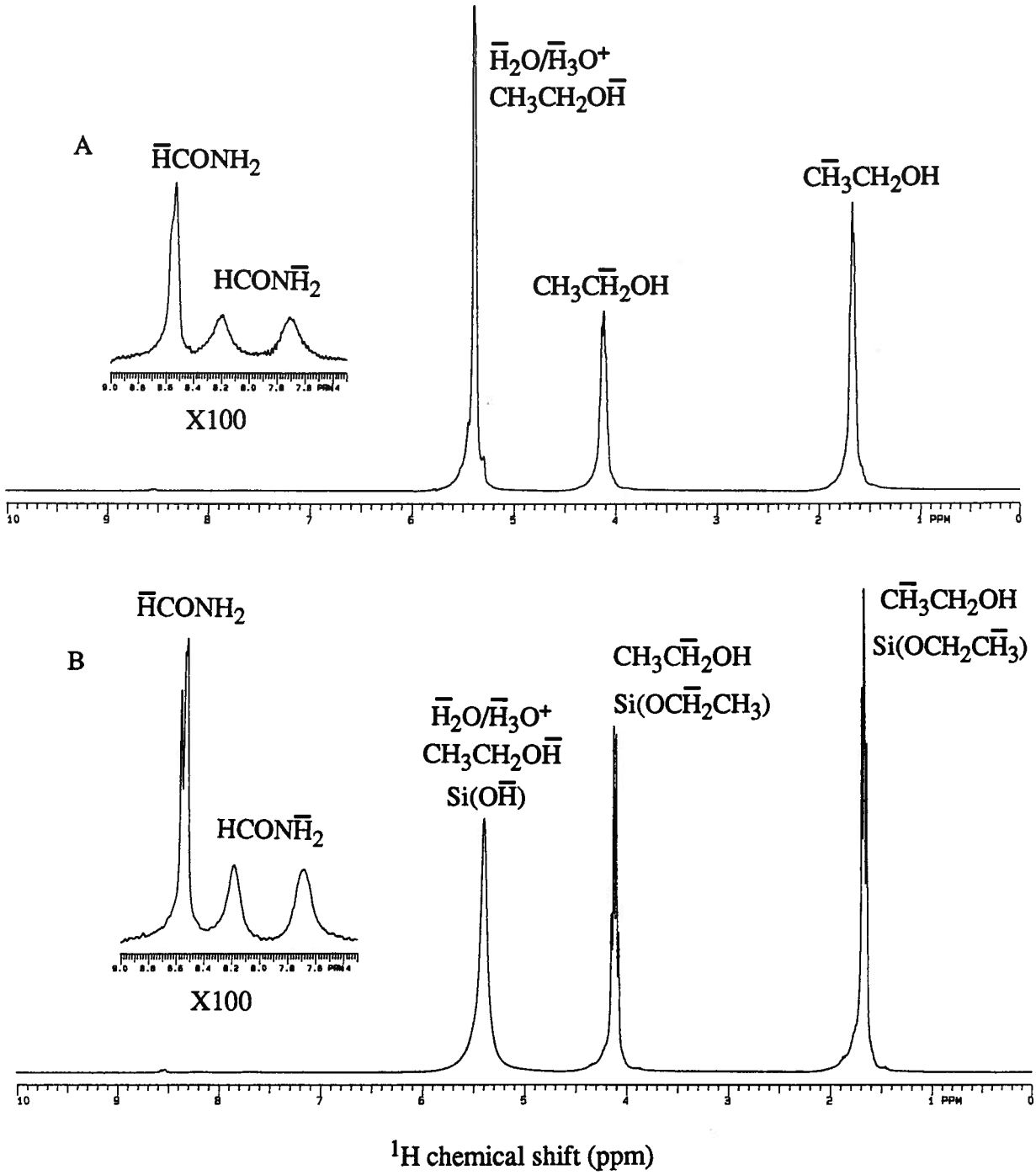

Figure 5.8 - ^1H solution NMR spectra of solutions containing:
A - Formamide/H_2O/Ethanol in the ratios used for the TEOS polymerization reaction
B - Formamide/H_2O/Ethanol/TEOS in the ratios used for the TEOS polymerization reaction. The spectra were acquired with 2000 scans, a 0.1 second recycle delay and 10^o pulse angle.

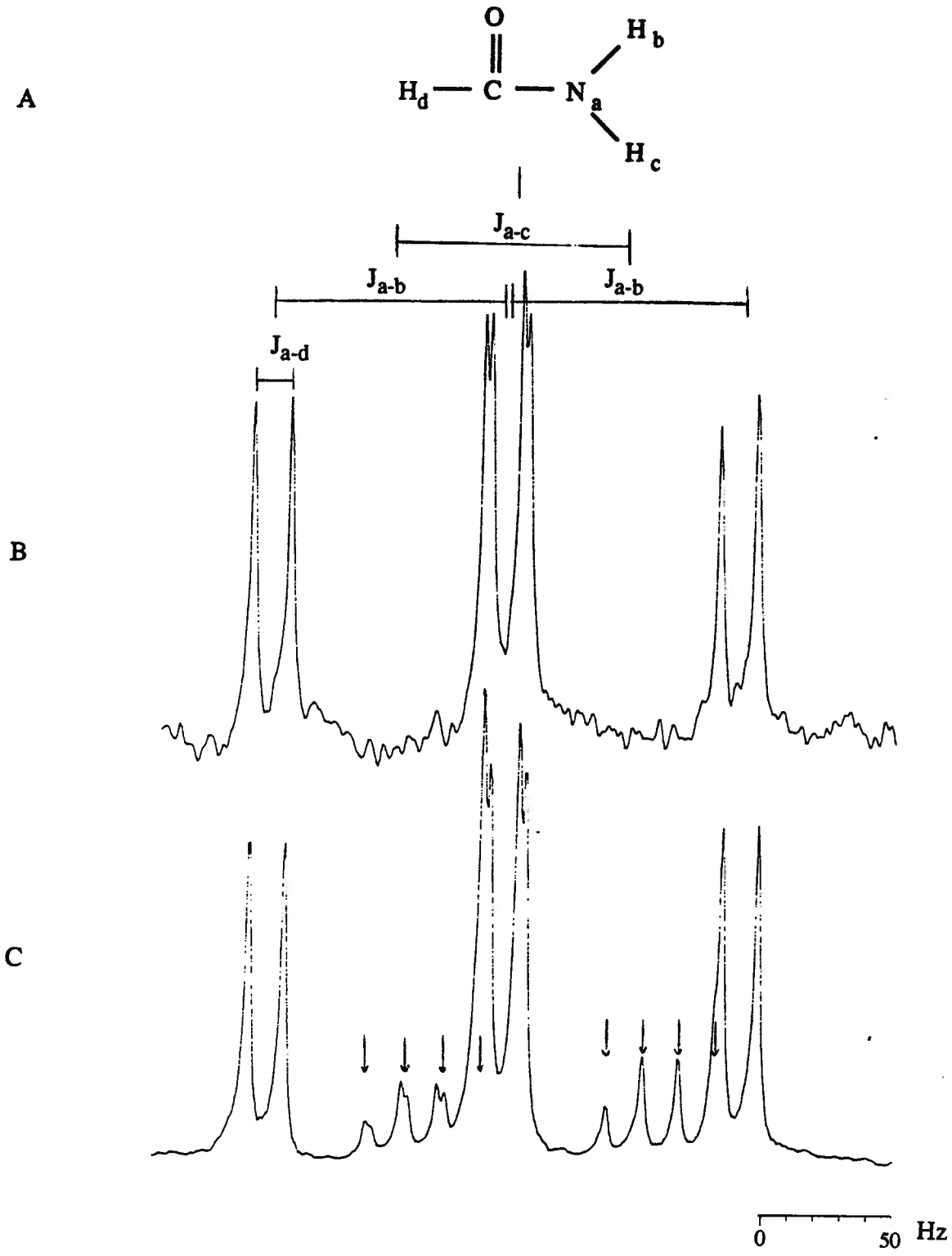

Figure 5.9 A - Formamide molecular structure, labelled according to [5.6]
B - ^{15}N solution NMR spectrum of neat formamide in deuterated acetone
C - ^{15}N solution NMR spectrum of neat formamide in H_2O/D_2O.
The ^{15}N solution NMR spectra were acquired with 2000 scans, a 1 second recycling delay, a 45^{o} pulse angle and no decoupling.

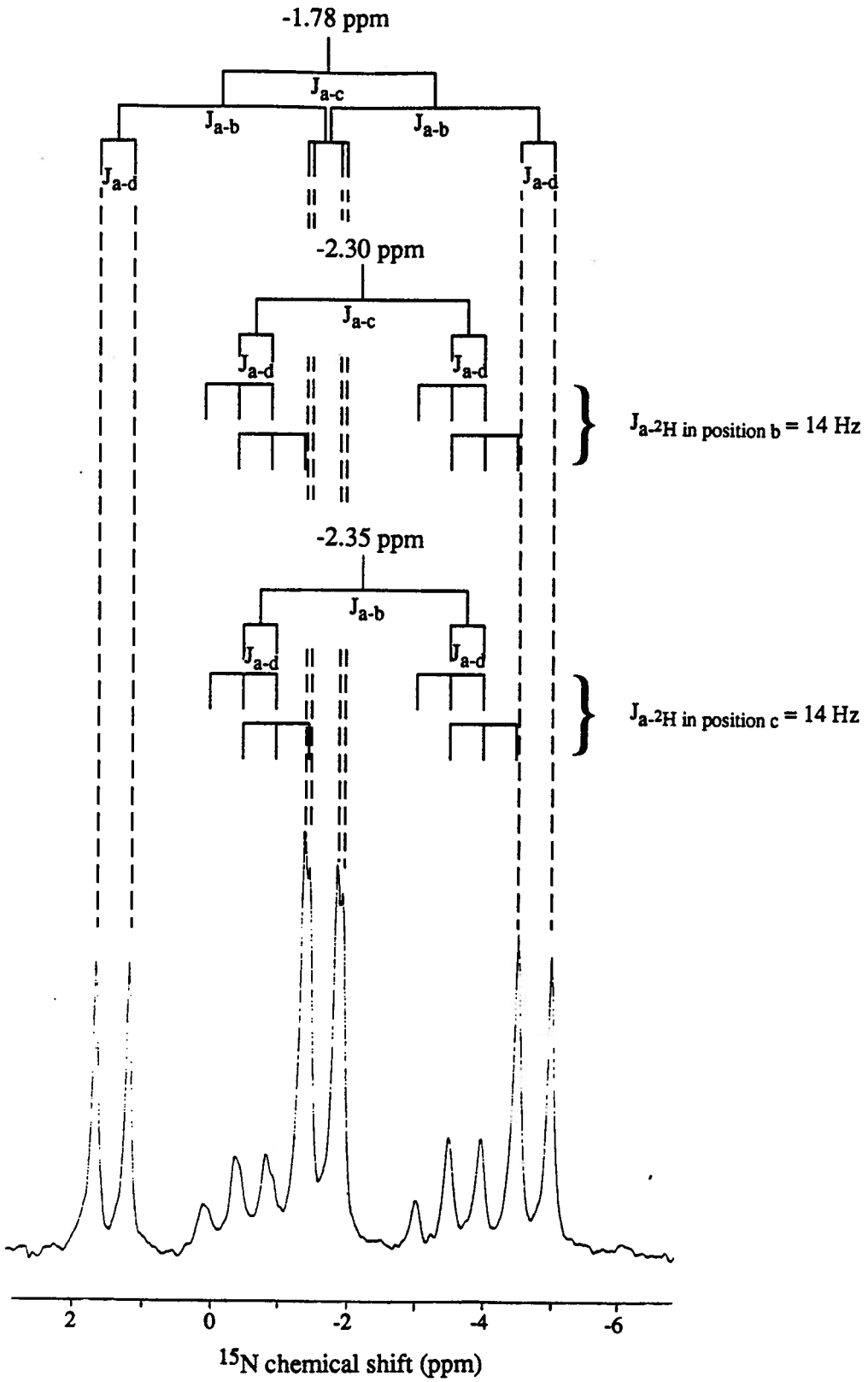

Figure 5.10 - Analysis of the coupling patterns in the ^{15}N NMR spectrum of formamide in the TEOS reaction mixture.

refer to Figure 5.9A) is due to the coupling between ^{15}N and $^{1}H_c$.[5.6] The second doublet J_{a-b} of 88 Hz is due to the coupling between ^{15}N and $^{1}H_b$.[5.6] The third doublet J_{a-d} (14 Hz) is assigned to the coupling between ^{15}N and $^{1}H_d$.[5.6] The presence of two different N-H coupling constants J_{a-b} and J_{a-c} indicates restricted rotation about the C-NH_2 bond.

If the solvent is a mixture of water and deuterated water the ^{15}N solution NMR spectrum of formamide shows additional peaks (arrows), as indicated in Figure 5.9C, which increase in intensity as the D_2O/H_2O ratio is increased. This suggests that the amide hydrogens in formamide exchange with the deuterium in the D_2O and that the additional lines can be interpreted as originating from partially deuterated formamide. The replacement of either H_b or H_c by deuterium does not lead to equivalent structures due to the restricted rotation around the C-N amide bond. Therefore, two additional groups of lines are expected, each showing the coupling pattern of the ^{15}N with two protons and one deuterium. The replacement of a ^{1}H by ^{2}H results in three different ^{15}N chemical environments and hence three different isotopic shifts assigned as; $CHONH_2$ -1.78 ppm, $CHON^1H^2H$ -2.30 ppm and $CHON^2H^1H$ -2.35 ppm. The chemical shifts are referenced with respect to formamide in deuterated acetone. An analysis of the coupling pattern is given in Figure 5.10.

Figure 5.11A shows the ^{15}N spectrum when the TEOS polymerization was initiated. The sample gelled after two days at pH=1.15. Figure 5.11B presents the ^{15}N NMR spectrum of the same sample after 30 days. Even after gelation, and aging for 90 days at room temperature, no significant changes in the ^{15}N NMR spectrum were observed.

The ^{15}N NMR data clearly show that no chemical shifts or intensity changes are observed in the ^{15}N spectra of formamide during the hydrolysis, condensation, gelation and aging of TEOS. It is concluded therefore that the formamide does not form covalent bonds or strong hydrogen bonding interactions via the amide group to either TEOS or to the

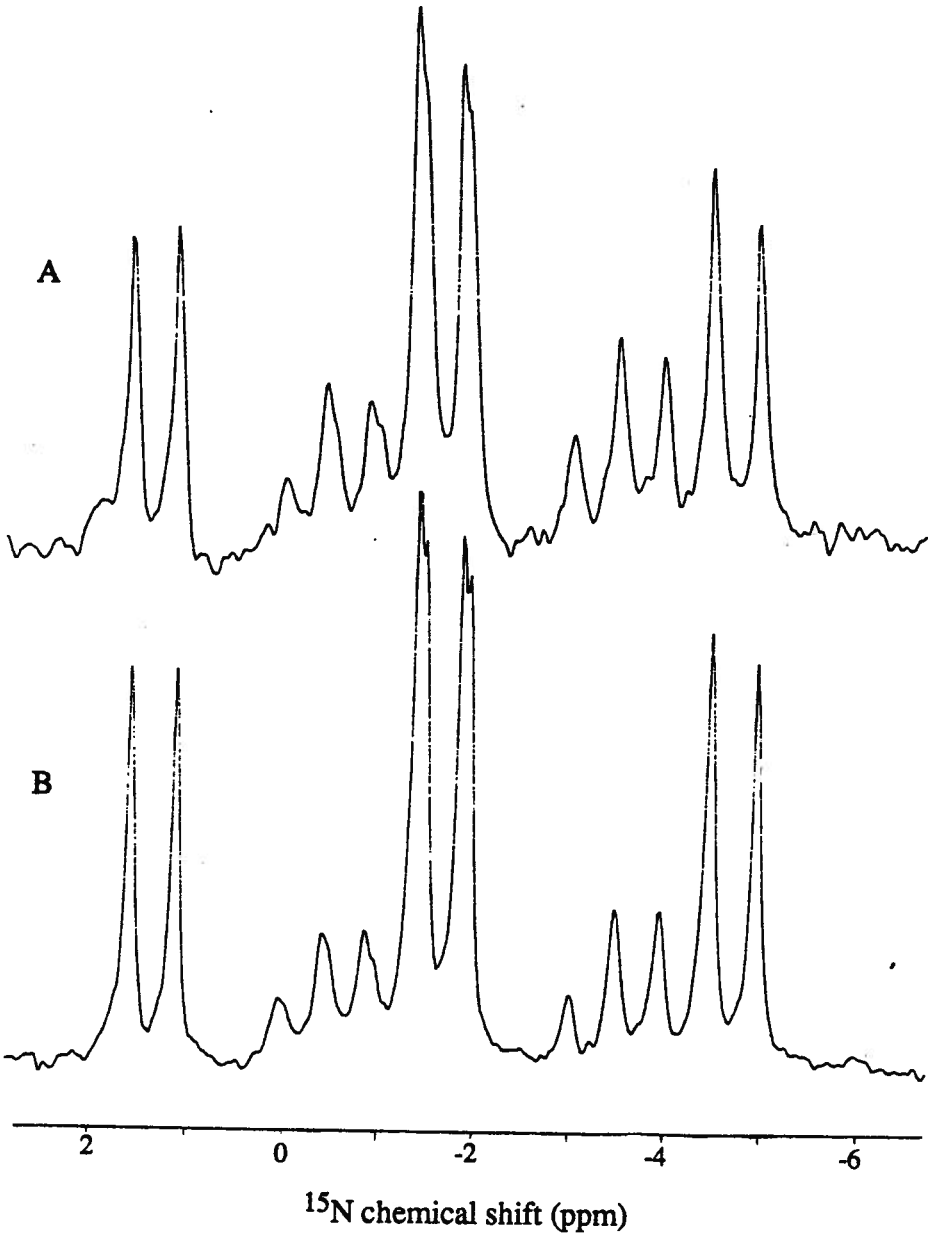

Figure 5.11 - ^{15}N solution NMR spectra of ^{15}N labelled formamide (20 mole %) in a TEOS polymerization mixture. The spectra were acquired at 30.4 MHz with 600 scans, a 1 second recycle delay and a 45^{o} pulse angle,
A - at time zero and
B - after 30 days.

intermediate species formed during the hydrolysis, condensation, gelation and aging of the sample.

5.3.4 High Resolution ^{13}C Solution NMR Investigation

In a similar manner, ^{13}C solution NMR and ^{13}C enriched formamide were used to follow the behaviour of formamide during the reaction. An example of the ^{13}C NMR spectra obtained is shown in Figure 5.12. The sample gelled after 2 days, and the ^{13}C NMR spectrum shown is taken on the third day. The signal at 165 ppm is split into a doublet of 15 Hz due to the carbon-proton coupling. A carbon coupling to the amide protons is not observed. However, if this region is magnified (see insert) two smaller doublets of nearly equal intensity with the same splitting as the main signal are detected. These signals are due to isotope shifts from the exchange of an amide proton by deuterium. In agreement with the ^{15}N NMR spectra, no chemical shifts or intensity changes were observed in the ^{13}C NMR spectra taken over a period of 50 days.

The fact that no change is observed in the ^{13}C solution NMR spectra during the TEOS polymerization process again suggests that formamide does not chemically bond to any species in the reaction mixture, in this case, via the carbonyl functionality.

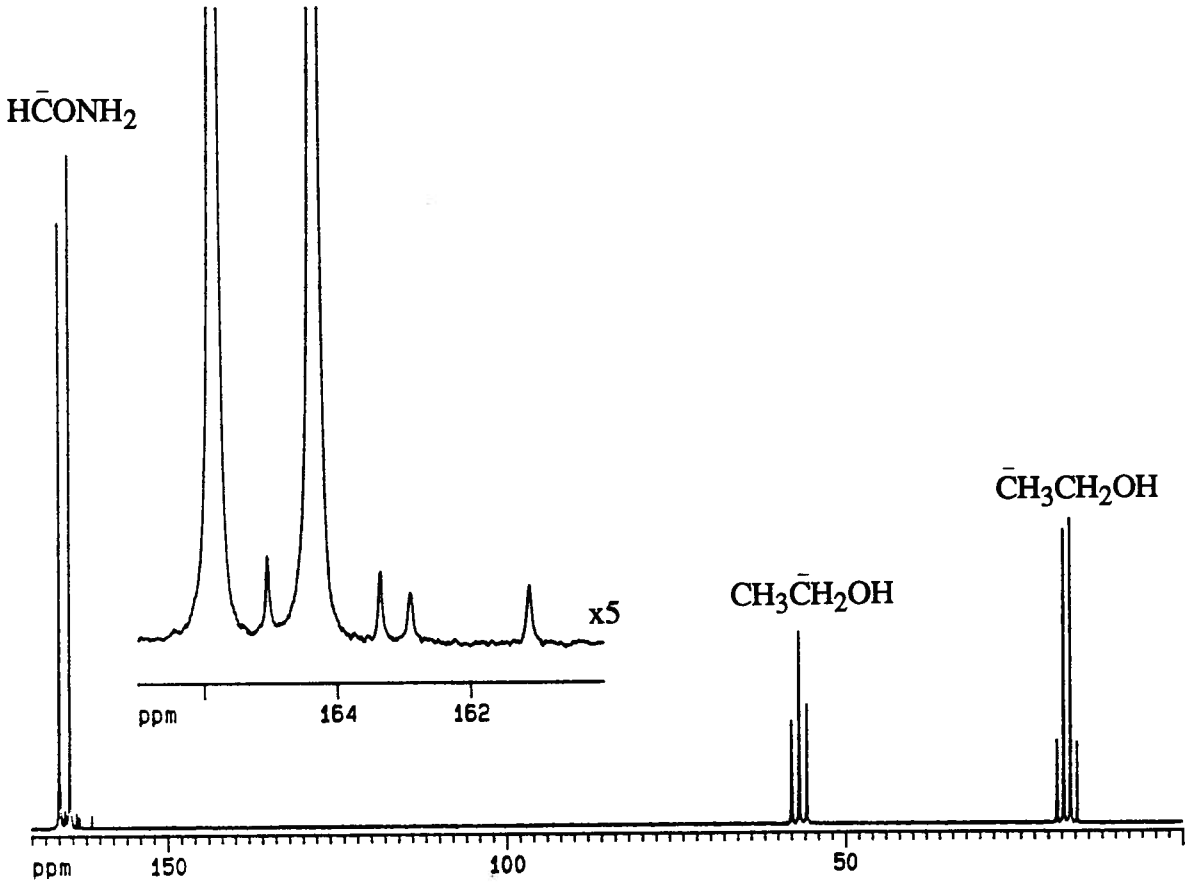

Figure 5.12 - 125.8 MHz ^{1}H coupled ^{13}C solution NMR spectrum of a TEOS polymerization mixture with 20 mole % formamide after three days. The spectrum was acquired with 384 scans, a 5 seconds recycle delay and a 90° pulse angle.

5.4 CONCLUSIONS

The hydrolysis and dimer formation reactions of the TEOS and MTES homopolymers and MTES/TEOS copolymer are affected dramatically by the presence of formamide when the formamide concentration exceeds 10 mole % when excess water is used in the reaction. No significant effect is observed on the hydrolysis and dimer formation reactions when the formamide concentration is below 10 mole %.

In the homopolymerization of TEOS in the presence of formamide, the hydrolysis rates are not significantly affected when formamide concentrations below 10 mole % are used. Yet the greatest reduction in gelation time is acquired when 2.5 mole % formamide is used. This is the first evidence that the decrease in gelation time caused by the presence of formamide is not a consequence of a change in the mechanisms or rates of the hydrolysis and dimer formation reactions.

At formamide concentrations of 20 mole %, the high resolution ^{1}H, ^{13}C and ^{15}N solution NMR study clearly demonstrate that the formamide remains intact during the TEOS polymerization over a period of 90 days with no change in the spectra. Therefore, chemical bonding to the polymer or one of its precursors via either the carbonyl or the amide group can be ruled out.

CHAPTER 6

SOLID STATE NMR AND THERMAL ANALYSIS STUDIES OF THE THERMAL STABILITIES OF FUNCTIONALIZED SILICA GELS PREPARED BY THE COPOLYMERIZATION METHOD

6.1 INTRODUCTION

Glasses are conventionally made by melting powders of crystalline mixed oxides at temperatures greater than 1000°C, followed by undercooling the sample below the glass transition temperature (T_g). The conventional fabrication of glasses thus involves such high temperatures that all organic functionalities decompose.

Glasses could also be manufactured from thermally treated alkoxide derived gels. The advantage of this latter process is that lower temperatures are required to convert the gel into a glass.[6.8] Yamane et al. found that glasses made from silica gel heated to 900°C were identical to glasses made from molten silica in density, refractive index and hardness.[6.4] Fabrication of glasses at temperatures lower than 1000°C from gels raises the possibility of making functionalized low-temperature glasses where the functionality could be distributed within the glass structure. The limit to the synthesis of low-temperature functionalized glasses is the thermal stability of the functionality to be incorporated.

Extensive literature is available on the thermal behaviour of silica gel.[6.4, 6.5, 6.6, 6.9] Yet only one study was found concerning organofunctionalized silanes. Kamiya et al [6.11] investigated the thermal evolution of gels derived from $CH_3Si(OEt)_3$ with IR and thermal analysis techniques. They found that the methyl functionality was stable up to around 700°C under nitrogen while above this temperature they observed the formation of ≡Si-H bonds. In the present work, the thermal stabilities of the organic functionalities in a

number of different functionalized copolymers were measured. The thermal stabilities of the methyl, ethyl, phenyl and phenethyl functionalities were characterized in order to determine what is the weakest point in an organofunctionalized silane/TEOS copolymer. The thermal stabilities were characterized by solid state ^{29}Si, ^{13}C and ^{1}H NMR, differential scanning calorimetry (DSC), thermogravimetric analysis (TGA), and TGA-mass spectroscopy (TG/MS).

DSC experiments measure the power difference needed to keep a zero temperature differential between the sample and a reference sample.[6.1] This experimental technique detects endo- and exothermic processes but is limited to temperatures up to approximately 600°C. The thermogravimetric analysis (TGA) technique will also be used to characterize the samples since it reaches temperatures of up to 1200°C. TGA characterizes thermal decomposition events by measuring weight changes as a function of temperature.[6.1, 6.2] The TG/MS data complement this information and provide insight into the chemical nature of the volatile decomposition products.

6.2 EXPERIMENTAL

6.2.1 Sample Preparation

Seven different copolymers were synthesized using the procedure of the "kinetic preparation" described in Chapter 2. This preparation involves mixing ethanol, the organofunctionalized triethoxysilane and tetraethoxysilane (TEOS) and then slowly adding the acidified water. After the sample gelled it was crushed, washed and dried at 100°C. The different gel compositions are summarized in Table 6.1.

Each sample was divided into 12 small portions of which 10 were individually thermally treated for two hours in a quartz tube furnace at temperatures of either 200, 300, 400, 500 or 600°C, under either nitrogen or air. Nitrogen was used to provide an inert atmosphere during the heating so that degradation due to oxidation could be minimized. Nitrogen (purity 99.9%) was flowed at a constant rate through the sample before heating, in order to expel any remaining air, and during the actual heating. One untreated portion of the sample was used as a reference for all the NMR studies and another untreated portion was used for the TGA, DSC and TG/MS measurements.

6.2.2 Solid State NMR Experiments

All the NMR spectra were acquired at room temperature. The ^{29}Si CP/MAS NMR spectra were acquired on a Bruker MSL 400 spectrometer using a Bruker double tuned MAS probe with a 7 mm ceramic spinner. The ^{29}Si MAS NMR spectra were acquired on a Bruker AM 400 spectrometer using a home built single tuned probe with a 9 mm vespel spinner. Quantitative ^{29}Si MAS NMR spectra were acquired using a recycle delay of 180 seconds ($3*T_1$) and a 45° pulse angle. The ^{13}C CP/MAS NMR spectra were acquired on either a Bruker MSL 400 or a CXP 100 spectrometer using a double tuned MAS probe with a 7 mm ceramic spinner. The ^{1}H MAS NMR spectra were acquired on a Bruker MSL 400

Table 6.1 - Sample compositions used in the thermal analysis investigations.

SAMPLE	R-Si(OEt)$_3$ (moles)	Si(OEt)$_4$ (moles)	Ethanol (moles)	Water* (moles)
TEOS	0	1.791	1.0343	1.98
25/75 MTES/TEOS	0.0448 R = CH_3	0.1340	1.0343	1.98
50/50 MTES/TEOS	0.0895 R = CH_3	0.0897	1.0343	1.98
25/75 ETES/TEOS	0.0448 R = CH_2CH_3	0.1340	1.0343	1.98
50/50 ETES/TEOS	0.0896 R = CH_2CH_3	0.0897	1.0343	1.98
25/75 PTES/TEOS	0.0448 R = C_6H_5	0.1340	1.0343	1.98
25/75 PETES/TEOS	0.0448 R=$C_6H_5CH_2CH_2$	0.1340	1.0343	1.98

TEOS = tetraethoxysilane
MTES = methyltriethoxysilane
ETES = ethyltriethoxysilane
PTES = phenyltriethoxysilane
PETES= phenethyltriethoxysilane

*The water was acidified to pH=1.15 with HCl.

spectrometer. The experimental conditions for the different spectra are given in the appropriate figure captions. The ^{29}Si, ^{13}C and ^{1}H chemical shifts are all referenced to the appropriate resonances of TMS.

6.2.3 DSC and TGA Measurements

The thermal analyses (TGA and DSC) were carried out using a TA Instruments Thermal Analyst 2000 system. Both the DSC and TGA studies were carried out under nitrogen gas (purity 99.9%) unless otherwise indicated. During the DSC experiments a nitrogen flow rate of 40 cc/min and a temperature increase of 10 °C/min were maintained. The sample size for the DSC studies was kept under 10 mg. For the TGA experiments, a nitrogen flow rate of 50 cc/min and a temperature increase of 10°C/min were used. The sample size for the TGA studies was kept between 10 and 20 mg. All the samples were ground to fine powders with a mortar and pestle.

Independent TG/MS measurements on all the copolymers and pure silica gel were carried out by Dr. K. MacKenzie at the New Zealand Institute for Industrial Research and Development. For these experiments, a Stanton Redcroft TG770 Thermobalance connected to a quadrupole mass spectrometer (Extranuclear Laboratories Inc.) was used. The partial pressure of each species in the TG/MS graphs given is the fraction of the total vacuum in the spectrometer which is contributed by that species. It is related to the ion current for each species by an instrumental calibration factor which pertains to the conditions inside the mass spectrometer. The calibration factor was determined by the manufacturer. All of the TG/MS experiments were run under similar conditions, i.e. roughly the same amount of sample, flow rate, etc. Consequently, the results for any fragment mass number of one sample can be reasonably compared to those of another.

6.3 RESULTS AND DISCUSSION

In a TGA experiment, the temperature ranges observed for different processes are partly dependent on operational and instrumental factors. For example, some of the observed discrepancies in the temperature ranges of thermal events may be accounted for by the sample particle size which would affect the transfer of heat and the diffusion of volatile compounds, such as water through the sample.

6.3.1 Tetraethoxysilane (TEOS) Homopolymer - Pure Silica Gel

The DSC and TGA data for silica gel are useful as references for the DSC and TGA results on the different functionalized silica gels. The silica gel DSC thermal analysis curve, Figure 6.1A, shows two endothermic processes: one occurs over a temperature range of approximately 100°C centered around 140°C, and another throughout the whole temperature range studied (20°C to 600°C) since the signal never reaches a clear plateau.

The TGA thermal analysis curve for silica gel is shown in Figure 6.1B and confirms the above observations. In the temperature range of 45°C to 172°C there is a weight loss of 14%. This is followed by a further weight loss of 6% between 200°C and 1000°C. A plateau corresponding to a constant chemical composition, is not reached below 1000°C.

In order to further characterize these thermal events the TGA exhaust was fed into a mass spectrometer (work done by Dr. K. MacKenzie). These data are shown in Figure 6.2. Hydroxyl groups (fragment mass number 17) are detected throughout the temperature range as shown by the slow but linear rise in the partial pressure, indicative of the removal of hydroxyl groups and water from the surface. The initial detection of hydroxyl groups corresponds to the first endothermic thermal event around 140°C in the DSC, and to the initial thermal event in the TGA resulting in a mass loss of 14%. The initial loss of water is probably due to the loss of physisorbed water molecules. This is followed by the elimination

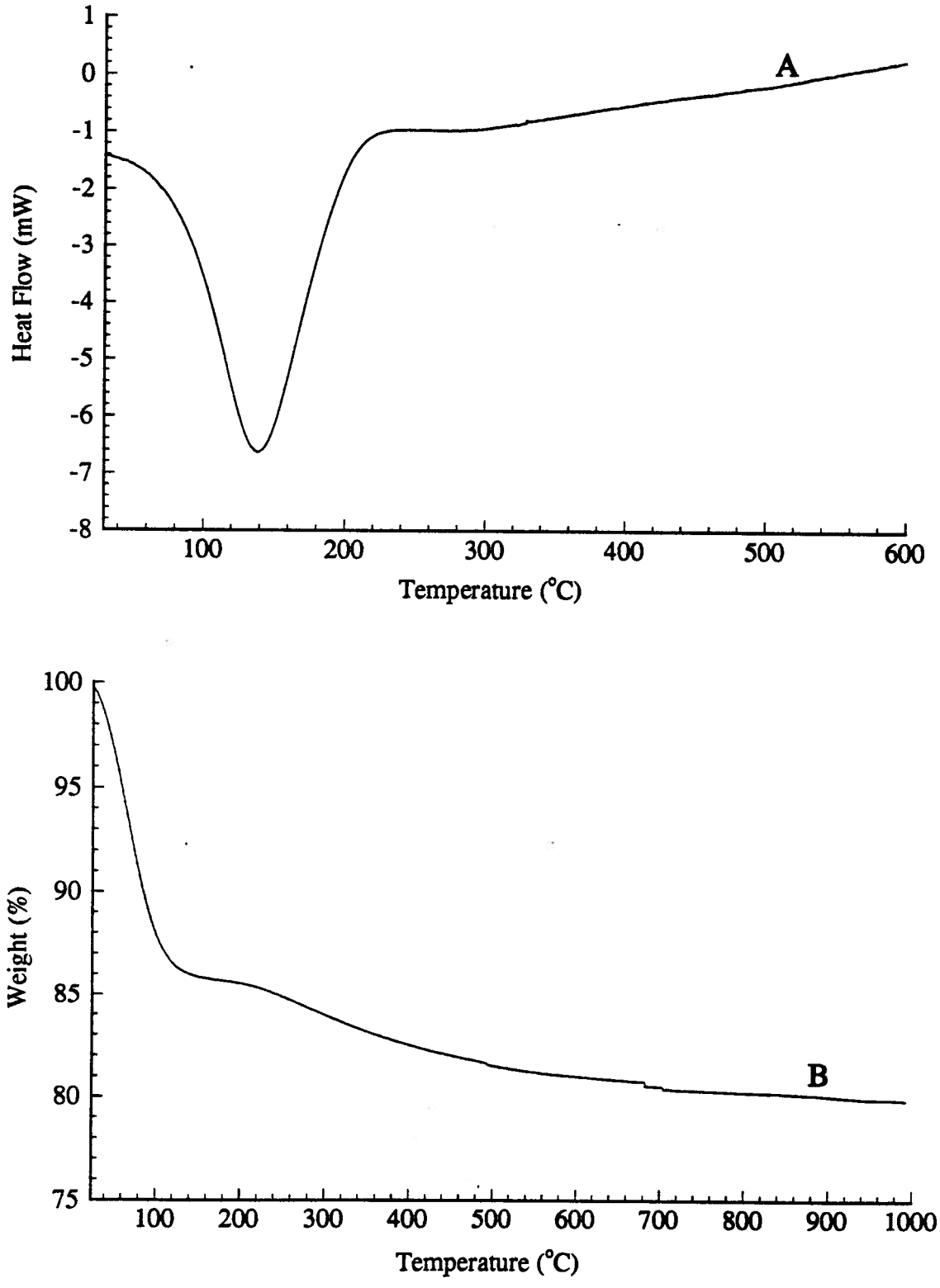

Figure 6.1 - (A) DSC and (B) TGA analysis curves for silica gel obtained under nitrogen.

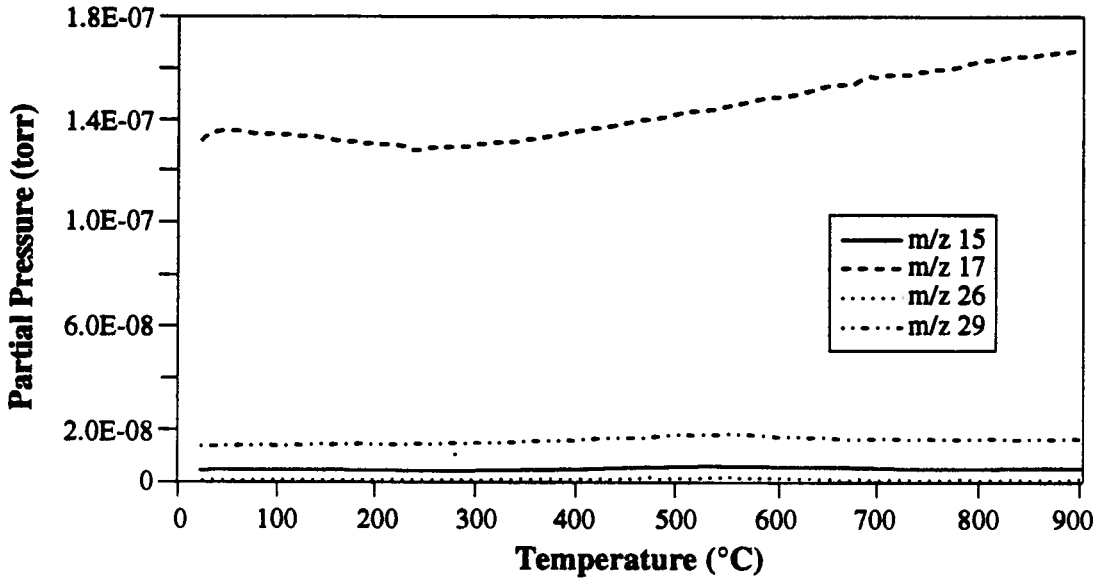

Figure 6.2 - TG/MS data for the silica gel sample with the identifying mass number for each curve.

of water presumably produced by the condensation of neighbouring hydroxyl groups to form siloxane bonds. Smaller concentrations of fragments with mass numbers such as 26 (C_2H_2), 28 (C_2H_4) and 29 (C_2H_5) are observed due the elimination and degradation of residual ethoxy groups on the surface. The curve for mass number 28 is not taken into account because here the major contribution is not from ethoxy fragments but from the carrier N_2 gas. The elimination of ethoxy and hydroxy groups via surface condensation are not resolved as discrete events in the TGA and DSC thermal analysis curves but are presumably responsible for the absence of a plateau in both data sets.

Previous studies [6.9] on the hydration/dehydration characteristics of silica gel suggest that the dehydration of silica gel occurs in three steps: 1) the physisorbed water is eliminated (25 to 170°C), 2) surface silanol groups start to condense (above 170°C), 3) the dehydration process becomes irreversible above 400°C so that above 800°C only isolated silanol groups remain.[6.6, 6.9] The present thermal data are in excellent agreement with these conclusions.

Boonstra and Mulder observed that their silica gel samples which were made by a two-step reaction process turned blackish-grey when heated to 400°C in air.[6.5] They suggested that this was due to the pyrolysis of remaining ethoxy ligands on the surface. The samples of silica gel used in the present work all remained white powders, even when heated to 1000°C suggesting that very few alkoxy ligands remained on the surface with this preparation in agreement with the TG/MS data.

6.3.2 Methyltriethoxysilane (MTES)/TEOS Copolymer

A typical ^{29}Si CP/MAS NMR spectrum for the methyltriethoxysilane/ tetraethoxysilane (MTES/TEOS) copolymer is shown in Figure 6.3D. As described in Chapter 2, the downfield peaks are due to silicons with directly attached organic functionalities, while the group of upfield peaks originate from the unfunctionalized silicons. An overview of the ^{29}Si NMR

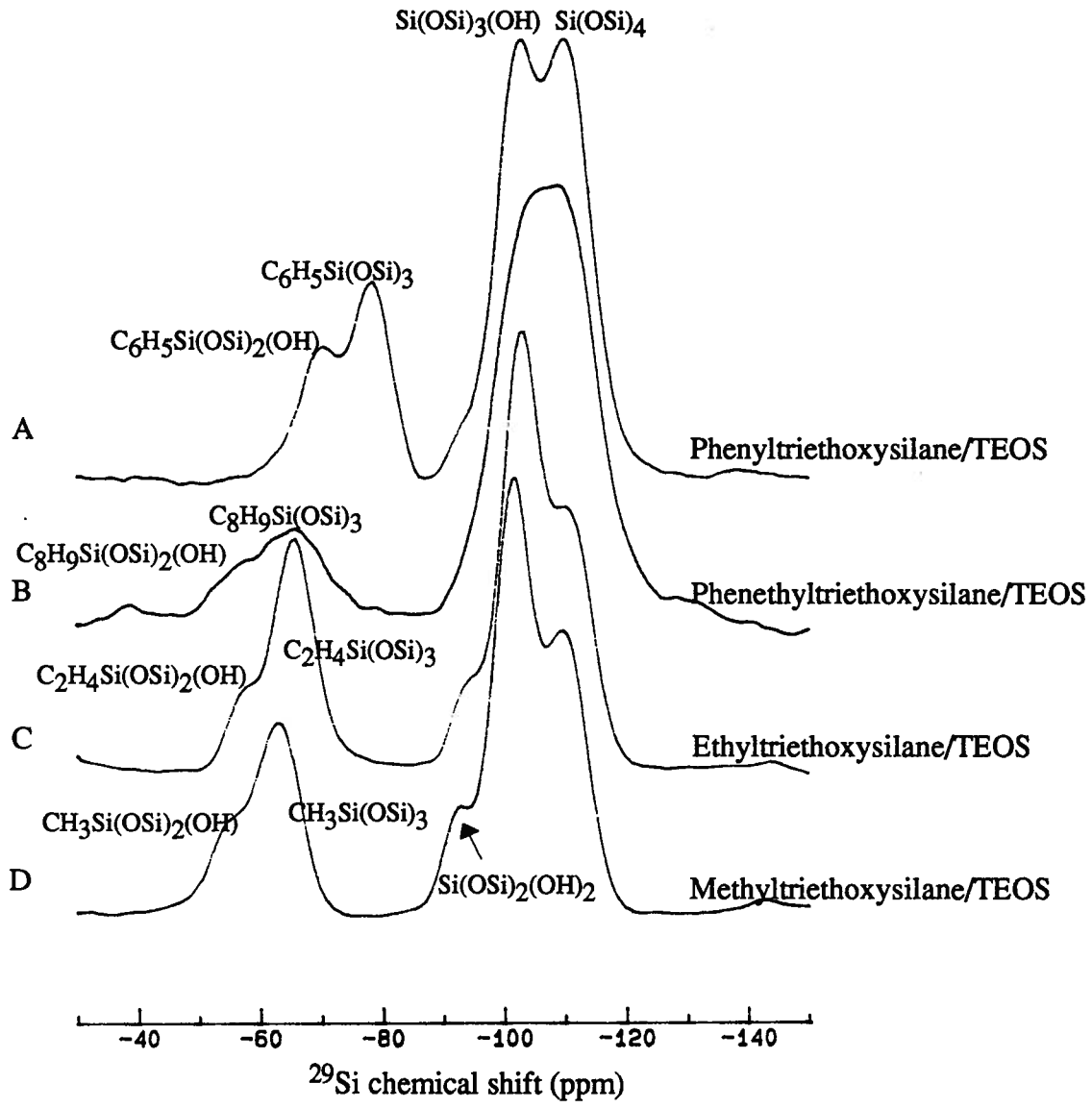

Figure 6.3 - ^{29}Si solid state MAS NMR spectra for the four 25/75 organofunctionalized copolymers investigated. The different silicon chemical shifts are summarized in Table 6.2.

chemical shifts for the different copolymers studied is given in Figure 6.3 and Table 6.2.

Table 6.2 - Observed ^{29}Si chemical shifts for the different copolymers shown in Figure 6.3 together with their assignments.

$CH_3\text{-}\overline{Si}(OH)(OSi)_2$	-60 ppm	$C_6H_5CH_2CH_2\text{-}\overline{Si}(OH)(OSi)_2$	-58 ppm
$CH_3\text{-}\overline{Si}(OSi)_3$	-64 ppm	$C_6H_5CH_2CH_2\text{-}\overline{Si}(OSi)_3$	-66 ppm
$CH_3CH_2\text{-}\overline{Si}(OH)(OSi)_2$	-58 ppm	$\overline{Si}(OH)_2(OSi)_2$	-93 ppm
$CH_3CH_2\text{-}\overline{Si}(OSi)_3$	-65 ppm	$\overline{Si}(OH)(OSi)_3$	-102 ppm
		$\overline{Si}(OSi)_4$	-110 ppm
$C_6H_5\text{-}\overline{Si}(OH)(OSi)_2$	-70 ppm		
$C_6H_5\text{-}\overline{Si}(OSi)_3$	-78 ppm		

The ^{29}Si CP/MAS NMR spectra for the series MTES/TEOS copolymer samples thermally treated for two hours in either air or nitrogen at the temperatures indicated, are shown in Figure 6.4. A comparison of the two series of spectra clearly shows that the methyl functionality is stable to higher temperatures (600°C vs. 300°C) when the MTES/TEOS copolymer is heated under nitrogen rather than air.

The broadening of the ^{29}Si CP/MAS NMR lines indicates that structural changes occur as the temperature increases (Figure 6.4). These could be due to a number of reactions such as: 1) loss of water, 2) elimination of metastable three-membered rings, 3) condensation of adjacent hydroxyls and ethoxy ligands, 4) the loss of organic groups, and/or 5) relaxation of the SiO_2 framework.[6.5, 6.9] The elimination of the hydroxy and ethoxy ligands on the

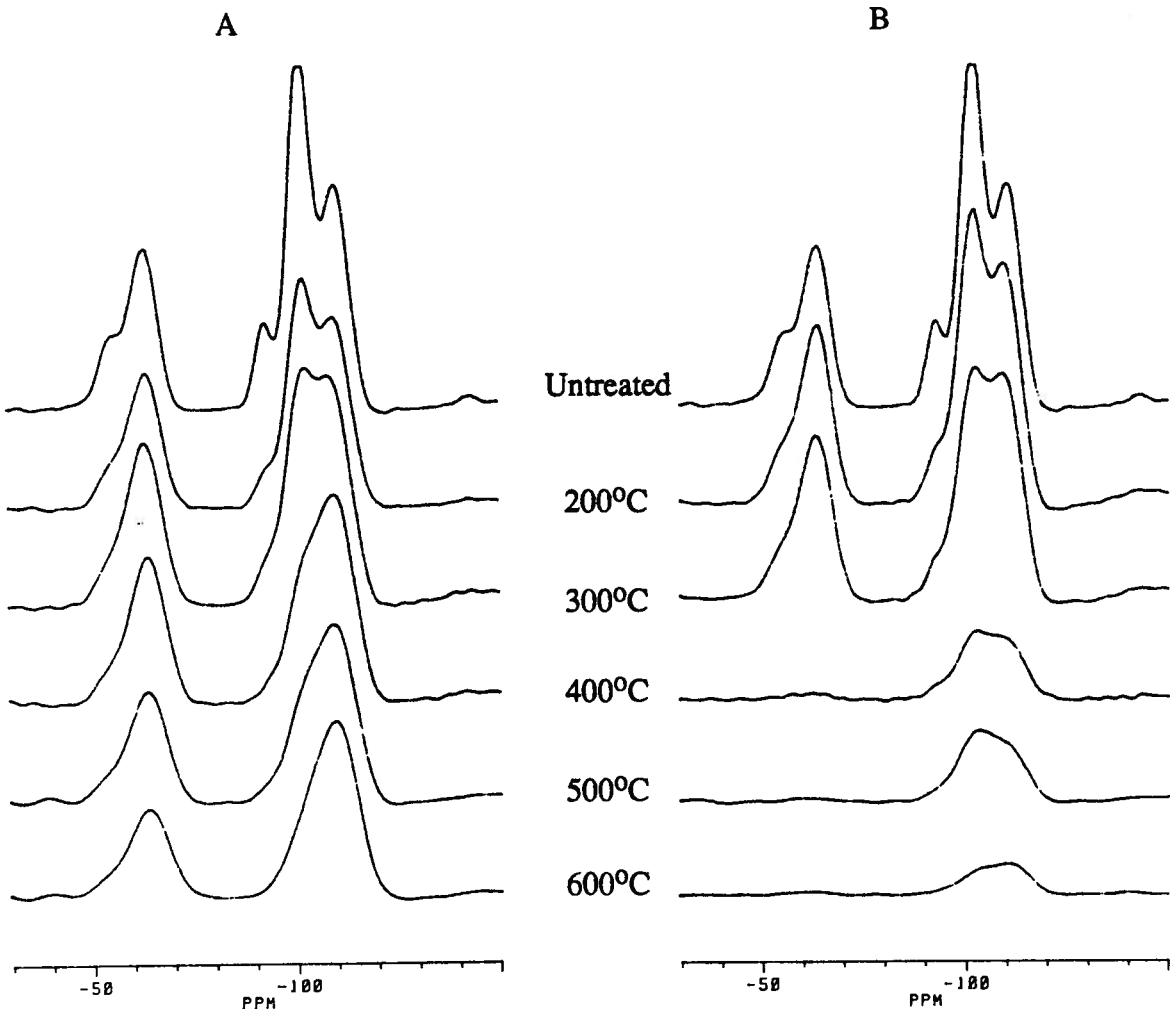

Figure 6.4 - Room temperature 79.5 MHz ^{29}Si CP/MAS NMR spectra of the 25/75 MTES/TEOS copolymer sample heated for two hours at the temperatures indicated. These spectra were obtained with 400 scans, 10ms contact time, 4s recycle delay and 3.2 kHz sample spinning rate. Two series of experiments were performed, the spectra acquired for those samples thermally treated under nitrogen are shown in series A and the spectra for those samples thermally treated in air are shown in series B.

surface of the silica gel, as a consequence of thermal treatment forms distorted Si-O-Si bond angles and changes in siloxane lengths.[6.3, 6.6] This results in a larger distribution of bond angles and lengths, i.e. silicon environments, increasing the width of the ^{29}Si NMR resonances. In general, the elimination of the ^{1}H polarization source, i.e. the removal of hydroxyl groups and the oxidation of methyl groups, as the temperature increases, results in weaker ^{29}Si CP/MAS signals (Figure 6.4).

The ^{13}C CP/MAS NMR spectra of the same samples, Figure 6.5, confirm that the majority of the methyl groups are intact at 600°C when the sample is thermally treated under nitrogen but are oxidized when thermally treated in air above 300°C. These results are in agreement with Kamiya et al.[6.11]

The ^{1}H MAS NMR spectra presented in Figure 6.6 show that the methyl group is oxidized in air at approximately 300°C; however, even for the sample heated at 600°C a significant concentration of hydroxyl groups remain on the sample surface at least after cooling and running the spectra at room temperature. In contrast, the spectra of the samples thermally treated under nitrogen at 600°C, Figure 6.6A, show a methyl signal but no hydroxyl resonance. This might be due to the more hydrophobic nature of the sample. The 2D ^{1}H-^{29}Si heteronuclear correlation NMR spectrum shown in Figure 6.7 confirms that the only cross polarization source in this sample is the methyl protons. This sample will be further investigated in Chapter 7.

Quantitative ^{29}Si NMR spectra were acquired for the untreated sample and the sample thermally treated at 600°C for two hours. The samples were calculated to have a composition of 24% and 17% functionalized silicons, respectively, confirming the good stability of the methyl functionality under nitrogen at temperatures up to 600°C. The small loss of methyl groups may be due to oxidation by oxygen impurity (about 0.1%) in the nitrogen gas over the

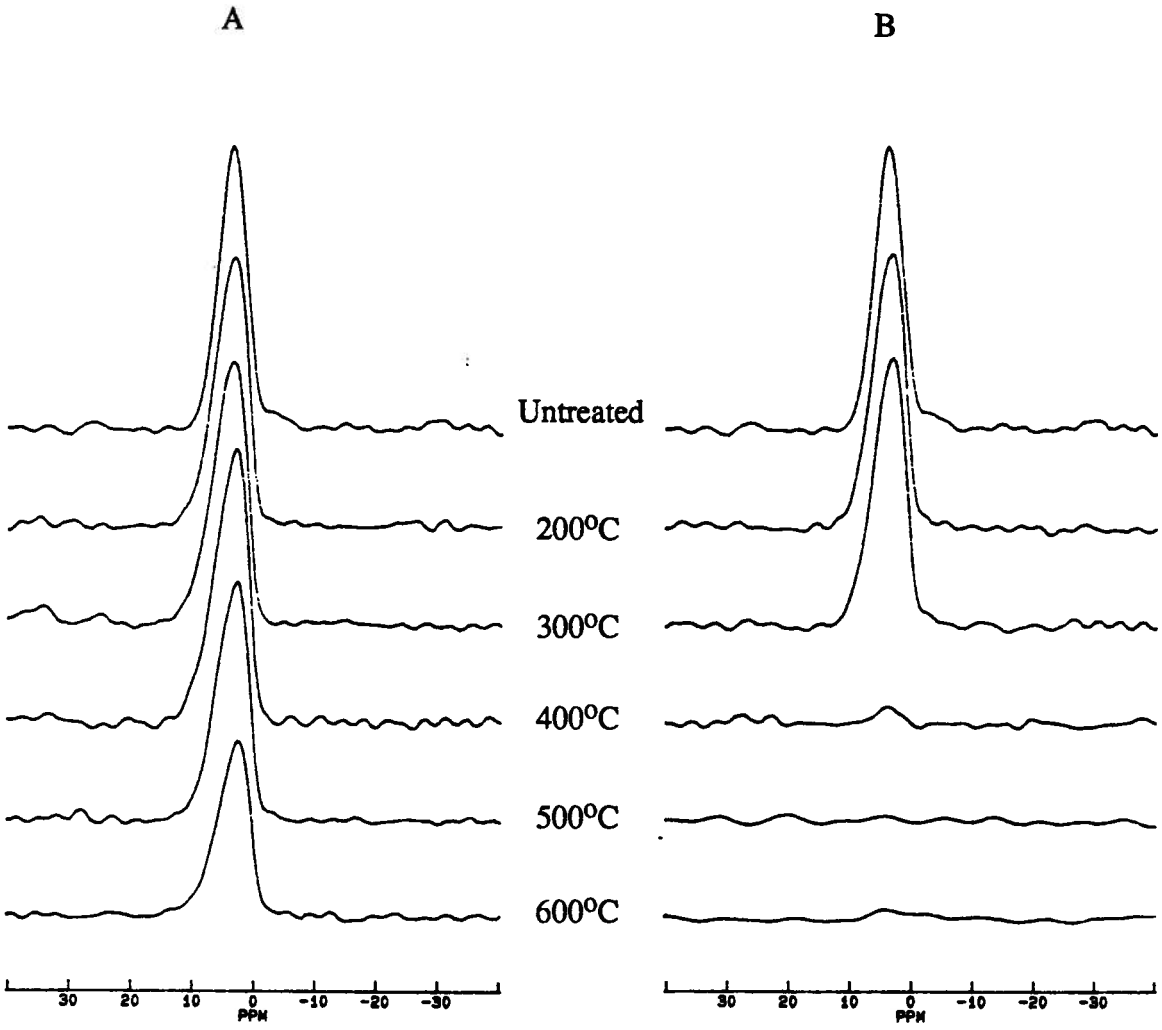

Figure 6.5 - Room temperature 100.6 MHz ^{13}C CP/MAS NMR spectra of the 25/75 MTES/TEOS copolymer sample heated for two hours at the temperatures indicated. These spectra were obtained with 296 scans, 5ms contact time, 4s recycle delay and 3.2 kHz sample spinning rate. Two series of experiments were performed, the spectra acquired for those samples thermally treated under nitrogen are shown in series A and the spectra for those samples thermally treated in air are shown in series B.

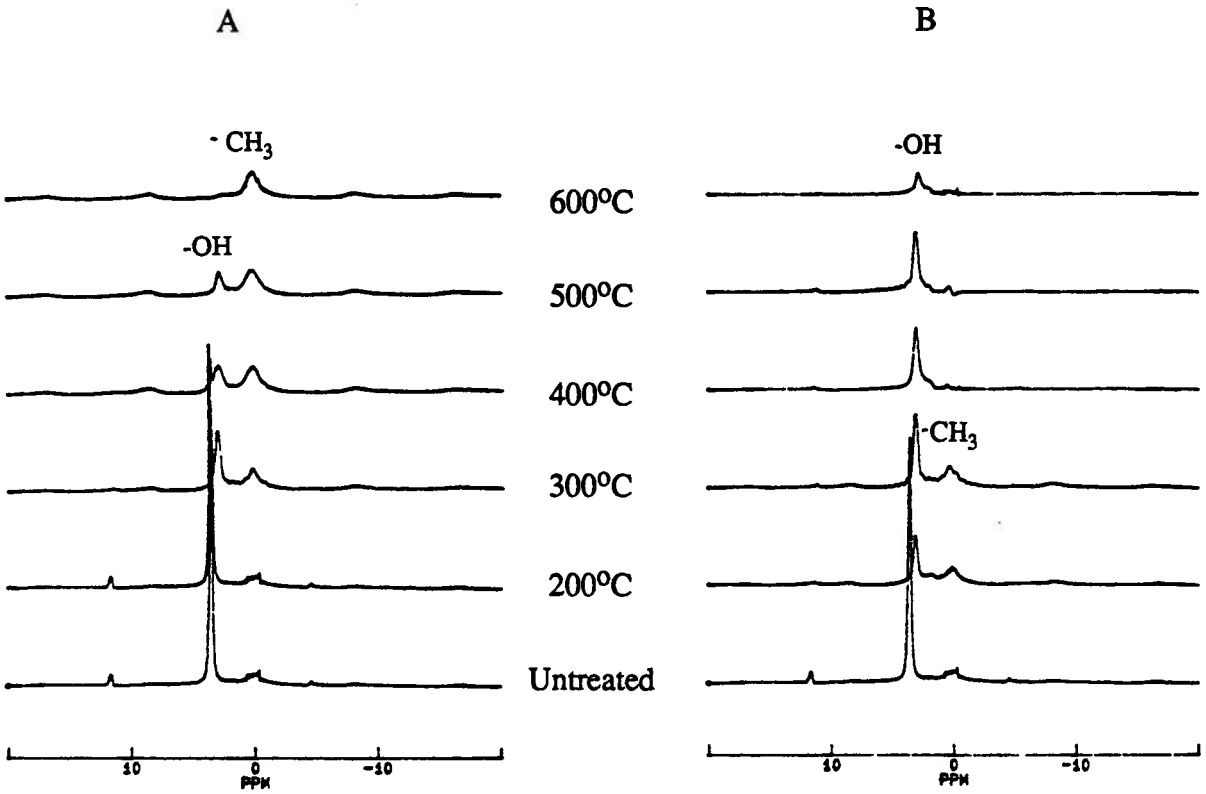

Figure 6.6 - Room temperature 400.1 MHz ^{1}H MAS NMR spectra of the 25/75 MTES/TEOS copolymer sample heated for two hours at the temperatures indicated. These spectra were obtained with 4 scans, 4s recycle delay, a 90° pulse and 3.2 kHz sample spinning rate. Two series of experiments were performed; the spectra acquired for those samples thermally treated under nitrogen are shown in series A and the spectra for those samples thermally treated in air are shown in series B.

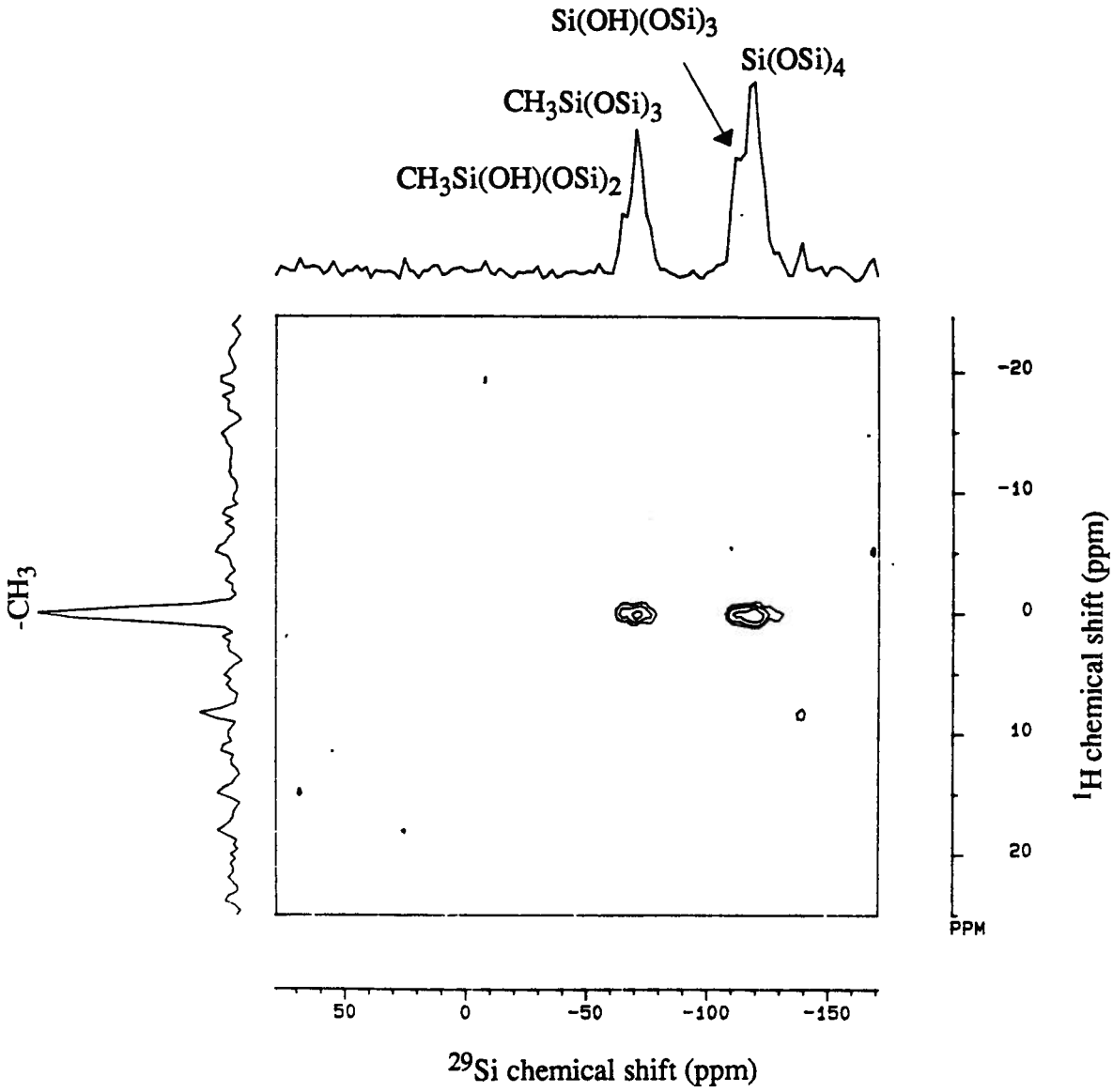

Figure 6.7 - 2D $^{1}H/^{29}Si$ heteronuclear correlation contour plot of the thermally treated 25/75 MTES/TEOS copolymer. The spectrum consists of 64 experiments. Each experiment was acquired with 320 scans, a 10 millisecond contact time, a 3 second recycle delay and a 4 kHz spinning speed.

two hour heating period. A similar study was carried out on a 50/50 MTES/TEOS copolymer. The series of ^{29}Si and ^{13}C CP/MAS NMR spectra for these samples heated under nitrogen and air indicate that the thermal stability is the same as that of the 25/75 MTES/TEOS copolymer.

The DSC and TGA thermal analysis curves for the 50/50 MTES/TEOS copolymer and the unfunctionalized silica gel are shown in Figures 6.8 and 6.9, respectively. The general form of the DSC curve under nitrogen for the MTES/TEOS copolymer is similar to that of the unfunctionalized silica gel, Figure 6.8. This implies that no endo- or exothermic process corresponding to a decomposition of the methyl groups is detected up to 600°C. The slight shift of the temperature range where the physisorbed water is released may be explained by the difference in macroscopic structure due to the presence of the methyl groups in the MTES/TEOS copolymer and the less hydrophilic nature of this system. Both the DSC and NMR data indicate that the methyl functionality in the MTES/TEOS copolymer is stable up to 600°C, when thermally treated under nitrogen .

The first inflection in the TGA curves shown in Figure 6.9 (20°C to 175°C) is due to the loss of physisorbed water. The TGA for the MTES/TEOS copolymer suggests that the loss of hydroxyl and remaining ethoxy groups overlaps with the decomposition of the methyl groups in the temperature range above 600°C.

A comparison of the fragment mass number 15 curve for silica gel (Figure 6.2) and the MTES/TEOS copolymer (Figure 6.10) in the TG/MS data clearly shows a rise above 600°C indicating the decomposition of the methyl functionality in the MTES/TEOS copolymer. The curves for mass numbers 26 and 29 for the MTES/TEOS copolymer show no significant variation suggesting that the ethoxy ligand concentration is negligible, as in the case of silica gel. The mass number 17 is indicative of the elimination of hydroxyl groups.

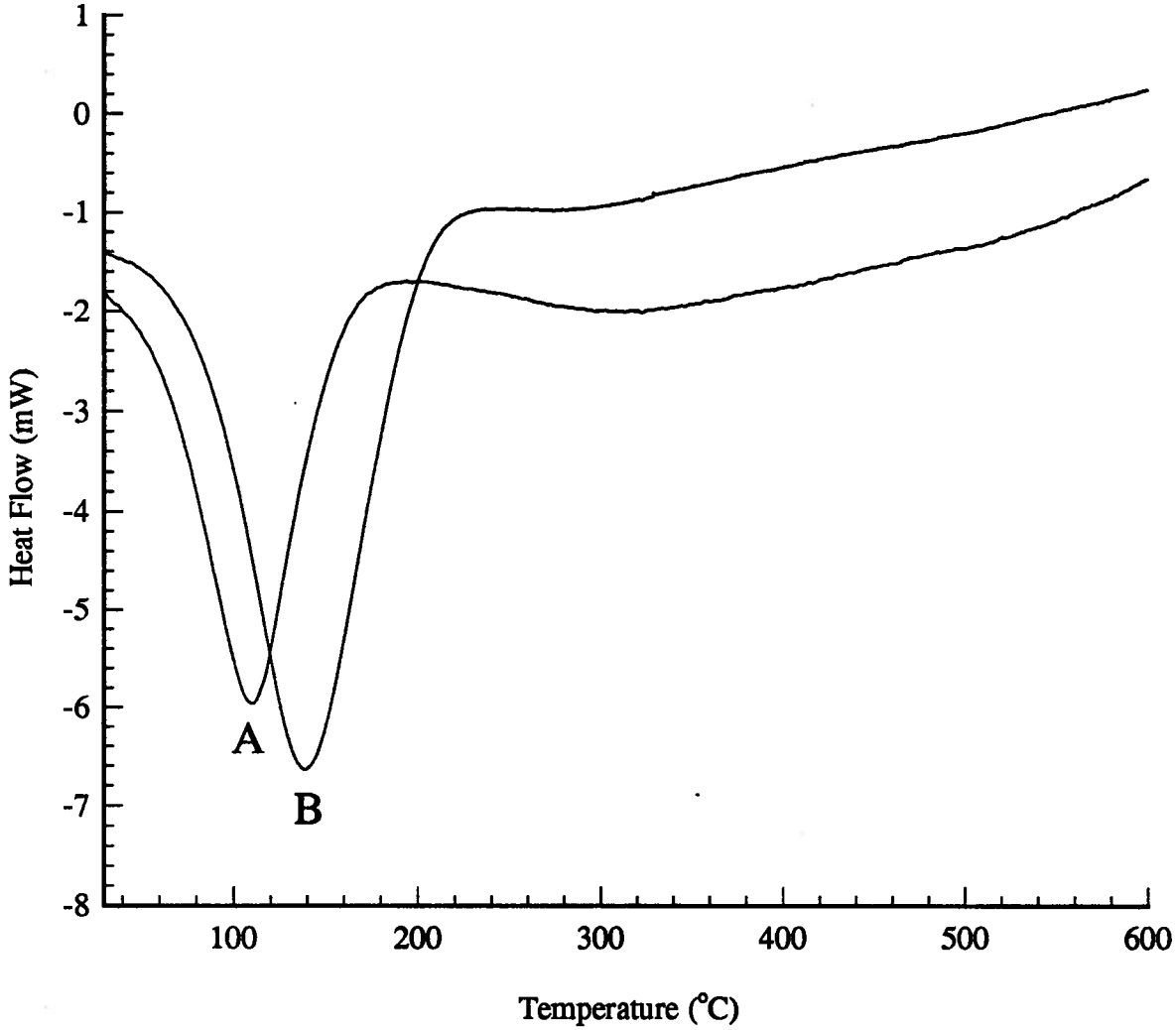

Figure 6.8 - DSC thermal analysis curves obtained under nitrogen for
A - 50/50 MTES/TEOS copolymer and
B - silica gel

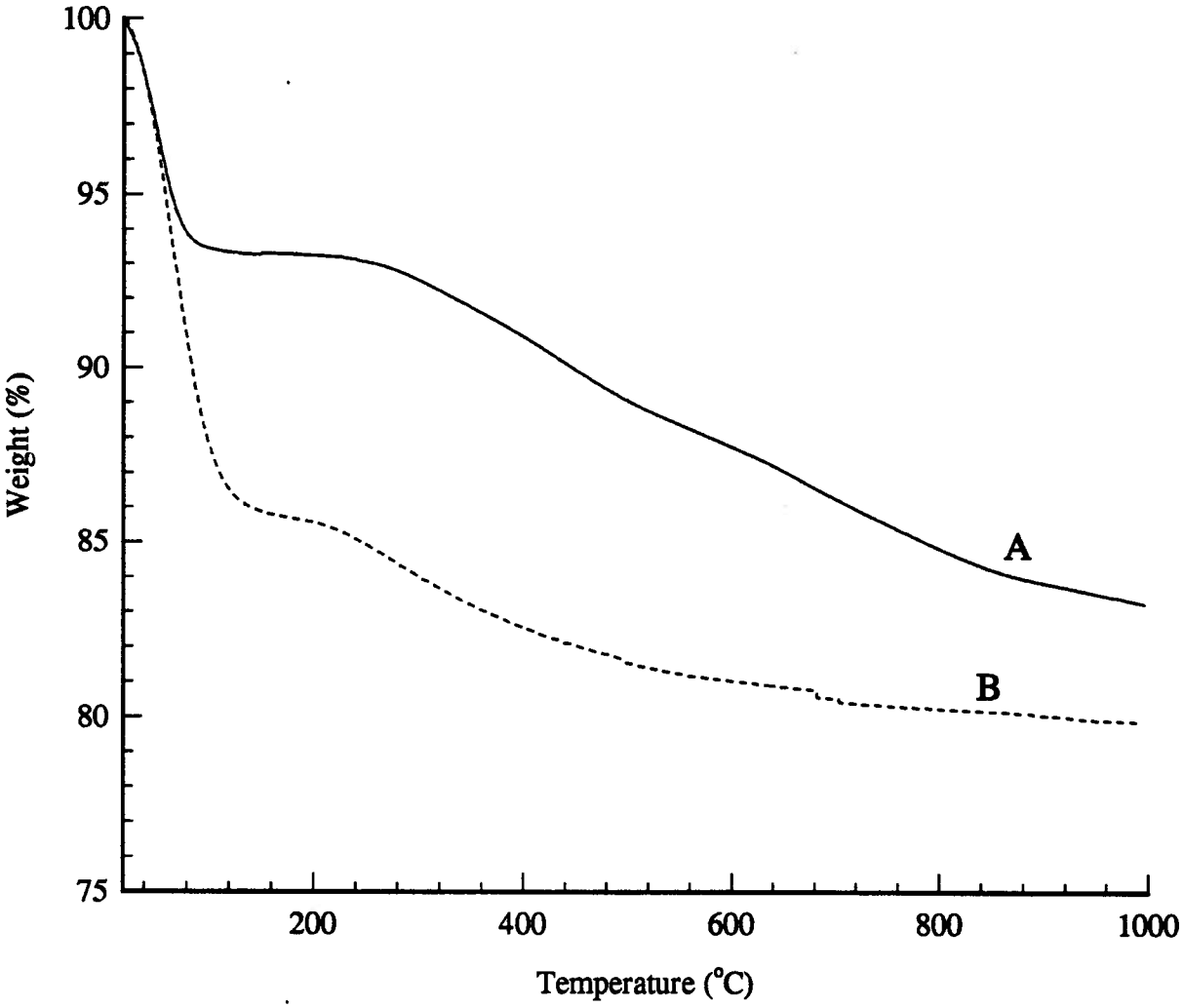

Figure 6.9 - TGA thermal analysis curves obtained under nitrogen for
A - 50/50 MTES/TEOS copolymer and
B - silica gel

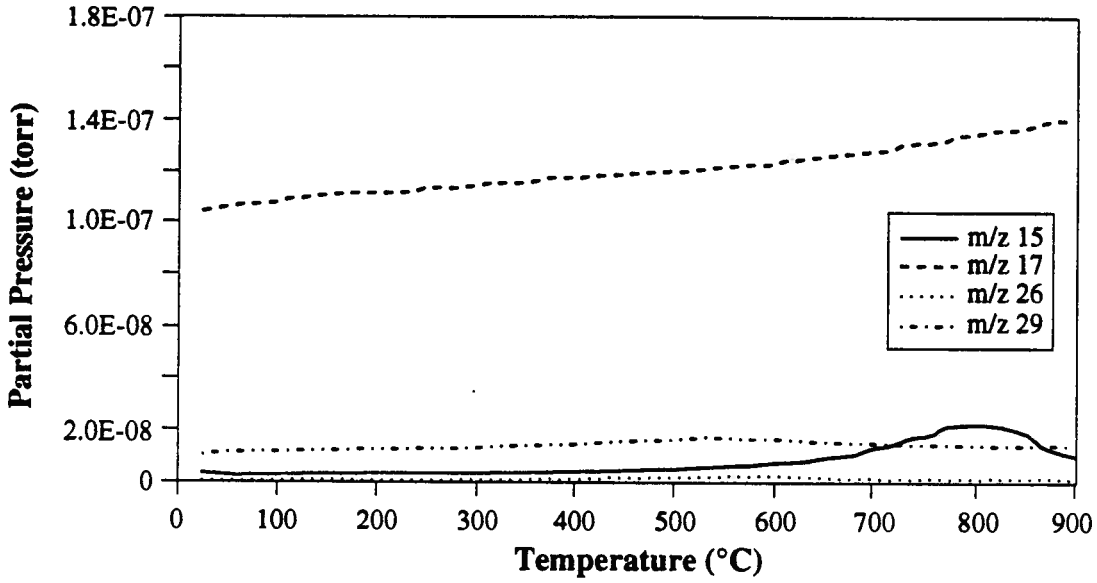

Figure 6.10 - TG/MS data for the 25/75 MTES/TEOS copolymer sample with the identifying mass number for each curve.

6.3.3 Phenyltriethoxysilane (PTES)/TEOS Copolymer

The ^{29}Si CP/MAS NMR spectra for the thermally treated 25/75 PTES/TEOS copolymer samples are shown in Figure 6.11. They show that heating the sample in air oxidizes the phenyl group at temperatures above 400°C, but under nitrogen the phenyl group is stable up to 600°C. Increasing the temperature of the thermal treatment broadens the ^{29}Si resonances. As discussed for the MTES/TEOS copolymer, this is indicative of structural change resulting from internal condensations.

The large chemical shift anisotropy of the phenyl group results in a large number of spinning side bands in the ^{13}C CP/MAS NMR spectra acquired at 400 MHz (9.4 Tesla) unless very high spinning speeds are used.[1.10] The ^{13}C CP/MAS spectra were therefore obtained on a Bruker CXP 100 spectrometer where spinning speeds around 2-3 kHz are adequate to remove the spinning side band pattern. The series of ^{13}C CP/MAS NMR spectra shown in Figure 6.12 prove that the majority of the phenyl groups are still intact at 500°C; however, decomposition of a small proportion of the phenyl groups has occurred as shown by the appearance of an additional resonance at 143 ppm. If the phenyl functionality is oxidized, phenolic groups could be formed. In solution, the phenolic group shows a ^{13}C resonance around 155 ppm for the carbon directly attached to the oxygen.[6.7] Therefore, the new low-field resonance can be interpreted as a result from the oxidation of the phenyl group to a C_6H_5O- group by the oxygen impurity in the nitrogen gas.

The DSC data acquired under nitrogen and in air for the PTES/TEOS copolymer are shown in Figure 6.13. The curve obtained under nitrogen, Figure 6.13A, is similar to those of the MTES/TEOS copolymer and silica gel samples, suggesting that the phenyl group when thermally treated under nitrogen for short time periods is stable up to temperatures of 600°C. In air, the thermal treatments result in the oxidation of the phenyl functionality at

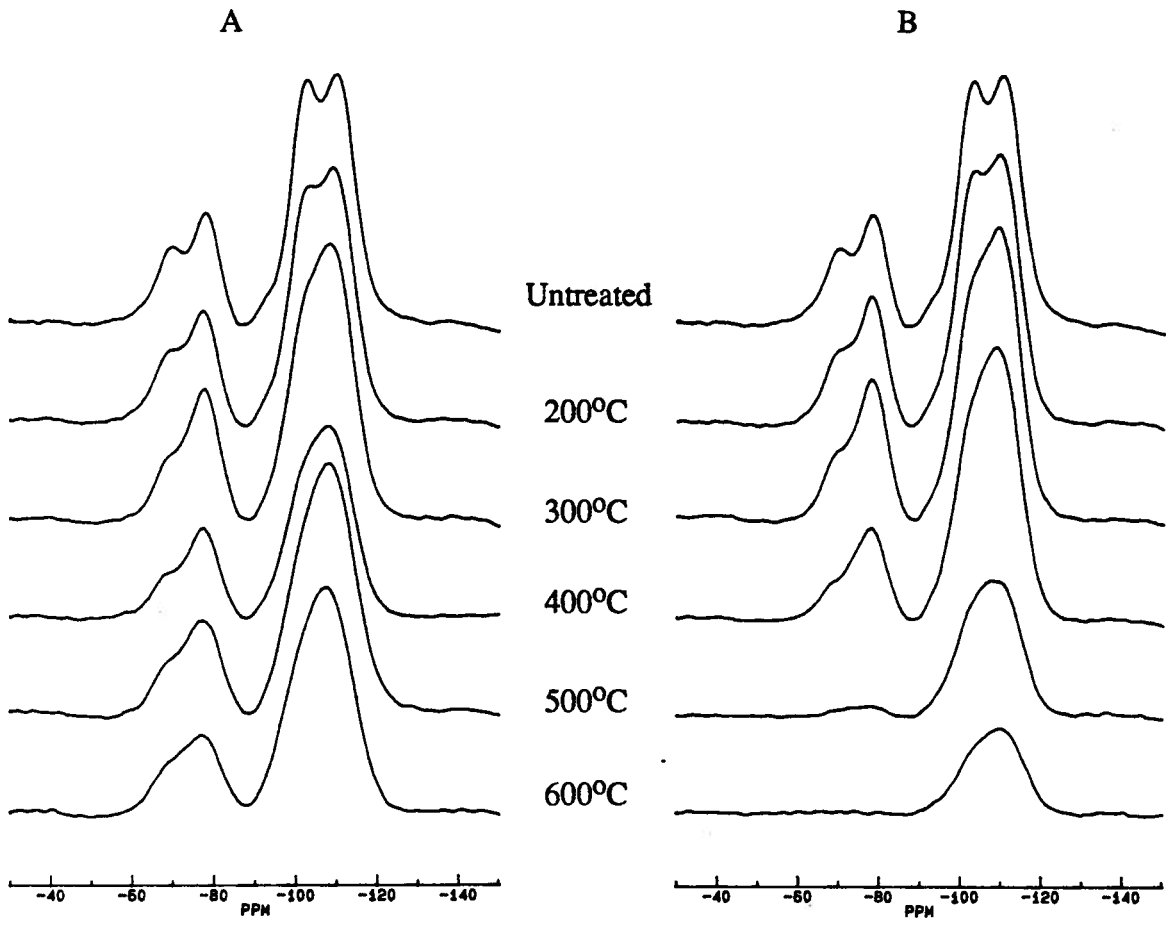

Figure 6.11 - Room temperature 79.5 MHz ^{29}Si CP/MAS NMR spectra of the 25/75 PTES/TEOS copolymer sample heated for two hours at the temperatures indicated. These spectra were acquired with 800 scans, 10ms contact time, 2s recycle delay and 2.5-3 kHz sample spinning rate. Two series of experiments were performed, the spectra acquired for those samples thermally treated under nitrogen are shown in series A and the spectra for those samples thermally treated in air are shown in series B.

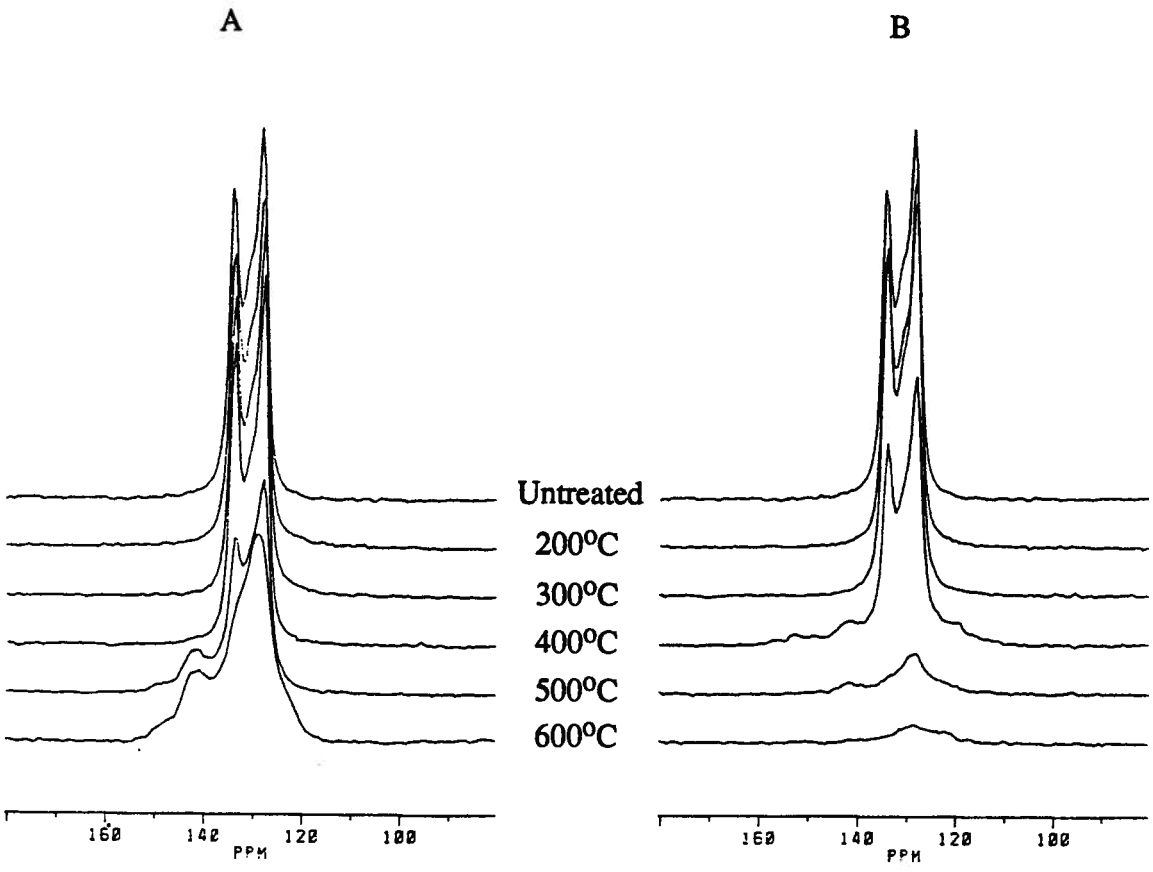

Figure 6.12 - Room temperature 25.2 MHz ^{13}C CP/MAS NMR spectra of the 25/75 PTES/TEOS copolymer sample heated for two hours at the temperatures indicated. These spectra were acquired using 13000 scans, 5ms contact time, 3s recycle delay and 3 kHz sample spinning rate. Two series of experiments were performed the spectra acquired for those samples thermally treated under nitrogen are shown in series A and the spectra for those samples thermally treated in air are shown in series B.

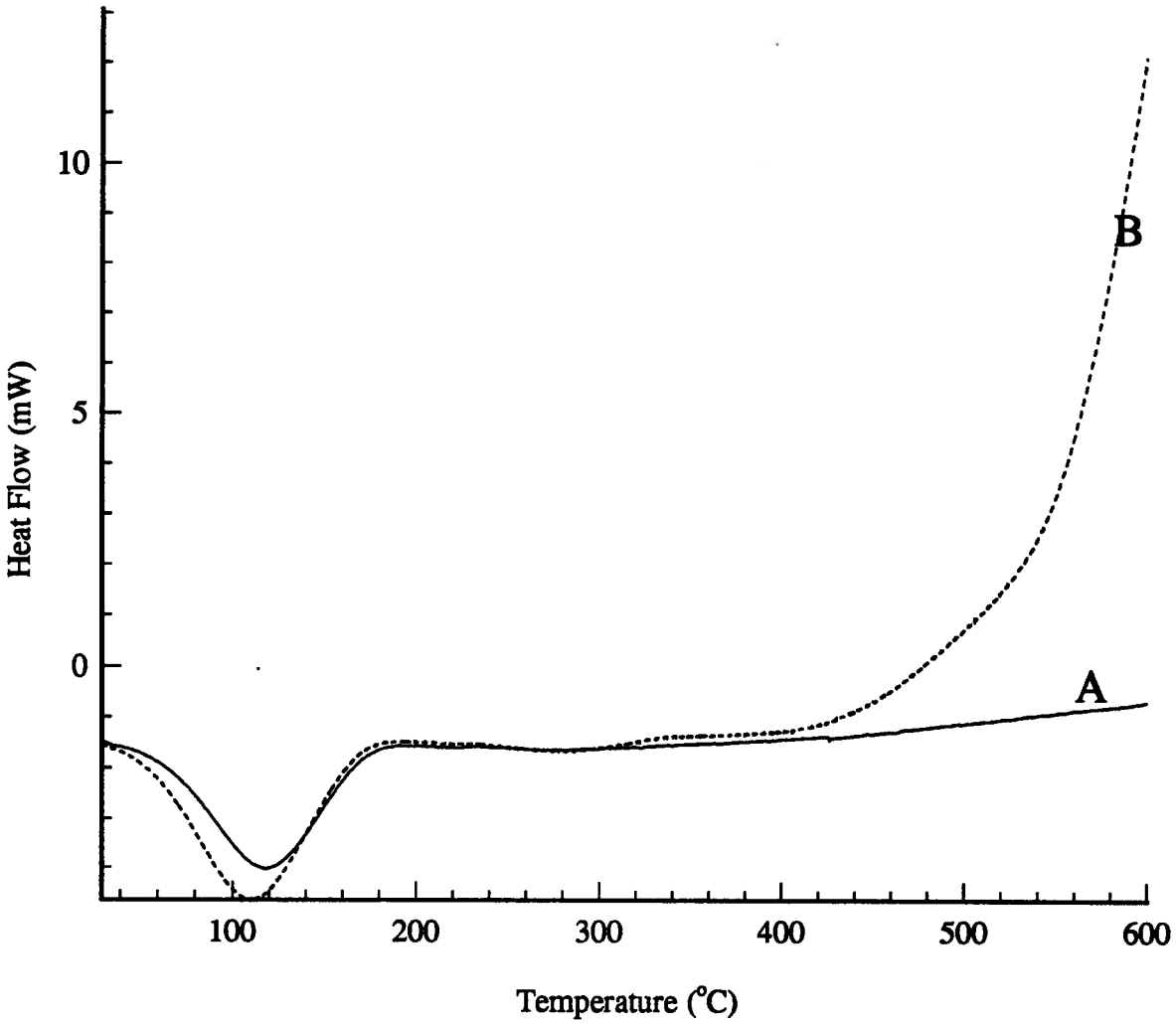

Figure 6.13 - DSC thermal analysis curves for the 25/75 PTES/TEOS under (A) nitrogen and (B) air, with all the other experimental parameters kept constant.

temperatures greater than 400°C. The ^{13}C NMR spectra suggest that the decomposition of the phenyl groups under nitrogen starts at 500°C, this is not reflected in the DSC curve. The dynamic heating in the thermal analysis versus the long-term (two hours) isothermal heating in the NMR studies may well account for this discrepancy. The PTES/TEOS copolymer TGA data acquired under nitrogen are presented in Figure 6.14. A comparison of the TGA curve for the PTES/TEOS copolymer with that of silica gel indicates that the phenyl functionality in the PTES/TEOS copolymer decomposes between 500°C and 700°C. The TGA data show no decomposition of the functionality below 500°C when acquired under nitrogen.

The TG/MS data acquired under nitrogen for the PTES/TEOS copolymer are shown in Figure 6.15. There are three groups of fragment mass numbers, as illustrated in Figure 6.15. The fragment mass number 79 is identifiable as a six carbon species indicative of a phenyl group. The mass number 79 curve maximum is detected before that of the other fragments implying that the weakest link is the C-Si bond. The maxima for the four, two and one carbon species, fragment mass numbers 50-53; 26,29 and 15, respectively, are reached at higher temperatures. Thus, they are probably products of the decomposition of the phenyl group after the cleavage of the C-Si bond. Another possible explanation for the 26, 29 and 15 curves is that there are still some ethoxy ligands present in this copolymer, which are cleaved under the thermal treatment.

Quantitative ^{29}Si MAS spectra indicate that, out of the possible 23%, 18% of the PTES monomer is still intact after thermal treatment under nitrogen at 500°C. The 5% loss is possibly due to oxidation by impurities in the nitrogen gas during the two hour time period of the heating process.

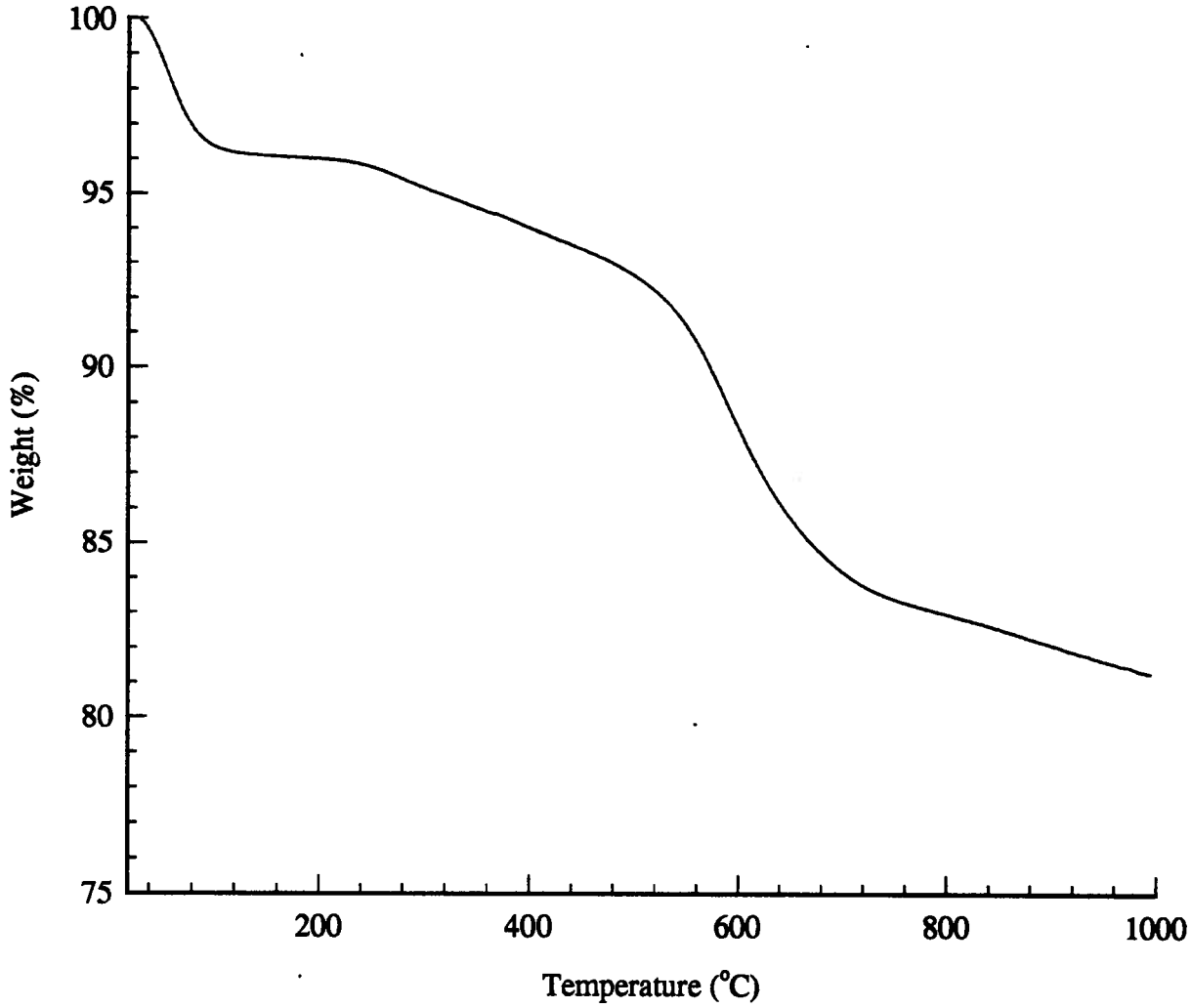

Figure 6.14 - TGA thermal analysis curves for 25/75 PTES/TEOS under nitrogen.

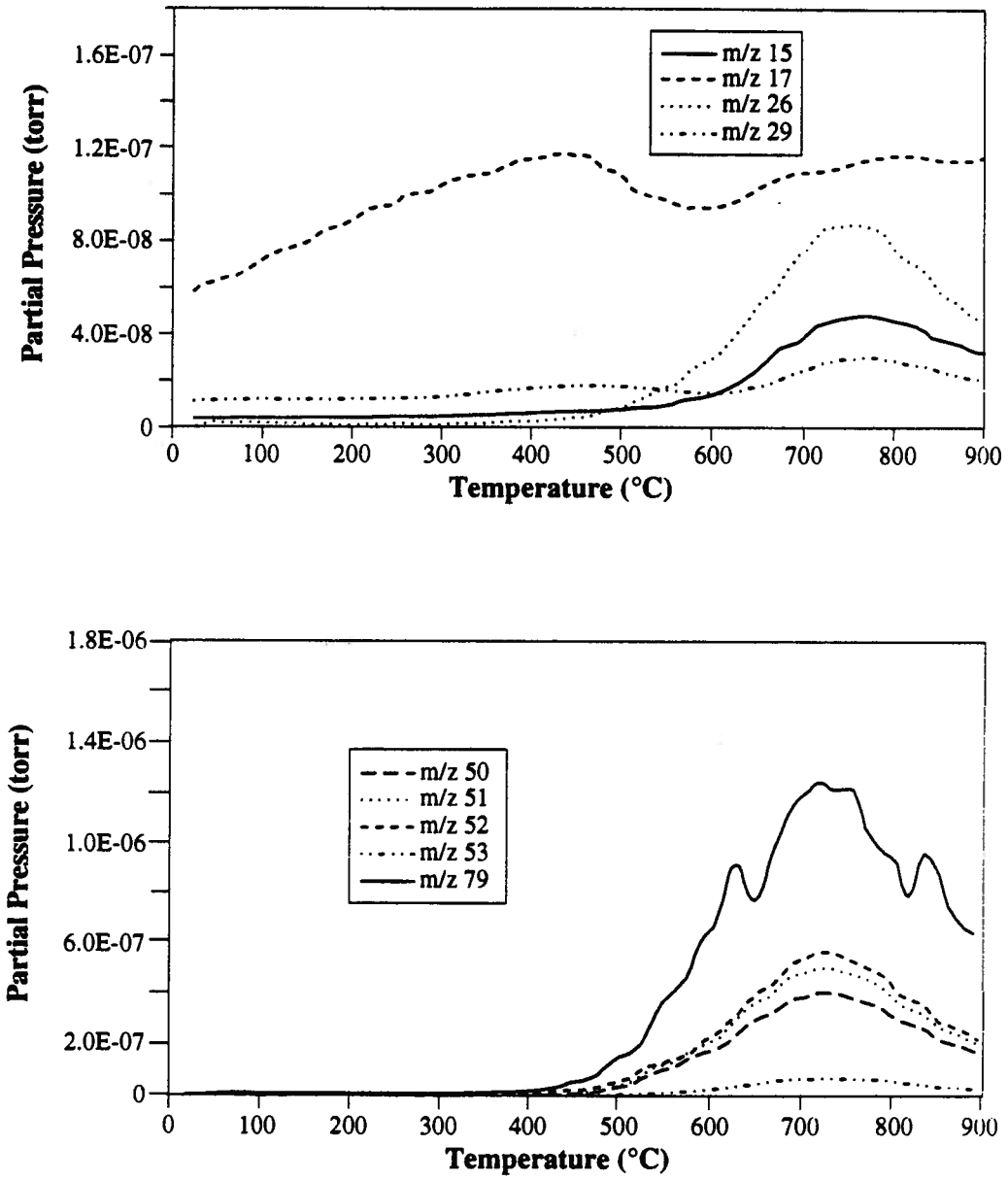

Figure 6.15 - TG/MS data for the 25/75 PTES/TEOS copolymer sample with the identifying mass number for each curve.

6.3.4 Ethyltriethoxysilane (ETES)/TEOS Copolymer

The ^{29}Si CP/MAS NMR spectra of the thermally treated 25/75 ETES/TEOS copolymer samples, are shown in Figure 6.16. These two series of spectra are similar to those presented for the MTES/TEOS and PTES/TEOS copolymers (Figures 6.4 and 6.11), As the temperature of the thermal treatment is increased, the resonances of the resulting material broadens. This is indicative of a larger distribution of silicon environments, again a consequence of internal condensations during the thermal treatment.

The ^{29}Si CP/MAS NMR spectra suggest that the ethyl functionality has almost completely decomposed after thermal treatment in air at temperatures greater than 200°C. A 50/50 ETES/TEOS copolymer was synthesized in order to increase the contribution from the functionalized silane in the ^{29}Si NMR spectra. It is evident from Figure 6.17 that the ethyl functionalized silane starts to decompose above 400°C under nitrogen. In comparison to the methyl and phenyl functionalities, the ethyl functionality decomposes more readily. The large decrease in intensity observed in the spectra of the samples thermally treated at higher temperatures is due to the decomposition of the ethyl groups resulting in a loss of protons which are the polarization source in this CP/MAS experiment.

The spectra of the ETES/TEOS copolymer sample thermally treated under an inert atmosphere, i.e. nitrogen, at temperatures above 400°C contain an additional resonance at ~-85 ppm. This resonance suggests the formation of ≡Si-H bonds.[6.10] This is in agreement with the conclusions of Kamiya et al, in their study of the thermal decomposition of the MTES homopolymer.[6.11] As expected, the resonance at ~-85 ppm is absent in the series of spectra acquired for the ETES/TEOS sample thermally treated in air.

The TG/MS data shown in Figure 6.18 provide some additional information. The

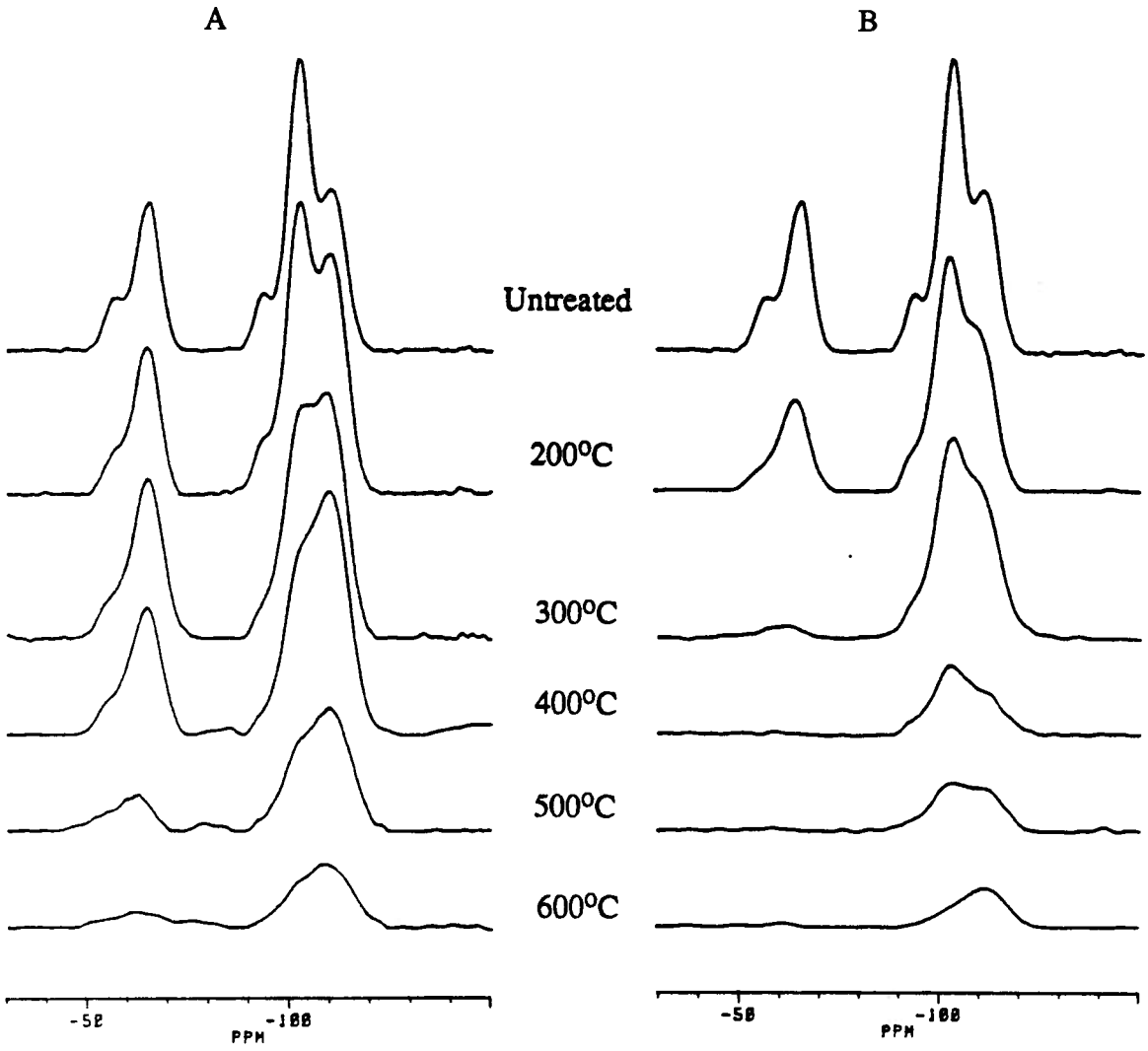

Figure 6.16 - Room temperature 79.5 MHz ^{29}Si CP/MAS NMR spectra of the 25/75 ETES/TEOS copolymer sample heated for two hours at the temperatures indicated. These spectra were acquired using 400 scans, 10ms contact time, 4s recycle delay and 3.2 kHz sample spinning rate. Two series of experiments were performed, the spectra acquired for those samples thermally treated under nitrogen are shown in series A and the spectra for those samples thermally treated in air are shown in series B.

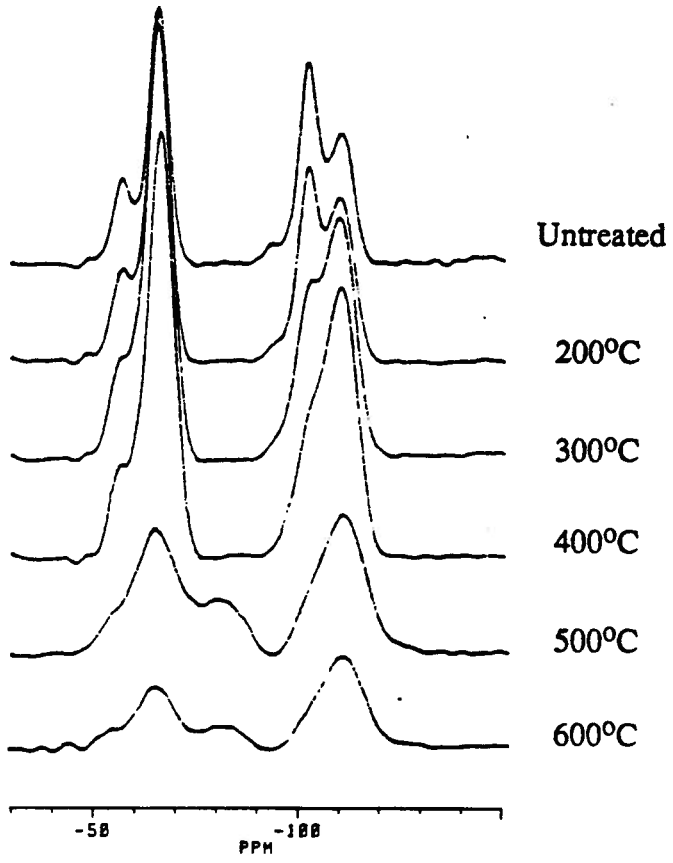

Figure 6.17 - Room temperature 79.5 MHz ^{29}Si CP/MAS NMR spectra of the 50/50 ETES/TEOS copolymer sample heated for two hours under nitrogen at the temperatures indicated. These spectra were acquired using 400 scans, 10ms contact time, 4s recycle delay and a 3.2 kHz sample spinning rate.

curves representing the fragment mass numbers 26-31 (ethyl fragments) reach a maximum at 610°C (Figure 6.18B) before the one for the fragment mass number 15 (corresponding to a methyl group) at 640°C. Therefore, the decomposition of the ethyl functionality, as was the case for the phenyl, involves the cleavage of the C-Si bond before the C-C bond. The curve of mass number 29 possesses two maxima: one maximum coincides with the maximum of the mass number 31 at 540°C, and the other with the maximum observed for the mass number 26 and 30 at 610°C. The fact that ethyl fragments are released at two different temperatures could be explained considering that ethyl functionalities in the bulk and those on or near the surface of the sample may contribute differently to the curve. It is possible that the decomposition products of the ethyl functionalities near or on the surface are detected as soon as the Si-C bond is broken, but those in the bulk may be trapped within the copolymer matrix until further changes in the SiO_2 framework allow these trapped fragments to escape.

The fragments with mass numbers 77-79 (Figure 6.18C) can be explained by recombination of ethyl fragments. The maxima of the ethyl fragment curves, mass numbers 26-31 (610°C), precede the curve maxima of mass numbers 77-79 (660°C) which is also compatible with the notion of ethyl fragments trapped in the copolymer matrix, encouraging recombination. Again, the fragment mass number 17 (Figure 6.18A) indicative of the elimination of hydroxyl groups is observed throughout the whole temperature range.

Figure 6.19 presents a series of ^{13}C CP/MAS NMR spectra for the 25/75 ETES/TEOS copolymer thermally treated under nitrogen and air. A single resonance for both carbons of the ethyl functionality is observed due to the small chemical shift difference between them. The results of the ^{13}C CP/MAS spectra confirm that the ethyl group decomposes in air above 200°C, and above 400°C when thermal treatment is carried out in nitrogen. With the decomposition of the ethyl functionality, an additional resonance appears at 0 ppm in the ^{13}C

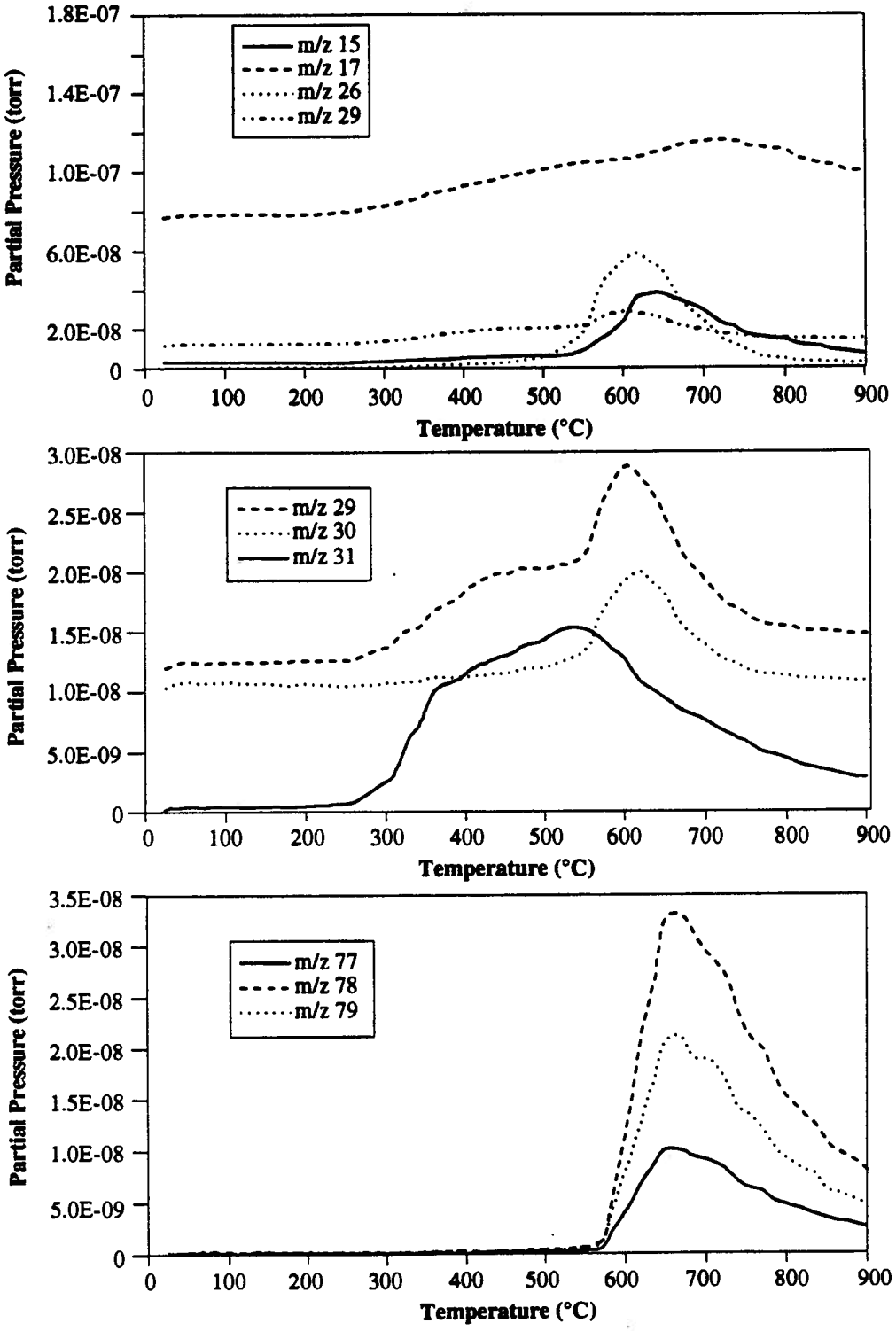

Figure 6.18 - TG/MS data for the 50/50 ETES/TEOS copolymer sample with the identifying mass number for each curve.

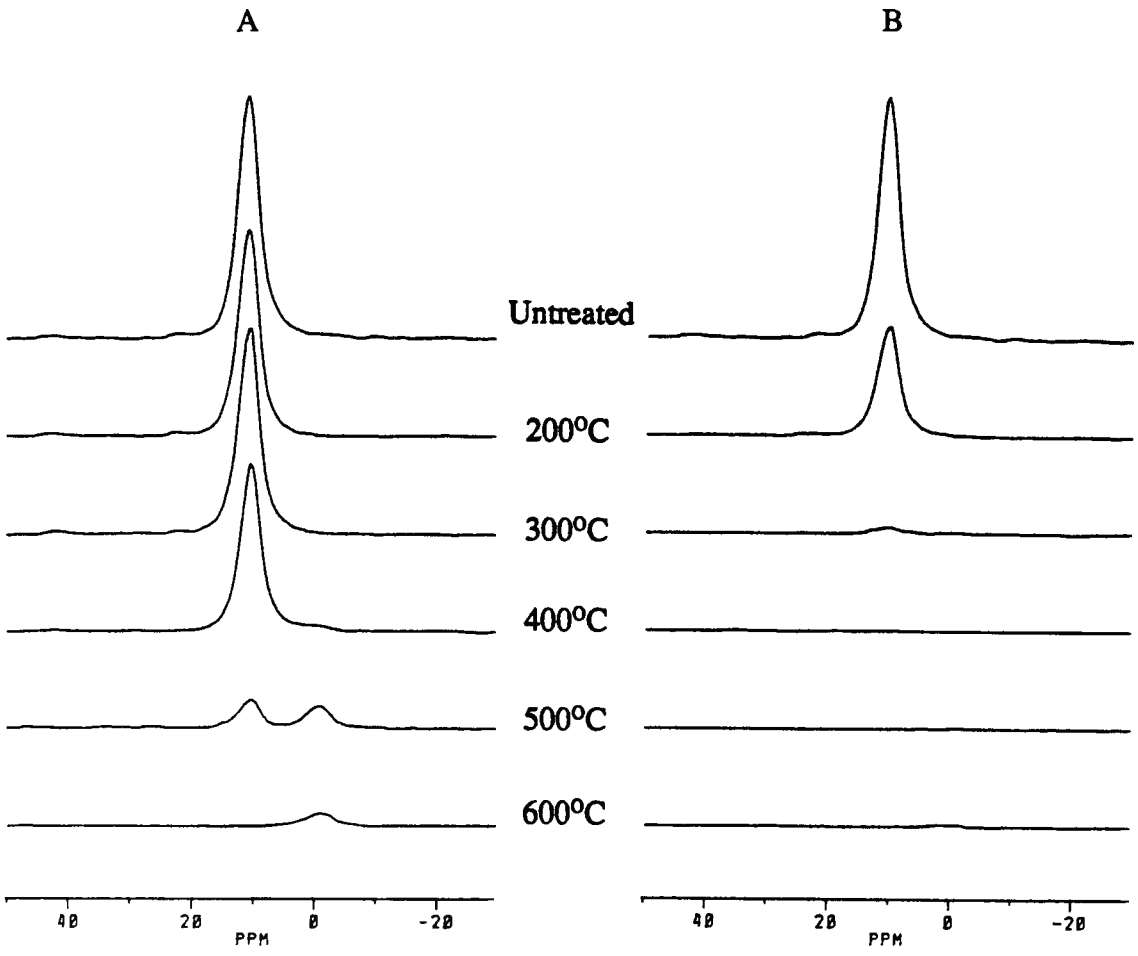

Figure 6.19 - Room temperature 100.6 MHz ^{13}C CP/MAS NMR spectra of the 25/75 ETES/TEOS copolymer samples heated for two hours at the temperatures indicated. These spectra were acquired using 296 scans, 5ms contact time, 4s recycle delay and 3.2 kHz sample spinning rate. Two series of experiments were performed, the spectra acquired for those samples thermally treated under nitrogen are shown in series A and the spectra for those samples thermally treated in air are shown in series B.

CP/MAS NMR spectra. This peak may be due to a methyl functionality derived from the decomposition of the ethyl functionality. No peaks appear downfield from the ethyl ^{13}C resonance indicating that no conjugated functionalities are formed.

The ^{1}H MAS NMR spectra for the thermally treated 50/50 ETES/TEOS copolymer samples under nitrogen are shown in Figure 6.20. There is a narrow resonance due to water and hydroxyl groups, and a broader resonance due to the five ethyl protons (with a width at half height of approximately 3 ppm in the untreated sample). The ^{1}H spectrum changes dramatically after the sample is thermally treated at 500°C (under nitrogen). The proton signals narrow and three distinguishable resonances are resolved, which remain even after a thermal treatment at 600°C. The chemical shifts are in accordance with protons in the following different chemical environments: ≡Si-H, -OH and $-CH_2CH_3$, as indicated in Figure 6.20.

The DSC curve of the ETES/TEOS copolymer is shown in Figure 6.21. The removal of physisorbed water is the first endothermic process, as seen previously in Figures 6.1A, 6.8A and 6.13. Above 540°C, the second endothermic process is the decomposition of the ethyl group. In the DSC data acquired in air, the second thermal event is exothermic and starts at 240°C. Since the NMR results indicate that the ethyl functionality is stable up to 200°C in air this thermal event can be understood as the decomposition of the ethyl functionality.

The TGA curve for the ETES/TEOS copolymer, Figure 6.22, is very similar to that obtained for the PTES/TEOS copolymer. Initially there is a loss of water, then a loss of surface hydroxy and ethoxy ligands which overlaps with the decomposition of the ethyl functionality. Interestingly, a plateau exists above 650°C for the next 200°C in the ETES/TEOS copolymer TGA curve signifying a constant chemical composition.

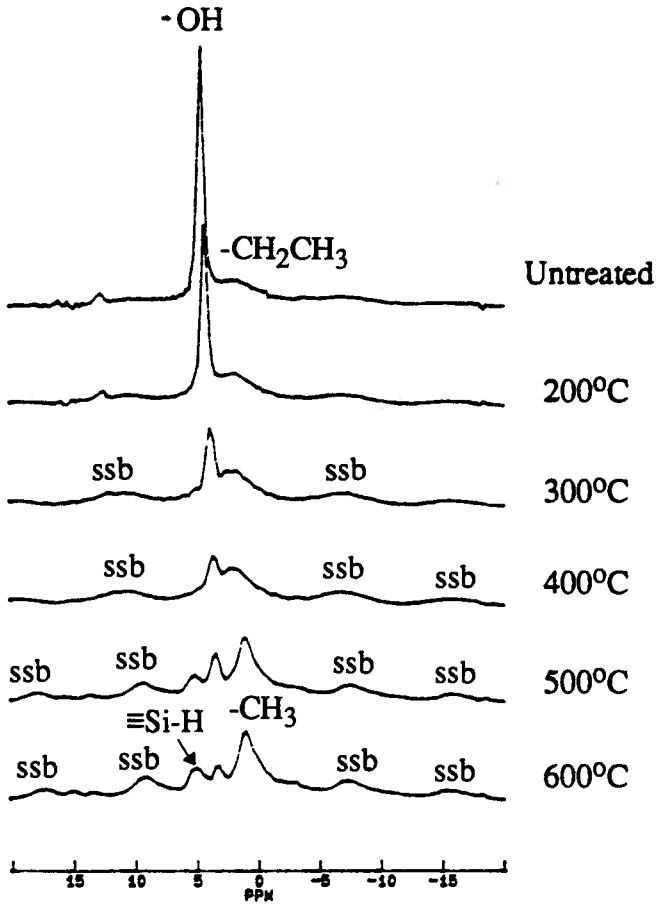

Figure 6.20 - Room temperature ^{1}H MAS NMR spectra of the 50/50 ETES/TEOS copolymer sample heated for two hours under nitrogen at the temperatures indicated. These spectra were acquired using 4 scans, a 4s recycle delay, a 90° pulse and 3.3 kHz sample spinning rate.

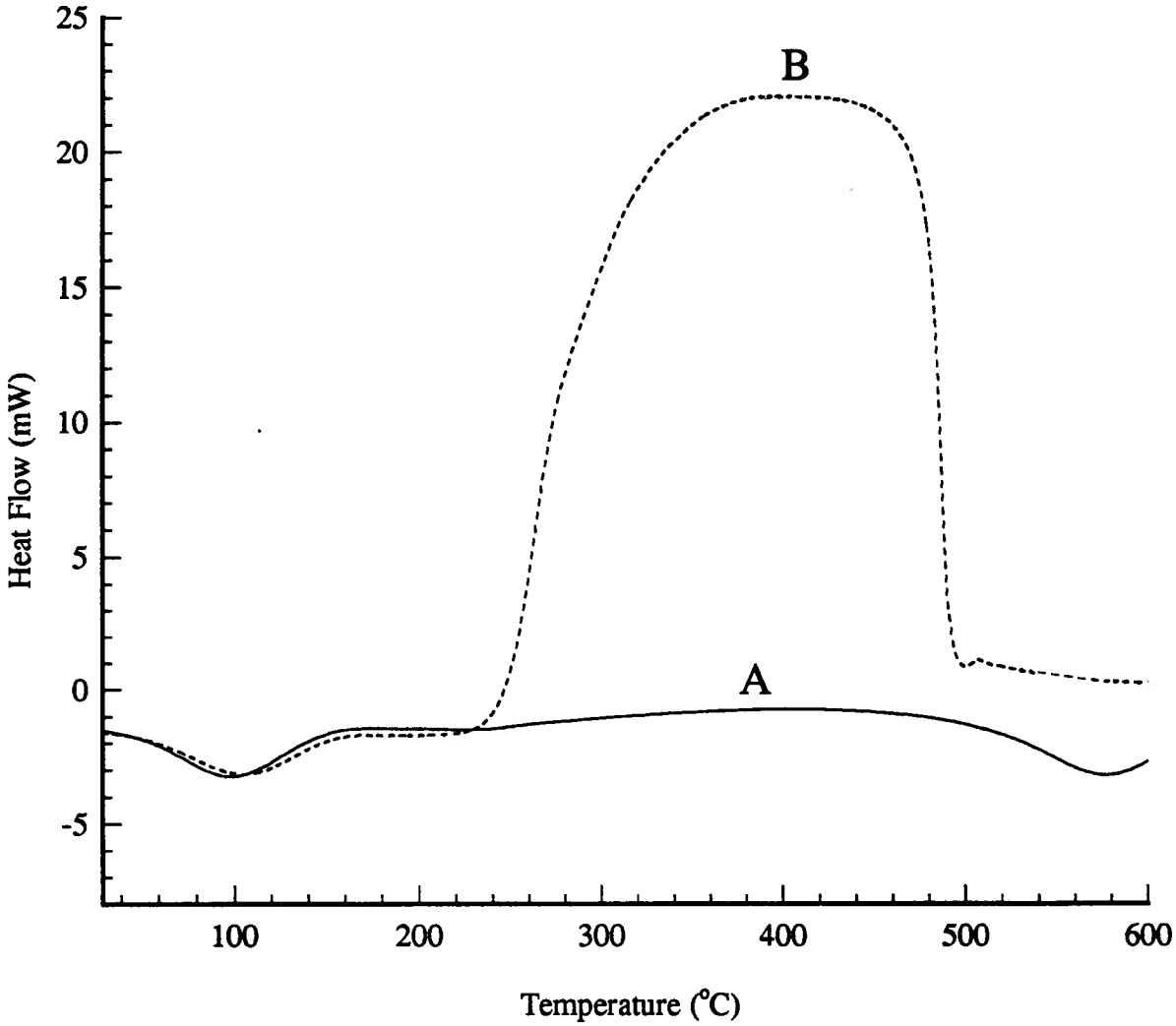

Figure 6.21 - DSC thermal analysis curves for the 25/75 ETES/TEOS copolymer sample obtained under (A) nitrogen and (B) air, with all the other experimental parameters kept constant.

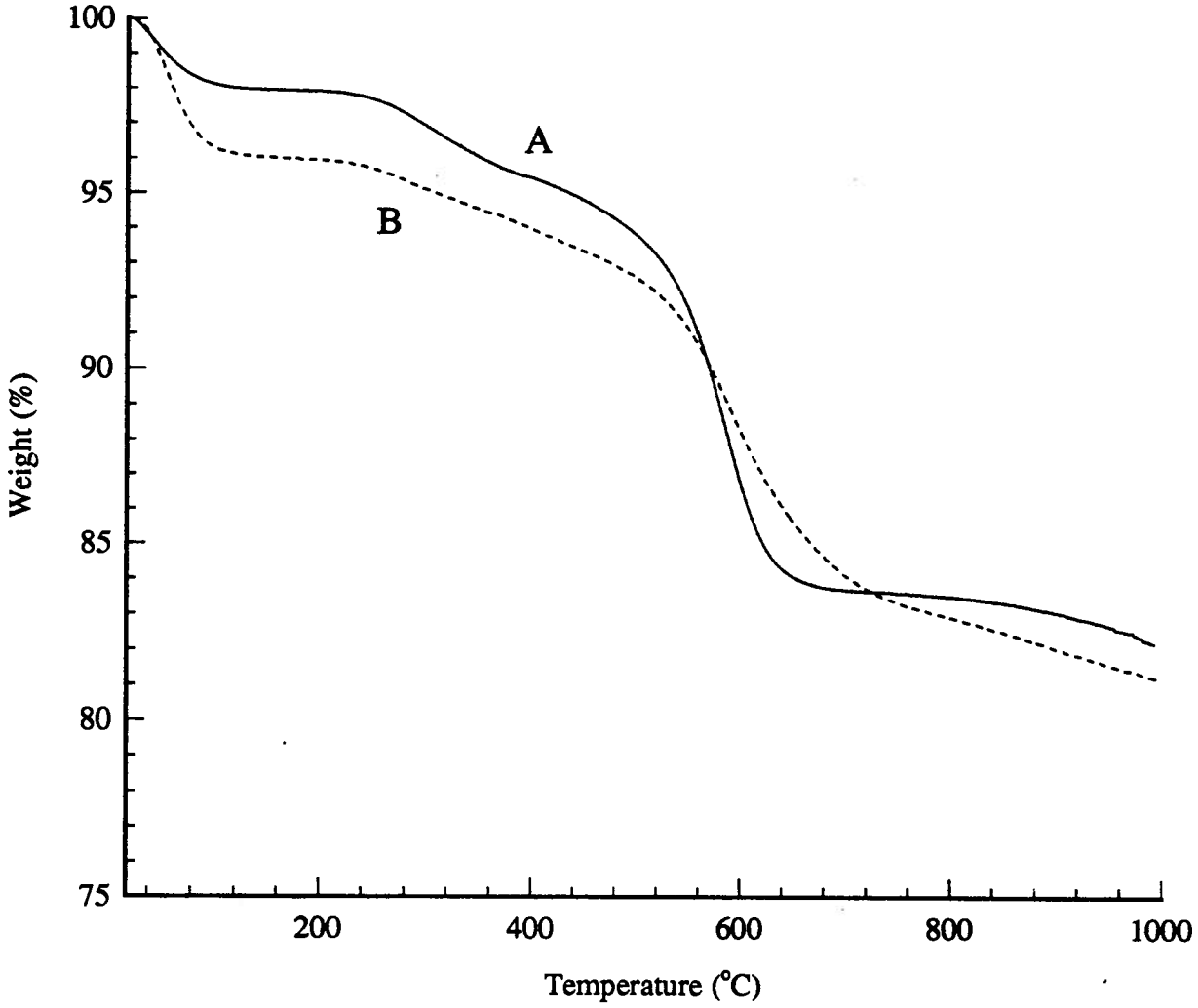

Figure 6.22 - TGA thermal analysis curves obtained under nitrogen for
A - 25/75 ETES/TEOS copolymer and
B - 25/75 PTES/TEOS copolymer.

6.3.5 Phenethyltriethoxysilane (PETES)/TEOS Copolymer

The previous results suggest that the weakest point in an organofunctionalized silane/TEOS copolymer is the initial ≡Si-C≡ bond not the initial ≡C-C≡ bond. In order to confirm this, the thermal stability of the phenethyl functionality was investigated. This functionalized silane serves as a model for many organofunctionalized silanes with the structure $X\text{-}CH_2\text{-}CH_2\text{-}SiY_3$ (where X is any organic or inorganic ligand and Y is a halide or alkoxide ligand). Organofunctionalized silanes with the structure $X\text{-}CH_2CH_2\text{-}SiY_3$ are very common since they can be synthesized in a single step reaction between the appropriate alkene and a trihalo-silane as shown in equation (6.1).

$$X\text{-}CH{=}CH_2 + HSiY_3 \rightarrow X\text{-}CH_2\text{-}CH_2\text{-}SiY_3 \qquad (6.1)$$

The ^{29}Si MAS NMR spectra for the series of thermally treated PETES/TEOS copolymer samples, Figure 6.23, show that the phenethyl functionality also decomposes faster in air than in nitrogen. After treatment at 600°C under nitrogen the ^{29}Si spectrum possesses an additional resonance at ~-85 ppm similar to that observed in the ETES/TEOS case (Figure 6.17). Again, the formation of ≡Si-H is postulated. The ^{13}C CP/MAS NMR spectra (Figure 6.24) confirm that the phenethyl functionality decomposes faster in air than in nitrogen.

The DSC curve (Figure 6.25A) shows the three anticipated endothermic events, a dominant one around 100°C due to the removal of water, a second one over the whole temperature range due to the removal of hydroxy and ethoxy groups from the sample, and a third one due to the decomposition of the phenethyl functionality above 430°C. The TGA data (Figure 6.25B) are in agreement with the DSC data.

The TG/MS data, Figure 6.26, suggest that a ≡C-C≡ bond is cleaved before the first

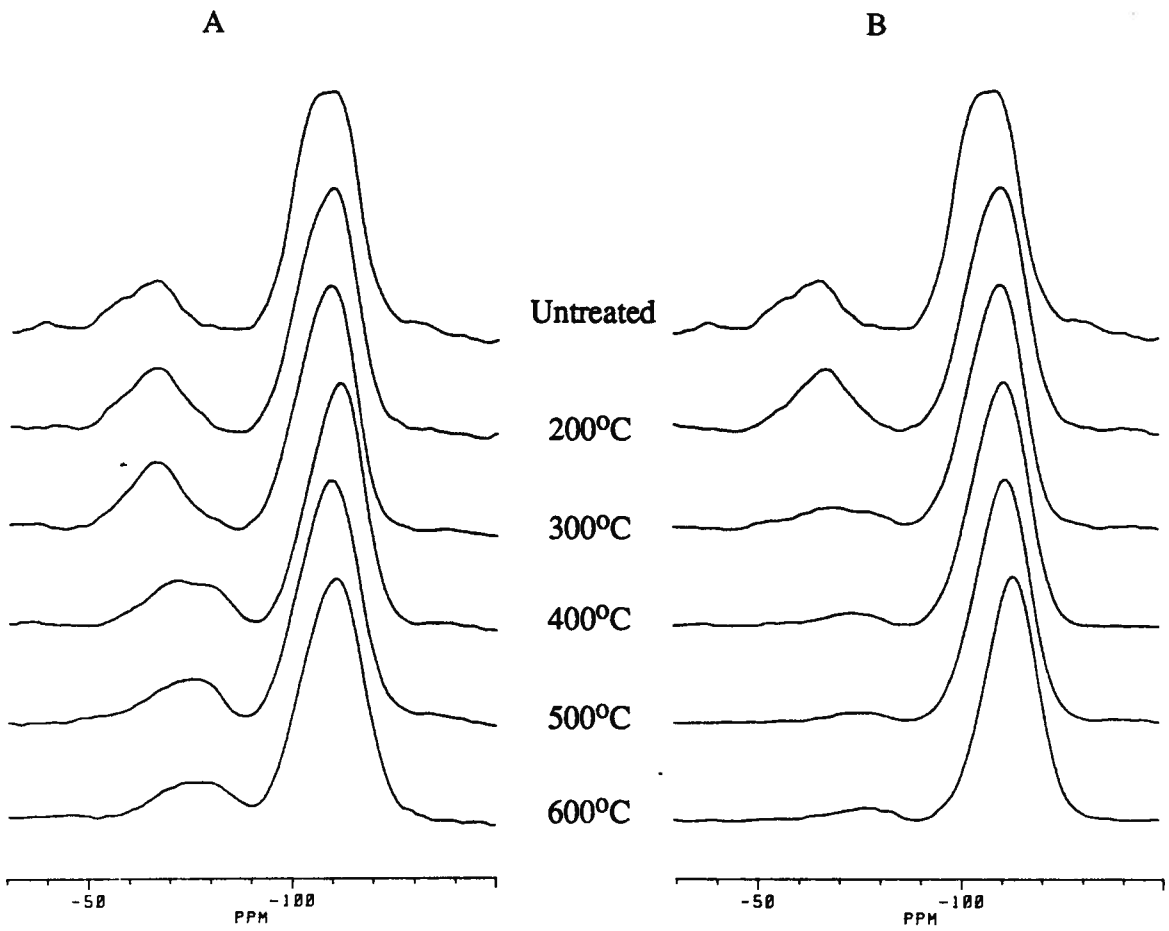

Figure 6.23 - Room temperature 79.5 MHz ^{29}Si MAS NMR spectra of the 25/75 PETES/TEOS copolymer sample heated for two hours at the temperatures indicated. These spectra were acquired using 856 scans, a 42 s recycle time, and a 60° pulse angle. Two series of experiments were performed, the spectra acquired for those samples thermally treated under nitrogen are shown in series A and the spectra for those samples thermally treated in air are shown in series B.

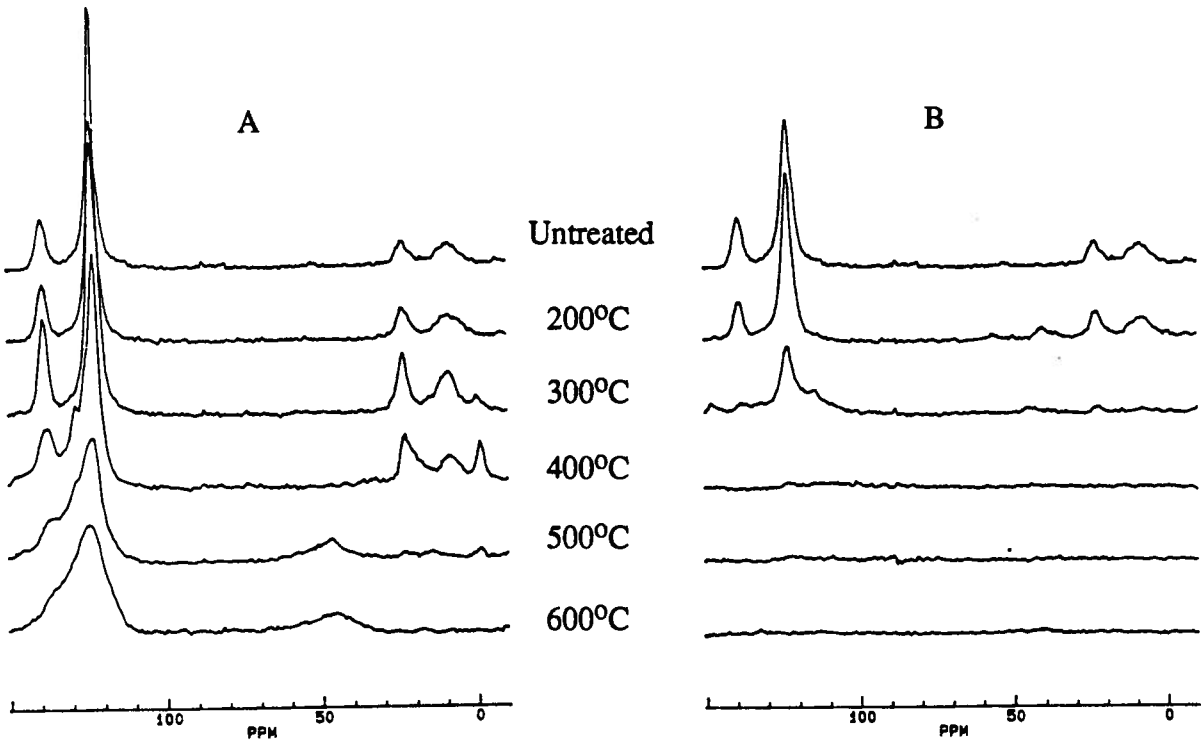

Figure 6.24 - Room temperature 25.2 MHz ^{13}C CP/MAS NMR spectra of the 25/75 PETES/TEOS copolymer sample heated for two hours at the temperatures indicated. These spectra were acquired using 14000 scans, a 5 msec contact time, a 3 s recycle delay and 2kHz spinning speed . Two series of experiments were performed; the spectra acquired for those samples thermally treated under nitrogen are shown in series A and the spectra for those samples thermally treated in air are shown in series B.

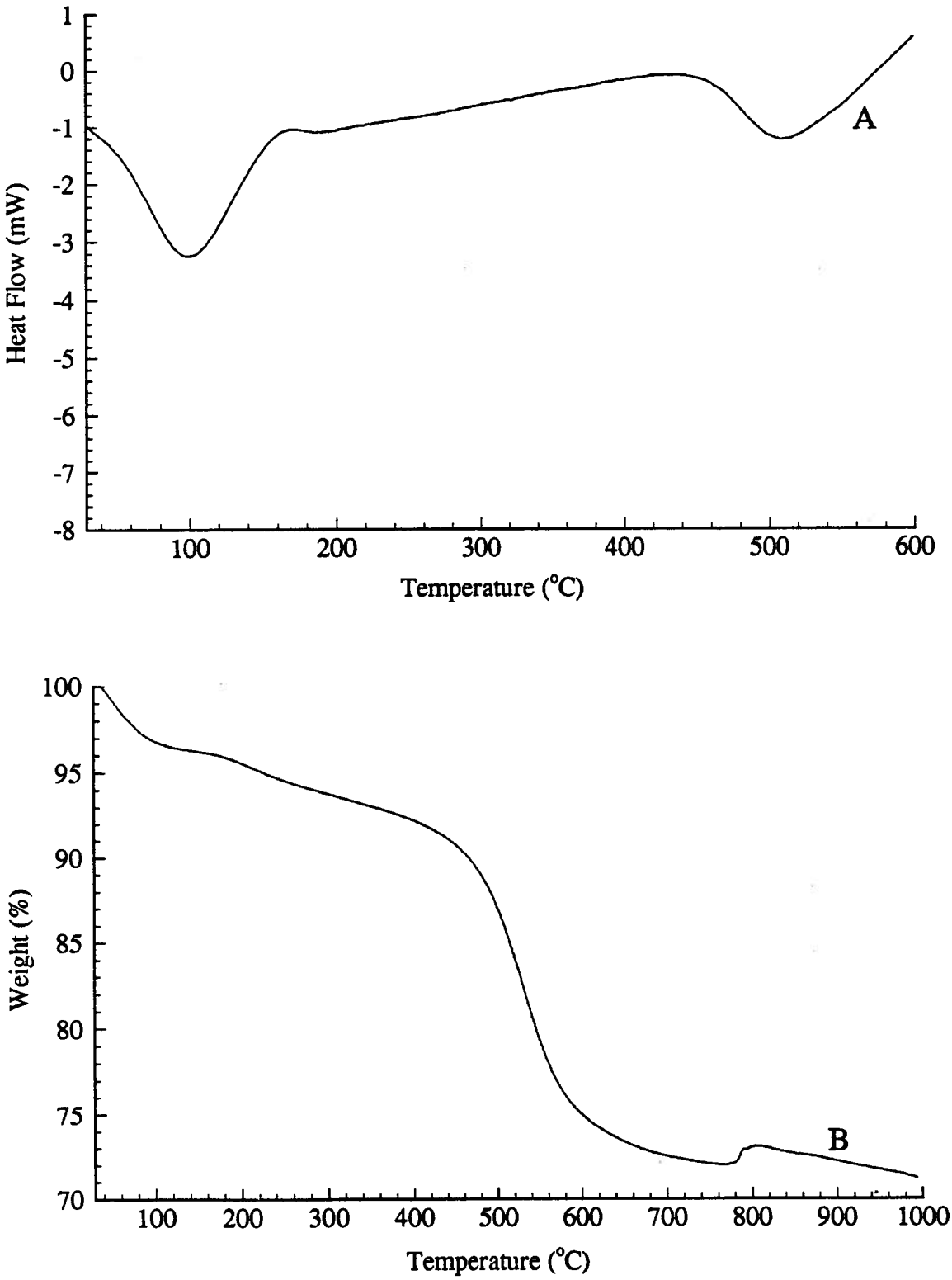

Figure 6.25 - (A) DSC and (B) TGA analysis curves for the 25/75 PETES/TEOS copolymer obtained under nitrogen.

≡Si-C≡ bond. Phenyl fragments are observed first, followed very closely by ethyl fragments, but the phenethyl fragments reach a maximum much later (at temperatures greater than 800°C). The TG/MS data therefore implies that in the PETES/TEOS copolymer the weakest bond in the phenethyl functionality is the ≡C-C≡ bond between the phenyl group and the ethyl chain.

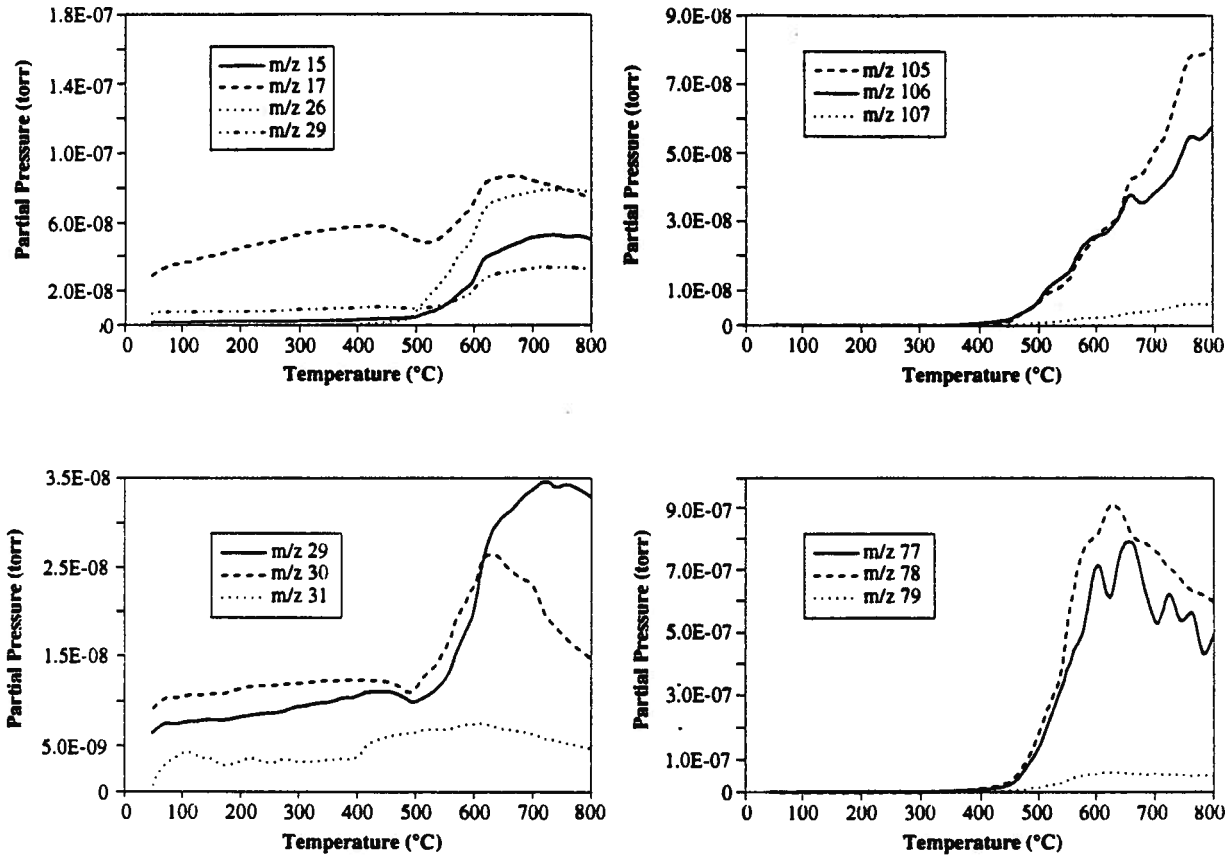

Figure 6.26 - TG/MS data for the 25/75 PETES/TEOS copolymer sample with the identifying mass number for each curve.

6.4 CONCLUSIONS

Four different organofunctionalized copolymers were studied. These organic functionalities showed different temperature stabilities (Table 6.3). In all cases the stability was much higher in nitrogen than in air. Since "hot pressing" gels into glasses requires thermal treatment for much shorter periods of time then used in the NMR study, the temperatures summarized in Table 6.3 are, realistically, the lower limits to the highest temperatures that might be used.

Table 6.3 - The minimum limits of the thermal stabilities of different functionalized copolymers for thermally treatments in air and under nitrogen.

SAMPLE	AIR	N_2
MTES/TEOS	300°C	> 600°C
PTES/TEOS	400°C	> 500°C
ETES/TEOS	200°C	> 400°C
PETES/TEOS	200°C	> 300°C

Of the four functionalities studied, the methyl group was stable to the highest temperature under nitrogen. The least thermally stable was the phenethyl functionality which decomposed under nitrogen at temperatures above 300°C. From the results obtained no completely general statement can be made about which bond is the least thermally stable.

CHAPTER 7

FURTHER SOLID STATE NMR STUDIES TO INVESTIGATE THE EXTENT OF MIXING IN THE MTES/TEOS COPOLYMER GEL

7.1 INTRODUCTION

The solid state NMR data presented in Chapter 2 showed that the MTES/TEOS copolymer was "mixed". In Chapter 4, the ^{29}Si solution NMR data provided evidence that the MTES/TEOS copolymer synthesized under acidic conditions with excess water tended toward a random copolymer, confirming the findings of Chapter 2.

This chapter provides additional structural information, from ^{1}H-^{29}Si variable contact time experiments on silica gel and MTES/TEOS copolymer samples. These experiments were considered earlier but not pursued since the initial solid state NMR experiments (Chapter 2) demonstrated the difficulty of completely removing the hydroxyl functionalities thus making the source of ^{1}H polarization ambiguous for quantitative investigations of the polarization transfer. Variable contact time experiments were carried out on a number of MTES/TEOS copolymer gels, which had been treated with deuterated water to minimize the -OH contents, after the ^{1}H MAS spectra of the thermally treated sample heated to 600°C for two hours under nitrogen exhibited no observable hydroxyl proton resonance (Chapter 6). Thus it was felt that, at least for the thermally treated sample, the results should be ambiguous and could be used as benchmark data for the other samples which were treated with deuterated water. The cross polarization rate T_{cp}^{-1} describes the magnetization transfer between the abundant nuclei (^{1}H or ^{19}F) to the dilute (^{29}Si).[1.19C] As discussed in Chapter 1, T_{cp} can be determined from the ^{29}Si signal intensity measured as a function of the contact time. These T_{cp} values are analyzed with the goal of determining a distance range between the methyl group protons and the non-functionalized silicons. These data provide further evidence for the extent of mixing

in the MTES/TEOS copolymer.

The complications from the possible presence of hydroxyls in the MTES/TEOS copolymers, are absent when ^{19}F is the polarization source and a system containing ^{19}F in the organic functionality was studied. The $CF_3CH_2CH_2Si(OMe)_3$/TEOS copolymer was chosen because it contained fluorine and it had a single probe group, i.e. $-CF_3$, comparable in structure to that in the MTES/TEOS copolymer, i.e. $-CH_3$. Together, these two complementary studies provide sufficient evidence for a conclusive statement to be made about the extent of mixing in these copolymer gel samples.

7.2 EXPERIMENTAL

7.2.1 Samples Used in the ^{1}H-^{29}Si Contact Time Experiments

A control sample of unfunctionalized silica gel was synthesized as described in preparation 2.3.1.2, and dried at 120°C for several hours in order to remove any adsorbed water.

Four copolymer samples were synthesized as described in preparation 2.3.3.3 with the following treatments aimed at minimizing the concentration of hydroxyl groups in order to obtain informative data from the ^{1}H-^{29}Si contact time experiments. A 10/90 MTES/TEOS copolymer sample was washed several times with 99% D_2O and stored in a D_2O saturated atmosphere. The other three samples were 25/75 MTES/TEOS copolymers. The 25/75 MTES/TEOS copolymer subsequently used in the series of 2D experiments was soaked in D_2O six times, for several days each time, and subsequently dried at 120°C under vacuum. The second 25/75 MTES/TEOS copolymer was synthesized using D_2O rather then water, washed several times with D_2O, dried at 120°C under vacuum and stored in a D_2O environment. The third 25/75 MTES/TEOS copolymer sample was soaked in D_2O and dried several times, after which it was thermally treated at 600°C under nitrogen for four hours. This procedure was based on the results of Chapter 6 which demonstrated that a very efficient way to reduce the hydroxyl group concentration was through high temperature treatment (600°C under nitrogen).

7.2.2 Samples Used in the ^{19}F-^{29}Si Contact Time Experiments

The $CF_3CH_2CH_2Si(OMe)_3$/TEOS copolymer was synthesized following the procedure outlined in preparation 2.3.3.3. Two 25/75 $CF_3CH_2CH_2Si(OMe)_3$/TEOS copolymer samples were studied. One of these was thermally treated under nitrogen for 2.5 hours at 300°C. The third $CF_3CH_2CH_2Si(OMe)_3$/TEOS copolymer sample contained a smaller percentage of the

functionalized monomer (approximately 10%).

7.2.3 Variable Contact Time Experiments

The cross polarization (CP) experiment pulse sequence was illustrated in Figure 1.6 and discussed in detail in section 1.5.3. A 'contact time' experiment involves acquiring a series of CP spectra as a function of the contact time. An example of the ^{29}Si signal intensities versus contact time is shown in Figure 7.3. The curves grow exponentially with the time constant T_{cp}. This exponential growth overlaps with an exponential decay of the spin-locked magnetization $T_{1\rho}$ (^{1}H or ^{19}F depending which is the source nucleus for the cross polarization experiment). Therefore the fitting of each curve depends on three variables, M_o (the maximum signal intensity which would be obtained with an infinitely long $T_{1\rho}$ (^{29}Si) and $T_{1\rho}$ (^{1}H or ^{19}F)), T_{cp} and $T_{1\rho}$ as described by equation (1.17).

One of the 25/75 MTES/TEOS copolymer samples was used to acquire a series of 2D ^{1}H-^{29}Si heteronuclear (CP) correlation experiments at different contact times. The pulse sequence for the 2D ^{1}H-^{29}Si heteronuclear correlation experiment was given in Figure 1.8. The advantage of the set of 2D experiments is that the interactions from the hydroxyl and methyl protons can be clearly distinguished. The disadvantage is that they require substantial spectrometer time, one 2D experiment took about 16 hours. Thus, the complete set of data points shown in Figure 7.7 took 10 days in total to acquire.

All the ^{1}H-^{29}Si and ^{19}F-^{29}Si contact time experiments were carried out on a Bruker MSL 400 MHz spectrometer. In order to synthesize the ^{19}F frequency some hardware modifications had to be carried out. The schematic for these modifications is given in Appendix 3. Further experimental details of the acquisition parameters are given in the figure captions.

7.3 RESULTS and DISCUSSION

7.3.1 ^{1}H-^{29}Si Contact Time Experiments

7.3.1.1 Analysis of the Contact Time Results

A typical set of spectra obtained from a $^{1}H/^{29}Si$ variable contact time experiment are shown in Figure 7.1, for the thermally treated MTES/TEOS copolymer. To obtain the relative peak intensities for such a data set, the Bruker deconvolution program "Glinfit" was used. This program does not allow for referencing between spectra, therefore all the intensities were referenced to the total area (A_{tot}) of each spectrum:

$$I = \frac{I_G}{\sum_i I_i} * A_{tot} \qquad (7.1)$$

where I is the intensity of the deconvoluted signal referenced to the spectra with the maximum intensity, I_G is the deconvoluted area obtained from "Glinfit" and ΣI_i is the sum of the deconvoluted areas for all of the peaks in one single spectrum.

The decay, of the $Si(OH)(OSi)_3$ curve for the silica gel sample and the $CH_3Si(OSi)_3$ curve for the MTES/TEOS copolymer samples, was fitted to a single $T_{1\rho}$ (^{1}H). These were chosen because there were clear decays for these resonances which covered a substantial time interval.

To determine T_{cp} the ^{29}Si peak intensities as functions of contact time were fitted to equation (1.17), using a non-linear least squares fitting program available in the "Mathematica" software, keeping the $T_{1\rho}$ (^{1}H) value fixed.

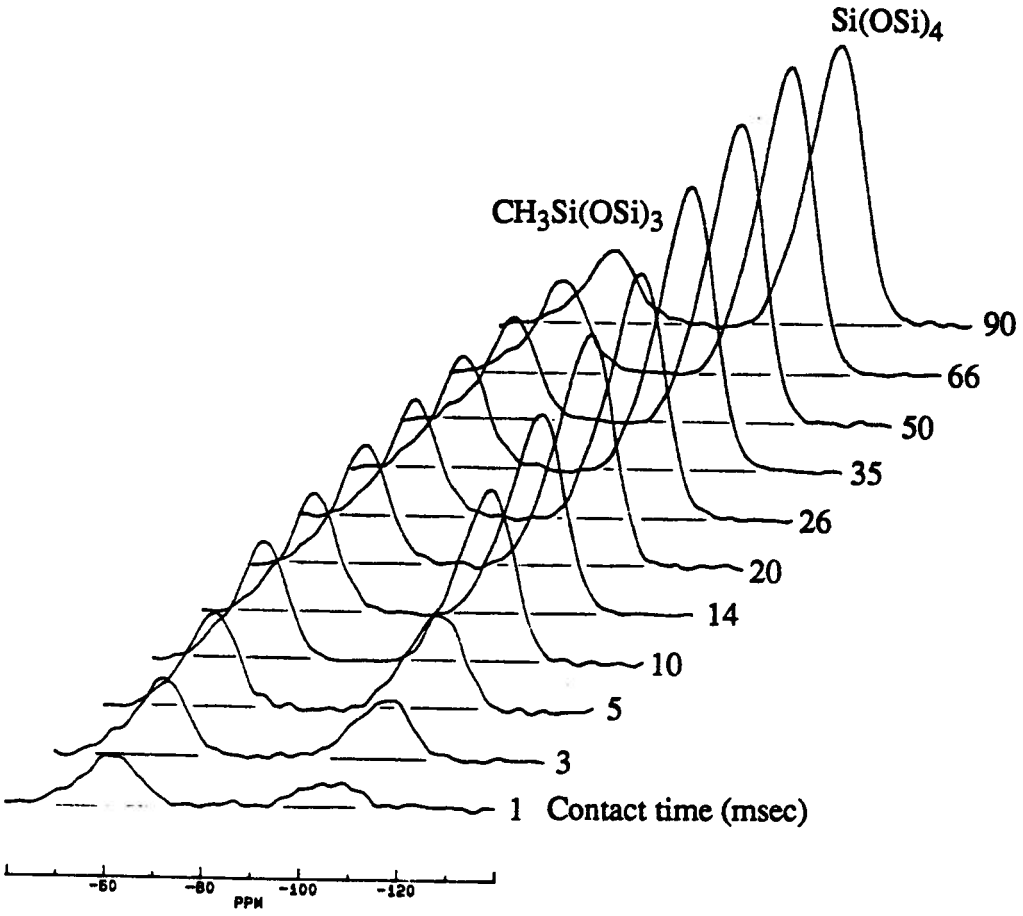

Figure 7.1 - The ^{1}H-^{29}Si CP/MAS NMR spectra as a function of the contact time for the thermally treated 25/75 MTES/TEOS copolymer sample.

$$M(t) = M_o * \frac{\frac{1}{T_{cp}}}{\frac{1}{T_{cp}} - \frac{1}{T_{1\rho}(^1H)}} * \left(e^{-\frac{t}{T_{1\rho}(^1H)}} - e^{-\frac{t}{T_{cp}}}\right) \qquad (1.17)$$

As discussed in section 1.5.3, the cross polarization time constant (T_{cp}) is proportional to the inverse of the sixth power of the distance (r^{-6}) between the ^1H (the polarization source) and the dilute ^{29}Si nuclei. In the case of pure silica gel and the MTES/TEOS copolymer samples, the calculation of the distance is simplified since there are silicons within the sample, such as ≡Si-OH and ≡Si-CH_3, that are connected to a polarization source over two covalent bonds. The distance to these protons can be calculated using literature data on bond lengths and bond angles [7.6-7.8]. Therefore, instead of solving equation (1.18) explicitly, the distance for ^1H-$^{29}Si_c$ (Si_c is a non-functionalized fully condensed silicon, refer to Figure 7.2) can be calculated from a ratio of two cross polarization rates, equation (7.2), one of which is determined by this known distance.

$$\frac{T_{cp_A}}{T_{cp_B}} = \frac{r_A^6}{r_B^6} \qquad (7.2)$$

The subscripts A and B refer to the two different silicon environments in the sample, one of which is the silicon with an already defined distance to the methyl or hydroxyl protons. The ≡Si_a-CH_3 (Si_a is a methyl functionalized fully condensed silicon, refer to Figure 7.2) and ≡Si_b-OH (Si_b is a non-functionalized silicon with one hydroxyl group attached, refer to Figure 7.2) distances, calculated using literature values for bond angles and lengths, are shown in Figure 7.2. The T_{cp} values were evaluated from fitting of the contact time curves and the ^1H-$^{29}Si_c$ distances were then determined from equation (7.2). For future comparison, Figure 7.2 gives the calculated ^1H-Si_c distances using literature values for bond lengths and angles.

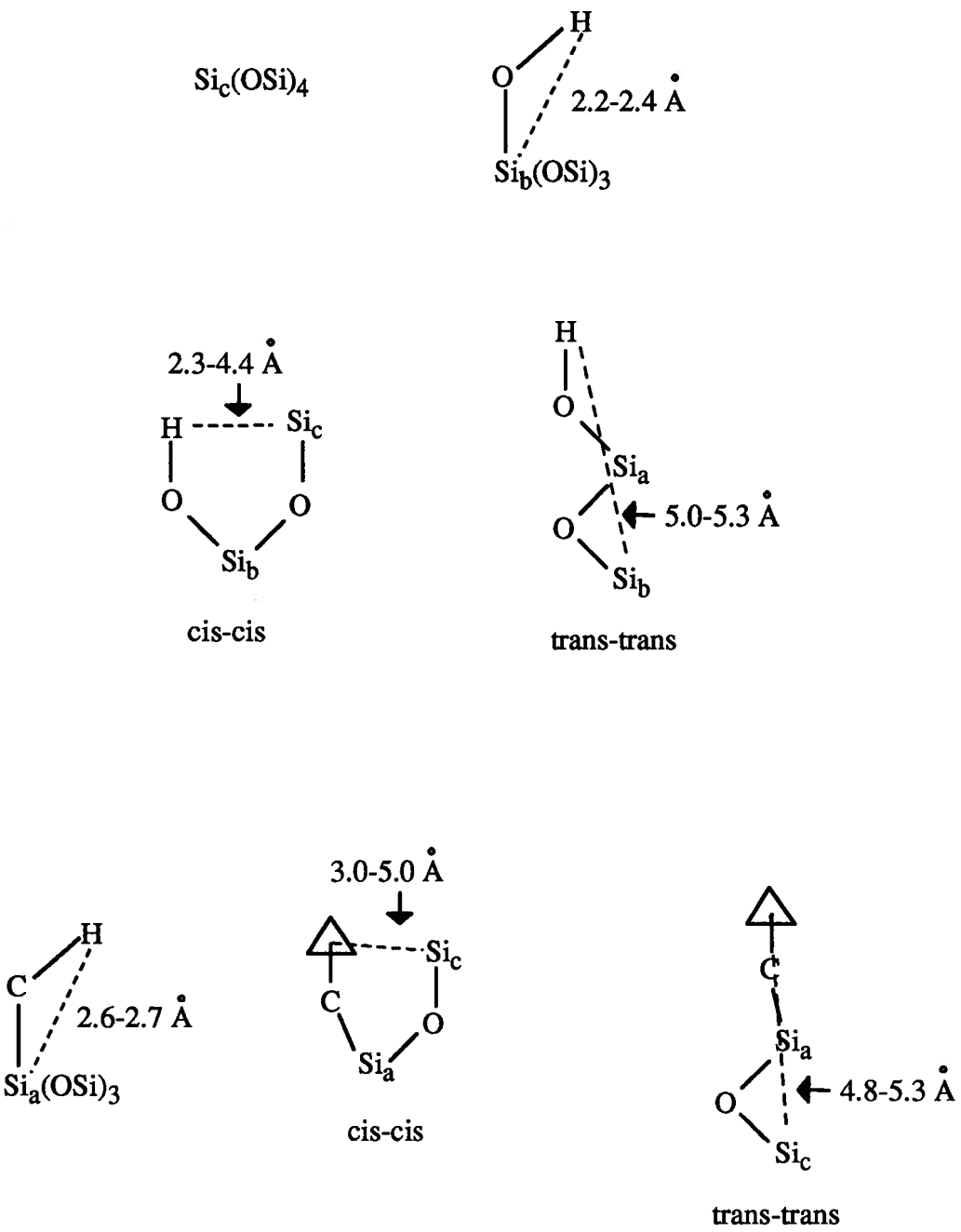

Figure 7.2 - The definition of Si_a, Si_b and Si_c and the distances calculated using literature data [7.6-7.8].

7.3.1.2 Pure Silica Gel Contact Time Experiments

The $^1HO\text{-}Si_b(OSi)_3$ distance was calculated from the literature data to be 2.2-2.4 Å (Figure 7.2). The T_{cp} values for $Si(OH)(OSi)_3$ and $Si(OSi)_4$ were determined from fitting the respective contact time curves and are summarized in Table 7.1. Using the above information and equation (7.2), the ^1H to $^{29}Si_c(OSi)_4$ distance for silica gel was calculated to be 2.7-2.9 Å. These results are in good agreement with those previously published by Maciel et al.[1.20]

Using literature bond lengths and angles [7.6-7.8], the shortest calculated distance between a hydroxyl proton to a neighbouring Si_c results from a cis-cis configuration, 2.3-4.4 Å (Figure 7.2). Distances calculated from cross polarization experiments are heavily weighted in favour of the shortest distances to the polarization source due to the r^{-6} distance dependence. As expected, the determined $^1H\text{-}Si_c$ distance lies at the lower end of the range of distances defined by the possible configurations.

In conclusion, when the hydroxyl groups are the main source of polarization transfer, the calculated $^1H\text{-}Si_c$ distance should lie in the range of 2.7-2.9 Å.

7.3.1.3 MTES/TEOS Copolymer Contact Time Experiments

The MTES/TEOS copolymer contains principally $CH_3Si_a(OSi)_3$ and $Si_c(OSi)_4$ silicons. The methyl protons are the closest and therefore the dominant source of cross polarization to Si_a. Therefore it is reasonable to fit the $CH_3Si_a(OSi)_3$ contact time data considering only a single T_{cp} value, equation (1.17).

The $T_{1\rho}$ (^1H) and T_{cp} values for $CH_3Si(OSi)_3$, for the different MTES/TEOS copolymer samples studied, determined by fitting the variable contact time data as described above are consistent with one another, Table 7.2.

Table 7.1 - The T_{cp} values from the non-linear least squares fitting of the contact time curves for the indicated silicons for the pure silica gel sample.

Silicon signal	T_{cp} (msec)
$Si(OH)(OSi)_3$	8
$Si(OSi)_4$	27

Table 7.2 - The $T_{1\rho}$ and T_{cp} values from the non-linear least squares fitting of the $CH_3Si(OSi)_3$ contact time curves for the samples indicated.

Sample	$T_{1\rho}$ (^1H) (msec)	T_{cp} (msec)*
25/75 MTES/TEOS copolymer thermally treated for four hours at 600°C	136	3-4
25/75 MTES/TEOS copolymer washed with D_2O	153	4-5
10/90 MTES/TEOS copolymer washed with D_2O	283	5-6

* The range in the T_{cp} values results from fitting the data with and without fixing the M_o parameter in equation (1.17).

Each of the $Si_c(OSi)_4$ contact time curves for all the MTES/TEOS copolymer samples showed only one maximum with a relatively slow growth of the magnetization (long T_{cp}). Therefore they were initially fitted with a single T_{cp} value, while fixing the $T_{1\rho}$ value to that determined from the decays of the respective $CH_3Si_a(OSi)_3$ curves. The results are summarized in Table 7.3 and the experimental data together with the calculated curves obtained from the fitting procedure are given in Figures 7.3-7.5. Figures 7.3-7.5 clearly show that the calculated curves (solid line) obtained with a single T_{cp} value are in very good agreement with the experimental data. Since the sample is amorphous a range of T_{cp} values might be expected. However, the average distance range between the probe group ($-CH_3$) and Si_c is narrow enough that the contact time curve is well characterized by a single T_{cp} value, implying that the methyl groups are evenly distributed throughout the copolymer matrix.

For comparison purposes and for completeness, two T_{cp} values with different weighted contributions, equation (7.3), were considered.

$$M(t) = M_o * [\, X * \frac{\frac{1}{T_{cp1}}}{\frac{1}{T_{cp1}} - \frac{1}{T_{1\rho}(^1H)}} * (e^{-\frac{t}{T_{1\rho}(^1H)}} - e^{-\frac{t}{T_{cp1}}}) + (1-X) * \frac{\frac{1}{T_{cp2}}}{\frac{1}{T_{cp2}} - \frac{1}{T_{1\rho}(^1H)}} * (e^{-\frac{t}{T_{1\rho}(^1H)}} - e^{-\frac{t}{T_{cp2}}})] \quad (7.3)$$

It is expected that the fit to the experimental data should improve since the number of parameters in the fitting process has increased from two (T_{cp} and M_o) to four (T_{cp1}, T_{cp2}, the relative proportions (X) and M_o). The weighted contributions considered were 10/90, 20/80, 30/70, 40/60 and 50/50. The best results from these weighted fittings are plotted in Figures

Table 7.3 - T_{cp} values derived from fitting the $Si_c(OSi)_4$ contact time curves for the different samples indicated, using equation (1.17) and fixing the $T_{1\rho}$ value (Table 7.2).

Sample	T_{cp} (msec)*		
	single T_{cp}	weighted T_{cp}	
		20%	80%
25/75 MTES/TEOS copolymer			
thermally treated	23-30	6	38-41
D_2O washed	19-21	3	27
10/90 MTES/TEOS copolymer	30-41	4	50-51

* The T_{cp} range is obtained from fitting the contact time curve with and without M_o as a variable in the fit. In the cases when M_o was not a variable, it was fixed to the average M_o value obtained from the previous T_{cp} fits.

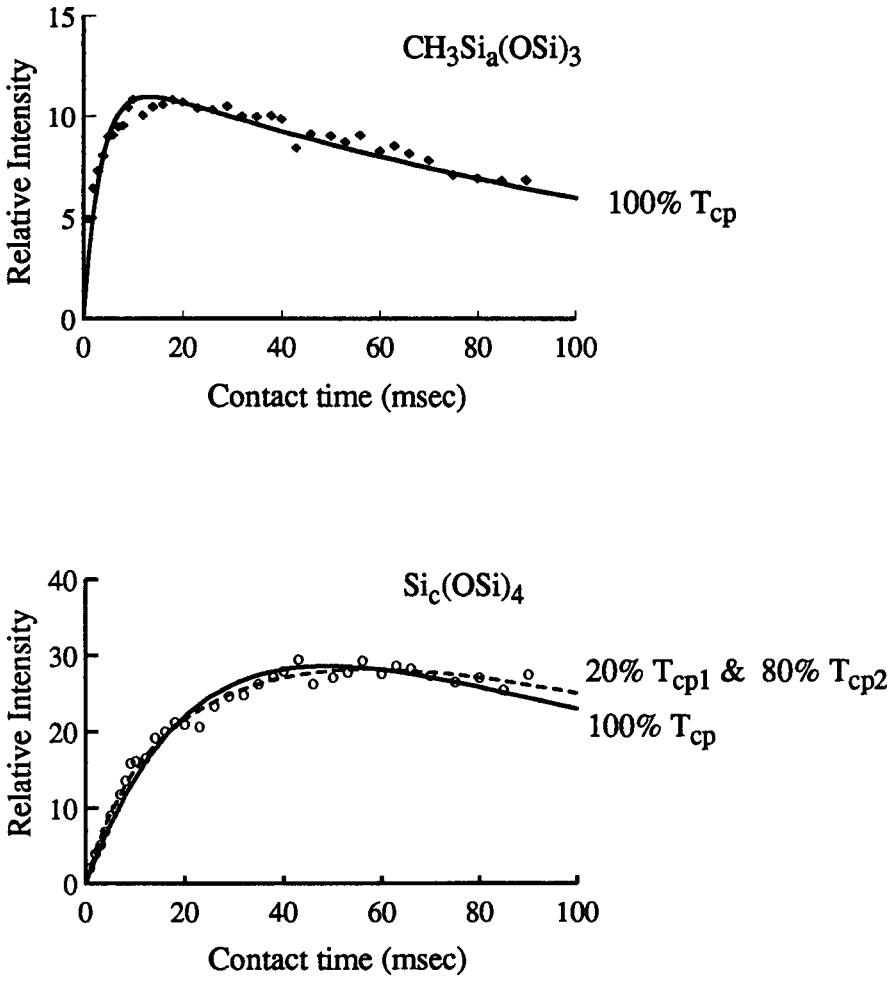

Figure 7.3 - Contact time curves for the $CH_3Si_a(OSi)_3$ and $Si_c(OSi)_4$ silicons in the thermally treated 25/75 MTES/TEOS copolymer together with the calculated curves obtained with equation (1.17) (solid lines) and equation (7.3) (dashed lines) and the parameters given in Tables 7.2 & 7.3.

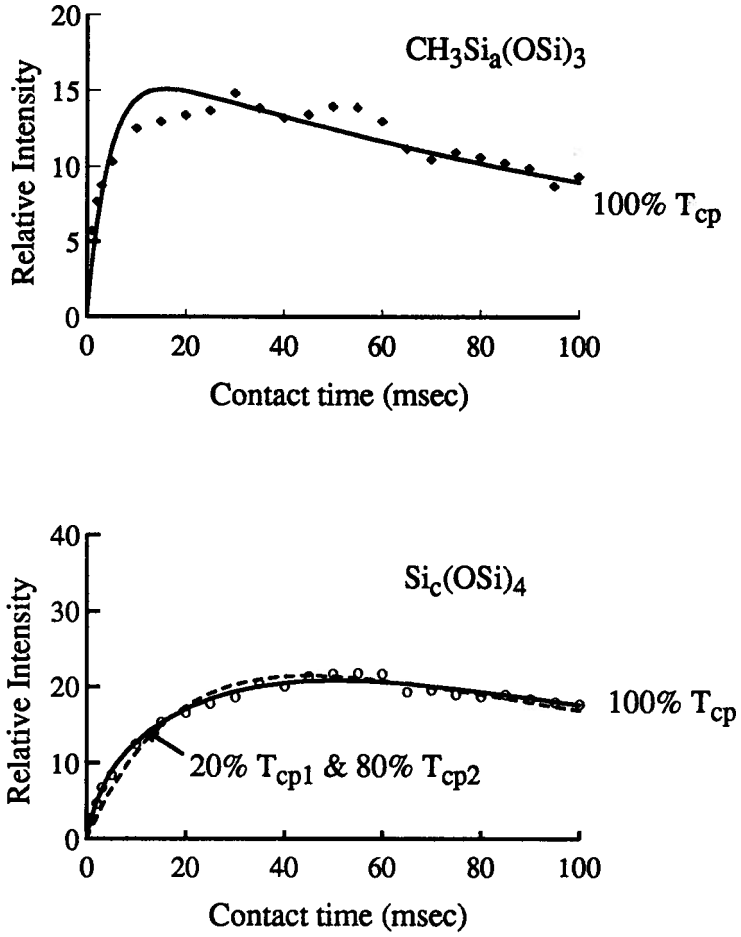

Figure 7.4 - Contact time curves for the $CH_3Si_a(OSi)_3$ and $Si_c(OSi)_4$ silicons in the D_2O washed 25/75 MTES/TEOS copolymer sample together with their calculated curves obtained using equation (1.17) (solid lines) and equation (7.3) (dashed line) and the parameters given in Tables 7.2 & 7.3.

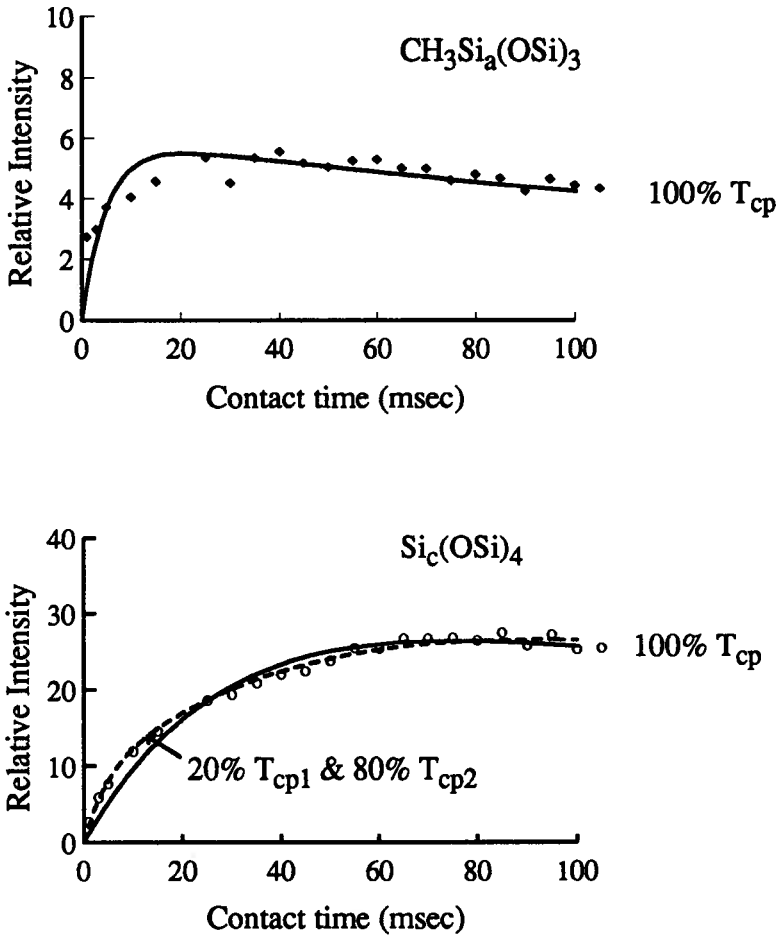

Figure 7.5 - Contact time curves for the $CH_3Si_a(OSi)_3$ and $Si_c(OSi)_4$ silicons in the D_2O washed 10/90 MTES/TEOS copolymer sample, together with their calculated curves obtained using equation (1.17) (solid lines) and equation (7.3) (dashed line) and the parameters in Tables 7.2 & 7.3.

7.3-7.5 (dashed lines). A comparison of the calculated curves (solid and dashed lines) in Figures 7.3-7.5 demonstrates that the consideration of two T_{cp} values instead of one results in only a marginal improvement to the fits.

Substituting the data in Tables 7.1-7.3 and using the $CH_3Si_a(OSi)_3$ calculated distance into equation (7.2), the methyl ^1H to $Si_c(OSi)_4$ distance was calculated for the different samples. These results are presented in Table 7.4.

7.3.1.4 MTES/TEOS Copolymer: Series of 2D Heteronuclear Correlation Experiments

The series of fifteen 2D experiments were processed slightly differently from the previous data sets discussed. In this case, the 2D data was processed with respect to a common reference so that comparable intensities were obtained. The "volumes" of the cross peaks between the methyl protons and the different silicon resonances were determined and plotted as functions of the contact time. An example of the 2D ^1H-^{29}Si heteronuclear correlation contour plot obtained (which corresponds to one data point in Figure 7.7) is shown in Figure 7.6. The $T_{1\rho}$ (^1H) was determined to be 67 msec from the Si_a contact time curve as discussed previously. The T_{cp} for this curve was then determined to be 9-10 msec and that of the $Si_c(OSi)_4$ cross peak was 18 msec, Figure 7.7. Using these data and equation (7.2), the ^1H to Si_c distance was calculated to be 2.9 Å for this sample.

Table 7.4 - ^1H to Si_c distances calculated for the MTES/TEOS copolymer samples, using equation (7.2), a ^1H-Si_a distance of 2.6-2.7 Å, and the $CH_3Si_a(OSi)_3$ and $Si_c(OSi)_4$ T_{cp} values given in Tables 7.2 and 7.3, respectively.

Calculated ^1H to $Si_c(OSi)_4$ distances (Å) for the copolymer samples indicated:	Distances in (Å)		
	single T_{cp}	weighted T_{cp}	
		20%	80%
25/75 MTES/TEOS thermally treated	3.5-4.0	2.8-3.0	3.8-4.2
25/75 MTES/TEOS washed with D_2O	3.3-3.6	2.4-2.6	3.4-3.7
10/90 MTES/TEOS washed with D_2O	3.4-3.8	2.4-2.6	3.7-4.0

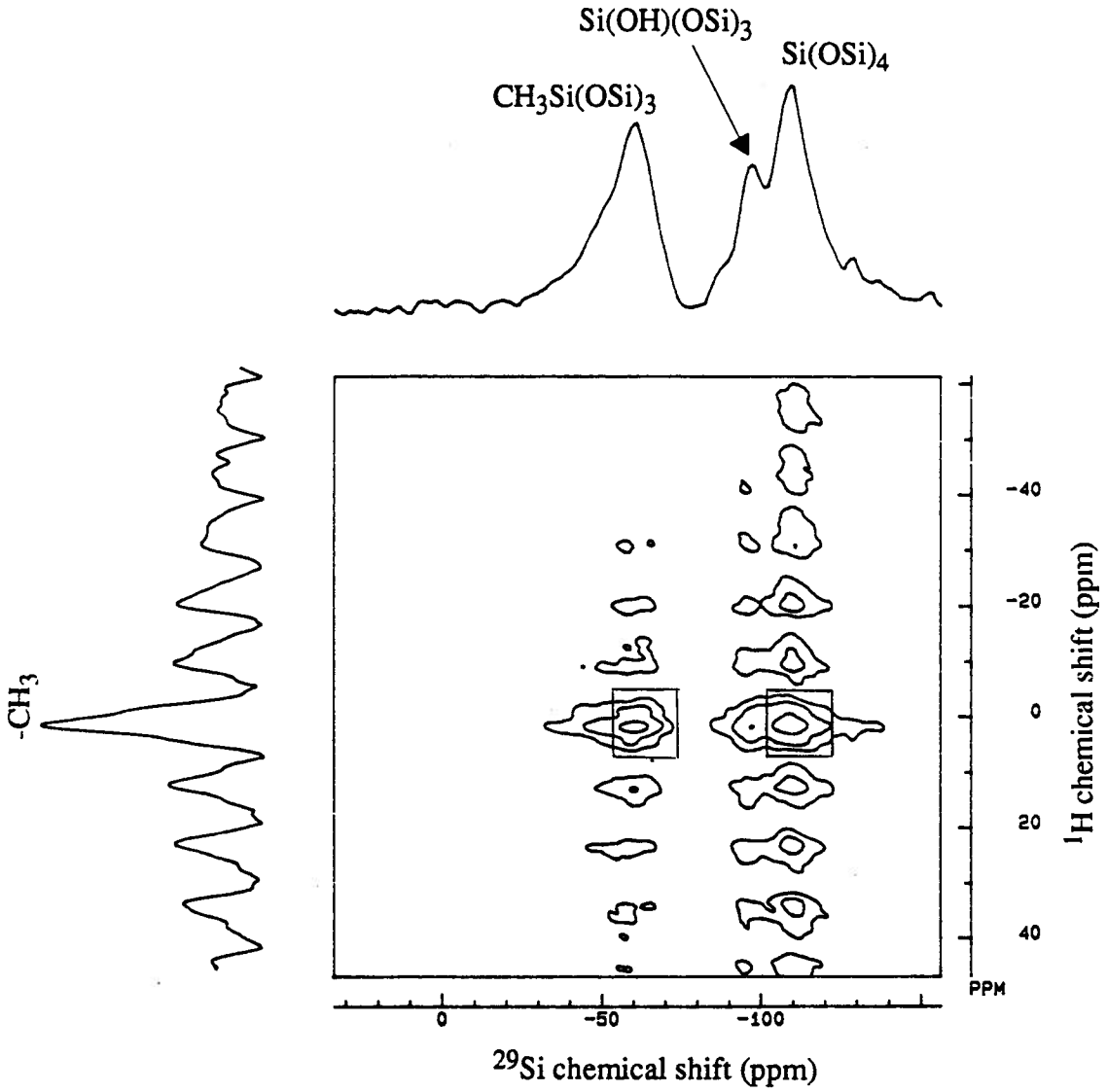

Figure 7.6 - 2D ^{1}H - ^{29}Si heteronuclear correlation contour plot of the 25/75 MTES/TEOS copolymer, with the rectangle indicating the "volume" of the cross peaks used in the analysis of the set of 2D data. There are 300 scans per experiment acquired using a 10 msec contact time, a 3 second recycle delay and 4 kHz spinning speed. This spectrum consists of 64 experiments. The projections are shown along the F1 and F2 axis.

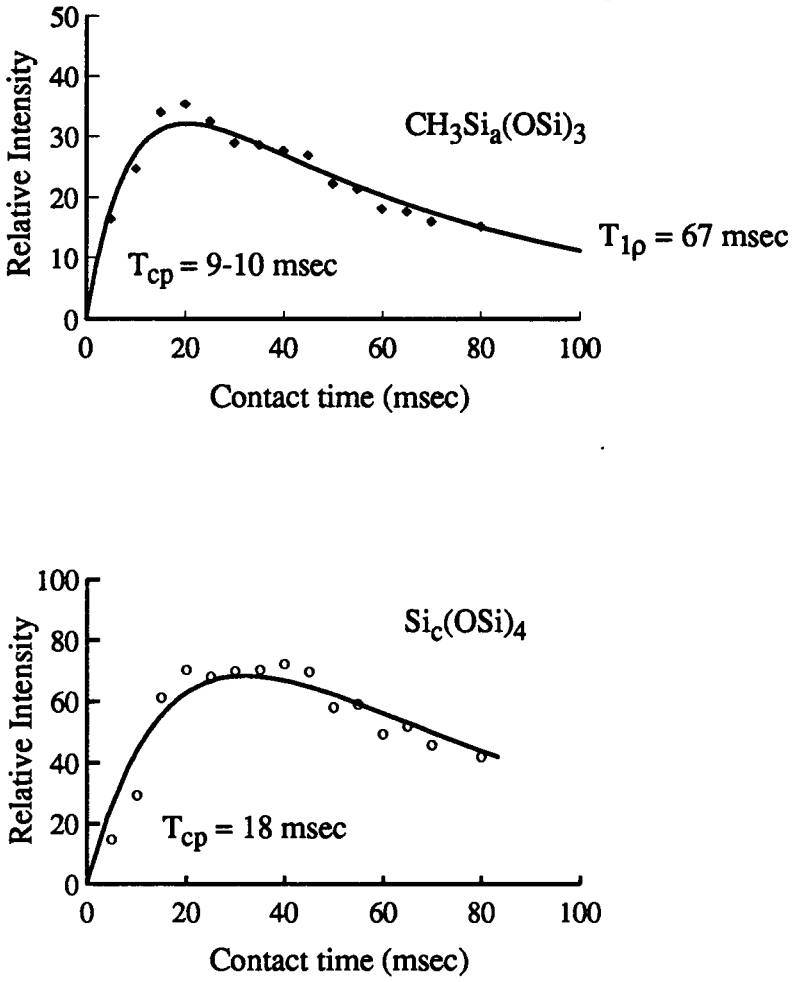

Figure 7.7 - Contact time curves for the $CH_3Si_a(OSi)_3$ and $Si_c(OSi)_4$ silicons in the 25/75 MTES/TEOS copolymer sample from 15 2D ^1H-^{29}Si heteronuclear correlation experiments, together with the calculated curves.

7.3.1.5 Discussion

The $Si_c(OSi)_4$ contact time data for the different MTES/TEOS copolymers were fitted slightly better when two weighted cross polarization rates were used (Figures 7.3-7.5). In the weighted fitting of the contact time curves the larger T_{cp} value was in all cases very similar to that obtained from fitting the curve with a single T_{cp} value. The implication is that although a range of cross polarization rates would be expected due to the amorphous nature of the copolymers, the methyl groups are distributed evenly enough throughout the whole polymer matrix that the average distance range between a probing group ($-CH_3$) and the fully condensed quaternary silicons ($Si_c(OSi)_4$), is narrow, providing further evidence that the monomers in the MTES/TEOS copolymers are randomly mixed.

The ^1H to Si_c distance was determined using: equation (7.2), a $\equiv Si_a-CH_3$ distance of 2.6-2.7 Å, $CH_3Si_a(OSi)_3$ T_{cp} values in Table 7.2 and the $Si_c(OSi)_4$ dominant T_{cp} values listed in Table 7.4. The distance range determined for each sample is:

1)25/75 MTES/TEOS copolymer thermally treated	3.5-4.2 Å
2)25/75 MTES/TEOS copolymer - washed with D_2O	3.3-3.7 Å
3)10/90 MTES/TEOS copolymer	3.4-4.0 Å.

All these distances fall within the range calculated for a methyl proton to Si_c (3.0-5.3 Å) and they exclude the distance range of 2.7-2.9 Å which the study of pure silica gel demonstrated was the distance when hydroxyl groups are the principal source of polarization. Therefore it is concluded that the methyl groups are the principal source of polarization transfer to $Si_c(OSi)_4$ in the MTES/TEOS copolymer samples.

In addition, if the hydroxyl protons were the principal source for cross polarization then the calculated distances should be dramatically different from sample to sample due to the different hydroxyl concentrations. The distances determined from the contact time data of

all three samples are all within the same range. Therefore the principal source of cross-polarization to Si_c must be the methyl groups which are evenly distributed throughout the copolymer. An implication of this is that at these concentrations of $\equiv Si_a\text{-}CH_3$, all the Si_c nuclei are close to one or more $-CH_3$ groups. Therefore in a cross polarization experiment all the Si_c nuclei should be cross polarized.

Little ambiguity exists in the data from the set of 2D experiments since the second dimension differentiates the two cross polarization sources. The fact that these experiments also gave a narrow $^1H\text{-}Si_c$ distance range, of approximately the same magnitude, provides further evidence that the methyl groups are distributed throughout the copolymer matrix.

All the ^1H to $Si_c(OSi)_4$ distances strongly suggest that the two monomers are intimately mixed at a molecular level, confirming the previous conclusions of Chapter 4 that the methyl functionality is distributed throughout the MTES/TEOS copolymer matrix, i.e. the monomers do not form a phase separated copolymer.

The ^{29}Si intensities (M_o values) obtained from fitting the contact time data provide information with respect to the proportion of silicons in different environments that are cross polarized. These data compare well with the quantitative 1D spectrum in which the relative signal intensities are indicative of the actual proportion of different silicons present, Table 7.5. These results suggest that essentially all of the $Si_c(OSi)_4$ are cross polarized by the methyl protons, supporting the above conclusion that the two monomers are intimately mixed in the copolymer.

Table 7.5 - The percentage of $Si_c(OSi)_4$ and $CH_3Si_a(OSi)_3$ which are cross polarized (determined from the fitting of the variable contact time curves) together with the actual percentages that exist in the thermally treated 25/75 MTES/TEOS copolymer sample (determined from a quantitative 1D ^{29}Si NMR spectrum). Note that the quantitative 1D ^{29}Si NMR spectrum contains a small signal for $Si(OH)(OSi)_3$ which is not included in this table, so the concentrations do not sum to 100%.

^{29}Si resonances	M_o (from fit)*	^{29}Si NMR spectrum**
$CH_3Si_a(OSi)_3$	(18 ± 2)%	(19 ± 2)%
$Si_c(OSi)_4$	(73 ± 2)%	(75 ± 7)%

* The errors given are estimates obtained by fitting the contact time data with a range of $T_{1\rho}$ values.

** error estimated to be 10%.

7.3.2 ^{19}F-^{29}Si Contact Time Experiments

To complement the ^{1}H-^{29}Si cross polarization studies, ^{19}F-^{29}Si contact time experiments were carried out on another functionalized silane copolymer containing ^{19}F. These experiments provide complementary data that are not compromised by the possible presence of hydroxyl groups.

7.3.2.1 Simplification of the T_{cp} Expression for the TFPTMS/TEOS Copolymer

The $CF_3CH_2CH_2Si(OMe)_3$/TEOS copolymer (TFPTMS/TEOS), unlike the MTES/TEOS copolymer, does not contain an internal reference, i.e. an unambiguous ^{19}F to Si_a distance, that can be used for the T_{cp} calculations. Therefore the internuclear distance between ^{19}F and $Si_c(OSi)_4$ (Figure 7.8) cannot be calculated using equation (7.2), as was done previously. Instead, the ^{19}F to Si_c distance must be calculated explicitly using equation (1.18), which means that the homo- and heteronuclear second moments for the ^{19}F and ^{29}Si nuclei must be evaluated.

7.3.2.1A ^{19}F Second Moment Considerations

There are three possible contributions to the total second moment of ^{19}F: dipolar interactions between the ^{19}F nuclei in a single $-CF_3$ group, dipolar interactions between the ^{19}F nuclei in two different $-CF_3$ groups and dipolar interactions between the ^{19}F in the $-CF_3$ group and the ^{29}Si nuclei. The dipolar interaction has a $1/r^6$ dependence and therefore the further apart the two dipoles are, the weaker the interaction. Consequently, the contributions to the total second moment of ^{19}F can be simplified. The dipolar interaction between two ^{19}F in two different $-CF_3$ groups is expected to be significantly smaller interaction than that of two ^{19}F in the same $-CF_3$ group for two reasons. First, the two ^{19}F are much further apart when located on two different $-CF_3$ groups and secondly, the motion of both $-CF_3$ groups will further reduce the dipolar interactions between them.[1.22] Thus the interaction between ^{19}F in two

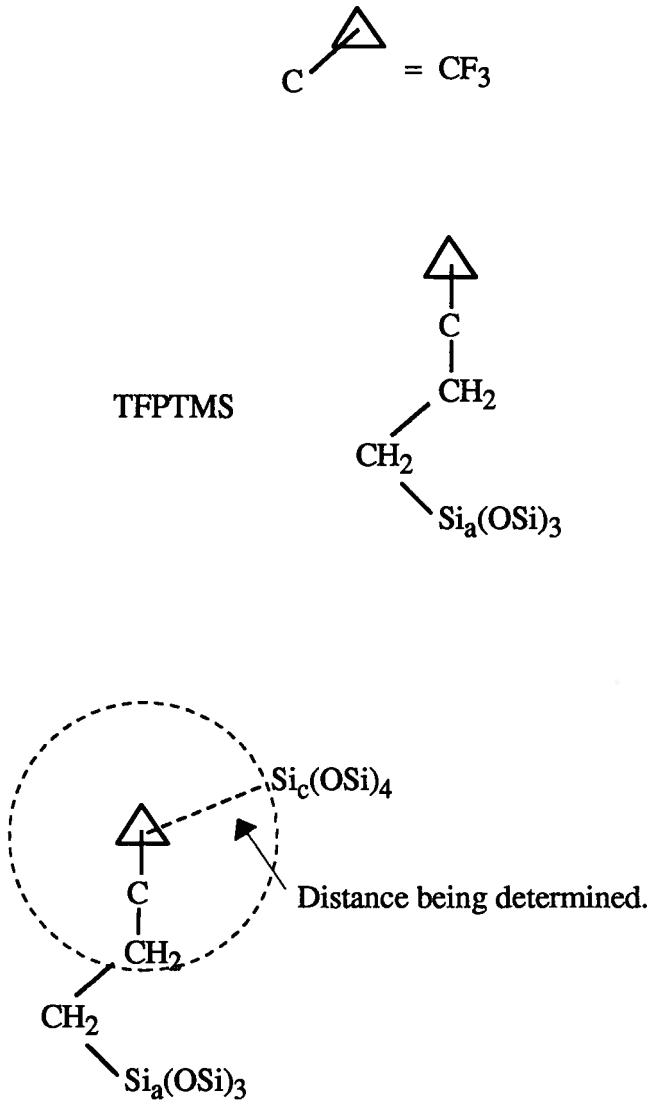

Figure 7.8 - The definition of Si_a and Si_c for the TFPTMS/TEOS copolymer samples.

different -CF_3 groups will not be considered in the homonuclear second moment calculations. The magnitude of the dipolar interaction between the ^{19}F in a -CF_3 group and a ^{29}Si nucleus is insignificant compared to the dipolar interaction between two ^{19}F in the same CF_3 group, principally due to the low natural abundance of ^{29}Si (4.7%), the low ^{29}Si magnetogyric ratio and the large distances involved. The above arguments reduce the defining interactions of the total second moment for ^{19}F to only one term, the dipolar interaction between the ^{19}F in a single -CF_3 group averaged over the motion of the group. The total second moment is in fact invariant to the presence of motion, but the *measured* second moment is not because part of the resonance is shifted far from the center of the resonance where it is hidden in the noise and consequently not measured.[1.10, 1.35, 7.5]

The TFPTMS/TEOS copolymer is a powder sample, with motion around the -CF_3 three-fold axis and possible motion within the chains of the polymer. In the second moment calculation, equation (1.20), the term $(3\cos\theta_{ij}-1)$, is therefore first averaged over the motion to obtain the second moment for a single orientation of the group. Then the average over all possible orientations is calculated.[1.22]

Equation (7.4) is the general equation for the homonuclear second moment when considering motion.[1.22]

$$\langle \Delta\nu^2 \rangle_{SS\ rot} = \frac{3}{4} \left(\frac{\gamma_S^2\, \hbar\, \mu_o}{4\pi}\right)^2 S(S+1) * \sum_i \left[\frac{3\cos^2\alpha_{ij} - 1}{2}\right]^2 \left[\frac{3\cos^2\theta_{ij} - 1}{r_{ij}^3}\right]^2 \tag{7.4}$$

The -CF_3 group in the TFPTMS/TEOS copolymer rotates about its C_3 axis. It has been shown by Pake that for the special cases where the rotation axis is perpendicular to the internuclear vector ($\alpha_{ij} = 90°$), as is the case for the -CF_3 group, the intramolecular second

moment for a powder is reduced to one-fourth that of the rigid lattice yielding equation (7.5).[1.22]

$$\langle \Delta\nu^2 \rangle_{SS\ rot} = \frac{3\ \gamma_S^4\ \hbar^2\ \mu_o^2\ S(S+1)}{256\ \pi^2} \sum_i \frac{(3\cos^2\theta_{ij} - 1)^2}{r_{ij}^6} \qquad (7.5)$$

The sum is over all relevant nuclei i when considering the jth nucleus. In the example being studied, S refers to ^{19}F (spin of ½) and the three ^{19}F atoms forming an equilateral triangle, giving $\Sigma\ r_{ij}^{-6} = 2r_{F\text{-}F}^{-6}$.

The $-CF_3$ groups can have any orientation with respect to the external magnetic field. The second moment is thus averaged over all possible orientations [1.22], i.e. $\langle(3\cos^2\theta_{ij}-1)^2\rangle=4/5$ (where <..> means average value), simplifying the homonuclear second moment equation when considering motion to equation (7.6).

$$\langle \Delta\nu^2 \rangle = \frac{9\gamma_F^4\ \hbar^2\ \mu_o^2}{640\ \pi^2\ r_{F\text{-}F}^6} \qquad (7.6)$$

or in terms of field:

$$\langle \Delta B^2 \rangle = \frac{9\gamma_F^2\ \hbar^2\ \mu_o^2}{160\ r_{F\text{-}F}^6} \qquad (7.6B)$$

7.3.2.1B ^{29}Si Second Moment Considerations

The other second moment to be calculated is that of the ^{29}Si nuclei. There are two different dipolar interactions which contribute to the total second moment of ^{29}Si: dipolar interactions between two ^{29}Si and that between ^{19}F and ^{29}Si. The dipolar interaction between two ^{29}Si is negligible in comparison to the latter term due to the low natural abundance of ^{29}Si

(4.7%), with correspondingly large distances between two ^{29}Si nuclei. Consequently, the total ^{29}Si second moment is calculated considering only the heteronuclear dipolar interaction between the abundant ^{19}F nuclei in a $-CF_3$ group and the ^{29}Si nuclei, equation (1.21).

The polar coordinates, i.e. θ_{im} and r_{im} (Figure 1.7) in the heteronuclear second moment for a rigid lattice, equation (1.21), must be averaged over all space when considering motion, equation (7.7).

$$\langle \Delta\nu^2 \rangle_{IS\ rot} = \frac{\gamma_S^2 \gamma_I^2 \hbar^2 \mu_o^2 I(I+1)}{48\pi^2} \left(\frac{(3\cos^2\theta_{im} - 1)^2}{r_{im}^6} \right) \tag{7.7}$$

To evaluate equation (7.7), $\langle (3\cos^2\theta_{im}-1)^2 r_{im}^{-6} \rangle$ must be evaluated. The $\langle (3\cos^2\theta_{im}-1)^2 r_{im}^{-6} \rangle$ value is:

$$\left(\frac{(3\cos^2\theta_{im} - 1)^2}{r_{im}^6} \right) = \frac{1}{(p\ q)^2} \sum_{i,m}^{p\ q} \left[r_{im}^{-6} \left[\frac{(3\cos^2\theta_{im} - 1)^2}{5} + \frac{4(3\sin\theta_{im}\cos\theta_{im}\cos\phi_{im})^2}{15} + \frac{4(3\sin\theta_{im}\cos\theta_{im}\sin\phi_{im})^2}{15} + \frac{(3\sin^2\theta_{im}\sin 2\phi_{im})^2}{15} + \frac{(3\sin^2\theta_{im}\cos 2\phi_{im})^2}{15} \right] \right] \tag{7.8}$$

The derivation of equation (7.8) is given in Appendix 4. In equation (7.8), p represents the number of equivalent sites that the S (^{19}F) nucleus can occupy over the motion and q represents the number of equivalent sites that the I (^{29}Si) nucleus can occupy over the motion.

The evaluation of equation (7.8) for the amorphous TFPTMS/TEOS copolymer will consider the $-CF_3$ group at the center of a sphere where $Si_c(OSi)_4$ can be located anywhere on the surface of this sphere. Therefore the angles, θ_{im} and ϕ_{im} in equation (7.8) are averaged over all space. The distance calculated is well approximated by the distance from $Si_c(OSi)_4$ to

the center of the -CF_3 group, thus $\Sigma r_{Si\text{-}F}^{-6} = 3r_{Si\text{-}F}^{-6}$. With additional substitutions of I=½, p=3 and q=1, the final form for the heteronuclear second moment including motion is equation (7.9).

$$\langle \Delta\nu^2 \rangle_{IS} = \frac{\gamma_F^2 \gamma_{Si}^2 \hbar^2 \mu_o^2}{240 \pi^2 r_{Si\text{-}F}^6}$$

$$\langle \Delta B^2 \rangle_{IS} = \frac{\gamma_F^2 \hbar^2 \mu_o^2}{60 r_{Si\text{-}F}^6} \qquad (7.9)$$

7.3.2.1C Geometrical Factor in Equation (1.18)

The last term to be evaluated in equation (1.18) is the geometrical factor C_{IS}, equation (1.19). Consider once again the ^{29}Si nucleus and the three ^{19}F nuclei in the CF_3 group. The term a_{ij} in equation (1.19), defined by equation (1.19A), is independent of the relative ^{19}F to Si_c positions. The terms b_{im} and b_{jm} in equation (1.19), defined by equation (1.19B), are affected by the relative orientation of the ^{19}F to the $^{29}Si_c$.

In the case that Si_c is located anywhere on the shell of a sphere where the -CF_3 group is in the center, the terms in equation (1.19) involving b_{im} and b_{jm} must be averaged over all space:

$$\langle b_{im}^2 \rangle = \frac{\gamma_I^2 \gamma_S^2 \hbar^4 \langle (1-3\cos^2\theta_{im})^2 \rangle}{\sum_i r_{im}^6}$$

$$\therefore \quad \langle b_{im}^2 \rangle = \frac{4\gamma_I^2 \gamma_S^2 \hbar^4}{5 \sum_i r_{im}^6} \qquad (7.10)$$

and

$$\begin{aligned}
\langle(2b_{im} + b_{jm})^2\rangle &= \gamma_I^2\,\gamma_S^2\,\hbar^4 \left[\frac{2(1-3\cos^2\theta_{im})}{r_{im}^3} + \frac{(1-3\cos^2\theta_{jm})}{r_{jm}^3} \right]^2 \\
&= \gamma_I^2\,\gamma_S^2\,\hbar^4 \left[\frac{4\,\langle(1-3\cos^2\theta_{im})^2\rangle}{\sum_i r_{im}^6} \right. \\
&\quad \left. + \frac{2\langle(1-3\cos^2\theta_{im})(1-3\cos^2\theta_{jm})\rangle}{\sum_{i,j\ w/i\neq j} r_{im}^3\, r_{jm}^3} + \frac{\langle(1-3\cos^2\theta_{jm})^2\rangle}{\sum_j r_{jm}^6} \right]
\end{aligned} \tag{7.11}$$

As already discussed, the ^{19}F to Si_c distance being calculated is that to the middle of the $-CF_3$ group; therefore $r_{im}^{-6}=r_{jm}^{-6}$ and $\theta_{im}=\theta_{jm}$, and since $\langle(3\cos^2\theta_{im}-1)^2\rangle= 4/5$, equation (7.11) simplifies to:

$$\langle(2b_{im} + b_{jm})^2\rangle = \frac{28\gamma_I^2\,\gamma_S^2\,\hbar^4}{5\sum_i r_{im}^6} \tag{7.12}$$

$$\therefore \quad \langle(2b_{im} + b_{jm})^2 + (b_{im} + 2b_{jm})^2\rangle = \frac{56\gamma_I^2\,\gamma_S^2\,\hbar^4}{5\sum_i r_{im}^6} \quad .$$

Equation (1.19) can be re-expressed in terms of the average values of the individual terms. Then by substituting equations (7.10) and (7.12), and $N_S=3$ into equation (1.19), equation (7.13) is obtained for C_{IS}.

$$C_{IS} = 3\pi \sqrt{\frac{\langle a_{ij}^2\rangle\langle b_{im}^2\rangle}{N_S \langle a_{ij}^2\rangle\langle (2b_{im} + b_{jm})^2 + (b_{im} + 2b_{jm})^2\rangle}}$$

$$\therefore \quad C_{IS} = 3\pi \sqrt{\frac{\langle b_{im}^2\rangle}{N_S \langle (2b_{im} + b_{jm})^2 + (b_{im} + 2b_{jm})^2\rangle}} \tag{7.13}$$

$$\therefore \quad C_{IS} = \pi \sqrt{\frac{3}{14}}$$

The equation to determine the ^{19}F to Si_c distance ($r_{Si\text{-}F}$), equation (7.14), in terms of known parameters: $r_{F\text{-}F}$ (the ^{19}F-^{19}F distance within the CF_3 group) and T_{cp} is obtained, by substituting equations (7.13), (7.9) and (7.6) into equation (1.18) .

$$r_{Si\text{-}F} = \sqrt[6]{\frac{\gamma_S^2 \hbar \mu_o r_{F\text{-}F}^3 T_{cp}}{6\sqrt{105}}} \tag{7.14}$$

7.3.2.2 Analysis of the ^{19}F-^{29}Si Contact Time Experimental Results

A typical set of spectra obtained from the ^{19}F-^{29}Si contact time experiment is shown in Figure 7.9. As before, this series of 1D spectra was Fourier transformed, integrated relative to each other, and the relative peak intensities calculated using equation (7.1).

The ^{19}F-^{19}F distance in a -CF_3 group was determined to be 2.16 Å using a trigonometric calculation and literature values [7.8] for the F-C-F bond angle and ≡C-F bond length. The contact time curves and the fits obtained for one sample are shown in Figure 7.10. The $T_{1\rho}$ (^{19}F) value for each sample was determined from the decay of the $CF_3CH_2CH_2Si_a(OSi)_3$ silicon intensity as a function of contact time, as described previously for the MTES/TEOS copolymer since this resonance shows the clearest decay. The T_{cp} values

were determined from the non-linear least squares fitting of the Si_c contact time curve with equation (1.17), keeping $T_{1\rho}$ (^{19}F) fixed. A summary of the $T_{1\rho}$ (^{19}F) and T_{cp} values are given in Table 7.6. The $r_{Si\text{-}F}$ distances for the different ^{29}Si environments for each sample given in Table 7.7 were calculated using equation (7.14), the $r_{F\text{-}F}$ distance and the T_{cp} data given in Table 7.6.

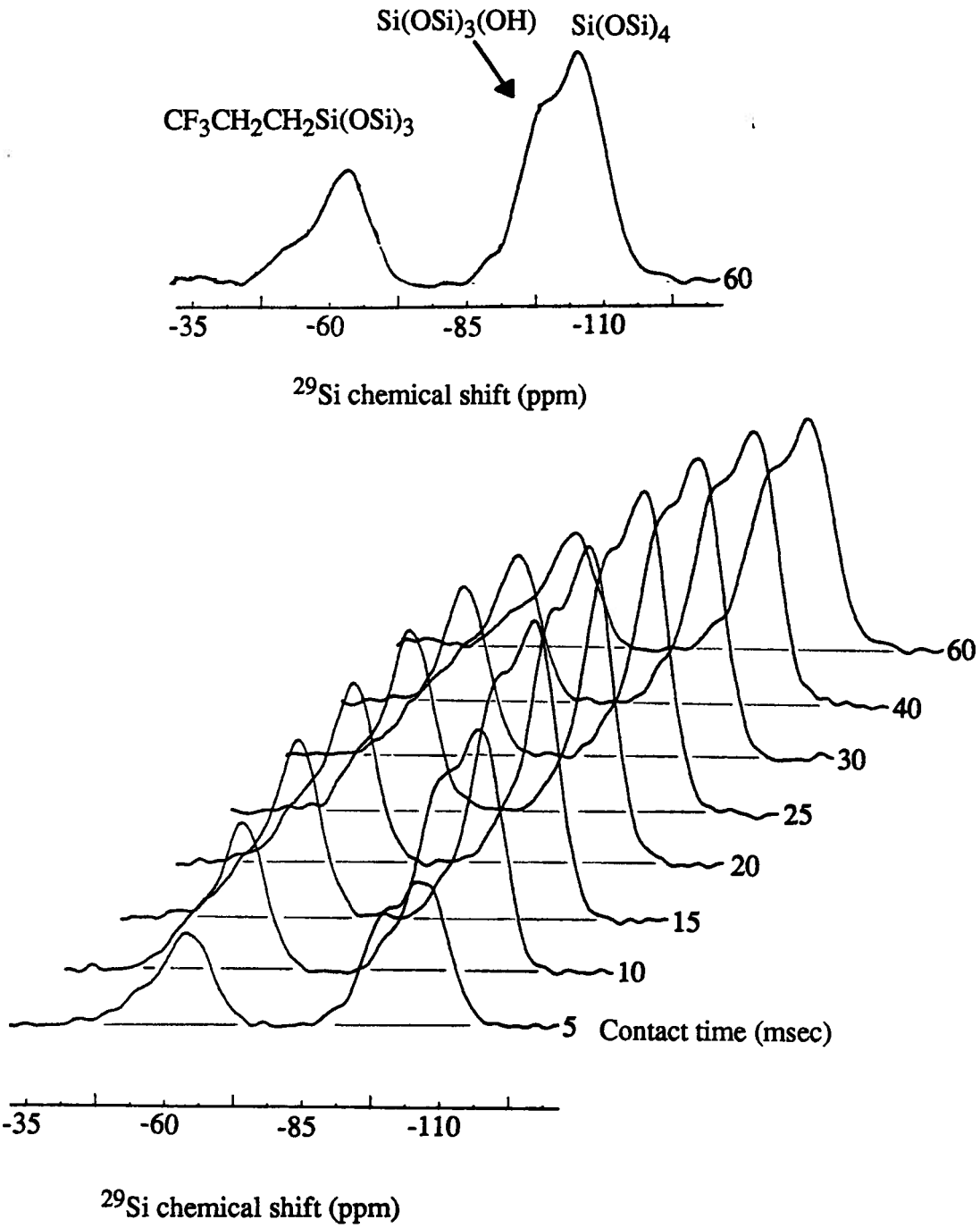

Figure 7.9 - ^{19}F-^{29}Si CP/MAS spectra for the thermally treated 25/75 $CF_3CH_2CH_2Si(OMe)_3$/TEOS copolymer sample.

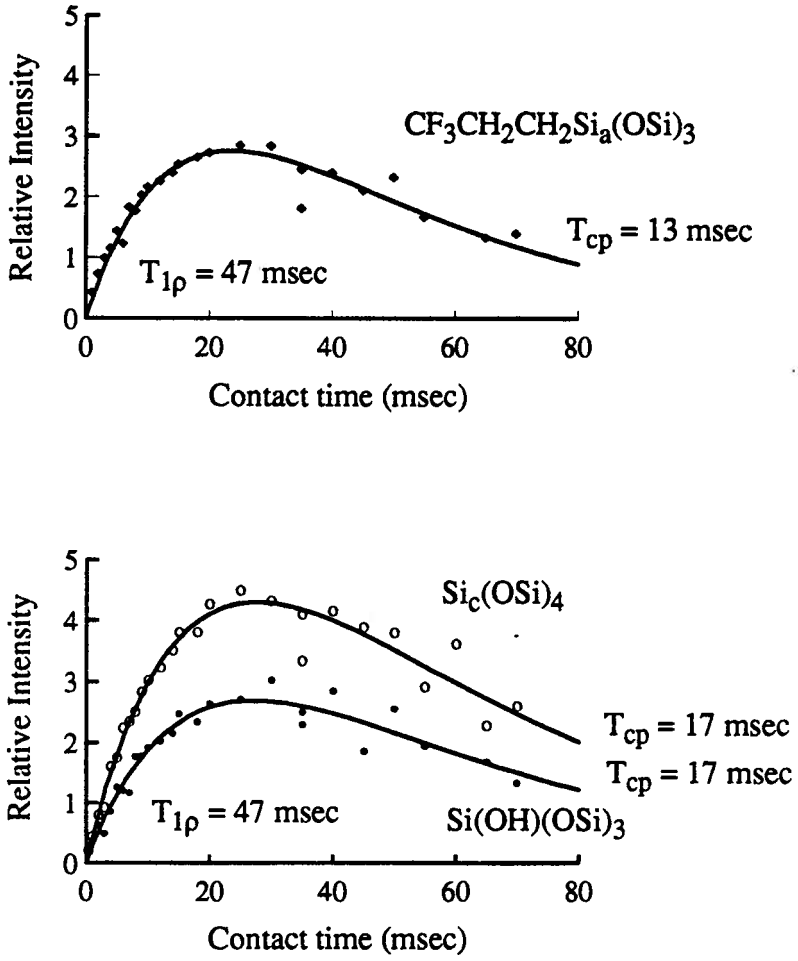

Figure 7.10 - Contact time curves for the $CF_3CH_2CH_2Si_a(OSi)_3$ and $Si_c(OSi)_4$ silicons in the thermally treated TFPTMS/TEOS copolymer sample, together with the calculated curves obtained using equation (1.17) and the data in Table 7.6.

Table 7.6 - The $T_{1\rho}$ and T_{cp} values for the ^{29}Si resonances in different TFPTMS/TEOS copolymer samples. The $T_{1\rho}$ values were determined by fitting the decay of the CF_3···$Si(OSi)_3$ contact time curve and the T_{cp} values by fitting the indicated Si signal contact time curve. The $T_{1\rho}$ was fixed when the T_{cp} values were determined.

Samples	^{29}Si resonance	$T_{1\rho}$ (msec)*	T_{cp} (msec)*
25/75 TFPTMS/TEOS	CF_3···$\overline{Si_a}(OSi)_3$	47 ± 5	13 ± 1
	$\overline{Si_c}(OSi)_4$		17 ± 2
Thermally treated 25/75 TFPTMS/TEOS**	CF_3···$\overline{Si_a}(OSi)_3$	65 ± 7	10 ± 1
	$\overline{Si_c}(OSi)_4$		11 ± 1
10/90 TFPTMS/TEOS	CF_3···$\overline{Si_a}(OSi)_3$	45 ± 5	15 ± 2
	$\overline{Si_a}(OSi)_4$		30 ± 3

* error estimated to be 10%.

** Thermally treated at 300°C under nitrogen for 2.5 hours.

Table 7.7 - Distance between $^{29}Si_c(OSi)_4$ and the $-CF_3$ functionality (Å) obtained using equation (7.14), $r_{F\text{-}F} = 2.16 \pm 0.01$ Å and the T_{cp} data presented in Table 7.6.

Samples	$r_{F\text{-}Si} \pm 0.1$ Å
25/75 TFPTMS/TEOS	3.2
Thermally treated 25/75 TFPTMS/TEOS	3.0
10/90 TFPTMS/TEOS	3.5

* The $T_{1\rho}$ value was obtained from fitting the decay of the $CF_3 \cdots Si_a(OSi)_3$ contact time curve.

7.3.2.3 Discussion

Using equation (7.14), the r_{F-F} distance and the T_{cp} values given in Table 7.6, the ^{19}F-Si_c distance was determined for each TFPTMS/TEOS copolymer sample. As expected, the calculated distances are similar for all three samples. The $Si_c(OSi)_4$ contact time curves are fitted well with only a single T_{cp} value. This implies that although the copolymer is amorphous, the probe group ($-CF_3$) is well distributed throughout the copolymer matrix such that the average distance from a $-CF_3$ group to a $Si_c(OSi)_4$ lies within a narrow range. This is a similar situation to that observed for the MTES/TEOS copolymer samples investigated.

To determine the relative concentrations of the silicons in different environments and to confirm the validity of the assumed approximations, quantitative 1D ^{29}Si NMR spectra for the 25/75 and 10/90 TFPTMS/TEOS copolymers were acquired. The relative concentrations of Si_a and Si_c were compared to the M_o values from the contact time curves, Table 7.8. The relative concentrations obtained by the latter method are an indication of the percentage of the $Si_c(OSi)_4$ taking part in the cross polarization process. In both TFPTMS/TEOS copolymers, most of the $Si_c(OSi)_4$ are cross polarized, supporting the conclusion that functionalized silica gels synthesized using the copolymerization preparation have the functionality evenly distributed throughout the copolymer matrix.

The ^1H to Si_c distances calculated for the different MTES/TEOS copolymers were in the range of 3.3-4.2 Å. The ^{19}F to Si_c distance calculated for the different TFPTMS/TEOS copolymers is in the range of 3.0-3.5 Å. The calculated distances for both sets of variable contact time experiments are consistent with the fact that the 'probe' groups in both copolymers ($-CH_3$ in the MTES/TEOS copolymers and $-CF_3$ in the TFPTMS/TEOS copolymers) are well distributed throughout the copolymer matrix. These "probe" groups are evenly enough distributed that the average distance from any probe group to $Si_c(OSi)_4$ lies

Table 7.8 - The percentages of $Si_c(OSi)_4$ and $CF_3{\cdots}Si_a(OSi)_3$ which are cross polarized (determined from the fitting of the contact time curves) and the actual percentages that exist in the samples indicated (as determined from quantitative 1D ^{29}Si NMR spectra).

Sample	^{29}Si resonances	M_o (from fit) *	^{29}Si NMR spectrum **
25/75 TFPTMS/TEOS			
	$CF_3{\cdots}Si_a(OSi)_3$	(23 ± 1)%	(21 ± 2)%
	$Si_c(OSi)_4$	(44 ± 1)%	(48 ± 5)%
10/90 TFPTMS/TEOS			
	$CF_3{\cdots}Si_a(OSi)_3$	(13 ± 3)%	(8 ± 1)%
	$Si_c(OSi)_4$	(56 ± 3)%	(65 ± 7)%

* estimated errors obtained by fitting the experimental contact time data with a range of $T_{1\rho}$ values.

** error estimated to be 10%

within a relatively narrow distance range.

7.4 SUMMARY OF CONCLUSIONS

^{1}H-^{29}Si contact time measurements were performed on four MTES/TEOS copolymers. The fitting of the silicon intensities as functions of contact time for the different samples provided T_{cp} values. The methyl proton to Si_c distances were determined using these T_{cp} values and the known $\equiv Si_a$-CH_3 distance. The ^{1}H to Si_c distances for all the samples were in the range of 3.3-4.2 Å.

^{19}F-^{29}Si contact time measurements were performed on three TFPTMS/TEOS copolymer samples. T_{cp} values were determined for Si_c as described above. The -CF_3 to Si_c distances were calculated for all of the samples using the Si_c T_{cp} values and the known $r_{F\text{-}F}$ distance in a -CF_3 group. The ^{19}F to Si_c distance for all the samples was in the distance range of 3.0-3.5 Å.

The estimated distance range for -CH_3 to Si_c and -CF_3 to Si_c are relatively narrow and the results are very similar for all seven copolymer samples studied. The determined distances, their narrow distributions and the fact that essentially all the $Si_c(OSi)_4$ nuclei were cross polarized in the samples, provide conclusive evidence that in all cases the functionality is evenly distributed throughout the copolymer matrices.

CHAPTER 8

8.1 SUMMARY

The principal goal of this thesis was to structurally characterize a particular class of functionalized silica gels using NMR spectroscopy. An alternative synthesis for the functionalized silica gel was introduced that results in a reproducible product and leaves the functionalities evenly distributed and accessible for future reactions.

The integrity of the functionalities was established utilizing ^{13}C and ^{29}Si CP/MAS NMR experiments. Deconvoluted quantitative ^{29}Si MAS NMR spectra provide information about the relative proportions of the different silicon environments in the samples. Two-dimensional ^{1}H-^{29}Si heteronuclear correlation experiments, which identify the ^{1}H sources of cross polarization for each silicon resonance, were used to distinguish between domain structured and "mixed" copolymers. The 2D NMR results unambiguously demonstrate that the MTES and TEOS monomers in a MTES/TEOS copolymer are "mixed" and not "phase separated".

To quantify the extent of mixing in the MTES/TEOS copolymer the kinetic constants for the hydrolysis and dimer formation were determined. Both homopolymer systems, MTES and TEOS, were first studied in order to obtain reference data for the more complex kinetics of the MTES/TEOS copolymerization.

The TEOS hydrolysis and dimer formation reactions were investigated first to provide reference data, so that the effect of such variables as: an organic functionality (Chapter 4), the presence of two different monomers (Chapter 4), and the presence of organic drying agents (Chapter 5) on the hydrolysis and dimer formation rate constants could be determined. The kinetic constants for all the sequential hydrolysis and dimer formation of the TEOS polymerization were calculated from the experimental data for a series of pH values, using a

simple kinetic model. The kinetic model considered only one re-esterification reaction, the one between $Si(OH)_3(OEt)$ and $Si(OH)_4$, which proved to be essential to respect the curve shape of $Si(OH)_3(OEt)$. From the series of pH dependent kinetic constants, pH independent kinetic constants for the hydrolysis and dimer formation reactions were derived for the first time. The magnitudes of the hydrolysis kinetic constants ($k_{T1\text{-}T3}$) increase with the number of hydroxyls, but they are not related in any simple incremental fashion.

In the study of the MTES homopolymerization, pH dependent kinetic rate constants for the hydrolysis and dimerization reactions were also determined. As in the TEOS case, pH independent kinetic rate constants were also calculated for the first time. These kinetic rate constants provide the first quantitative evidence that the MTES monomer hydrolyzes faster than the TEOS monomer in each sequential hydrolysis step. The homodimerization rate constant, however, was found to be slower for the MTES than for the TEOS monomer. As in the TEOS case, the kinetic model had to include the last hydrolysis as an equilibrium reaction in order to respect the shape of the $CH_3Si(OH)_2(OEt)$ relative concentration curve.

The kinetic constants determined for the MTES and TEOS hydrolysis and dimer formation reactions were used as the starting point for the analysis of the MTES/TEOS copolymer kinetic data. The kinetic constants for the MTES/TEOS copolymer hydrolysis and dimer formation reactions were found to be somewhat different from those of the homopolymerizations, due at least in part to the unavoidable differences in reaction mixture compositions. The TEOS monomer, in comparison to the MTES monomer, was more affected by the presence of the other type of monomer. Reactivity ratios of 0.8 and 1 were calculated from the dimer formation rate constants for the MTES and TEOS monomers, respectively. These reactivity ratios indicate that the MTES/TEOS reaction mixture tends toward forming a random copolymer. Altering the relative monomer proportions and the

water/(total silane) ratio had little effect on the relative dimer ratios, suggesting that the MTES/TEOS copolymer has a very strong tendency to form a random copolymer.

The final step in the characterization of the MTES/TEOS copolymer involved a detailed analysis of the ^{1}H-^{29}Si CP/MAS contact time curves for a number of different samples with minimal -OH content in order to determine average -$\overline{CH_3}$ to $\overline{Si_c}(OSi)_4$ distances. These calculated distances confirmed that the methyl functionality was the principal source of cross polarization and is distributed throughout the copolymer matrix. These results were supported by a similar ^{19}F-^{29}Si CP/MAS contact time study, on $CF_3CH_2CH_2Si(OMe)_3$/TEOS copolymer samples.

One possible application of these functionalized silica gels is the production of organofunctionalized glasses where the functionality would be evenly distributed throughout the copolymer matrix. Formamide is a commonly used drying agent, which prevents cracking so that large pieces of glass may be formed. The kinetic study of its effect on the hydrolysis and dimer formation of the TEOS, MTES homopolymerizations and MTES/TEOS copolymerization at a water/silane ratio of 11, found that only when the formamide concentration exceeds 20 mole % of the silane does it have a significant effect on the hydrolysis and dimer formation reactions. However, the largest reduction in the gelation time for TEOS occurred at lower formamide concentrations. This is the first evidence that the decrease in gelation time caused by the presence of formamide is not a consequence of a change in the hydrolysis and dimer formation rates. High resolution ^{1}H, ^{13}C and ^{15}N solution NMR studies over a 90 days period clearly demonstrated that the majority of the formamide remained intact during the TEOS homopolymerization, i.e. no chemical bonds were formed neither to the carbonyl nor to the amide functional group. Since the conversion of functionalized silica gels to glasses involves "hot pressing" the gel, the thermal stabilities of a

number of different functionalized copolymers were determined. Of the copolymers studied, the methyl functionalized copolymer has the highest thermal stability.

Suggestions for Future Investigations

The present research has established a simple kinetic model and supplied reference data for the hydrolysis and dimer formation reactions of the TEOS and MTES homopolymerizations, as well as that of the MTES/TEOS copolymerization. Further investigations on the effect of the functionality's structure on the hydrolysis and dimer formation rate constants could provide further insight into the reaction mechanism.

The results presented in Chapter 5 clearly show that formamide significantly reduces the gelation time of TEOS, even at concentrations that do not affect the hydrolysis rate. Further investigations are required to determine if the reduction in the gelation time is due to the interference of formamide with the cross-linking mechanism.

Attempts at directly measuring the $T_{1\rho}$ (^1H) yielded results that were not in all cases in agreement with the values obtained from the contact time curve fits. The effect of the method of detection and of other experimental parameters, such as the spinning rate and the pulse power, should be investigated, since in some cases especially when no significant decay of the contact time curve is observed, reliable direct measurements of the $T_{1\rho}$ (^1H) may be necessary.

Preliminary results suggest that thermal treatment removes differences in the extent of crosslinking which seems to occur in samples synthesized with an acid versus those synthezised with a base catalyst. Further work is required to determine the effect of thermal treatment on the final polymeric structure.

Overviewing the thermal stabilities of the different functionalitized copolymers, I propose that for saturated alkanes the weakest bond is the initial C-Si bond and for large functionalities involving unsaturated groups, such as the phenyl group in the phenethyl functionality, the weakest bond is the C-C bond connecting the unsaturated group to the rest

of the functionality. To confirm this hypothesis the thermal stabilities of a number of other functionalized copolymers must be determined.

Borosilicate glasses have a lower glass transition temperature than the corresponding silicate glasses (as low as 600°C).[6.4] Based on the thermal stability data gathered, it is proposed that an appropriate first attempt to make functionalized low-temperature glasses should involve a methyl functionalized *borosilicate* copolymer gel which is thermally treated under nitrogen.

REFERENCES

1.1 U.Deschler, P. Kleinschmidt and P. Panster
Angew. Chem. Int. Ed. Engl., 25, (1986), 236

1.2 Kirk-Othmer Encyclopedia of Chemical Technology, Third Edition, 20, 967
Eds. E.P. Plueddemann
Wiley, NY, (1982)

1.3 S. R. Elliott
J. Non-Cryst. Solids 123, (1990), 149

1.4 L.W. Jelinski and M.T. Melchior in
NMR Spectroscopy Techniques
Eds. C. Dybowski and R.L. Lichter
Marcel Dekker Inc., N.Y., (1987), 253

1.5 M.Mehring in
NMR - Basic Principles & Progress
Eds. P. Diehl, E. Fluck and R. Kosfeld
Springer-Verlag, Heidelberg, Germany, (1976), 112

1.6 F.K. Chow and E.Grushka in
Silylated Surfaces
Eds. D.E. Leyden and W.T. Collins
Gordon & Breach Science Publishers Ltd., N.Y., (1980), 301

1.7 G.L. Wilkes, H. Huang and R.H. Glaser in
ACS Advances in Chemistry Series: Silicon-Based Polymer Science
Eds. J.M. Zeigler and F.W.G. Fearon
American Chemical Society, Washington, DC, (1990), 207

1.8 G.P. Royer and F.A. Liberatore in
Silylated Surfaces
Eds. D.E. Leyden and W.T. Collins
Gordon & Breach Science Publishers Ltd., (1980), 189

1.9 Nuclear Magnetic Resonance Spectroscopy
F.A. Bovey
Academic Press, NY, (1987)

1.10 Solid State NMR for Chemists
C.A. Fyfe
Ampersand Printing, Guelph, Canada, (1984)

1.12 A) E.R. Andrew, A. Bradbury and R.G. Eades
Nature, 182 , (1958), 1659

B) I.J. Lowe
Phys. Rev. Lett., 2, (1959), 285

1.13 "^{29}Si-NMR Spectroscopic Results", 65
H.Marsmann
NMR Basic Principles & Progress, 17
Eds. P. Diehl, E. Fluck and R. Kosfeld
Springer-Verlag, Berlin, (1981)

1.14 A) J. Schaefer, S.H. Chin and S.I. Weissman
Macromolecules, 5, (1972), 798;
B) J. Schaefer, E.O. Stejskal and R. Buchdahl
Macromolecules, 8, (1975), 291;
C) J. Schaefer and E.O. Stejskal
J. Am. Chem. Soc., 98, (1976), 1031

1.15 A) The Chemistry of Silica
R.K. Iler
Wiley, N.Y., (1979)
B) R.K. Iler
J. Coll. Int. Sci., 75, (1980), 138

1.16 Silane Coupling Agents
E.P. Plueddeman
Plenum Press, N.Y., (1982), 333

1.17 R.J. Burt, G.J. Leigh and C.J. Pickett
J.C.S. Chem. Comm., (1976), 940

1.18 Nuclear Magnetic Resonance Spectroscopy, A Physicochemical View
R.K. Harris
Pitman, London, (1983)

1.19 A) A. Pines, M.G. Gibby and J.S. Waugh,
Chem. Phys. Lett., 15, (1972), 273
B) M.G. Gibby, A. Pines and J.S. Waugh,
Chem. Phys. Lett., 16, (1972), 296
C) A. Pines, M.G. Gibby and J.S. Waugh,
J. Chem. Phys., 59, (1973), 569

1.20 G.E. Maciel and D.W.J. Sindorf
J. Am. Chem. Soc., 102, (1980), 7606

1.21 Modern NMR Spectroscopy
J.K.M. Sanders and B.K. Hunter
Oxford University Press, N.Y., (1989)

1.22 Principles of Magnetic Resonance
C.P. Slichter
Springer-Verlag, NY, (1990)

1.23 S.R. Hartmann and E.L. Hahn
Phys. Rev., 128, (1962), 2042

1.24 L.W. Jelinski in
Chain Structure and Conformation of Macromolecules
Ed. F.A. Bovey
Academic Press, NY, (1982), 223

1.25 R.A. Komoroski in
High Resolution NMR Spectroscopy of Synthetic Polymers in Bulk
Ed. R.A. Komoroski
VCH Publishers, Inc., Deerfield Beach, Florida, (1986), 19

1.26 C.S. Yannoni
Acc. Chem. Res., 15, (1982), 201

1.27 G.G. Almond, R.K. Harris and P. Graham
J. Chem. Soc., Chem. Commun., (1994), 851

1.28 F. Bloch
Phys. Rev., 11, (1958), 841

1.29 Experimental Pulse NMR: A Nuts and Bolts Approach
E. Fukushima and S.B. Roeder
Addison-Welsey Publishing, Co., Reading, Massachusetts (1981)

1.30 R.A. Wind in
Modern NMR Techniques and Their Application in Chemistry Practical Spectroscopy Series, 11
Eds. A.I. Popov and K. Hallenga
Marcel Dekker, Inc., N.Y., (1991), 125

1.31 M. Alla and E. Lippmaa
Chem. Phys. Lett., 37, (1976), 260

1.32 G.E. Maciel and D.W. Sindorf
J. Am. Chem. Soc., 103, (1981), 4263

1.33 D.W. Sindorf and G.E. Maciel
J. Phys. Chem., 86, (1982), 5208

1.34 J.H. Van Vleck
Phys. Rev., 74, (1948), 1168

1.35 G.E. Pake in
Solid State Physics Advances in Research and Application 2
Eds. F. Seitz and D. Turnbull
Academic Press Inc., NY, (1956), 1

1.36 A) J. Jeener
Ampere International Summer School
Basko Polje, Yugoslavia, (1971)
B) C.A. Fyfe, G.C. Gobbi and G.J. Kennedy
J. Phys. Chem., 89, (1985), 277

1.37 A. Kumar, D.D. Welti and R.R. Ernst
J. Magn. Reson., 18, (1975), 69

1.38 P. Caravatti, G. Bodenhausen, R.R. Ernst
Chem. Phys. Lett., 89, (1982), 363

1.39 W.P. Aue, E.Bartholdi and R.R. Ernst
J. Chem. Phys., 64, (1976), 2229

1.40 C. Lin and J.D. Basil
Mat. Res. Soc. Symp. Proc., 73, (1986), 585
Better Ceramics Through Chemistry II
Eds. C.J. Brinker, D.E. Clark and D.R. Ulrich
Materials Research Society, Pittsburgh, Pennsylvania

1.41 M.W. Colby, A. Osaka and J.D. Mackenzie
J. Non-Cryst. Solids, 99, (1988), 129

1.42 I. Artaki, M. Bradley, T.W. Zerda and J. Jonas
J. Phys. Chem., 89, (1985), 4399

1.43 K.D. Keefer
Mat. Res. Soc. Symp. Proc., 32, (1984), 15
Better Ceramics Through Chemistry
Eds. C.J. Brinker, D.E. Clark and D.R. Ulrich
Elsevier Science Publishing Co., N.Y.

1.44 N. Zumbulyadis
Phys. Review B, 33(9), (1986), 6495

1.45 R. Dupree in
Nuclear Magnetic Resonance in Modern Technology NATO ASI series
Ed. G.E. Maciel
Kluwer Academic Publ., (1994), 87

Chapter 2

2.1 J.B. Peri and A.L. Hensley, Jr.
J. Phys. Chem., 72 (8), (1968), 2926

Chapter 3

3.1 Chemical Processing of Advanced Materials, Ch.4
Eds. L.L. Hench and W.J. Kenneth
John Wiley and Sons, N.Y., (1992)

3.2 L.W. Kelts, N. J. Effinger and S. M. Melpolder
J. Non-Cryst. Solids, 83, (1986), 353

3.3 A.H. Boonstra and T.N.M. Bernards
J. Non-Cryst. Solids, 108, (1989), 249

3.4 Modern NMR Techniques for Chemistry Research
A.E. Derome
Pergamon Press, Oxford, (1987)

3.5 Y. Sugahara, S. Okada, K. Kuroda, C. Kato
J. Non-Cryst. Solids, 139 (1992) 25

3.6 R.K. Harris and C.T.G. Knight
J. Chem. Soc. Chem. Comm., 421, (1980), 726

3.7 A) C.W. Gear
Numerical Initial Value Problems in Ordinary Differential Equations
Prentice-Hall, New Jersey, (1971)
B) C. Moore
Systemized collection of Ordinary Differential Equation Solvers
UBC Computing Center, Canada, (1989)

3.8 J.D. Satterlee
Concepts in Magnetic Resonance, 2, (1990), 119

3.9 J.L. Lippert, S.B. Melpolder and L.M. Kelts
J. Non-Cryst. Solids, 104, (1988), 139

3.10 Y. Hui, D. Zishang, J. Zhonghua and X. Xiaoping
J. Non-Cryst. Solids, 112, (1989), 449

3.11 M.F. Bechtold, R.D. Vest and L. Plambeck
J. Am. Chem. Soc., 90 (17), (1968), 4590

3.12 W.G. Klemperer and S.D. Ramamurthi
Mater. Res. Soc. Proc., 121, (1988), 1
Better Ceramics Through Chemistry III
Eds. C.J. Brinker, D.E. Clark and D.R. Ulrich
Materials Research Society, Pittsburgh, Pennsylvania

3.13 R.A. Assink and B.D. Kay
J. Non-Cryst. Solids, 99, (1988), 359

3.14 C.A. Balfe, K.J. Ward, D.R. Tallant and S.L. Martinez
Mater. Res. Soc. Proc. 73, (1986), 619
Better Ceramics Through Chemistry II
Eds. C.J. Brinker, D.E. Clark and D.R. Ulrich
Materials Research Society, Pittsburgh, Pennsylvania

3.15 J.C. Pouxviel, J.P. Boilot, J.C. Beloeil and J.Y. Lallemand
J. Non-Cryst. Solids, 89, (1987), 345

3.16 J.C. Pouxviel and J.P. Boilot
Mat. Res. Soc. Symp. Proc., 121, (1988), 37
Better Ceramics Through Chemistry III
Eds. C.J. Brinker, D.E. Clark and D.R. Ulrich
Materials Research Society, Pittsburgh, Pennsylvania

3.17 R. Aelion, A. Loebel and F. Eirich
J. Amer. Chem. Soc., 72, (1950), 575

3.18 R.A. Assink and B.D. Kay
Mat. Res. Soc. Symp. Proc., 32, (1984), 301
Better Ceramics Through Chemistry
Eds. C.J. Brinker, D.E. Clark and D.R. Ulrich
Elsevier Science Publishing Co., N.Y.

3.19 C.J. Brinker
J. Non-Cryst. Solids, 100, (1988), 31

3.20 M.T. Harris, R.R. Brunson and C.H. Byers
J. Non-Cryst. Solids, 121, (1990), 397

3.21 J.C. Ro and I.J. Chung
J. Non-Cryst. Solids, 110, (1989), 26

3.22 B.D. Kay and R.A. Assink
J. Non-Cryst. Solids, 104, (1988), 112

3.23 R.A. Assink and B.D. Kay
J. Non-Cryst. Solids, 107, (1988), 35

3.24 A) J. Chojnowski, M. Cypryk, K. Kazmierski and K. Rozga
J. Non-Cryst. Solids, 125, (1990), 40
B) G.E. Forsythe, M.A. Malcolm and C.B. Moler
Computer Methods for Mathematical Computations
Prentice-Hall, New York, 1977
C) H.H Rosenbrock, J. Computer, 3 (1960) 175

3.25 T.N.M. Bernards, M.J. van Bommel and A.H. Boonstra
J. Non-Cryst. Solids, 134, (1991), 1

3.26 C.W. Turner and K.J. Franklin
J. Non-Cryst. Solids, 91, (1987), 402

3.27 J.C. Pouxviel and J.P. Boilot
J. Non-Cryst. Solids, 94, (1987), 374

3.28 R.A. Assink, B.D. Kay
Mat. Res. Soc. Symp. Proc., 121, (1988), 25
Better Ceramics Through Chemistry III
Eds. C.J. Brinker, D.E. Clark and D.R. Ulrich
Materials Research Society, Pittsburgh, Pennsylvania

3.29 H. Schmidt, H. Scholze and A. Kaiser
J. Non-Cryst. Solids, 63, (1984), 1

Chapter 4

4.1 Organic Silicon Compounds
K.A. Andrianov
State Sci. Publ. House for Chemical Literature, Moscow, (1955)

4.2 E.Akeman
Acta Chem. Scand., 10, (1956), 298; 11, (1957), 298

4.3 Polymers: Chemistry & Physics of Modern Materials
J.M.G. Cowie
International Textbook Company Ltd., England, (1973)

4.4 The Chemistry of Silica: Solubility, Polymerization, Colloid and Surface Properties and Biochemisty
R.K. Iler
Wiley-Interscience Publication (1979)

4.5 M.J. Van Bommel, T.N.M. Bernards and A.H. Boonstra
J. Non-Cryst. Solids, 128, (1991), 231

Chapter 5

5.1 J.B. Chan and J. Jonas
J. Non-Cryst. Solids, 126, (1990), 79

5.2 C.J. Brinker
J. Non-Cryst. Solids, 100, (1988), 31

5.3 A.H. Boonstra and J.M.E. Baken
J. Non-Cryst. Solids, 122, (1990), 171

5.4 Sol-gel Technology for Thin Films, Fibers, Preforms, Electronics and Specialty Shapes
Ed. L.C. Klein
Noyes, New Jersey (1988)

5.5 A) M.J. Shapiro in
NMR Spectroscopy Techniques
Eds. C. Dybowski and R.L. Lichter
Marcel Dekker Inc., N.Y., (1987), 229
B) ^{15}N NMR Spectroscopy
G.J. Martin, M.L. Martin and J.P. Gouesnard, 18
Springer-Verlag, N.Y., (1981)

5.6 R.J. Chuck, D.G. Gillies and E.W. Randall
Mol. Phys., 16(2), (1969), 121

5.7 S.Wallace and L.L. Hench
Mat. Res. Soc. Symp. Proc., 32, (1984), 47
Better Ceramics Through Chemistry
Eds. C.J. Brinker, D.E. Clark and D.R. Ulrich
Elsevier Science Publishing Co., N.Y.

5.8 L.L. Hench, G. Orcel and J.L. Nogues
Mat. Res. Soc. Symp. Proc., 73, (1986), 35
Better Ceramics Through Chemistry II
Eds. C.J. Brinker, D.E. Clark and D.R. Ulrich
Materials Research Society, Pittsburgh, Pennsylvania

5.9 G. Orcel and L. Hench
J. Non-Cryst. Solids, 79, (1986), 177

5.10 G. Orcel, J. Phalippou and L. Hench
J. Non-Cryst. Solids, 104, (1988), 170

5.11 L.L. Hench and G. Orcel
J. Non-Cryst. Solids, 82, (1986), 1

5.12 G. Orcel, L.L. Hench, I. Artaki, J. Jonas and T.W. Zerda
J. Non-Cryst. Solids, 105, (1988), 223

5.13 T. Horiuchi
J. Non-Cryst. Solids, 144, (1992), 277

5.14 C.J. Brinker, E.P. Roth, D.R. Tallant, G.W. Scherer in
Science of Ceramic Chemical processing
Eds. L.L. Hench and D.R. Ulrich
John Wiley, NY, (1986), 37

5.15 A.H. Boonstra, T.N.M. Bernards and J.J.T. Smits
J. Non-Cryst. Solids, 109, (1989), 141

Chapter 6

6.1 Thermal Analysis
T. Daniels
Kogan Page Limited, London, England, (1973)

6.2 Instrumental Methods of Analysis, Fourth Edition, 457
H.H. Willard, L.L. Merritt and J.A. Dean
D.Van Nostrand Company, Canada, (1965)

6.3 S. Leonardelli, L. Facchini, C. Fretigny, P. Tougne and A.P. Legrand
J. Amer. Chem. Soc., 114 (16), (1992), 6412

6.4 Advances in Chemistry Series: Silicon-Based Polymer Science, 745
J.M. Zeigler and F.W.G. Fearon
American Chemical Society, Washington, DC, (1990)

6.5 A.H. Boonstra and C.A.M. Mulder
J. Non-Cryst. Solids, 105, (1988), 201

6.6 H.P. Boehm
Angewandte Chemie International Ed., 5 (6), (1966), 533

6.7 Carbon-13 NMR spectroscopy
H.Kalinowski, S. Berger and S.Braun
John Wiley and Sons, Toronto, (1988)

6.8 M.C. Weinberg
Mat. Res. Soc. Symp. Proc., 73, (1986), 431
Better Ceramics Through Chemistry II
Eds. C.J. Brinker, D.E. Clark and D.R. Ulrich
Materials Research Society, Pittsburgh, Pennsylvannia

6.9 L.L. Hench and J.K. West
Chem. Rev., 90, (1990), 33

6.10 H. Marsmann in
NMR Basic Principles and Progress, 17
Eds. P. Diehl, E. Fluck and R. Kosfeld
Springer-Verlag, N.Y., (1981), 65

6.11 K. Kamiya, T. Yoko, K. Tanaka, M. Takeuchi
J. Non-Cryst. Solids, 121 (1990) 182

Chapter 7

7.1 B. Pfleiderer, K. Albert, E. Bayer, L. van de Ven, J. de Haan and C. Cramers
J. Phys. Chem., 94, (1990), 4189

7.2 R.K. Harris
Analyst, 110, (1985), 649

7.3 Physical Chemistry
J.H. Noggle
Little, Brown and Company, Toronto, (1985)

7.4 Mathematical Methods for Physists, Third Edition
G. Arfken
Academic Press, Inc., N.Y., (1985)

7.5 A) E.R. Andrew and R.G. Eades
Nature, 182, (1958),, 1659;
B) Nature, 183, (1959), 1802;
C) Proc. Roy. Soc. (London) A216, (1953), 398

7.6 High Resolution Solid State NMR of Silicates and Zeolites
G. Engelhardt and D. Michel
John Wiley, N.Y., (1987)

7.7 C.A. Fyfe, Y.Feng and H. Grondrey
Microporous Materials, 1, (1993) 393-400

7.8 CRC
Chemical Rubber Publishing Company, US, (1990)

7.10 Murray R. Spiegel
Mathematical Handbook of Formulas and Tables
Schaum's Outline Series
McGraw-Hill Book Company, Toronto, (1968)

Appendix 1 : First approximation of the TEOS kinetic constants

Average pH dependent kinetic rate constants ($M^{-1}min^{-1}$) for the reaction of TEOS determined from the non-linear least squares fitting of equations (3.13)-(3.16).

pH	k_{T1}	k_{T2}	k_{T3}	k_{T4}
3.35	0.00049±0.00005	0.002±0.0005	0.0091±0.0005	0.003±0.001
3.04	0.00039±0.00008	0.0034±0.0004	0.022±0.001	0.03±0.02
2.88	0.00072±0.00002	0.004±0.0001	0.016±0.001	0.007±0.001
2.76	0.00082±0.00002	0.0065±0.0005	0.04±0.005	0.0073±0.0005
2.55	0.0016±0.0001	0.011±0.001	0.07±0.03	0.014±0.005
2.45	0.0022±0.0002	0.012±0.001	0.05±0.007	0.013±0.001
2.33	0.003±0.0001	0.02±0.004	0.12±0.03	0.023±0.002
2.13	0.0052±0.0002	0.028±0.003	0.1±0.02	0.025±0.003

Appendix 2 : First approximation of the MTES kinetic constants

Average pH dependent kinetic rate constants ($M^{-1}min^{-1}$) for the reaction of MTES determined from the non-linear least squares fitting of equations (4.9)-(4.11).

pH	k_{M1}	k_{M2}	k_{M3f}
3.35	0.0014±0.0003	0.006±0.001	0.0048±0.0002
3.04	0.0037±0.0004	0.015±0.002	0.009±0.0002
2.88	0.005±0.001	0.019±0.003	0.01±0.01
2.76	0.04±0.03	0.1±0.07	0.025±0.005
2.55	0.03±0.01	0.10±0.05	0.029±0.005
2.45	0.0205±0.0005	0.07±0.01	0.037±0.005

Appendix 3 : Schematic of the modifications made to the Bruker MSL 400 spectrometer for ^{19}F to ^{29}Si cross polarization.

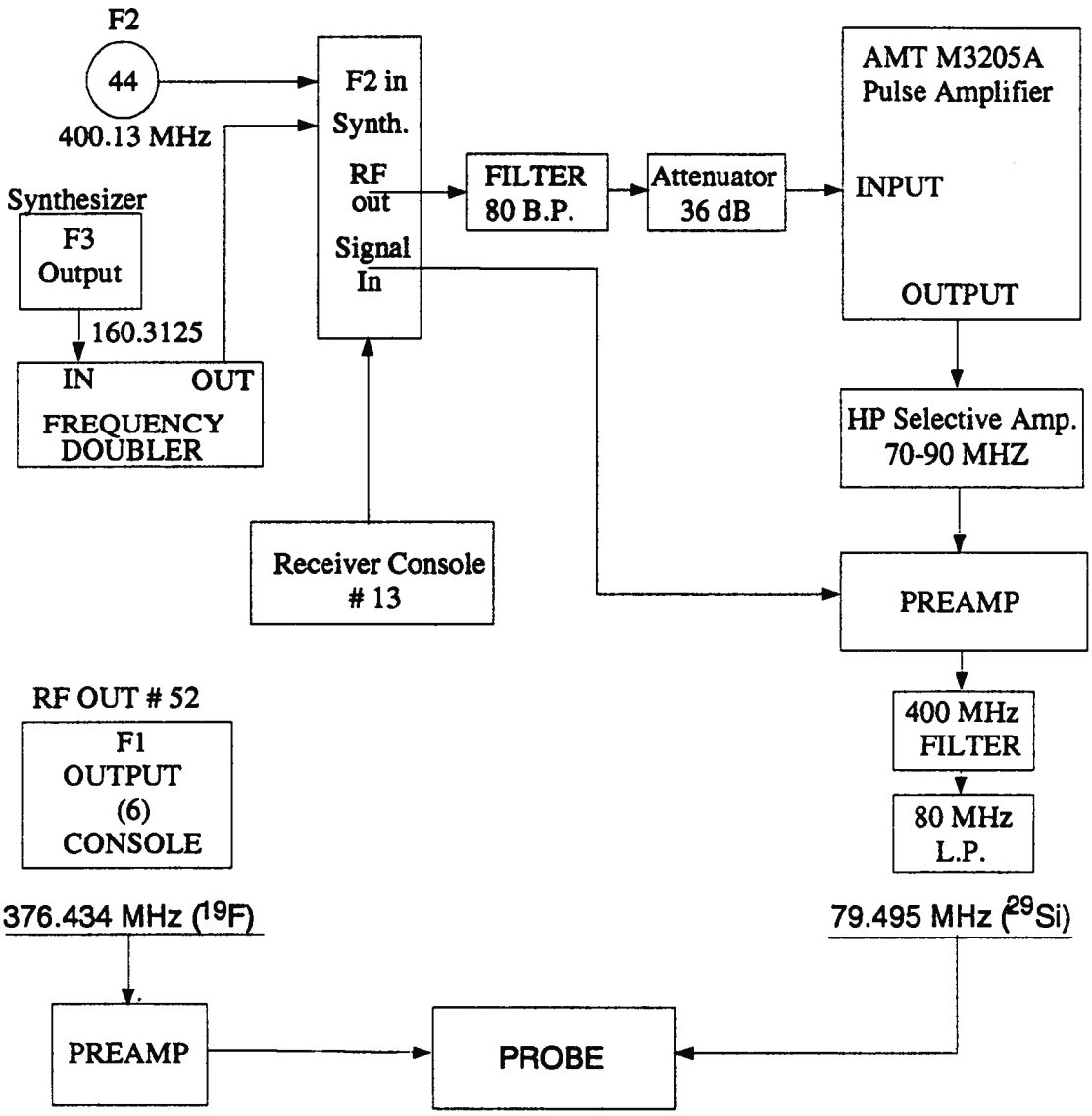

Appendix 4 : Deduction of Equation (7.8)

To solve the heteronuclear second moment in the presence of motion, equation (7.7) must be evaluated. Therefore the term shown in (1) must be evaluated over all the

$$\left[\frac{3\cos^2\theta_{im} - 1}{r_{im}^3} \right]^2 \tag{1}$$

orientations of the vector r_{im} over the motion. The angle between the external magnetic field, B_o, and the the internuclear vector, r_{im}, is θ_{im}. Consider that B_o is along the z-axis of the coordinate system.

Equation (1) can be re-expressed in terms of Legendre Polynomials (P_2) [7.10]:

$$\left[\frac{(3\cos^2\theta_{im} - 1)}{r_{im}^3} \right]^2 = \left[\frac{2P_2(\cos\theta_{im})}{r_{im}^3} \right]^2 \tag{2}$$

From the addition theorem [7.4] of spherical harmonics, the following is true:

$$\left[\frac{2P_2(\cos\theta_{im})}{r_{im}^3} \right]^2 = \left[\frac{8\pi}{5r_{im}^3} \sum_{n=-2}^{n=2} Y_{2n}(\theta_{im},\phi_{im})\, Y_{2n}^*(\theta_2,\phi_2) \right]^2 \tag{3}$$

where Y_{2n} is an orthonormal function called a spherical harmonic, θ_{im} & ϕ_{ij},and θ_2 & ϕ_2 are the spherical coordinates (Figure A4.1) of the internuclear vector before and after motion, respectively. Expressions for the spherical harmonics can be found in references [7.3, 7.4].

If i can occupy p sites and m can occupy q sites equation (3) becomes,

$$\left[\frac{3\cos\theta_{im} - 1}{r_{im}^3} \right]^2 = \left[\frac{8\pi}{5} \sum_{n=-2}^{n=2} Y_{2n}^*(\theta_2,\phi_2) \left[\frac{1}{pq} \sum_{i=1}^{p} \sum_{m=1}^{q} \frac{1}{r_{im}^3} Y_{2n}(\theta_{im},\phi_{im}) \right] \right]^2 \tag{4}$$

Expanding the Associated Legendre Polynomials one obtains:

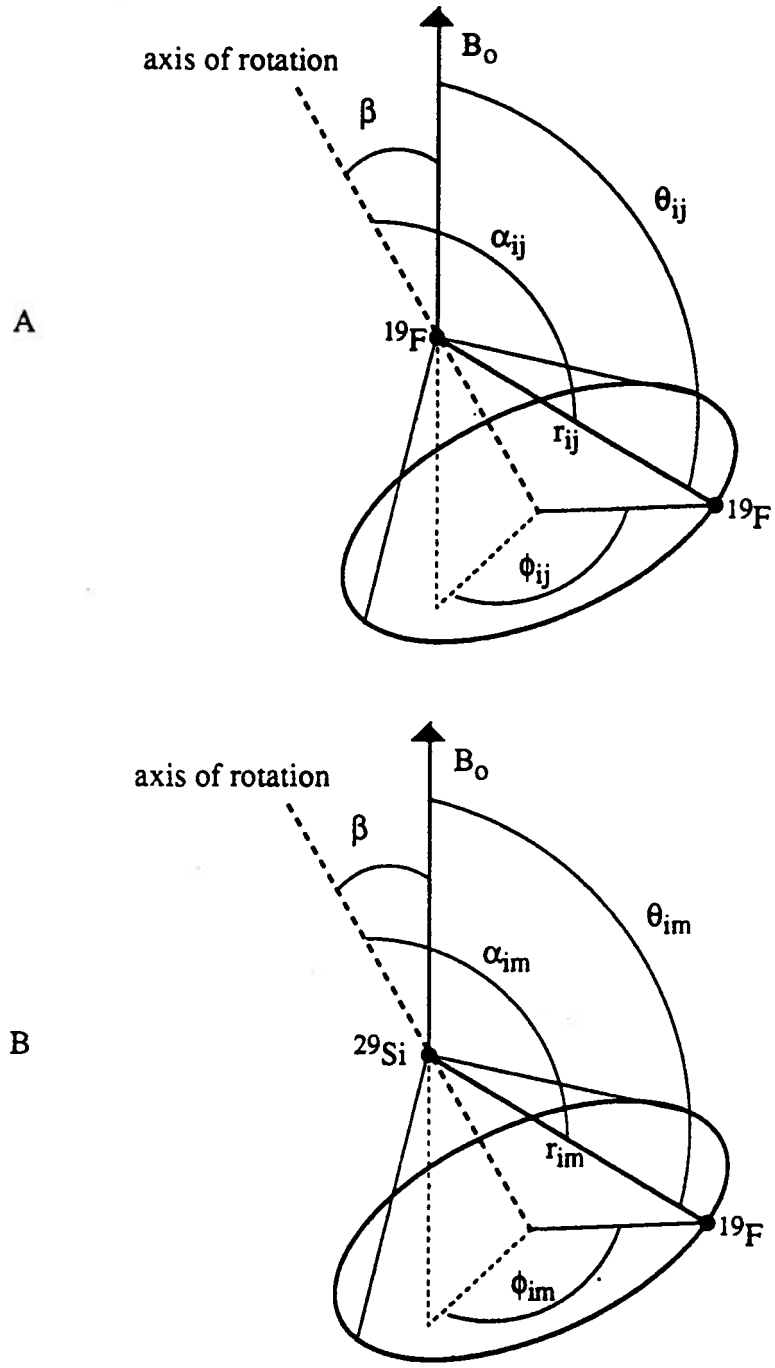

Figure A4.1 - Model for a nuclear pair in motion about an axis with the appropriate angles labelled for
A - the homonuclear second moment equation and
B - the heteronuclear second moment equation.

$$\left\langle \left[\frac{3\cos^2\theta_{im} - 1}{r_{im}^3} \right]^2 \right\rangle =$$

$$\frac{1}{pq}\sum_{i=1}^{p}\sum_{m=1}^{q}\frac{1}{r_{im}^6}\left[\left[\frac{8\pi}{5}\frac{5}{16\pi}(3\cos^2\theta_{im} - 1)\,(3\cos^2\theta_2 - 1)\right]^2 + \left[\frac{8\pi}{5}\frac{5}{12\pi}(3\sin\theta_{im}\cos\theta_{im}\cos\phi_{im})(3\sin\theta_2\cos\theta_2\cos\phi_2)\right]^2 + \left[\frac{8\pi}{5}\frac{5}{12\pi}(3\sin\theta_{im}\cos\theta_{im}\sin\phi_{im})\,(3\sin\theta_2\cos\theta_2\cos\phi_2)\right]^2 + \left[\frac{8\pi}{5}\frac{5}{48\pi}(3\sin^2\theta_{im}\sin 2\theta_{im})\,(3\sin^2\theta_2\sin 2\theta_2)\right]^2 + \left[\frac{8\pi}{5}\frac{5}{48\pi}(3\sin^2\theta_{im}\cos 2\theta_{im})\,(3\sin^2\theta_2\cos 2\theta_2)\right]^2\right] \quad (5)$$

The internuclear vector orientation is described by the spherical coordinates θ_{im} and ϕ_{im}. After some motion these internuclear vectors can have all orientations, so θ_2 and ϕ_2 must be averaged over all space

$$\langle(3\cos^2\theta_2 - 1)^2\rangle = \frac{4}{5}$$

$$\langle(3\sin\theta_2\cos\theta_2\cos\phi_2)^2\rangle = \langle(3\sin\theta_2\cos\theta_2\sin\phi_2)^2\rangle = \frac{3}{5}$$

$$\langle 3\sin^2\theta_2\cos 2\phi_2)^2\rangle = \langle(3\sin^2\theta_2\sin 2\phi_2)^2\rangle = \frac{12}{5}$$

Substituting these values into equation (5), the final form for $\langle(3\cos^2\theta_{ij} - 1)^2/r^6_{ij}\rangle$ is:

$$\left\langle \frac{(3\cos^2\theta_{im} - 1)^2}{r_{im}^6} \right\rangle =$$

$$\frac{1}{p^2 q^2} \sum_{i=1}^{p} \sum_{m=1}^{q} \frac{1}{r_{im}^6} \left[\frac{2(3\cos^2\theta_{im} - 1)^2}{5} \right.$$

$$+ \frac{4(3\sin\theta_{im}\cos\theta_{im}\cos\phi_{im})^2}{15} + \frac{4(3\sin\theta_{im}\cos\theta_{im}\sin\phi_{im})^2}{15} \qquad (7.8)$$

$$\left. + \frac{(3\sin^2\theta_{im}\sin 2\theta_{im})^2}{15} + \frac{(3\sin^2\theta_{im}\cos 2\theta_{im})^2}{15} \right]$$